Flame Simulation in Rotary Kilns Using Computational Fluid Dynamics

von **M.Sc. Hassan Fawzy Mohamed Elattar**
geb. am 24. September 1976 in Kairo, Ägypten

Preface

This dissertation is submitted to Otto-von-Guericke-University, Magdeburg for the degree of Doctor of Engineer. The research described herein was conducted under the supervision of Prof. E. Specht between October 2008 and September 2011. To the best of my knowledge, this work is original, except where suitable references are made to previous works. Neither this, nor any substantially similar dissertation has been submitted for any degree, diploma or qualification at any other university or institution.

Hassan Elattar
Magdeburg, Germany
30 June 2011

If we knew what it was we were doing, it would not be called research, would it?

Albert Einstein (1879-1955)

Acknowledgement

First and foremost, I would like to express my sincere gratitude and appreciation to my supervisor (Doktorvater); **Prof. Dr.-Ing. Echehard Specht**, for his continual support, encouragement and financial support. His knowledge, experience, guidance, and patience have also benefited me immensely. Further acknowledgment goes to **Prof. Dr.-Ing. Dominique Thévenin** who accepted to review my thesis and took over the chair in examination committee. I would also like to express my deepest gratefulness to **Prof. Dr.-Ing. Rayko Stanev** for his repetitive support, for reviewing this dissertation and for valuable comments and suggestions. I am deeply grateful to **Prof. Dr.-Ing. Ulrich Krause** for his elaborated review of my thesis and constructive comments.

I would like to thank all colleagues of the Institute of Fluid Dynamics and Thermodynamics, University of Magdeburg for their assistances, friendships and many enjoyable times. Special thanks are given to **Dr.-Ing. Hemdan Shalaby**, **M.Sc. Essam Elgendy** and **Dipl.-Ing. Fabian Herz** for their help during the writing of this dissertation. Also I would like to thank our department secretary; **Christin Hasemann** for her help in the past three years.

I would like to thank all the Egyptian friends in Magdeburg for their endless sharing and companionship, and also to all my friends in Magdeburg and anywhere else in Germany.

Finally, I would like to take this opportunity to express my warm thankfulness to my father; **Fawzy Elattar**, to my wife; **Rehab Abdelhalim**, to my daughters; **Rofida** and **Rawan**, to my brothers, sisters and to every member in my extended family for their unconditional love and support.

Last but not least I would like to dedicate this work to the soul of my mother, the first teacher in my life.

Hassan Elattar
Magdeburg, Germany
30 June 2011

Contents

Nomenclature

Only commonly used symbols are listed below. The meanings of all other symbols are defined explicitly within the text.

Latin letter symbols

A	$[m^2]$	area
A_g	$[m^2]$	total area of enclosing gas
A_g	$[m^2]$	tangential inlet area of swirl combustor
a	[-]	weighted factor for gray-plus-clear gas model, emissivity
b	[-]	weighted factor for gray-plus-clear gas model, absorptivity
C	[-]	Chapman-Rubesin parameter
Cp	$[kJ/kgK]$	constant pressure specific heat
C_t	[-]	Curtet number
D	$[m]$	kiln diameter or body diameter of swirl combustor
D_e	$[m]$	equivalent diameter
D_H	$[m]$	hydraulic diameter
D_t	$[m]$	burner tube diameter
$\bar{D}$	$[m^2/s]$	average value of molecular diffusion constant
d	$[m]$	initial jet diameter of fuel-nozzle diameter
dA	$[m^2]$	element area
d^*	$[m]$	momentum diameter
$d_{a,i}$	$[m]$	air inlet diameter
E	$[W/m^2K]$	black-body emissive power
F_r	$[-]$	Froude number
f	$[-]$	mixture fraction
f_i	$[1/m\,atm]$	absorption coefficient, absorptivity
G	$[kg/ms^2]$	momentum flux
g	$[m/s^2]$	gravitational acceleration
h	$[kJ/kg]$	specific enthalpy
h_{rad}	$[W/m^2K]$	heat transfer coefficient for radiation
h_u	$[MJ/kg]$	net heating value
$_ch$	$[W/m^2K]$	heat transfer coefficient for convection
I	$[W/m^2]$	radiation intensity
k	$[W/mK]$	thermal conductivity
k_i	$[1/m\,atm]$	absorption coefficient, emissivity
L	$[kg_{air}/kg_{fuel}]$ or $[m]$	stoichiometric air to fuel mass ratio or overall length
l	$[m]$	beam length
$L_{f,c}$	$[m]$	chemical flame length

L_m	$[m]$	radiation mean beam length for gas volume
L_t	$[m]$	burner tube length
$\tilde{L}$	$[m_{air}^3/m_{fuel}^3]$	stoichiometric air to fuel volume ratio
L^*	$[-]$	dimensionless flame length
M	$[kg/kmol]$	molecular weight
m	$[-]$	dimensionless parameter representing the thrust term
$\dot{m}$	$[kg/s]$	mass flow rate
Nu_D	$[-]$	diameter Nusselt number (hD/k)
Nu_{D_H}	$[-]$	hydraulic diameter Nusselt number (hD_H/k)
Nu_x	$[-]$	entrance length Nusselt number (hx/k)
P_r	$[-]$	Prandtl number $(C_p\mu/k)$
p	$[atm]$	partial pressure
Q	$[W]$	heat transfer rate
$\dot{Q}$	$[W/m]$	heat transfer rate per unit of axial length
$q_{f,rad}$	$[W]$	flame heat radiation
q_o	$[MW]$	burner power
$q_{rad}^{"}$	$[W/m^2]$	radiation heat flux
r	$[m]$	radius
Re_D	$[-]$	diameter Reynolds number (uD/ν)
Re_w	$[-]$	rotational Reynolds number (D^2/ν)
Re_x	$[-]$	entrance length Reynolds number (ux/ν)
R'	$[-]$	discharge ratio
Sc_t	$[-]$	turbulent Schmidt number
S_n	$[-]$	swirl number
T	$[K]$	temperature
Th	$[-]$	Thring-Newby number
ΔT	$[K]$	combustion characteristic temperature rise $(T_{ad} - T_\infty)$
u	$[m/s]$	velocity
$\bar{u}$	$[m/s]$	average velocity
$\dot{V}$	$[m^3/s]$	volume flow rate
w	$[m/s]$ or $[rad/h]$	air tangential angular speed
X	$[m]$	axial distance between burner exit and tube entrance
X_{fuel}	$[-]$	fuel concentration
x'	$[m]$	attachment distance
Y	$[-]$	mass fraction

Greek symbols

α	$[-]$	primary air ratio or absorptivity
α_t	$[-]$	stoichiometric ratio of reactant moles to product moles
δ^*	$[m]$	boundary layer displacement thickness
ϵ	$[m^2/s^3]$	turbulent dissipation rate
ε	$[-]$	emissivity
$\bar{\varepsilon}$	$[m^2/s]$	turbulent diffusion constant
η	$[\%]$	degree f solid fill
κ	$[m^2/s^2]$	turbulent kinetic energy
λ	$[-]$	excess air number

μ	$[N.s/m^2]$	dynamic viscosity
ν	$[m^2/s]$	kinematic viscosity (μ/ρ)
ρ	$[kg/m^3]$	density
σ	$[W/m^2 K^4]$	Stephan-Boltzman constant $(5.67 * 10^{-8})$
Φ	[-]	overall radiation exchange factor
ϕ	[-]	equivalence ratio $(air/fuel)_{actual}/(air/fuel)_{stoichiometric}$
Ω	$[rad/h]$	air tangential angular speed to inlet of swirl combustor

Subscripts

Ag	surface of enclosing gas
a	axial direction
ad	adiabatic
a,i	air inlet
cf	coflow
eb	exposed bed surface
ew	exposed wall surface
f	flame
g	gas
i	index
mi	end of the capture path
mj	microjet
o	nozzle fluid
ox	oxidizer
p	primary jet
pa	primary air
r	radial direction
rad	radiation
S	surface
s	secondary
sa	secondary air
st	stoichiometric
w	wall
∞	ambient gas

Abbreviations

CCD	Charge Coupled Device
CFD	Computational Fluid Dynamics
cpu	Central Processing Unit
DO	Discrete Ordinates
DLR	Deutschland für Luft und Raumfahrt
DTRM	Discrete Transfer Radiation Model
IFRF	International Flame Research Foundation
LHV	Lower Heating Value
LPG	Liquified Propane Gas
MAS	Mono Airduct System
NCG	Non Condensible Gases

NOx	Nitrogen Oxide air pollutants
pct	percentage
PFAR	Primary (atomizing) Air-Fuel mass flaw rate Ratio
RDF	Refused Derived Fuel
RNG	Renormalization group theory
rpm	revolutions per minute
RSM	Reynolds Stress Model
RTE	Radiation Transfer Equation
tpd	tons per day
TRS	Total Reduced Sulfur
UDF	Used Defined Functions
VOC	Volatile Organic Compounds
WSGGM	Weighted Sum of Gray Gases Model

Abstract

Rotary kilns have been widely used in industry beginning from calcination of limestone to cement manufacturing and incineration of waste materials, etc. These kilns have been used and continuously improved for over a century. CFD simulation has aided in design and operation of rotary kilns over several years. The literature review revealed that the information related to flame shape (e.g., flame length), thermal distribution (e.g., gas and wall temperatures, and radiation heat flux) and flow visualization inside rotary kilns are still not completely understood. In a trial to fill a part of the gap existing in this field, the present work was carried out. The flame is the source of heat inside the rotary kilns, which controls the processes and is responsible for the thermal distribution of combustion gas, solid bed and kiln wall.

Thermal processing of materials within rotary kilns includes energy generation by combustion and in consequence heat transfer by turbulent diffusion and radiation to the charge (the bed) and refractory walls. Hence the heat transfer, flame behavior and the combustion process can significantly effect on processing conditions. Proper burner design and flame control ensure high fuel utilization efficiency, long life time of the refractory lining (kiln walls), low pollutant emissions and high product quality. In the light of these facts, computational fluid dynamics (CFD) techniques using industrial flow simulation code (ANSYS-Fluent) have been used. An axi-symmetry 2D and 3D simulations have been assumed in order to simulate the steady state free jet, confined jet and rotary kiln flames. Furthermore, the simulated results have been validated against experimental measurements which obtained from literature. Therefore, this work accomplished in three main stages.

Firstly, a 2D-CFD simulation model for free jet flame was developed in order to give basic information about influencing parameters on the flame behavior as well as a preliminary step for confined jet flame simulation. In this stage, three burner geometries have been assumed and simulated to present the effects of operating and geometrical parameters on the flame length. Whereas, the flame length increases with increasing air temperature, burner annulus diameter and annulus air swirl number. On the other side, the fuel velocity and wall-supported burner have approximately no effect on the flame length. Furthermore, flame length correlations in dimensionless form in terms of air demand (mass basis), stoichiometric mean mixture fraction, fuel density and density of stoichiometric mixture were developed within reasonable errors. As well a comparison between predicted free jet flame length correlation and empirical correlation from literature was accomplished and gave error within $\pm 9.4\,\%$.
As stated by this basis and to minimize computational time, a 2D-CFD simulation model for confined jet flame was developed to investigate the flame behavior under three different confinements and burner configurations. The simulation model was applied for

a big cylinder of 2.6 m diameter by 20 m cylinder length in order to simulate the flame behavior in industrial rotary kilns. The reported results confirmed that the flame length increases with increasing of air inlet diameter, annulus air diameter and primary air swirl number in case of use fully opened cylinder configuration. On the other hand the flame length decreases with increasing both of excess air number and annulus air swirl number in case of use fully closed cylinder configuration. In addition to, dimensionless flame length correlations were obtained and presented in terms of air demand (mass basis), excess air number, stoichiometric mean mixture fraction, fuel density, density of stoichiometric mixture and dimensionless air inlet diameter. Comparisons between experimental measurements and simulated results were performed and gave satisfactory agreement.

Finally, to avoid undesirable thermal behavior in an industrial rotary kilns, as well to close as possible to actual kiln dimensions and operations, a 3D-CFD simulation model for full scale rotary kiln flame was accomplished and presented for 4 m diameter by 40 m kiln length, which is more typical of industrial scale. New influencing parameters were introduced to study such as, primary air ratio, burner configuration (two configurations with different fuel jet momentums), and burner power. The effects of these parameters on the flame length and radiant heat transfer inside the rotary kiln have been investigated and discussed. The reported results revealed that, the flame length was effectively increased by reducing both of the fuel jet momentum and primary air ratio. On the other hand the results demonstrated that, magnitude and location of the peak wall temperature (wall hot spots) can be relocated by changing the flame aerodynamics. Furthermore, the peak wall temperature can be achieved by operating the kiln at higher burner power and lower fuel jet momentum. Based on obtained results, operators were given guidance on how the controllable burner parameters might be adjusted to reduce wall hot spots and to improve product quality in addition to control the ringing problems.

Zusammenfassung

Drehrohrohröfen werden in vielen Bereichen der Industrie, wie z.B. zur Kalzination von Kalkstein, zur Zementherstellung oder zur Müllverbrennung, verwendet. Sie werden seit Jahrzehnten genutzt und stets weiterentwickelt. Seit einigen Jahren lassen sich CFD Simulationen zur Auslegung und zum Betrieb von Drehohröfen nutzen. Wie die Literaturrecherche zeigt, bestehen hinsichtlich der Flammenform (z.B. Flammenlänge), der thermischen Verteilung (d.h. Gas- und Wandtemperaturen und Strahlungswärmestrom) und der Strömungsvisualisierung Informationsdefizite. Um diese Defizite teilweise auszugleichen, wurde die vorliegende Arbeit verfasst. Die Flamme bildet die Wärmequelle im Innern von Drehrohröfen und ist somit die Prozesssteuergröße und verantwortlich für die thermische Verteilung des Verbrennungsgases, des Stoffbettes und der Ofenwand.

Zur thermischen Behandlung von Materialien in Drehrohröfen wird die notwendige Energie durch die Verbrennung erzeugt und dabei die Wärme durch die turbulente Diffusion und Strahlung auf das Bett und die Ofenwand übertragen. Daher nehmen der Wärmetransport, das Flammenverhalten sowie der Verbrennungsprozess einen wesentlichen Einfluss auf die Prozessbedingungen. Eine exakte Brennerkonstruktion und Flammenkontrolle gewährleisten effizienten Brennstoffumsatz, lange Lebensdauer der Feuerfestauskleidung, geringe Schmutzemission und hohe Produktqualität. Mit diesem Hintergrund wird die numerische Strömungssimulation (CFD) mit dem industriellen Code (ANSYS-Fluent) angewendet. Eine achsensymetrische 2D und 3D Simulation wurde für den stationären Freistrahl, den eingeschlossenen Strahl und die Drehrohrofenflamme durchgefhrt. Des Weiteren wurden die simulierten Ergebnisse mit experimentellen Messungen aus der Literatur validiert. Somit untergliedert sich diese Arbeit in 3 wesentliche Abschnitte.

Als einleitenden Schritt zur Simulation der Strahlflamme in begrenzten Räumen, wurde ein 2D-CFD Simulationsmodell für die Freistrahlflamme entwickelt. Um hierbei die grundlegenden Einflüsse der Betriebs- und Dimensionsparameter auf die Flammenlängedarzustellen, wurden 3 Brennerkonstruktionen berücksichtigt und simuliert. Die Flammenlänge nimmt hierbei mit steigender Lufttemperatur, Brennerdüsendurchmesser und Luftdrallzahl zu. Andererseits haben Brennstoffgeschwindigkeit und wandgestützte Brenner annähernd keinen Einfluss auf Flammenlänge. Zudem wurden Flammenlängenkorrelationen in Abhängigkeit vom Luftbedarf, des stöchiometrischen Mischungsanteils, der Brennstoffdichte und der Dichte des stöchiometrischen Gemisches entwickelt. Ein Vergleich zwischen den korrelierten Längen der Freistrahlflammen und den empirischen Korrelationen aus der Literatur ergeben eine Abweichung unter ±9,4%. Auf dieser Grundlage wurde ein 2D-CFD Simulationsmodell für die eingeschlossene Strahlflamme entwickelt, um das Flammenverhalten bei 3 verschiedenen Brennerkonfigurationen zu untersuchen. Ein Zylinder mit D = 2,6 m und L = 20 m diente

der Modellanwendung und konnte zur Darstellung des Flammenverhaltens in Industrieöfen angewendet werden. Für den Fall eines offenen Zylinders zeigt sich, dass die Flammenlänge mit zunehmendem Lufteinlass- und Ringspaltdurchmesser sowie mit steigender Luftdrallzahl größer wird. Andererseits verringert sich die Flammenlänge mit steigender Luftzahl und Ringspalt-Drallzahl für den Fall des geschlossenen Zylinders. Zusätzlich wurden Flammenlängenkorrelationen in Abhängigkeit vom Luftbedarf, derLuftzahl, des stöchiometrischen Mischungsanteils, der Brennstoffdichte, der Dichte des stöchiometrischen Gemisches und des dimensionslosen Lufteinlassdurchmessers aufgezeigt. Ein Vergleich mit experimentellen Messergebnissen liefert hinreichend genaue Übereinstimmung.

Um das thermische Verhalten innerhalb des Drehrohres realitätsnah zu berücksichtigen, wurde ein 3D-CFD Simulationsmodell für die voll ausgebildete Flamme in einem Drehrohrofen mit typisch industriellen Abmessungen von $L = 40$ m und $D = 4$ m entwickelt. Neue Einflussparameter, wie die Primärluftverhältnis, die Brenneranordnung (2 Anordnungen mit verschiedenen Brennstoffdüsenimpulsen) und die Brennerleistung wurde eingeführt und untersucht, wobei insbesondere die Auswirkungen dieser Parameter auf die Flammenlänge und den Strahlungswärmeübergang analysiert wurden. Die Ergebnisse zeigen, dass eine Verringerung des Brennstoffdüsenimpulses und Primärluftverhältnisses eine Vergrößerung der Flammenlänge bewirkt. Zudem wird ersichtlich, dass sich sowohlder Betrag als auchdie Position der maximalen Wandtemperatur mit Änderung der Flammenströmung verschieben. Die maximale Wandtemperatur wird bei höherer Brennerleistung und geringerem Impuls der Brennstoffdse erreicht. Die ermittelten Ergebnisse dienen für Drehrohrofenbetreiber als Anleitung, wie sich eine Variation der Brennerparameter auf die maximale Wandtemperatur und die Produktqualität auswirken kann.

Chapter 1

Introduction

1.1 Rotary kiln in the industry

A Rotary kiln is a pyroprocessing device used to raise materials to a high temperature (calcination) in a continuous process. Pyroprocessing is a process in which materials are subjected to high temperatures (typically over 800 °C) in order to bring about a chemical or physical change [1].

Rotary kilns are found in many processes that involve solids processing. These include drying, incineration, mixing, heating, roasting, cooling, humidification, calcination, reduction, sintering, melting, gasification, dehydration and gas-solid reactions [2]. Rotary kilns are widely fixtures of the chemical, metallurgical and pharmaceutical process industries. They are capable of operating at high burning zone temperature, for example: burning of cement clinker (2000 °C) [3], calcination of aluminium oxide (1300 °C) [4, 5], lime burning (1200 °C) [6], calcination of petroleum coke (1100 °C) [4]. The most common and industrially important application of rotary kilns is in cement production; all major producers use the rotary kiln as their equipment of choice. Cement kilns can be very large. Fig. 1.1 shows a 5500 tpd cement kiln from FLSmidth Inc. [7].

Another important application of rotary kilns is for the incineration of waste materials. Rotary kilns are popular for this role because of their flexibility. They can handle a large variety of feed materials, with variable calorific value, and removal of waste solids at the exit presents no problems. Typically, hazardous waste incinerators operate with relatively deep beds, and have a secondary combustion chamber after the rotary kiln to improve the heterogeneous combustion of waste [8, 9]. An example of such a hazardous waste incinerator is shown in Fig. 1.2. Also rotary kilns are used for gasification of waste tires or wood to obtain activated carbon [10, 11], in addition to thermal desorption of contaminated soils [12, 13].

Rotary kilns are amongst the most well-established unit operations in the process industry, yet are amongst the least understood. They can be used for 3 purposes: heating, reacting and drying of solid material, and in many cases, they are used to achieve a combination of these aims. In the design of kilns, there are four important aspects to consider from a process engineering point of view, and these are heat transfer, flow of material through the rotary kiln, gas-solid mass transfer and reaction [15]. Heat transfer rates amongst the most important of these aspects, because in many cases, it is

Figure 1.1: Rotax-2 cement kiln for 5500 tpd [7].

Figure 1.2: Rotary kiln waste incinerator [14].

the heat transfer that limits the performance of the rotary kiln, and it is strongly related with flame characteristics.

The characteristics of the burner flame (or flame patterns) can greatly affect kiln operation. The efficiency of the kiln depends on the effective heat transfer from the flame to solids. Because the burners are the only heat source in the kiln, their flame characteristics and patterns, i.e. length, shape and intensity, are critical to the kiln operation and performance. Flame characteristics strongly affect the rate of heat transfer, and therefore fuel consumption, product quality, Total Reduced Sulfur (TRS) emissions,

NOx emissions, and refractory life. The flame patterns also play an important role in the formation of mid kiln rings, which is a serious problem that reduces the kiln efficiency and increases its maintenance cost. An unstable flame causes a wide variation of gas temperatures. Short bushy flames can damage the refractory lining, while long lazy flame may not deliver enough heat to complete the reaction. As a result, it is important to optimize the flame shape and length. Flame characteristics are often influenced by geometric and operating factors related to fuel and combustion. These include the fuel type and flow rates. The fuel-to-primary air ratio and the primary air-to-secondary air ratio are important as well. Controlling the kiln flame characteristics is not an easy task because of the fluctuations in operating parameters that affect the operation of the kiln and its flame [16].

1.2   Scope on the thesis

1.2.1   Objectives

A precise numerical model can yield important information about the steady-state and dynamic characteristics of the combustion process. This information is necessary for the design of better control strategies and cost-saving improvements. Application of modeling and simulation techniques using CFD modeling is particularly beneficial for systems, such as rotary kilns, where experimentation on the actual process would prove to be very costly and time consuming. There is still a difference of opinion among equipment manufactures and users concerning the necessary features of the rotary kiln required to achieve optimum performance at minimum cost. The cost of fuel usually about 60 pct of the total production cost. A proper kiln and burner design and operation can help maximize environmentally and economically viable processes, while the role of a burner is the delivery of the thermal energy needed to drive the kiln processes.

In engineering industry and dispersion modeling, there is an increasing use of Computational Fluid Dynamics models (CFD) in combustion field, especially in calculating turbulent non-premixed diffusion flame which used in industrial furnaces like rotary kilns. In addition, measurement of internal parameters of the kiln is difficult to perform. In spite of recent progresses, the numerical modeling (CFD) of flame length in rotary kilns has remained an incompletely solved problem. The efficiency of the rotary kiln depends on how effectively the heat from the burner flame can be transferred to the solid particles as they move through the kiln. Since most direct heat rotary kilns operate in the thermal efficiency range of 30% to 40%, huge energy loss is apparent [17]. Since the burner is the only source of heat in the kiln, it produces the flame patterns (such as flame length, shape, and intensity). The flame patterns are critical to kiln operation and performance i.e. the flame pattern influences the heat transfer and, consequently, the product quality, emissions, and refractory life.

In the light of these facts, the economic and environmental importance of studying the flame pattern and flow visualization in rotary kilns is evident. Partial modeling such as fluid flow, solid flow, heat transfer, and flame utilizing empirical correlations that are limited in their range of application, has been a standard practice for design and optimization of rotary kilns.

From the above discussion, the objectives of this research accomplished in three stages as follows:

- Carrying out 2D numerical simulation with a commercial CFD code (FLUENT 6.3) to simulate free jet diffusion flame, utilizing axi-symmetric modeling. It was considered as a basic part for turbulent non-premixed diffusion flame simulation and its validation and as a preliminary step for confined flame simulation. In this part three burner geometries will study and discuss showing effect of operating and geometrical parameters on the flame length; plain tube burner, annulus tube burner, and wall-supported annulus tube burner.

- 2D numerical simulation using axi-symmetric CFD model of confined jet flame to study influence the jet confinement, boundaries, and geometrical parameters on the flame length will investigate and discuss, using three confinement and burner geometries; simple tube burner with variable air inlet diameter size, annulus tube burner with fully opened cylinder for secondary air, and annulus tube burner with fully closed cylinder for secondary air.

- Developing 3D-CFD geometrical axi-symmetric model for full scale rotary kiln flame simulation will present and discuss to examine the influence of kiln operating conditions and burner geometrical parameters on the flame behavior (aerodynamics and heat transfer) inside the rotary kilns, using two burners configurations, firing gas fuel.

1.2.2 Outline of the thesis

The thesis outline is as follows: Chapter 2 presents a review of common features of the rotary kilns and the factors affecting flow field (aerodynamics), heat transfer, and flame length inside the rotary kilns. Finally a review of the state of progress in the modeling of rotary kilns was presented.

In Chapter 3; computational methodology involves governing equations, turbulence and combustion modeling using FLUENT code, also the steps involved in the development of the steady state model for flame simulation including (mesh generation, mesh independence study, turbulence model selection, and model validation) were developed and presented.

Chapter 4 discussed the burner design factors on the free jet flame length for three burner types (simple tube burner, annulus tube burner and annulus tube burner with supported wall). The influencing factors include fuel kind, fuel nozzle diameter, fuel velocity, air swirl number were presented and discussed. Three different gases were used with a wide range of stoichiometric air demand. General flame length correlations in terms of stoichiometric air demand, stoichiometric mixture fraction and fuel to stoichiometric mixture density ratio were developed and compared with experimental correlation and showed good agreement.

In Chapter 5, the effects of fuel kind, excess air number, combustion air temperature, burner annulus diameter, air inlet diameter and annulus air swirl number on the flow field (flow visualization) and flame length for both plain tube and annulus tube gas

burners were performed and discussed. In addition to, flame length correlations in terms of the previous parameters were investigated and presented, also comparisons between numerical solutions and experimental measurements with and without burner annulus air swirl were performed and gave satisfactory agreement.

In Chapter 6, the effects of primary air ratio, burner configuration and burner power were discussed and presented on the rotary kiln flame aerodynamics and heat transfer using two different burner configurations.

In Chapter 7, the summary and conclusions were presented. Finally, Chapter 8 presents recommendations for future work .

Chapter 2

Literature Review

In this Chapter, a brief description of the common features in rotary kilns is presented. Factors affecting heat transfer, flow field (aerodynamics), flame length and radiation are discussed. Finally, a review of literature discussing the progress that leads to the current state of kiln modeling.

2.1 Diffusion flame and flame length definitions

2.1.1 Turbulent diffusion flame

Turbulent diffusion flames owe their name to the rate determining mechanism that controls the combustion in many applications: namely diffusion. In industrial furnaces, fuel and oxidizer are injected separately [18]. Mixing then occurs by turbulent and eventually molecular diffusion. Only when fuel and oxidizer are mixed at the molecular scales, combustion can take place. In diffusion flame only fuel issues from the tube as shown in the Fig. 2.1. It mixes with the surrounding air by convection and diffusion while combustion occurs already. Optimal conditions for combustion, however, are restricted to the around of the surface of stoichiometric mixture. This is the surface where fuel and air exist locally at a proportion that allows both to be entirely consumed. This will lead to the highest flame temperature and due to the temperature sensitivity of the chemical reactions to the fastest reaction rates. This is the reason why those flames, where the reactants are non-premixed, are called diffusion flames. In a diffusion flame, combustion takes place at the flame surface only, where the fuel meets oxygen in the right concentration - the interior of the flame contains unburnt fuel. This is opposite to combustion in a premixed flame. The fire breather's spurting of fuel (likely kerosene), combined with strong convection flows due to intense heat gives a turbulent diffusion flame (see Fig. 2.2)

All practical combustion systems are turbulent in nature and often have some form of recirculation region to stabilize the combustion. Laminar flames are impractical since they rely on either thermal (premix) or molecular (non-premixed) diffusion to occur, both of which are slow processes. Turbulence has the effect of greatly enhancing the mixing in systems and thus greatly enhances the local combustion intensity. It said that to have a successful system you need the three T's of combustion:
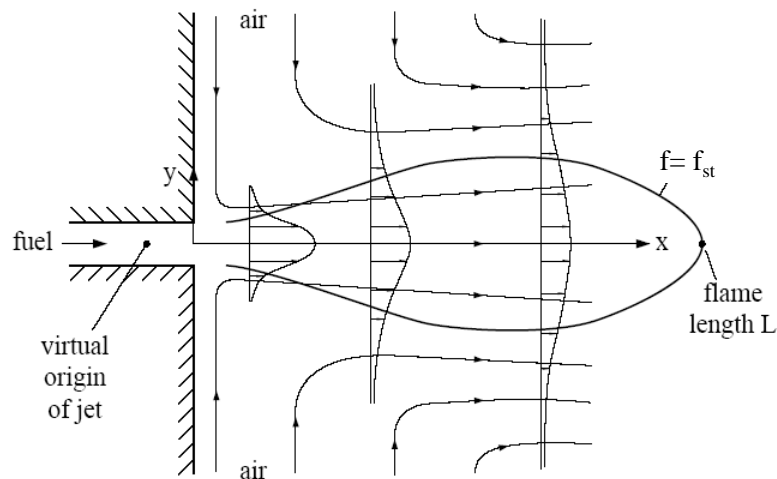
- Time

Figure 2.1: Plane jet diffusion flame.

Figure 2.2: Turbulent diffusion flame [19].

- Temperature

- Turbulence.

Studies of turbulence show how the unstable mixing layer between the fuel and oxidant or hot products allows entrainment and hence increases the mixing and/or ignition of fresh mixture. For turbulent jet diffusion flames, the result of increased jet speed and hence turbulence actually results in a reduction rather than increase in flame length. Often turbulence alone is still not enough for a stable flame, depending on the combustion intensity required. Recirculation is used as a method of increasing this yet higher. Recirculation may be achieved by one or a combination of three methods.

1. Bluff body recirculation: The body produces a low pressure region behind it which draws gas into it in a recirculation flow pattern. Fuel is injected into this zone and continually re-ignited sustaining combustion. Studies of the combustion behind bluff bodies show that they approximate to a well stirred reactor.

2. Swirl: A very common method, if a swirling component is placed on the flow by means of some form of swirler on the air or fuel streams, the resulting centrifugal force throws the flow outwards in a spiralling motion. Again a low pressure region is produced which draws flow back into the center. This phenomenon is known as vortex breakdown and occurs in flows where the ratio of tangential to axial momentum.

3. Sudden Expansion: This method relies on the sudden expansion of a confined jet into a co flowing stream. The entrainment "appetite" of the jet forces it to draw in products from downstream resulting in a donut shaped vortex around the base of the jet.

In practice, the gas burners have a huge number of different technical solutions than the other burners (i.e., liquid and gas burners), so these burners were preferred by the specialists in design and exploitation of industrial burners. The burners without preliminary mixing (i.e., non-premixed) are appropriate for high-calorific gases. These burners have a wide range for regulation for their power. Furthermore, they provide an opportunity for working with different gases. As well, these burners are preferred for direct radiation heat exchange, with a concentrated input of heat to the processed material in the furnace. Also they allow high temperature of preheating of the media, which gives a possibility for considerable economy of fuel [18].

2.1.2 Flame length definitions

Interest in being able to explain and predict turbulent jet flame lengths has a long history. The earliest, and now classical, studies are those of Hottel [20], Hawthorne *et al.* [21], and Wohl *et al.* [22] reported in the late 1940s and early 1950s. Major reviews of this subject were performed by Becker and Liang [23] and, more recently, by Delichatsios [24] and Blake and McDonald [25]

Many definitions and techniques for measuring flame lengths are found in the literature, and no single definition is accepted as preferred. Therefore, care must be exercised in comparing results of different investigators and in the application of correlation formulae. Common definitions of flame length include

- visual determinations by a trained observer,

- averaging a number of individual instantaneous visible flame lengths from photographic records,

- measuring the axial location of the average peak center line temperature using thermocouples,

- measuring the axial location where the mean mixture fraction on the flame axis is the stoichiometric value using gas sampling.

In general, visible flame lengths tend to be larger than those based on temperature or concentration measurements. For example, reference [26] reports temperature-based flame lengths to range between approximately 65 percent and 80 percent of time-averaged visible lengths, depending on fuel type.

2.1.3 Factors affecting flame length

For vertical flames created by a fuel jet issuing into a quiescent environment, four primary factors determine flame length:

- Relative importance of initial jet momentum flux and buoyant factors acting on the flame, Fr_f.

- Stoichiometric mixture fraction, f_{st} .

- Ratio of nozzle fluid to ambient gas density, ρ_o/ρ_∞

- Initial jet diameter, d_o

The first of these factors, the relative importance of initial momentum and buoyancy, can be characterized by a flame Froude number, Fr_f . For turbulent jet flames, the following definition of the flame Froude number is useful [24]

$$Fr_f = \frac{u_o f_{st}^{3/2}}{\left(\frac{\rho_o}{\rho_\infty}\right)^{1/4} \left[\frac{\Delta T}{T_\infty} g d_o\right]^{1/2}} \tag{2.1}$$

Where ΔT is the characteristic temperature rise resulting from combustion. Another similar definitions are defined in the literature [23] and [27]. For very small values of Fr_f, flames are dominated by buoyancy, while for very large values, the initial jet momentum controls the mixing and, hence, the velocity field within the flame. Figure 2.3[1] shows how increases mixing, produced from buoyancy-induced motion, results in relatively shorter flames in comparison with nonbuoyant case. The remaining three factors are important regardless of whether or not buoyancy exerts an influence. For example, fuels with small values of stoichiometric mixture fraction, f_{st} require greater quantities of air to be entrained per unit mass of fuel to achieve stoichiometric proportions in comparison with fuels with large values of f_{st}. This implies longer flames for smaller stoichiometric mixture fractions. As an illustration, the stoichiometric air requirement of propane is about six times that of carbon monoxide, and a propane flame is approximately seven times longer than a carbon monoxide flame [21]. The density ratio, ρ_o/ρ_∞, and initial jet diameter, d_o, can conveniently be combined as a single parameter, frequently referred to as the momentum diameter, d_o^*, and defined as

$$d_o^* = d_o \left(\rho_o/\rho_\infty\right)^{1/2} \tag{2.2}$$

Experimental results showing the combined influence of the four primary factors affecting flame length, discussed above, are shown in Fig. 2.4. The flame Froude number, Fr_f , appears as the abscissa, while the remaining three factors are used to define a dimensionless flame length, which is plotted on the ordinate, and given by

$$L^* = \frac{L_f f_{st}}{d_o \left(\rho_o/\rho_\infty\right)^{1/2}} \tag{2.3}$$

or

---

[1]This figure is used based on license agreement between the author and Elsevier with license number of 264412028418.
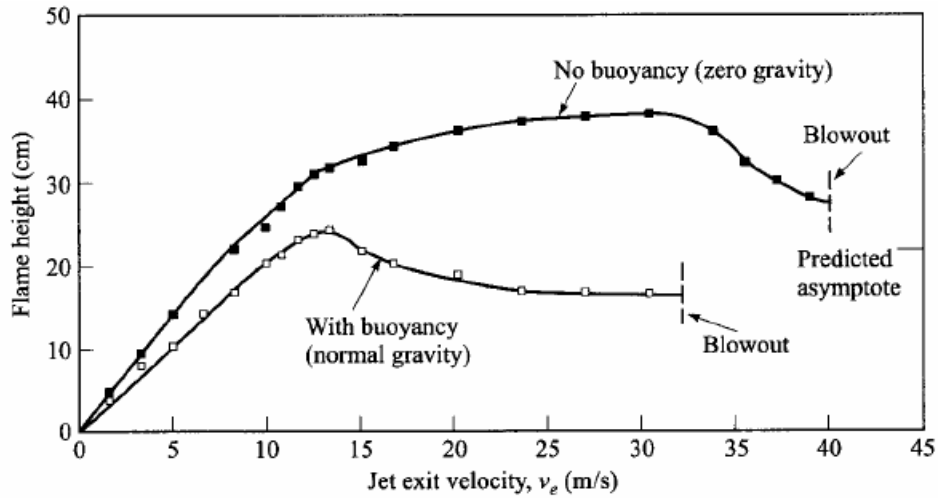
Figure 2.3: Comparison of jet flame height with and without buoyancy [28].

$$L^* = \frac{L_f f_{st}}{d_o^*} \tag{2.4}$$

Two regimes are identified in Fig. 2.4: a buoyancy-dominated regime that is correlated by the expression

$$L^* = 13.5 Fr_f^{2/5} \quad (\text{for } Fr_f < 5) \tag{2.5}$$

And a momentum-dominated regime where the dimensionless flame length L^* is constant, i.e.,

$$L^* = 23 \quad (\text{for } Fr_f \geq 5) \tag{2.6}$$

Another correlations have been proposed [23]; however, the above are easy to use and probably as accurate as others. As previously discussed, various investigators use different definitions and experimental techniques to determine flame lengths; hence, the accuracy of any correlation depends on the consistency of the database used to establish it. The data points shown in Fig. 2.4 represent averages of measurements taken from individual video frames.

Another experimental flame length correlation was developed by Hawthorne [21] and reported by Peters [29], the flame length L_f is given as

$$\frac{L_f}{d_o} = \frac{5.3}{f_{st}} \left(\frac{\rho_o}{\rho_{st}} \right)^{1/2} \tag{2.7}$$

Here the analytical flame length correlation was presented by Peters [29]. To provide understanding the basic properties of the jet diffusion flames, he considered the easiest case, the axisymmetric jet flame without buoyancy. He considered a fuel jet issuing from a round nozzle with diameter d and exit velocity u_o into a surrounding air stream which may have a constant co-flow velocity of $u_\infty < u_o$. The indices o and ∞ denote conditions at the nozzle and in the ambient air, respectively. The flame length is then defined as the
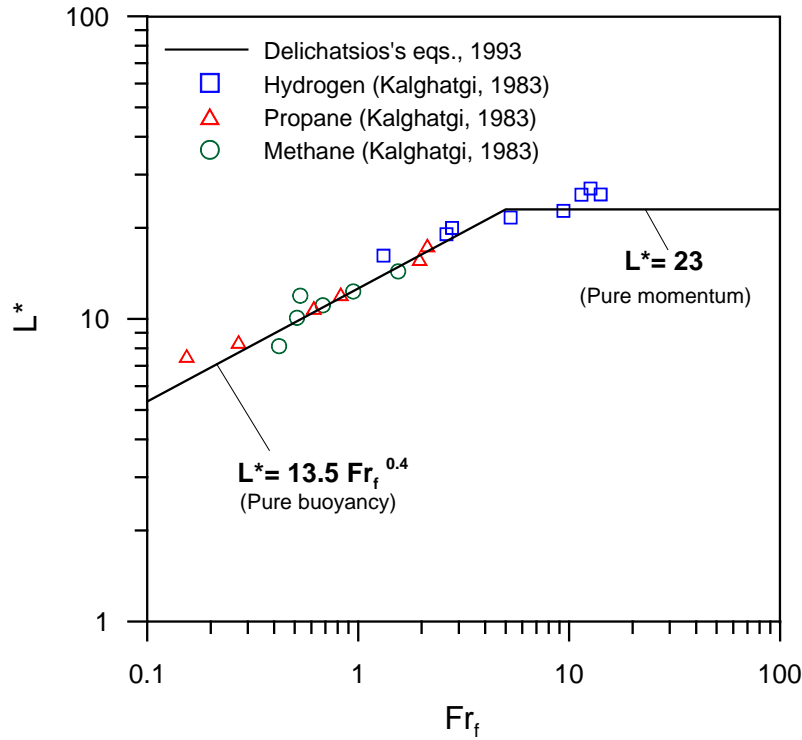
Figure 2.4: Flame lengths for jet flames correlated with flame Froude number [24].

distance from the nozzle on the centerline of the flame where the mean mixture fraction is equal to the stoichiometric value f_{st}. So the flame length is given by

$$\frac{L_f}{d_o} = \frac{2.19\,(1 + 2Sc_t)}{f_{st}} \frac{\rho_o}{\rho_\infty C} \tag{2.8}$$

The experimental correlation suggested by Hawthorne [21] (see equation 2.7). This fixes the turbulent Schmidt number as $Sc_t = 0.71$ and the Chapman-Rubesin parameter as

$$C = \frac{(\rho_o \rho_{st})^{1/2}}{\rho_\infty} \tag{2.9}$$

Peters [29] gives an approximation for flame length, by setting the molecular weight at the stoichiometric mixture equal to that nitrogen, thereby estimating the density ratio ρ_o/ρ_{st} from

$$\frac{\rho_o}{\rho_{st}} = \frac{M_o}{M_{N_2}} \frac{T_{st}}{T_o} \tag{2.10}$$

Here T_{st} is the combustion gas temperature at stoichiometric mixture, so it is assumed the maximum flame temperature. The flame length may then be calculated from Eqn. 2.7 for Methane ($f_{st} = 0.055$) at ambient condition as $L_f \approx 200 d_o$.

2.2 General characteristics of rotary kilns

As shown in Figure 2.5, rotary kilns are typically cylindrical, refractory- brick lines steel casing that may be from 30 to 230 m in length, and 2 to 8 m in internal diameter, inclined

to horizontal at about 2°, and rotating at about 1 RPM [30]. The granular material or bed is introduced at the elevated end, and is transferred by combined effects of rotation and gravity towards the firing end, where energy is supplied by a turbulent diffusion flame issuing from a burner. Hot gases pass along the kiln, sometimes in the same direction as the process material (co-current), but usually in the opposite direction (counter-current). However, industrial kilns are normally operated (counter-current). The burner is enclosed within the firing-hood, which is connected to a cooler. In some kilns; the burner is simply a pipe that supplies the primary air and fuel. Many kilns have more sophisticated burners. The next section explains many different types of rotary kiln burners. Depending on the current cost of fuels such as natural gas, fuel oil, coal and petroleum coke, these types of burners allow kiln operators to switch fuels on a short notice. The secondary combustion air is preheated in the cooler where the hot processed material is flowing in counter-current manner [31].
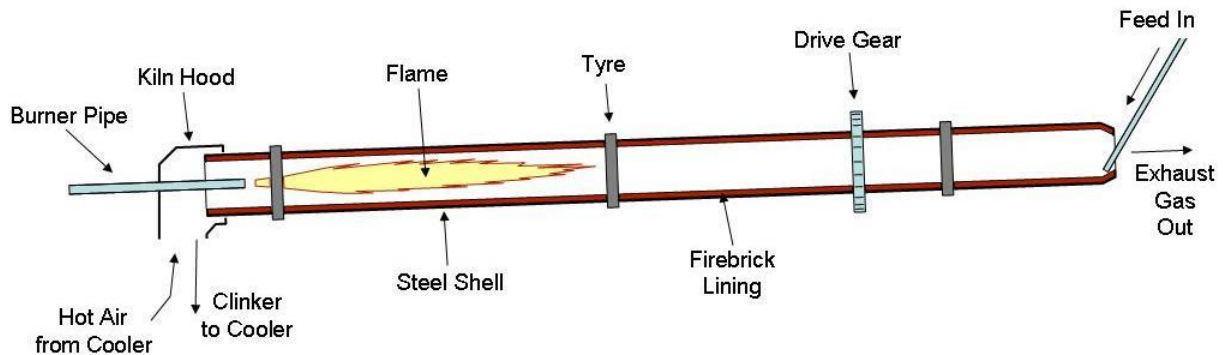
Figure 2.5: General Layout of a direct fired countercurrent rotary kiln used in cement manufacture [1].

2.3   Rotary kiln burners

The combustion system is a key element in efficient thermal processing of ores, minerals, and similar bulk solids in a rotary kiln. The process requirements are stringent in a variety of thermal processing systems such as in cement-making, limestone calcining, recovery of lime in pulp mills, and the combustion of wastes to name a few. The burner system is an important and an integral component of a rotary kiln system to optimize the combustion of fuels to release heat in the kiln. Safety considerations, ease and flexibility of operation, product quality, energy efficiency, maintenance costs, and the environmental impact of the products of combustion are some of the most critical areas that a kiln operator must evaluate in selecting a kiln burner. So, this section presents different kinds of rotary kiln burners with different geometries. These burners are designed and developed by many companies in the field of manufacturing and developing of rotary kilns and its components.

Metso, *Ltd.* [32], which has over half a century of experience in designing and manufacturing rotary kiln-based thermal processing systems, has the technical expertise and capability to provide rotary kiln operators with a kiln burner system that best meets their requirements. All burner systems are designed based on metso's vast burner experience. When designing a burner system, metso's engineers consider: the process, primary
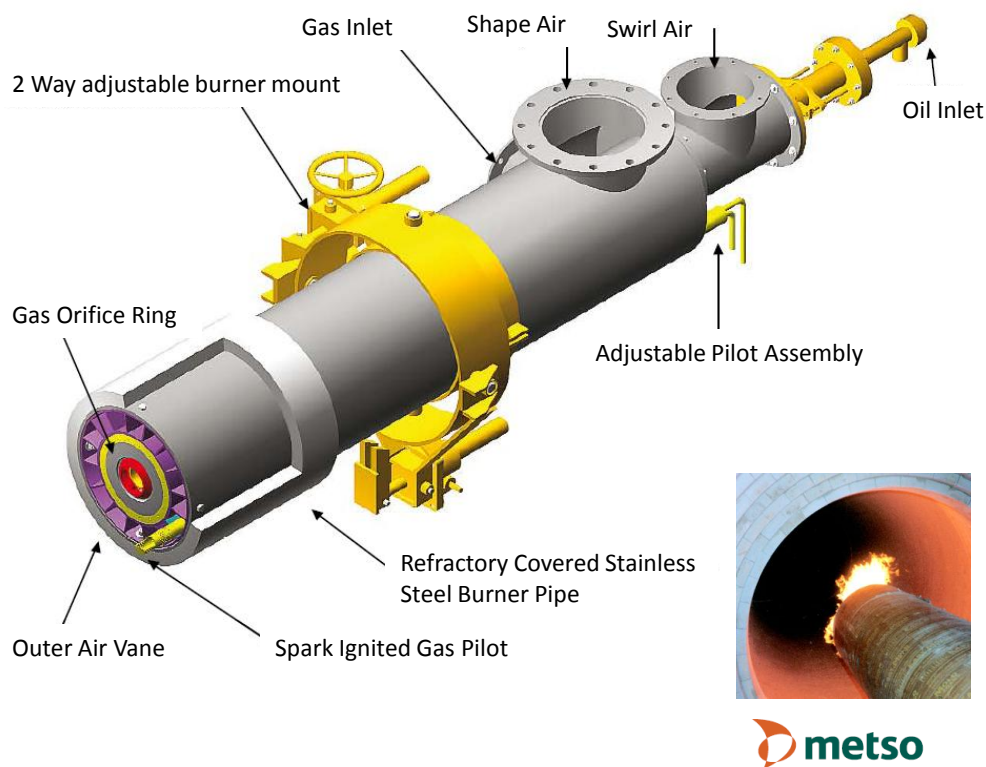
Figure 2.6: Typical cross section of a gas burner [32].

and secondary air momentum, system temperature profile requirements, and emissions requirements. Reduced NO_x emissions and optimum flame shape is achieved with the use of two primary air chambers. The metso kiln burners engineered for specific job requirements: Multi-fuel capability designed to handle gas, oil, pulverized coal, petroleum coke, or non-condensable gases separately or in combination are available (see Fig. 2.6 and Fig. 2.7), flame is directional adjustable, and flame shape control is obtained by dual air channels.

Figure 2.7: A typical pulverized fuel/gas burner [32].

A COEN, *Inc.* [33], kiln burner is especially adapted at handling alternative fuels, these alternative fuels can be burned by themselves or simultaneously with gas or oil firing. The typical alternatives or waste fuels used with COEN'S burner are: Petroleum Coke, Producer Gas, Coal, Woodwaste, Non-Condensible Gases, *NCG*, Refuse Derived Fuel, *RDF*, Toxic Waste, and Solvents. COEN has developed a dual air zone burner (see Fig. 2.8) for difficult to burn fuels. The outer zone transports solid fuels and conveying air axially and discharge from the burner. The inner zone incorporates a unique isokinetic spinner which sets up a recirculation zone to stabilize difficult to burn fuels. The COEN burner is designed to handle gas and oil firing simultaneously or in combination with solid fuels such as coal, petroleum coke, or wood. For precise flame shape control, COEN has developed dual zone gas burner. The annulus (outer) zone produces a wide, short flame while the core (inner) zone produces a long diffused flame pattern. Adjusting these two zones can produce any flame pattern required. The two zones allow the operator to adjust the flame to suit his particular needs whether it is for a lime recovery or cement kiln process.
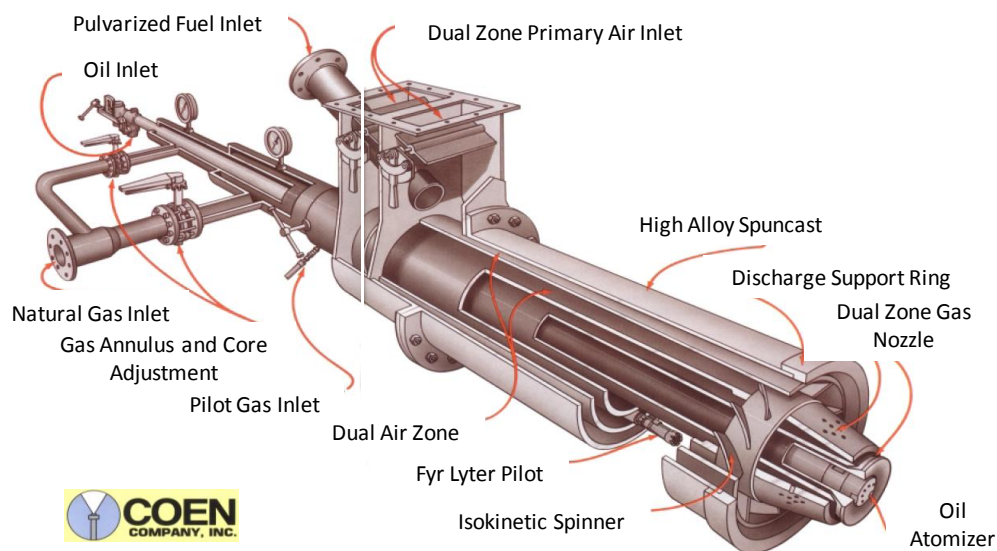
Figure 2.8: Coen's dual air zone kiln burner [33].

The DUOFLEX burner which developed by FLSmidth, *Inc.* [7], fires rotary kilns with pulverized coal or coke, oil, natural gas or any mixture of these fuels. The burner may be fitted with extra ducts for secondary fuels such as plastic chips, wood chips, sewage sludge, etc. (see Fig. 2.9). The DUOFLEX burner is unique in that it features a central duct for gaseous and liquid fuels placed inside an annular coal duct. This duct is surrounded by two concentric channels forming two channels for axial and radial primary air respectively. The two airflows are mixed before being injected via the conical air nozzle (see Fig. 2.10). The two outer ducts form a rigid support structure, minimizing deflection of the burner pipe and ensuring long refractory life. With one common nozzle for swirl air and axial air the degree of swirl can be altered without any appreciable change in total momentum. Standard types are available for any fuel combination and a maximum capacity ranging from 20 to 250 MW, catering for even the largest of rotary cement kilns. In order to explore the economical opportunities on the waste market to the maximum a high degree

of freedom is desired when adjusting the kiln feed rates of various alternative fuel types (see Fig. 2.11).
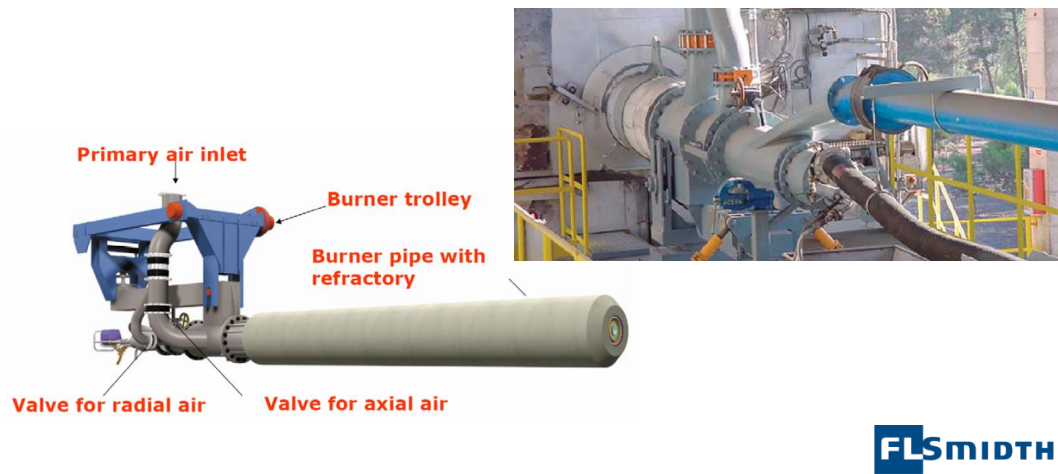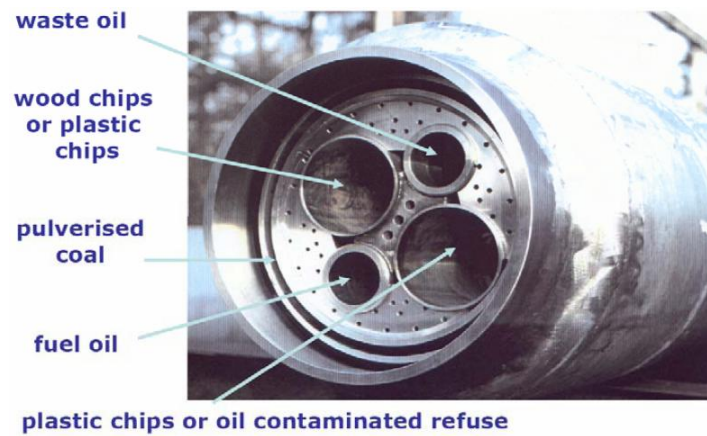

Figure 2.9: DUOFLEX kiln burner [7].

Figure 2.10: DUOFLEX burner for alternative fuels [7].

Figure 2.11: DUOFLEX burner using waste fuels, [7].

NorthStar Proflame [34], burner is simple, easy to perform adjustments to have a wide range of flame shaping ability and combustion optimization over an extreme range of firing capacities. Flame shaping and flame aiming ability allow the user optimum control of the kiln's heat profile which result in highest product quality and the lowest Btu/ton of production in the industry. The burner can be designed for any rotary kiln process or stoichiometric air requirement including kilns with high levels of reintrained secondary combustion air (tube coolers) to maximize system heat recovery. The dual air zones feature an inner zone with swirl air diffuser for maximum fuel/air mixing surrounded by an enveloping outer air annulus. It's like two burners in one. NorthStar Proflame burners can be designed to operate on single or multiple fuels simultaneously. Capabilities include natural gas, propane, steam, air and mechanically atomized fuel oils, methanol, hydrogen, NCG, petroleum coke, pulverized coal and other solid fuels (see Fig. 2.12).
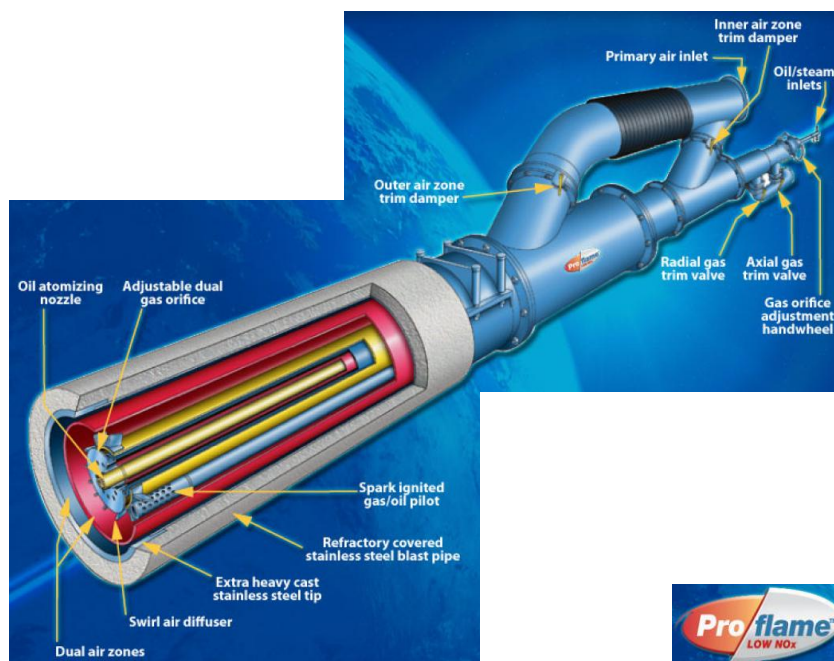
Figure 2.12: NorthStar Proflame burner [34].

Unitherm Cemcon, *GmbH.* [35], in September 1993 installed the first new generation M.A.S. burner (Mono-Airduct-System) (Fig. 2.13) which has been operated with coal, natural gas and heavy fuel oil. The primary air supply differs from the conventional burner in that the M.A.S. burners are equipped with only one primary air channel and all of the primary air streams out through one air nozzle. The flexible swirl setting device is located in the annular primary air channel, approximately 0.3 m from the burner mouth. In the annular channel, flexible hoses are arranged around the circumference. The front of these flexible tubes are mounted in a rotatable and axially slideable manner. The rear end of the hoses are held in a ring which can be distorted around the axis. Distortion of the ring is performed by means of a linkage mechanism which is actuated from the cold end via a gear unit (Figure 2.14). The flame setting device is designed considering the kiln dimensions, it is operated from the burner's cold end. If the ring is rotated, the flexible tubes will fit to the inner tube in a helical manner. Depending on the distortion

angle of the ring, the hose ends will be deflected in relation to the burner axis. The air will flow through the flexible tubes to the rotation chamber in front of the outlet nozzle. There, the air flow is swirled at an intensity which depends on the deflection angle of the flexible tube ends, and it then passes through the air nozzle into the kiln. Where the smaller rotation angle the longer the flame length and vice versa (see Fig. 2.15).
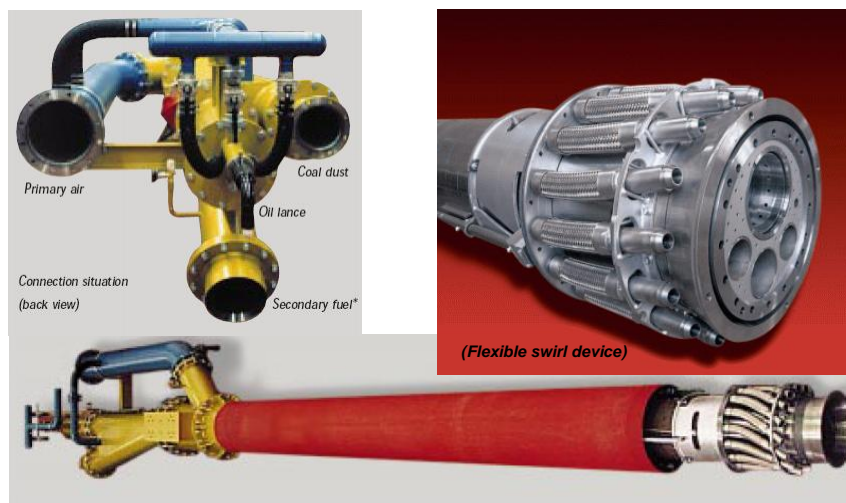

Figure 2.13: A typical M.A.S kiln burner [35].

Figure 2.14: Burner with disassembled outer jacket tube [35].

KHD Humboldt Wedag, *Ltd.* [36], had designed two types of burners; PYRO-JET and PYROSTREAM burner. The PYRO-JET burner has been installed in more than 700 rotary kilns in the last thirty years. PYRO-JET burner is a typical multi-channel burner for various fuels. To achieve highest substitution rates, the burner can fire different combustibles in mixed rates: sewage sludge, animal meal, coal, used oil, solvents and contaminated water (Figure 2.16). PYRO-JET burner is reliable and has a minimum environmental impact. The axial air exits the PYRO-JET burner at high speed via several separate jet nozzles arranged on the perimeter of the burner. This substantially reduces the amount of primary air required when compared with conventional burners while also reducing fuel consumption. The jets produce a flame with even heat build-up.

Air adjustment for a long flame M.A.S. hose deflection approx. 10°

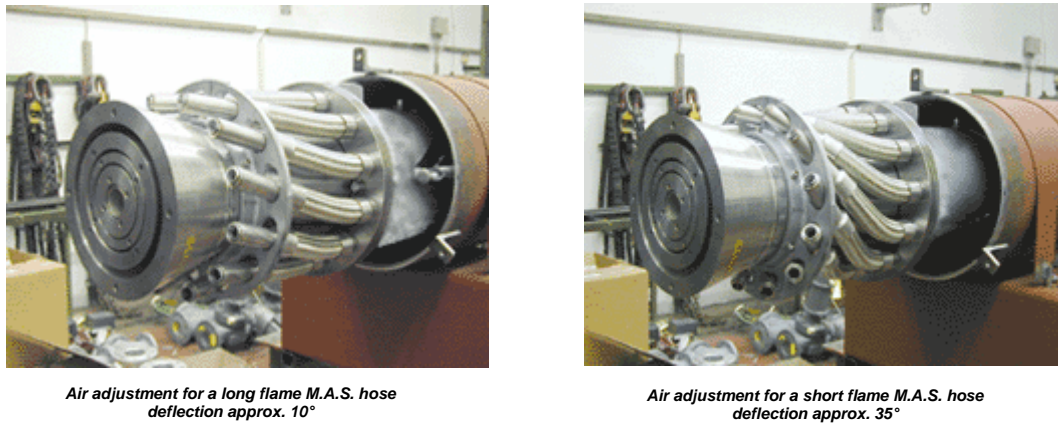*Air adjustment for a short flame M.A.S. hose deflection approx. 35°*

Figure 2.15: Flame setting with the M.A.S Burner [35].

Measurements show that the early ignition of the fuel at the outlet of the PYRO-JET substantially reduces NO_x emissions.

With all the experience gathered over the years, KHD has developed the PYROSTREAM high performance burner (Figure 2.17). The PYROSTREAM burner is designed to allow the highest possible alternative fuel substitution rates and can be used for animal meal, sewage sludge, fluff etc.

Sharing the double-pressure primary air system and the sandwich flame concept, the main design feature is the adjustable jet nozzle system. Each of the 12 angular nozzles is bolted to an independent jet air tube which can be rotated through $360\,°$. Each tube ends in a distributor and all tubes are synchronized by use of a chain. At the cold end of the burner, all tubes are equipped with hardly hexagonal ends to allow either single or synchronized adjustment. When turning the nozzles the jet streams can be set either in the main swirl direction or at counter flow, divergent or convergent. This adjustment allows a more precise flame setting than conventional burners without adjustable nozzles (see Fig. 2.18).

central channels

swirl air nozzle

sewage sludge / AM nozzle

coal nozzle

Jet nozzles

Oil / solvent / water nozzles
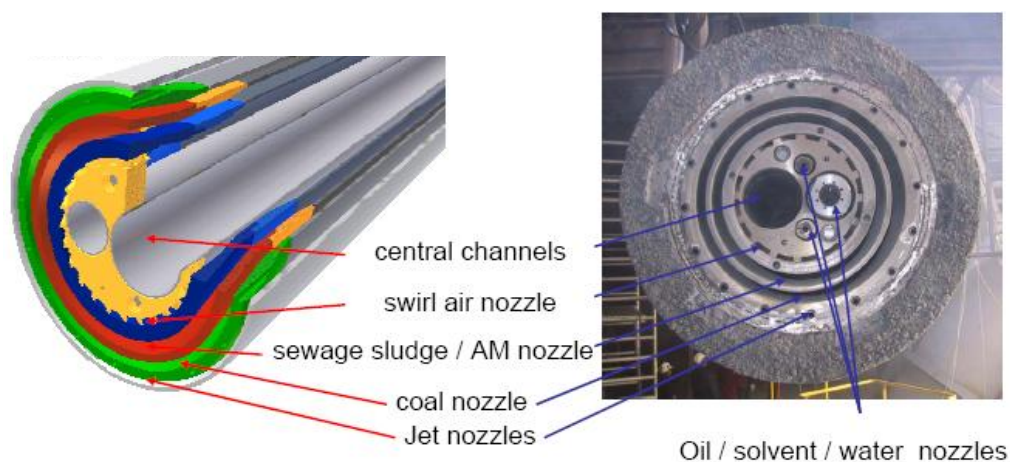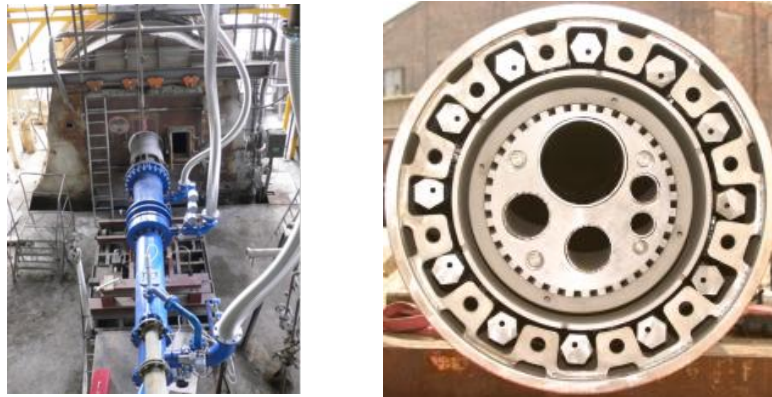
Figure 2.16: The PYRO-JET burner [36].

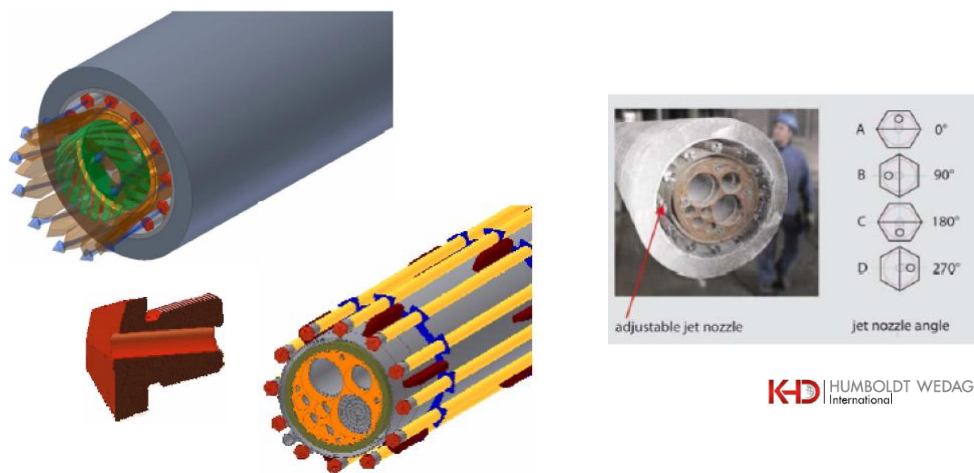Figure 2.17: The PYROSTREAM burner [36].

Figure 2.18: Adjustable jet nozzle system [36].

The Multi-Fuel kiln burner which developed by FCT, *Inc.* [37], allows the kiln to utilise the most economical fuel currently available. In many cases by-product fuels may be used in place of, or in addition to, the primary fuel. The burner requires a certain heat transfer pattern in order to optimise the product quality, the production rate and the fuel efficiency. Each fuel has different burning characteristics. For example the peak heat transfer with gas firing tends to be much further up the kiln compared to oil or coal firing (see Fig. 2.19).

Figure 2.19: FCT Multi-Fuel burner [37].

ROTAFLAM burner which manufactured by PILLARD, *GmbH.* [38], has been installed in more than 600 plants since 1989. ROTAFLAM multi-fuel burners are available for all standard fuels, e.g. pulverised coal, natural gas, diesel oil, light oil and any kind of heavy fuel oil. Fuel combustion proportions are achievable within a flexible capacity range up to 100 per cent. ROTAFLAM's range of performance depends on the customer's requirements and has nowadays a maximum capacity of 175 MW (see Figure 2.20 and 2.21). Apart from the ability to use all sorts of fuels in the center of the burner, ROTAFLAM burner has many advantages such as easily controllable flame formation, internal flue-gas circulation, stable ignition and burning throughout the complete turn down ration, swirl air circuit around the fuel-feed channel, etc.
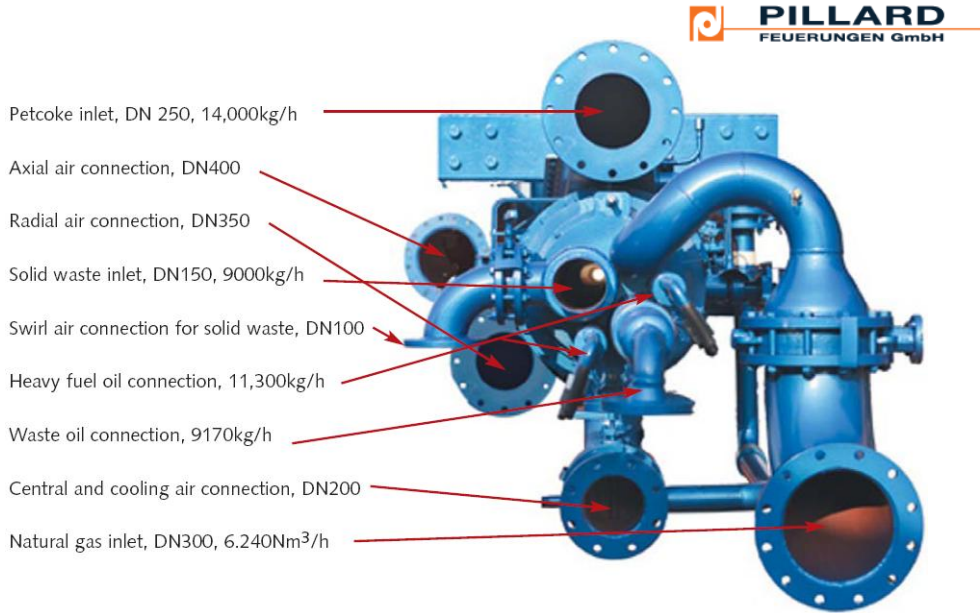
Figure 2.20: A large ROTAFLAM burner with a thermal capacity of 125 MW for a Holcim plant in Mexico [38].
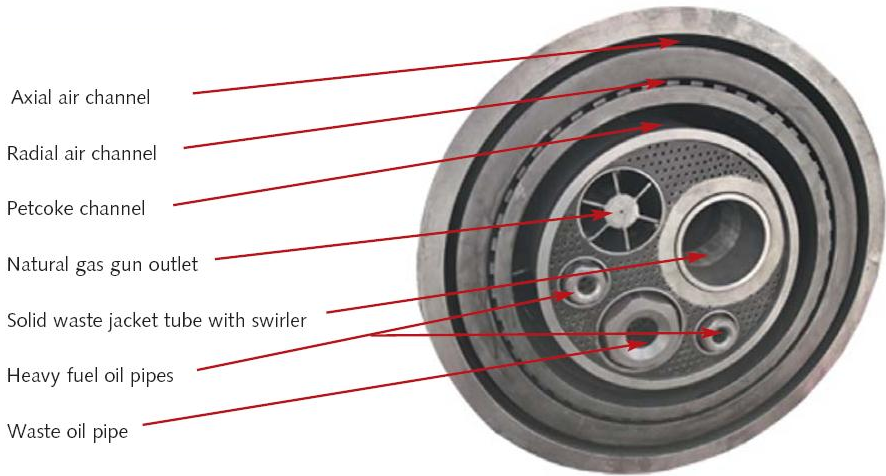
Figure 2.21: ROTAFLAM burner tip [38].

FlexiFlame burners are the most advanced technology developed by Greco-Enfil company [39], for rotary kilns firing pulverized fuel. Using three shaping airflows and a unique design; two of the airflows rotate to enfold the solid fuel injection flow (see Figure 2.22); it allows, through simple procedures, to optimize complex fuel firing and great control over NO_x emissions. FlexiFlame burners are customized to deliver thermal power up to 175 MW. They can use just one or multiple fuels, with variable mix, as:

- Solid fuels: petcoke, anthracite, lignite, bituminous coal, charcoal, etc.

- Liquid fuels: light and heavy fuel oil, diesel oil, vegetable oils, etc.

- Gas fuels: natural gas, lean gas, etc.

- Liquid waste: solvents, paint waste, water from cleaning oil products tanks, sewage sludge, etc.

- Solid waste: animal flour, plastic chips, sawdust, biomass, used tyres, etc.

With three independent air inlets, FlexiFlame burners deliver a flame with the best shape and settings for the production process, feedstock and fuel mix. Through simple procedures as opening (or closing) inlet air valves, kiln operators can optimize firing conditions.
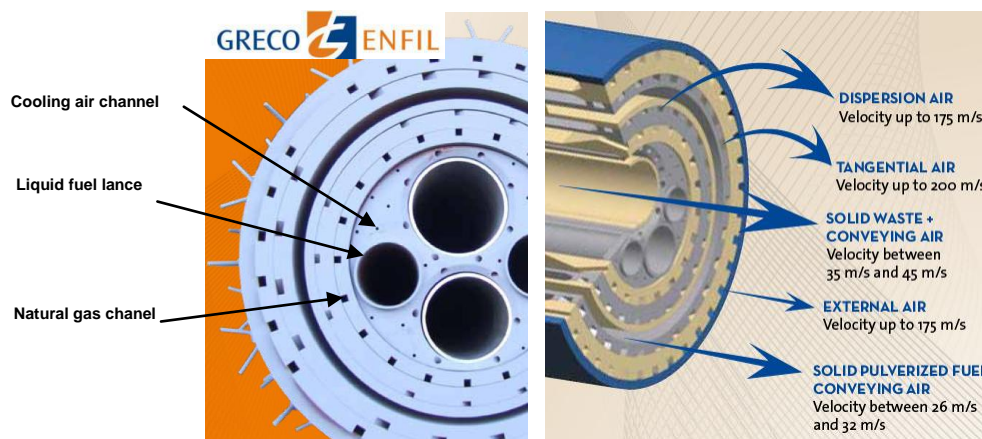

Figure 2.22: FLEXIFLAME burner tip [39].

Polysius, *Ltd.* [40], rotary kiln burner is designed in accordance with the process requirements for the standard fuels coal dust, fuel oil and/or natural gas. Alternatively or parallel to these standard fuels, substitute fuels or special gases (e.g. blast furnace gas, carbonisation gas) can be used (see Fig. 2.23). The flame shape can be varied over a wide range of possibilities by altering the air/gas outlet cross section. The new Polysius burner named POLFLAME, incorporates numerous innovative and design ideas of ultra-modern pyroprocessing technology. Depending on the process technological requirements, the burner is equipped for the traditional fuels such as coal, anthracite, oil, petroleum coke and natural gas or for the use of solid and liquid secondary fuels such as animal meal, dried sewage sludge, fluff etc. (Figure 2.24) The flame shape can be infinitely varied within broad limits during operation of the burner by means of the unique nozzle adjustment system (see Fig. 2.25). The design of the nozzle adjustment system and of the

burner tip ensures that this adjustment functions reliably even after a lengthy period of operation. The burners can also be specially dimensioned for widely differing production capacities - from below 1,000 tonnes to more than 12,000 tonnes of clinker per day and kiln line. Thermal outputs range from 10 MW to 300 MW. The POLFLAME burner permits optimum adjustment of the combustion to the respective fuels and product quality requirements. If desired, and if permitted by the product quality, it is therefore possible to achieve extremely low pollutant emission levels.

Figure 2.23: A typical Polysius burner [40].
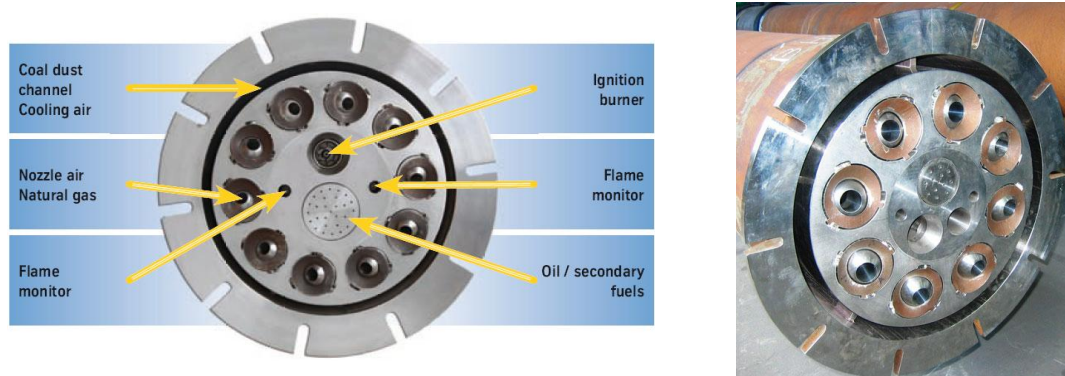
Figure 2.24: POLFLAME burner tip [40].
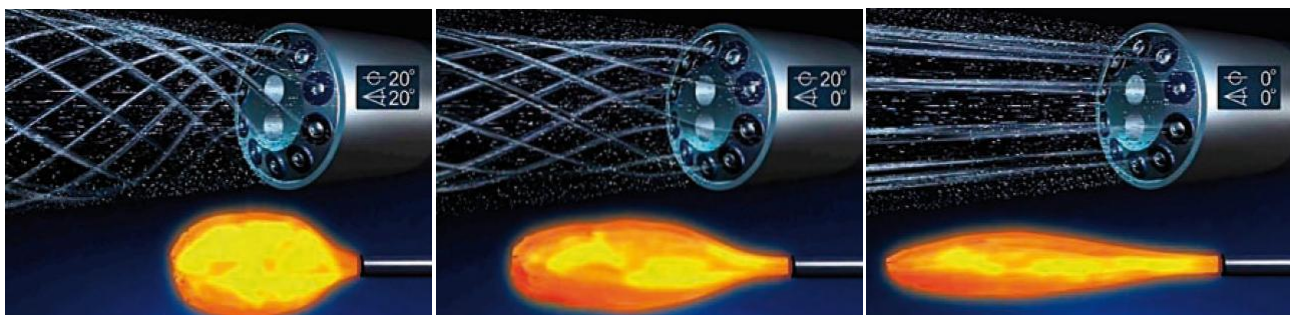
Figure 2.25: Flame shape adjustment [40].

2.4   Aerodynamics and flow field

Although there are common characteristics between rotary kilns, burner, firing hood and cooler are often unique to the particular kiln. In the Figure 2.26, some common rotary kiln features are shown. For example, in a natural gas-fired kiln, the fuel is supplied through the inner pipe of the burner, and the primary air is injected concentrically through an annulus around the fuel pipe. The combined momentum of the fuel and primary air (primary jet) is orders of magnitude higher than of the secondary air, which is supplied concentrically to the burner, through the firing hood [31].
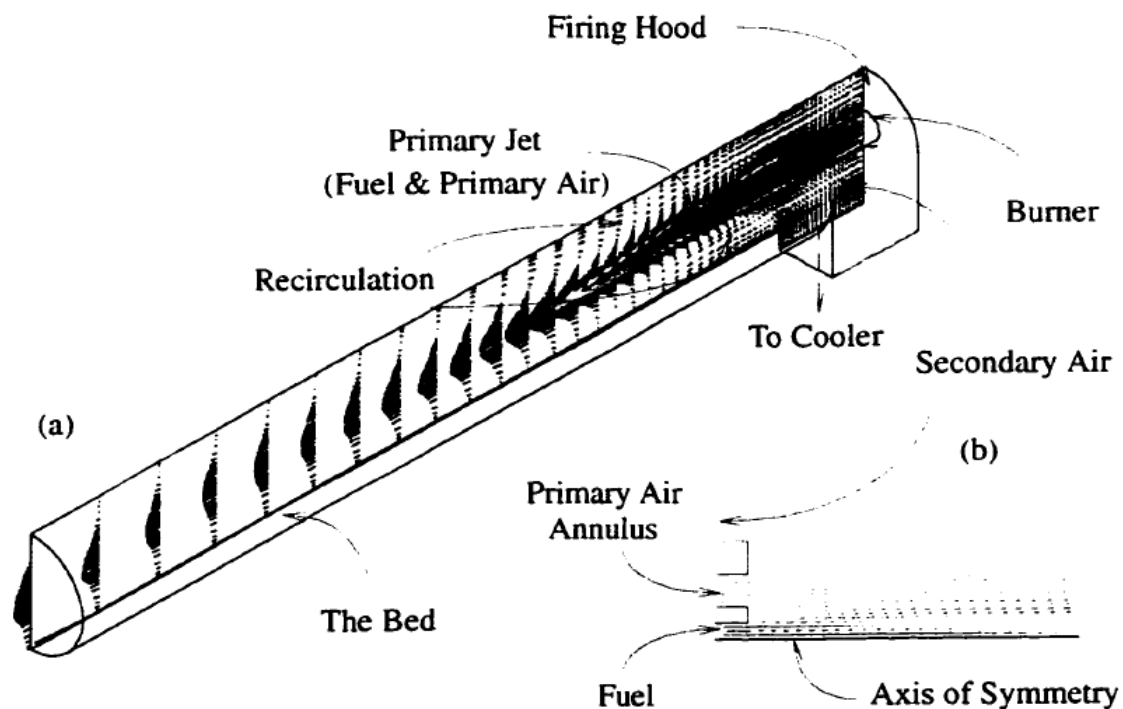
Figure 2.26: (a) An isometric diagram of the rotary kiln, showing a flow pattern of the primary jet and secondary air. (b) An axis-symmetric section showing the concentric type burner [31].

The typical rotary kiln firing conditions are influenced by physical and economic factors. To explore the relationship between economics and flow pattern (aerodynamics) in the rotary kiln, attention is directed towards previously established knowledge on confined jets [41]. When a jet issues into a confinement, such as rotary kiln, two extreme cases can occur. If the ambient fluid supply is high enough to satisfy the requirements for entrainment, the jet expands until it becomes attached to the wall, without recirculation. When the ambient fluid is less than that which the jet can entrain, recirculation is introduced as shown in the Fig. 2.27.

The strength and size of recirculation eddy affect both the stability and combustion length of the turbulent diffusion flame. In the rotary kiln, axial zones with different characteristics are set up as a result of changing heat transfer rates along the kiln. For example, in the cement kiln there are four different zones [3]. The region upstream of the burner is called the "cooling zone", referring to the area where the hot charge is
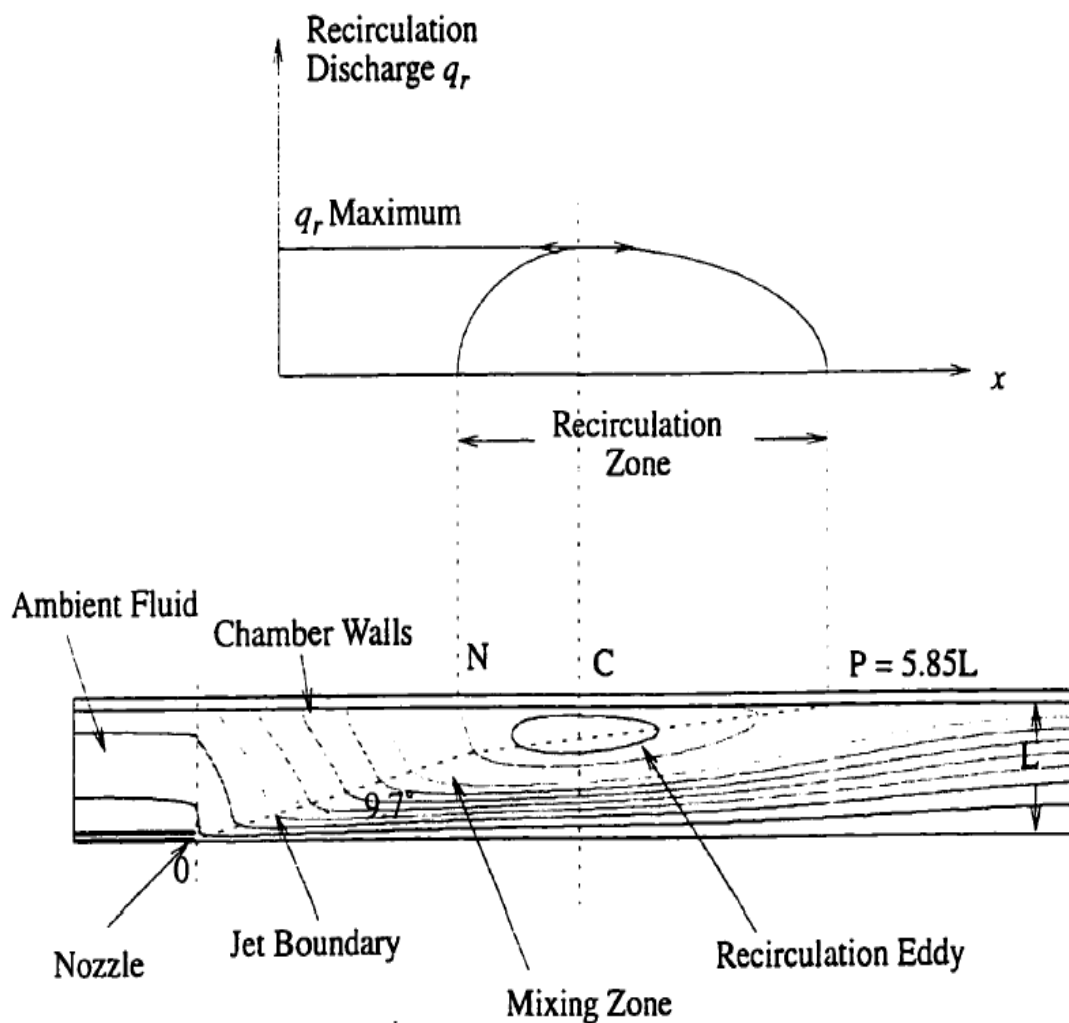
Figure 2.27: The Curtet model for the two-dimensional jet with recirculation [41].

being cooled as a result of its flow counter-current to the secondary air. This zone is followed by the "clinkering zone", where the solids reach a semi-fused state, at which the cement-making reactions are activated. Further downstream, the "calcinations" and "preheating" zones occur, as a result of axial thermal gradient. The length and thermal profile of each of these zones are controlled by the burner load, flame aerodynamics, thermal resistance of the refractory lining, feed rate, and speed of rotation. The momentum ratio between the primary and secondary flows governs recirculation and the overall aerodynamics of the flame [31]. Flame ignition and stability require that some of the air is introduced in close proximity to the fuel, and at a relatively high momentum. As the fraction of the primary air is increased, the strength of the recirculation zone is enhanced. Hence, the flame becomes shorter. Since the secondary air contains some of the heat recuperated from the solids, increasing the primary air ratio necessary increases the energy cost of the process.

Ruhland [42] developed an empirical flame length model for flames in the cement rotary kiln. This empirical model was based on experiments which used two liquid streams (primary and secondary) whose interaction represented the mixing in the burner

region. Assuming that "burnt is mixed", the well mixed region also represents the flame itself, so that the effective length could be visualized experimentally. The primary jet was represented by a mixture of caustic soda, water and thymolphthalein for the visual indicator. The secondary stream included a dilute solution of hydrochloric acid. Although a liquid representation was used, equivalence between the observed "flame length" and the flame length in the real kiln was confirmed by measurements of the flame in the full scale rotary kiln. Although useful, the correlation predicts the length of flames for a non-swirling jet of fuel from a smooth tubular nozzle. Additional aerodynamic complications such as hood/kiln interactions and detailed distortions of flames from buoyancy would require further empirical parametric investigation [6]. The primary core flow (fuel plus air) entrains secondary air as it would in a free jet.

Ricou and Spalding [43] measured this entrainment of a confined jet by surrounding the turbulent jet with a porous-walled cylindrical chamber. Air was injected through the wall until no pressure gradients were detected. The primary jet momentum (consisting of fuel and primary air) is typically at least one order of magnitude higher than the surrounding secondary air momentum entering the kiln hot end. The resulting primary to secondary momentum ratio may or may not result in a recirculation zone further down the kiln. The size, strength or existence of this recirculation eddy has important implications for rotary kiln flame stability, flame length and emissions. Reynolds number typically plays a secondary role. Flow exiting the burner is always turbulent. The Reynolds number of the turbulent diffusion flame (i.e. the core flow) based on the mean primary flow velocity and the burner diameter, is typically high enough ($> 10^5$) in rotary kilns to be Reynolds number independent [30].

Thring and Newby [44] assumed that until the core flow reaches the wall (attachment point of the recirculation eddy) it behaves as a free jet. Using Hinze's formula for the entrainment rate $\dot{m}_{entrain}$ [45],

$$\dot{m}_{entrain} = \dot{m}_p \left(0.2\frac{x}{r_p} - 1 \right) \tag{2.11}$$

plus the universal jet spreading angle, which yields,

$$x' \cong 4.5 r_s \tag{2.12}$$

they proposed a similarity based on the separation to attachment distance ratio. Here r_p and $\dot{m}_p$ are the radius and mass flow rate of the primary jet. r_s is the kiln radius and x' the axial distance from the nozzle exit to the point where the core flow spreads to the wall. The mass flow ratio at which the secondary flow exactly satisfies the entrainment requirement ($\dot{m}_s = \dot{m}_{entrain}$) as the core flow spread to the wall, could be evaluated by equating x' to x. In this unique situation ($Th = 1$) no recirculation would be observed. A similarity parameter Th was proposed as follows,

$$Th = \left(\frac{\dot{m}_p + \dot{m}_s}{\dot{m}_p} \right) \frac{r_p}{r_s} = \frac{Separation\ distance}{Attachment\ distance} \tag{2.13}$$

The attachment distance is the axial distance between burner exit and point P in Fig 2.27. The separation distance is the axial distance between burner exit and point N in

Fig 2.27. The entrainment requirements are satisfied for $Th \geq 1$. Recirculation is present for $Th < 1$. This parameter generally does not apply to typical rotary kilns for which $r_p/r_s > 0.05$. under such conditions there are excessive flow distortions in the nozzle region [30]. By simplifying the equations of motion for a constant density fluid and introducing experimental observations, Craya and Curtet [46, 41] defined a dimensionless parameter m representing the thrust term (momentum flux and pressure force). Parameter m is a function of the excess discharge ratio R', which is the ratio of the excess volumetric flow rate of the primary discharge q to the total volumetric flow rate Q, their analysis relates m to R' as follows:

$$m = R' - 1.5R'^2 + 0.579 \frac{R'^2}{(r_p/r_s)^2}$$

$$where \ R' = q/Q$$

$$q = \pi r_p^2 (u_p - u_s)$$

$$and \ Q = \pi (r_s - \delta^*)^2 u_s + q$$

(2.14)

Here u_p and u_s are the average velocities for primary and secondary flows. The boundary layer displacement thickness δ^* is usually negligible. The Craya-Curtet parameter m is also identified in the literature as a Curtet number [41]

$$C_t = \frac{1}{\sqrt{m}}$$

(2.15)

Recirculation occurs for a Craya-Curtet parameter of approximately $m > 1.5$ ($C_t < 0.8$). Moles *at al.* [30] have surveyed 63 rotary kilns and found that they operate in the range of medium to low recirculation intensity ($0.4 < C_t < 0.8$). They used cold flow (air and water) modeling techniques with operating conditions to cover the above range and have shown that similarity parameters such as C_t are useful indicators of recirculation levels. The apparent need to work in this range emphasizes the important role recirculation plays in the rotary kiln. If C_t is too high (little or no circulation) there may not enough mixing for complete combustion. This leads to excessive emissions, problems with fuel efficiency etc. If C_t is too low (very large recirculation region) the recirculation gases lower the oxygen concentration around the flame and may result in precisely the same conditions [30].

2.5 Heat transfer

Heat transfer paths in the rotary kiln are illustrated in Figure 2.28. The flame/hot flow region transmits energy by radiation and convection to the exposed wall and bed surfaces. Radiation heat exchange also occurs between these exposed surfaces. In most industrial rotary kilns radiative heat transfer is significant due to the high hot flow temperatures. Heat regeneration to the bed via the rotating wall is an integral part of the process in the rotary kiln. Within the bed, heat is both conducted and convected due the motion of the particles. Relative motion between particles (granular diffusion) adds to this heat transfer [6]. It was found that over 90 percent of the heat transfer in the rotary kiln is

by radiation [47]. Therefore, we will concentrate in the literature on the radiation heat transfer in freeboard region, as we show in the following part.
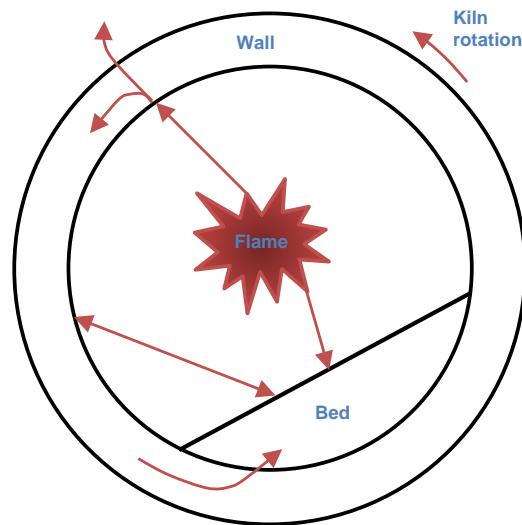

Figure 2.28: Basic heat transfer paths and processes for rotary kiln [6].

2.5.1 Radiation in freeboard region

The freeboard region of a rotary kiln forms an enclosure filled with the emitting/absorbing mixture of gases resulting from the combustion process and in many instances, the chemical reaction within the bed material [15].

The freeboard gases common to rotary kiln operation are composed mainly of $CO_2 - H_2O$ mixtures in nitrogen generated by the combustion of hydrocarbon fuels with air. Because these gases emit and absorb radiation in distinct bands, the use of a gray-gas approximation, i.e. the emissivity and absorptivity are equal and constant at a given gas temperature, is not valid. Rather, these mixtures should be treated as real gases in which the emissivity and absorptivity need not be equal because absorptivity, due to the banded characteristics of the CO_2 and H_2O, is a function of both the gas and the emitting surface temperatures. For these mixtures Hottel and Sarofim [48] suggest that gas radiation can be visualized as that due to the weighted summation of a sufficient number of gray and clear gas components to approximate the banded characteristics of a real gas [49]. Thus according to their approach the total gas emissivity may be represented by

$$\varepsilon_g = \sum_i a_i(1 - e^{-k_i pl}) \tag{2.16}$$

Subject to the restrictions that the a_i are all positive and

$$\sum_i a_i = 1 \tag{2.17}$$

Since emissivity approaches 1 with increasing pl. In a similar manner, the absorptivity

of a real gas at temperature T_g for black-body radiation from a surface at T_S, can be represented by

$$\alpha_g = \sum_i b_i(1 - e^{-f_i pl}) \tag{2.18}$$

Where again the b_i are all positive and

$$\sum_i b_i = 1 \tag{2.19}$$

Hottel and Cohen [50] presented a method for predicting the effect of radiation exchange on the distribution of temperature and heat transfer within a furnace chamber. The system is divided into surface zones and gas zones, the number being dependent on the desired accuracy of the result. Direct-exchange factors are available for gas-gas, gas-surface, and surface-surface zone interchange. From these factors one can determine the net exchange factor for any zone pair, making due allowance for interaction with all other zones. The resultant factors are then fed into a set of energy balances, one on each zone, which by simultaneous solution permit a determination of the space distribution of gas and surface temperatures and the distribution of heat flux over the surfaces.

Jenkins and Moles [51] developed a mathematical model to predict the gas and refractory temperature profiles occurring in a rotary kiln. The author's method based on Hottel and Sarofirm [48] but modified to take into account the specialized firing conditions necessary for cement making. The model predictions were reasonable agreement with experimental data obtained from tests on 100 tpd production cement kiln, so it is expected that the application of the results from this model will enable the cement, lime and refractory industries to predict operating conditions more accurately.

Gorog [52] carried out a theoretical study to calculate the radiative heat transfer in the freeboard of a rotary kiln. Gorog used a modified reflection method in joining with a weighted gray gas emissivity model. The radiative heat fluxes to elements on the exposed wall dA_{ew} and exposed bed dA_{eb} were calculated by dividing the freeboard into a number of axial slices extending in both directions from dA_{ew} and dA_{eb} and tracing the rays emitted by the gas volume zones and the wall and bed surface zones until they reach either dA_{ew} or dA_{eb}. Values of net surface heat input to the surface were calculated using the summations as follows

$$Q_{dA_{eb}} = \sum Q_{ew \to dA_{eb}} + \sum Q_{eb \to dA_{eb}} + \sum Q_{g \to dA_{eb}} - \varepsilon_{eb} dA_{eb} E_{eb} \tag{2.20}$$

$$Q_{dA_{ew}} = \sum Q_{ew \to dA_{ew}} + \sum Q_{eb \to dA_{ew}} + \sum Q_{g \to dA_{ew}} - \varepsilon_{ew} dA_{ew} E_{ew} \tag{2.21}$$

So the net rate of heat transfer from the freeboard was also calculated as

$$Q_g = \varepsilon_g L_m A_g E_g - \sum Q_{ew \to g} - \sum Q_{eb \to g} - \sum Q_{g \to g} \tag{2.22}$$

Where L_m is the mean beam length of the gas and Ag is the total area of the enclosing

gas and E_g is the black-body emmisive power of the gas.

Gorog *et al.* [49] presented some useful conclusions concerning radiative heat transfer in rotary kilns from the model: 1) Because the freeboard gases common to rotary- kiln operation contain CO_2 and H_2O which emit and absorb radiation in different bands, the gray-gas approximation is not valid; and these mixtures should be treated as real gases. 2) The majority, 86 pct, of radiant energy received by the kiln wall or the solids surface originates from gas within an axial slice 0.3 kiln diameters along the kiln axis. 3) The influence of temperature gradients in the freeboard gas on the radiative exchange between the gas and the kiln wall or the solids surface is negligible (see Fig 2.29)[2]. This is because of the poor transmissivity of the freeboard gas for its own radiation. 4) Greater than 80 pct of the freeboard gas radiation reflected from either the kiln wall or the solids surface is reabsorbed by the gas on the first reflection. Hence, the influence of reflected gas radiation on the total radiant heat transfer in rotary kilns is minimal and is a local phenomenon. 5) The influence of temperature gradients along the kiln wall or the solids surface has a negligible effect on the radiative exchange between the kiln wall and solids surface.
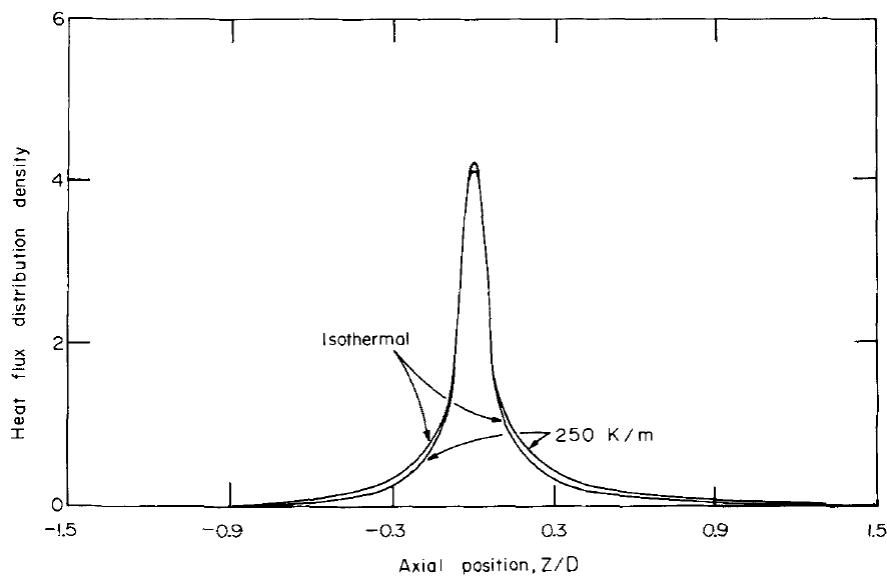
Figure 2.29: Showing the negligible influence of axial gas temperature gradients on gas to wall heat flux [49].

Unfortunately smaller exact relationships for the calculation of radiation in the freeboard have most often been employed. The most basic relationship can be obtained by assuming a gray freeboard gas relating to a gray, isothermal bounding surface. So the problem is reduced to two isothermal gray bodies and the solution is available [53].

$$Q_{g \to A_g} = \frac{A_g \sigma (T_g^4 - T_{A_g}^4)}{\frac{1}{\varepsilon_g} + \frac{1}{\varepsilon_{A_g}} - 1} \qquad (2.23)$$

Where A_g is the surface area of the bounding gas. Another relationship was suggested by

---

[2]This figure is used based on license agreement between the author and Elsevier with license number of 264140803300.

[48], also by assuming the bounding surface to be isothermal but dropping the gray gas assumption, was given as

$$Q_{g \to A_g} \cong A_g \frac{(\varepsilon_{A_g} + 1)}{2} \sigma(\varepsilon_g T_g^4 -_{Ag} \alpha_g T_{A_g}^4) \tag{2.24}$$

Where $_{Ag}\alpha_g$ is the gas absorptivity evaluated at the temperature of the bounding surface. For $\varepsilon_{Ag} > 0.8$ the error associated with Eqn. 2.24 is less than 10% with restriction that the difference between T_g and T_{Ag} must at least several hundred Kelvin degrees. A summary of correlations which used to calculate radiative exchange between the feeboard gas and exposed bed and wall surfaceses is presented in Table 2.1.

Table 2.1: Expressions proposed for radiative heat transfer coefficient of freeboard gas to surface [15].

Reference	$h_{rad,g \to A_g}\ W/m^2 K$	*Comments*
[54]	$\frac{\sigma(\varepsilon_g T_g^4 -_{Ag} \alpha_g T_{A_g}^4)}{T_g - T_{A_g}}$	Similar to Eqn. 2.24
[55], [56], [4]	$\frac{\sigma \varepsilon_g (T_g^4 - T_{A_g}^4)}{T_g - T_{A_g}}$	Gray gas similar to Eqn. 2.23
[57]	$4\Phi_{g \to A_g} \sigma T_g^4$	Φ=overall radiation exchange factor
[58]	$23 \rightarrow 113$	Author's estimate
[59]	$\frac{\sigma(T_g^4 - T_{A_g}^4)}{\frac{1}{\varepsilon_g} + \frac{1}{\varepsilon_{A_g}} - 1}$	Eqn. 2.24, T_g= Average radiating gas temperature

2.6   Flame length correlations

2.6.1   Free jet flame length

Hawthorne *et al.* [21] have been obtained visible flame lengths formed from free turbulent jet flames issuing from circular nozzle into still air. For flames in which the effects of buoyancy are small (high nozzle velocity, small diameter) the analysis leads to the following simple relation for the length of free turbulent flame jets:

$$\frac{L_f}{d_o} = \frac{5.3}{f_{st}} \sqrt{\frac{T_{ad}}{\alpha_T T_o} \left[f_{st} + (1 - f_{st})\frac{M_\infty}{M_o} \right]} \tag{2.25}$$

where L_f=visible flame length, d_o=nozzle diameter, T_{ad}=adiabatic flame temperature, absolute, T_o=absolute temperature of nozzle fluid, M_∞, M_o=molecular weights of surrounding and nozzle fluids, respectively, f_{st}=mol fraction of nozzle fluid in the unreacted stoichiometric mixture, and α_T=mols of reactants/mols products, for the stoichiometric mixture. The data which used for pervious correlation covered the small range of nozzle diameter of 0.12 to 0.3 inches the study used different kinds of gas fuels including propane, acetylene, hydrogen, carbon monoxide, city gas, mixtures of carbon dioxide with city gas, and mixtures of hydrogen with propane. The results presented that the turbulent flame lengths varying from 40 to 290 nozzle diameters. For example, for free turbulent hydrogen flames in air in which the effects of buoyancy are small, and with α_T=1.173, T_{ad}/T_o=8.04, f_{st}=0.296, M_∞/M_o=14.45 (Hawthorne *et al.* [21]) above equation casts as L_f/d_o=152, i.e. turbulent flame length is 152 nozzle diameters.

Golovichev and Yasakov [60] calculated theoretically the maximum length to diameter ratio as $L_f/d_o = 220$, and the maximum measured value for a subsonic release with velocity 365 m/s was $L_f/d_o = 205$ for Hydrogen flames. In 1974 the first systematic attempt to investigate hydrogen flame length over the whole range of operation from forced convection (jets) to natural convection (plumes) was undertaken by Baev [61].

Baev *et al.* [61] theoretically derived that at the momentum controlled limit a flame length $L_F \sim Re$, or $L_f/d_o \sim u_o \rho_o/\mu_o$, i.e. the dimensionless flame length is practically constant for sonic releases. In the presence of lifting forces $L_f \sim Re^{2/3} Fr^{1/3} \sim u_o^{4/3} d_o^{1/3}$. They concluded that depending on Fr number there will be a characteristic peak in $L(Re)$ dependence.

Schevyakov and Komov [62] confirmed that data on flame lengths were presented as dependence on the Froude number $Fr = u_o^2/g d_o$ and demonstrated saturation on the flame length dependence with increase of Fr number. A dependence of dimensionless flame length L_f/d_o on Reynolds number up to $Re = 20,000$ is given for nine stainless steel tubular burners of diameter from 1.45 mm to 51.7 mm (ratio of burner length to diameter was changing from 50 for smaller diameter burners to 10 for largest one). The dependence $L_f/d_o(Re)$ for small burners with diameter up to 6 mm has a characteristic peak of decreasing with diameter magnitude in the area of transition from laminar to turbulent flow ($Re < 2,300$). Then L_f/d_o increases with Re approaching a limit $L_f/d_o = 220 - 230$ for high Reynolds numbers. For the same Reynolds number L_f/d_o decreases with diameter increase. This is in line with previously obtained results by Baev *et al.* [61]. An engineering correlation for calculation of the dimensionless flame length of vertical hydrogen jet fire was developed by Shevyakov and Komov [62]. The correlation covers the whole range of conditions from buoyancy controlled (lower Fr) to momentum controlled (higher Fr) jet fires. The following modification of the original correlation by Schevyakov and Komov [62] is obtained by linear regression analysis and given by

$$\frac{L_f}{d_o} = 15.8 Fr^{1/5} \ (Fr < 10^5)$$

$$\frac{L_f}{d_o} = 37.5 Fr^{1/8} \ (10^5 < Fr < 2 \cdot 10^6) \tag{2.26}$$

$$\frac{L_f}{d_o} = 230 \ (Fr > 2 \cdot 10^6)$$

Becker and Liang [23] carried out experimental study to give general correlations for predicting flame length, over the range of operation from forced convection to natural convection. An equation for the length of forced-convection flames was correlated by the authors in the form of

$$\frac{L_f}{D_s} = \frac{C_f}{f_{st}} \left(\frac{\rho_\infty}{\rho_m}\right)^{1/2} \tag{2.27}$$

Where L_f is the visible flame length (m), D_s is the effective jet diameter at source (m), $D_s = (4m_o^2/\pi\rho_\infty G_o)^{1/2}$, G_o is the jet momentum flux (N), C_f is the decay coefficient of centerline mass fraction W_c of source-stream material in forced-convection jets (C_f=5.4 [23]), f_{st} is the mass fraction source stream material in stoichiometric mixture with the ambient gas (normally air) (kg/kg), and ρ_∞, ρ_m is the density of ambient gas (kg/m^3) and minimum value of center line density (kg/m^3), respectively.

Another semi empirical flame length correlation presented by Günther [63] reads

$$\frac{L_f}{d_o} = 6(L+1) \left(\frac{\rho_o}{\rho}\right)^{1/2} \tag{2.28}$$

Where

$$f_{st} = \frac{1}{L+1}, \ D_s = d_o \left(\frac{\rho_o}{\rho_\infty}\right)^{1/2} \tag{2.29}$$

Where d_o is the jet port diameter, ρ_o, ρ is the density of jet-source fluid and mean gas density in the flame (kg/m^3) respectively, and L is the mass air/fuel ratio in a stoichiometric mixture.

Kalghatgi [64] published experimental results for more than 70 tests with subsonic and supersonic releases of hydrogen into still air through nozzles with diameter from 1.08 to 10.1 mm (Figure 2.30). The maximum measured flame length for subsonic releases agree well with experimental data and recommendations of Shevyakov and Komov [62]. Kalghatgi clearly stated that his results disagree with Becker and Liang's predictions L_f/d_o=310 [23]. He also showed that lift-off height varies linearly with the jet exit velocity and is independent of the burner diameter for a given gas. An important conclusion that can be drawn from the study by Kalghatgi [64] is that flame length grows with mass flow rate for a constant diameter, and flame length grows with diameter for a constant mass flow rate.

Delichatsios [24] studied flame height relationships in the range from momentum to buoyancy-controlled turbulent jet diffusion flames with use of the "fire Froude number" for reacting flows in the form similar to used by Ricou and Spalding [24]. For the momentum limit he obtained

$$\frac{L_f}{d_o} = 23(L+1) \left(\frac{\rho_o}{\rho_\infty}\right)^{1/2} \tag{2.30}$$

where L is air to fuel mass stoichiometric ratio, ρ_o and ρ_∞ are the density of nozzle fluid and surrounding fluid, respectively.
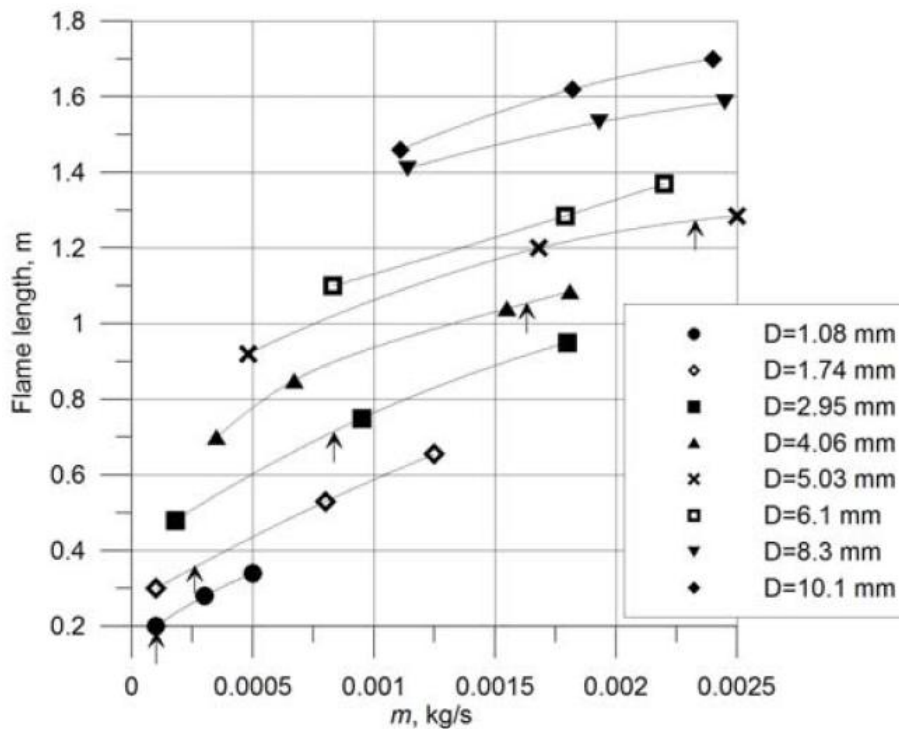
Figure 2.30: Experimental data by Kalghatgi [64]: Flame length-dependence on mass flow rate for different nozzle diameters (arrows indicate transition to sonic flow).

Wade and Gore [65] carried out experimental studs to measure visible and chemical flame heights for acetylene/air diffusion flames from 1 to 40 kW issuing from three burner diameter. The visible flame length (L_f) was measured by averaging 40 video frames obtained using a CCD camera, with a shutter time of 1 ms. The axial concentrations of the major gas species within the flame were measured using a water cooled stainless steel probe and gas chromatography. And the chemical flame length ($L_{f,c}$) was defined as the axial distance at which X_{fuel} drops to 0.0005, which is the lower detection limit of the instrument. This study shows that visible flame length and chemical flame length are not the same and don't follow the same scaling with flow rate in acetylene flames.

Morcos and Abdel-Rahim [66] carried out experimental work to study the flame length characteristics of light-fuel oil (solar) burned inside horizontal straight and swirl burners (see Fig.2.31). The tests were carried out to examine the effects of burner geometry, primary (atomizing) air-fuel mass flow rate ratio ($PFAR$), fuel-air pressure ratio (P_o/P_{air}), fuel mass flow rate ($\dot{m}_o$) and degree of swirling (S_n) on the flame length. The results showed that the flame length generally decreased with increasing primary (atomizing) air-fuel mass flow rate ratio, burner tube diameter, axial distance between combustor exit and entrance of burner tube, fuel-air pressure ratio and degree of swirling represented by air tangential angular speed. The flame length increased with increasing burner tube length. The authors developed empirical correlations to calculate the flame length for straight and swirl burners using multiple-regression analysis in terms of (D_t, L_t, X, $PAFR$, P_o/P_{air}, and $\dot{m}_o$) in the form of

$$L_f = 0.8 + L_t + D_t \left(\frac{X}{L_t}\right)^{0.5} \left\{ \frac{401.1}{(PAFR)} - \frac{776.25}{(PAFR)^2} \right.$$

$$\left. -27.37 \left(\frac{P_o}{P_{air}}\right)^{0.65} + \frac{10.39}{gD_t^5} \left(\frac{\dot{m}_o}{\rho_o}\right)^2 \right\}$$

(2.31)

$$, R^2 = 0.9$$

$$L_f = L_t - 0.2 + D_t \left\{ 347.42 + \frac{55.8}{(PAFR)} - 5.18 \left(\frac{P_o}{P_{air}}\right) \right.$$

$$\left. -353(D_t)^{0.02} + 68.51 \left[\left(\frac{D_t}{L_t}\right)^4 (PAFR) \right]^{0.9} \right\}$$

(2.32)

$$, R^2 = 0.93$$
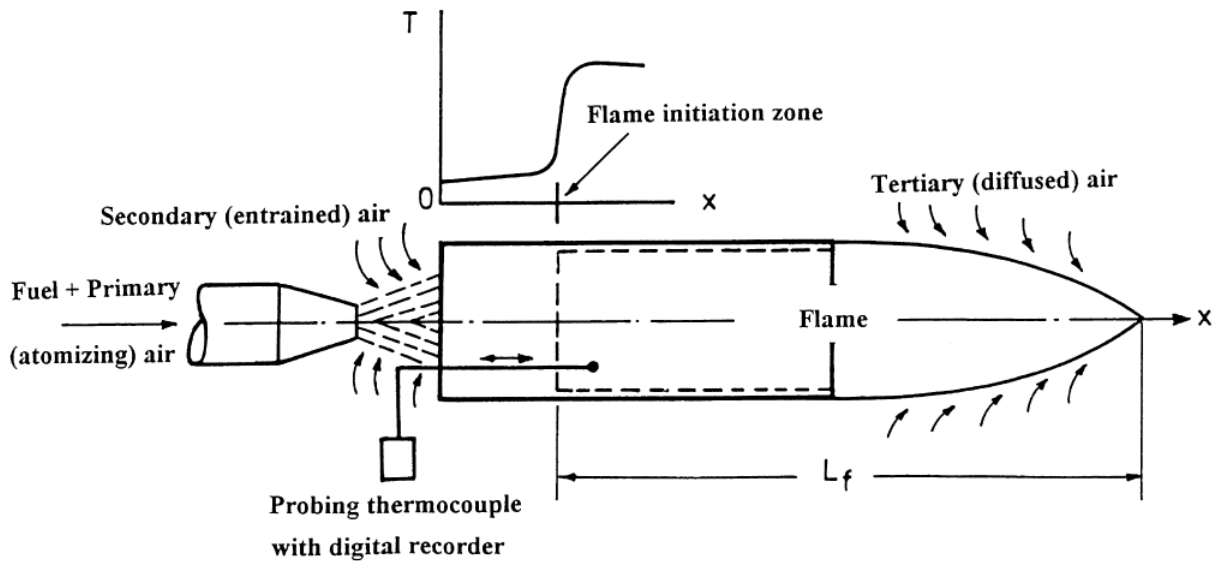
Figure 2.31: Determination of flame initiation zone inside burner tube and primary, secondary and tertiary air affecting the flame length [66]

Equations 2.31 and 2.32 calculate the flame length with an average absolute percentage error of 11.5 and 11.4%, respectively. Where L_f is the flame length (m), L_t is the burner tube length (m), D_t is the burner tube diameter (m), X is the axial distance between combustor exit and tube entrance (m), $PAFR = \dot{m}_a/\dot{m}_o = (\rho_{air}DA_tw)/\dot{m}_f$. where D is the body diameter of swirl combustor (m), A_t is the tangential inlet area of swirl combustor (m^2) and ω is air tangential angular speed to inlet of swirl combustor$= \dot{m}_a/\rho_{air}DA_t$ (rad/h).

Choi and Kim [67] described the results of experimental study of the visible flame lengths of coal-derived syngas jet diffusion flames. The experiments were performed using different nozzle size diameters and shapes varied at 1.23, 1.96, and 2.95 mm. The fuel gases used were various composition of CO and H_2, simulating the composition of coal synthetic gases. The results were compared with calculated flame lengths using pure methane flame from previous investigations, and it was found that: 1) the calculated Froude numbers for the experimental gaseous fuel matched well the results of previous studies; 2) the flame lengths of smaller diameter nozzles were longer, so the nozzle diameter was the key parameter determining the flame length; 3) the calculated flame lengths for various gases fuel compositions were smaller that the actual flame length.

Mogi *et al.* [68] investigated experimentally the flame characteristics of a high pressure hydrogen gas jet. A Hydrogen jet diffusion flame was injected horizontally from convergent nozzles of various diameters between 0.1 and 4 mm at reservoir over pressures between 0.01 and 40 MPa. The results showed that there is no stable flames were observed for nozzle diameters 0.1 and 0.2 mm - flame blew off although the spouting pressure increased up to 400 bar. The dimensionless flame length increases with the spouting pressure, measured close to the nozzle, as $L_f/d_o = 524.5P^{0.436}$, where pressure is in MPa. Also the flame length increases with increasing the mass flow rate according to increasing of spouting pressure, so the authors correlated the flame length to the mass flow rate regardless of the nozzle diameter as $L_f = 20.25\dot{m}^{0.53}$.

Molkov [69] derived a new dimensionless group for hydrogen jet flame length correlation. 95 experimental data on hydrogen subsonic, sonic, and supersonic jet flames at pressures up to 413 bar are fall in onto the same curve see Fig. 2.32, while the flame length can be calculated from $L_f = 76(\dot{m}_o d_o)^{0.347}$, in addition the author developed the nomogram for hydrogen jet flame length determination by only a nozzle diameter and a storage pressure.
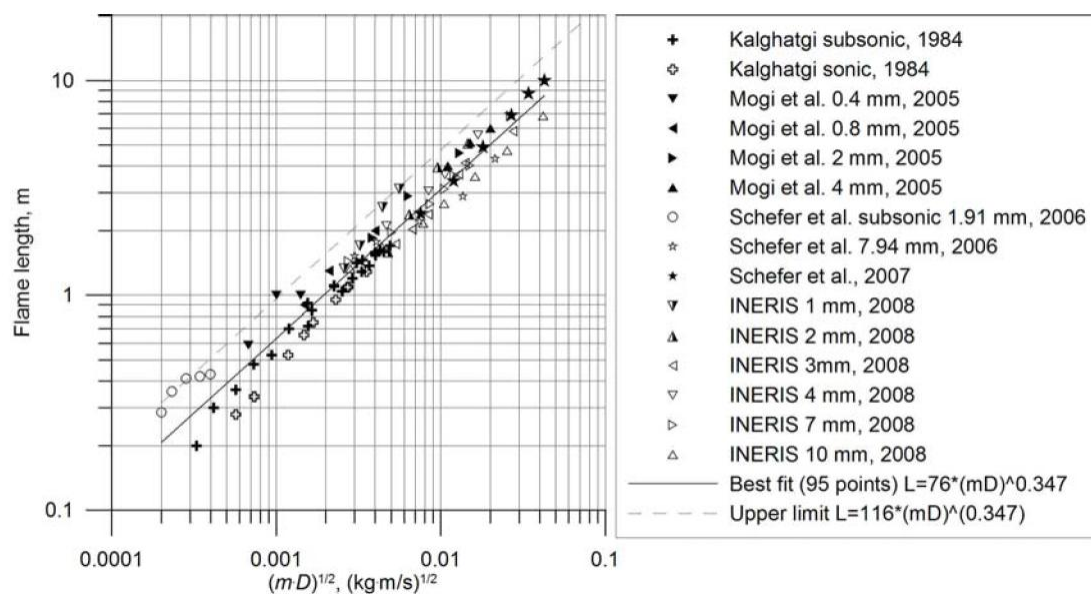
Figure 2.32: Experimental data and correlations for Hydrogen jet flame length [69].

2.6.2 Confined jet flame length

Pinto and Gollahalli [70] carried out experimental work to study the effects of varying primary air flow rate ($\dot{m}_p$), secondary air flow rate ($\dot{m}_s$), and coal feeding rate ($\dot{m}_c$) on the structure of pulverized bituminous coal flames. The flame appearance, flame length, axial and radial temperature profiles, and volumetric concentrations of particulate matter have been measured by means of color photography, thermocouples and $He - Ne$ laser beam attenuation. The results showed that the flame length increases with an increase of the coal feed rate and shifted the flame peak temperature downstream. Also the flame length increases with primary air ($\dot{m}_p$) until attained peak value at certain ($\dot{m}_p$) and then flame length decreases with ($\dot{m}_p$). Concerning the secondary air; the flame length and maximum flame temperature decrease with increasing the secondary air rate. A comparison of the flame length data at some typical conditions with the flame lengths predicted by the theoretical formulations from literature was performed and showed good agreement with measured values.

Yang and Blasiak [71] studied numerically the effect of high-temperature oxidizer and oxygen concentration oxidizer on the chemical flame length. Liquified propane gas (LPG) was used as the fuel. The following results were obtained: (1)flame length increases either the oxygen content decreases, the oxidizer temperature increases, or the fuel temperature decreases, (2)the flame length is independent of the fuel flow rate and the diameter of the fuel nozzle, (3) a simple correlation of the flame length with flow parameters has been derived in terms of a Fr_f number for momentum-buoyancy transition jet flame under the high-temperature oxidizer condition and can be calculated from Eqn. 2.1 (section 2.1). The criteria constants of the dimensionless flame length (L^*) to assess the momentum control or buoyancy-control flame are given as

$$L^* = \frac{L_f f_{st}}{d_o(\rho_o/\rho_{ox})^{1/2}} \tag{2.33}$$

Where f_{st} is stoichiometry, L_f if the flame length (m), ρ_o and ρ_{ox} are the density of fuel and oxidizer (kg/m^3), respectively, and d_o is the nozzle diameter (m).
A buoyancy-dominated regime was correlated by the expression

$$L^* = \frac{8.22 Fr_f^{0.4}}{(1 + 0.07 Fr_f^2)^{0.2}} \ (for Fr_f < 3) \tag{2.34}$$

And a momentum-dominated regime was correlated by the expression

$$L^* = 11 \ (for Fr_f \geq 3) \tag{2.35}$$

Sinha *et al.* [72] explored the feasibility of hydrodynamic control of confined nonpremixed flames by injecting air through a high-momentum microjet. An innovative strategy for the control of flame shape and luminosity is demonstrated based on a high-momentum coaxial microjet injected along the center of a confined nonpremixed flame burning in a coflowing oxidizer stream (see Fig. 2.33)[3]. The results of this study showed that the microjet assisted flame consists of a laminar base (zone I) and a turbulent trail (zone II) that are

---

[3]This figure is used based on license agreement between the author and Elsevier with license number of 264150854717.

separated by a "flame neck". For specified microjet and coflow velocities, the flame height is more sensitive to the fuel flowrate than for laminar or turbulent nonpremixed flames. The flame length can be calculated from the following empirical correlation

$$L_f = 12600 \prod +0.73, \ R^2 = 0.93 \tag{2.36}$$

Where $\prod$ is the velocity parameter and can be calculate as

$$\prod = u_o^2 u_{cf}^{0.1}/v_{mj} \ (m/s)^{1.1} \tag{2.37}$$

where v_{mj}, v_o, u_{cf} are the microjet, fuel jet and coflow velocity (m/s), respectively.
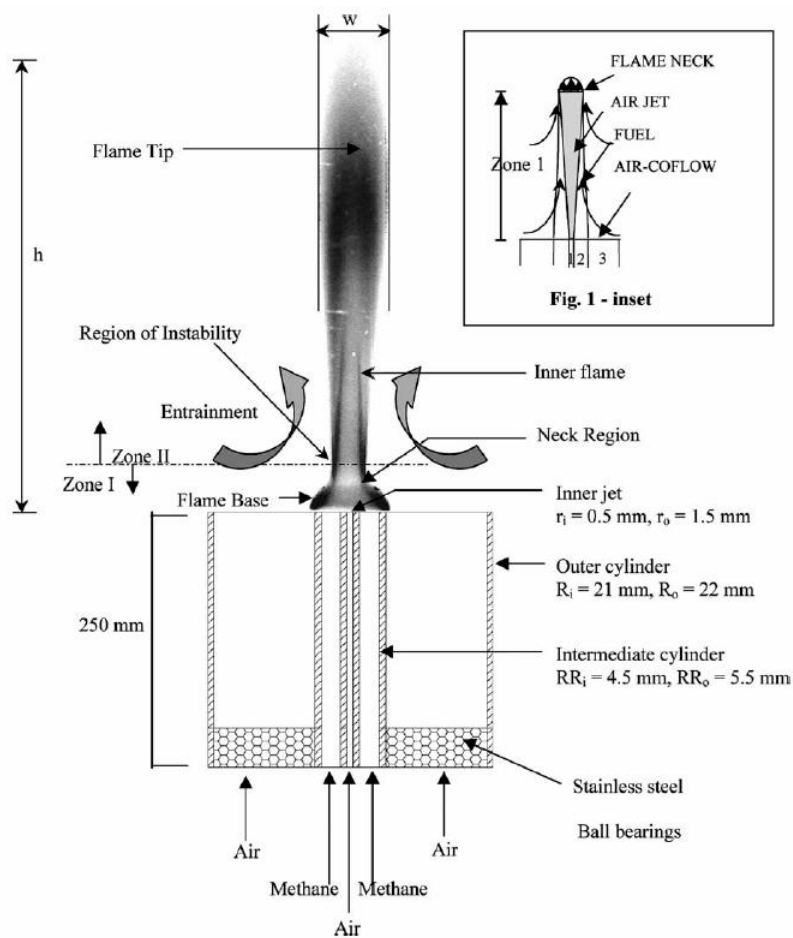
Figure 2.33: Schematic burner configuration and a microjet-assisted flame [72].

Kim *et al.* [73] studied experimentally combustion characteristics, flame structure, and flame length in an oxy-fuel combustor for a wide range of fuel nozzle diameters and fuel and oxidizer velocities. The following results can be drawn: (1) the oxy-fuel flame length was found to decrease with increased fuel and oxygen velocities due to higher turbulent mixing and entrainment, (2) the dimensionless flame lengths measured for the air-fuel flame are well-correlated with Delichatsios's relation [24]. However, the measured dimensionless flame length data of the oxy-fuel flame are considerably longer than

those estimated by the original Delichatsios's correlation and a modified Delichatsios's correlation correlated as follows

In a buoyancy-dominated regime, the dimensionless oxy-flame length is correlated as

$$L^* = 22.5 Fr_f^{0.4} \ (for Fr_f < 10) \tag{2.38}$$

The expression for the momentum-dominated regime is given as

$$L^* = 56.7 \ (for Fr_f \geq 10) \tag{2.39}$$

2.6.3 Rotary kiln flame length

Aloqaily *et al.* [74] studied experimentally the flame length in a lime kiln with a separate noncondensible gas, NCG burner using an acid-alkali visualization technique. Fig. 2.34 shows the schematic diagram of lime kiln with separate NCG burner.
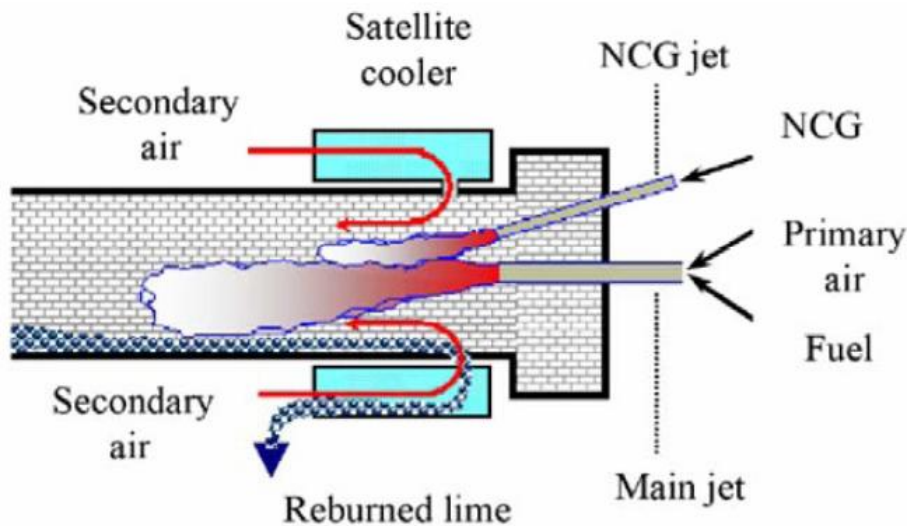
Figure 2.34: Schematic of the lime kiln with separate NCG burner [74].

The authors presented that the combined Craya-Curtet number (combined C_t) and excess air number were the dominant parameters affecting the flame length, shape, and temperature distribution a long the kiln. The results of this study were summarized as follows:

1. The flame length increased with an increase in combined C_t and with a decrease in excess air number.

2. The NCG burner angle between 0° and 8° had a significant effect on the flame length.

3. A comparison between the empirical correlation developed Aloqaily *et al.* [74] and Magnussen's formula [75] was conducted and showed good agreement, which means that both can be used to estimate the flame length.

4. Empirical equation was developed to calculate the flame length in the form of

$$\frac{L_f}{D} = 17.4 \left(\frac{(combined\ C_t)^2}{excess\ air} \right)^{0.3} \sqrt{\frac{\rho_f}{\rho_{secondary}}} \tag{2.40}$$

Combined Ct is given by

$$Combined\ Ct = \frac{U_k'}{(U_d'^2 - 0.5U_k'^2)^{\frac{1}{2}}} \tag{2.41}$$

$$U_k' = \frac{[r_1^2 u_1 + r_3^2 u_3 + (r_2^2 - r_1^2 - r_3^2)u_2]}{r_2^2} \tag{2.42}$$

$$U_d'^2 = \frac{[r_1^2 u_1^2 + r_3^2 u_3^2 + (r_2^2 - r_1^2 - r_3^2)u_2^2]}{r_2^2} - 0.5u_2^2 \tag{2.43}$$

Where, D is the kiln diameter (m), $u_1, u_2,$ and u_3 are nozzle exit velocity of main jet, the inlet velocity of the secondary air, and the NCG nozzle exit velocity (m/s), respectively. $r_1, r_2,$ and r_3 are nozzle exit radius of main jet, the kiln radius, and the NCG nozzle radius (m), respectively.

2.7 Computational fluid dynamics models

Pai *et al.* [76] formulated one of the first CFD models of flow and mixing in a cement kiln. Besides computational restrictions, early challenges in computer modeling of furnaces focused on the modeling of turbulence. Utilizing the $k - w$ model of turbulence, Pai *et al.* [76] predicted the flow and turbulence fields using the procedure of Spalding and co-workers and compared the results to measurements on a test model of the rotary kiln. The model consisted of an insulated steel pipe of 400 mm inside diameter and 3.4 m long with a 23 mm ID burner. Mass transfer was investigated by measurement of the concentration of helium which was injected as a tracer through the primary jet. To simulate non-isothermal conditions, the primary and secondary air were introduced at different temperatures. Although these early measurements and computations of the transport of heat, mass and momentum did not simulate realistic conditions of the rotary kiln flame, they were encouraging for the application of CFD in furnace modeling [31].

The recent development of CFD, availability of faster computers, and the widespread need for models which can account for coupling between fluid flow and heat transfer, led to the use of CFD models in the design and optimization of furnaces such as the rotary kiln.

Perron *et al.* [77] developed a mathematical model to simulate the operation of the coke calcining kilns. Petroleum coke used for the production of anodes is usually calcined in rotary kilns. The calcination process involves a number of different parameters which render the optimization of the calciner operation through plant tests very complicated and costly. So, the model was used to optimize the operation of the kiln in terms of improved calcined coke quality.

Leger *et al.* [78] presented a detailed numerical model of an industrial rotary kiln

incinerator using a commercial finite difference code. The focus of this model is on gasphase fluid mechanics, neglecting solid waste combustion and radiative heat transfer. Two baseline cases are tested (turbulence air on and off), and the results are analyzed for qualitative features in locations where experimental measurements have been unobtainable. The model predictions are shown to be physically realistic by comparison with experimental measurements obtained in the industrial rotary kiln that was modeled. Comparisons are made at only specific locations where experimental measurements have been taken. The overall conclusions concerning the quality and utility of the model predictions are as follows: (1) both baseline model cases predict qualitatively the gradient in temperature and species concentrations that have been measured experimentally near the kiln exit, (2) quantitative agreement between the predictions of both baseline model cases and experimental data is relatively good at the lower experimental location but poor at the upper experimental location, (3) a comparison between the baseline model cases suggests that the addition of turbulence air may increase stratification in the kiln rather than increase bulk gasphase mixing, (4) the turbulence air addition may be increasing stratification as the model predicts, rather than improving mixing as has been suggested on the basis of experimental data alone.

Chen and Lee [79] developed a simple steady state mathematical model for a rotary kiln incinerator operating under excess-air mode, where the governing equations were solved numerically. This model was used to examine the effects of some usually ignored factors, including the thermal radiation between all enclosed surfaces in a kiln, the solid/gas reaction and the existence of surface flame, on the kiln behaviour, The results demonstrate that, since the length/diameter ratio is small for a rotary kiln incinerator, The thermal radiation heat transfer between various enclosed surfaces is shown to be the most important factor in determining the kiln performance. Convection and conduction heat transfer contribution is relatively small, and can be neglected safely in calculations. Also the results show that it is reasonable to assume that the ignorance of gas phase will not change the basic characteristics of the simulation results for a rotary kiln incinerator. However, when large amount of soots formed or the kiln scale becomes very large, the significance of gas stream radiation will become more important.

Boateng and Barr [80] developed a mathematical model to predict heat transfer from the freeboard gas to the bed of a rotary kiln. The thermal mode1 includes a two-dimensional representation of the bed's transverse plane into a conventional one-dimensional, a simple model for rotary kilns. The result, a quasi threedimensional rotary kiln model, significantly improves the ability to simulate conditions within the bed without the necessity of rigorously accounting for the complex flow and combustion phenomena of the freeboard. The combined mode1 is capable of predicting the temperature distribution within the bed and the refractory wall at any axial position of the kiln.

Mastorakos *et al.* [81] presented computational model to study the clinker formation in coal-fired rotary cement kilns under realistic operation conditions with special emphasis given to the heat exchange between the coal flame and the kiln, the heat exchange between the kiln and the counter-flowing solids, and the chemical reactions that transform the solids into the final product (the clinker). An axisymmetric CFD code (the commercial package FLOW-3D) that includes a Monte-Carlo method for radiation has been used for the gaseous phase. The temperature of the kiln wall has been calculated

with a finite volume heat conduction code, and the species and energy conservation equations for the clinker have also been formulated and solved. The results show that radiation accounts for most of the heat transfer between the gas and the kiln walls, while the heat loss through the refractories to the environment accounts for about 10% of the heat input. The chemical reactions and heating of the charge absorb about 40% of the energy of combustion; it is hence imperative that these are accounted for. The calculated gas temperature at the centreline, the temperature $T_{RAD}(x)$, and the clinker temperature are compared in Fig. 2.35[4]. The peak gas temperature is located between 25 and 40 m, where the refractory inner surface temperature also peaks. The clinker is, surprisingly, hotter than the wall for the last few metres before it exits the kiln. The heat flux incident on the refractory by radiation is between 1 and 2 orders of magnitude higher than that by convection (Fig. 2.35) and the total heat transfer for the first 10 m of the kiln is towards the gas. The predictions are consistent with trends based on experience and available measurements from a full-scale cement kiln.
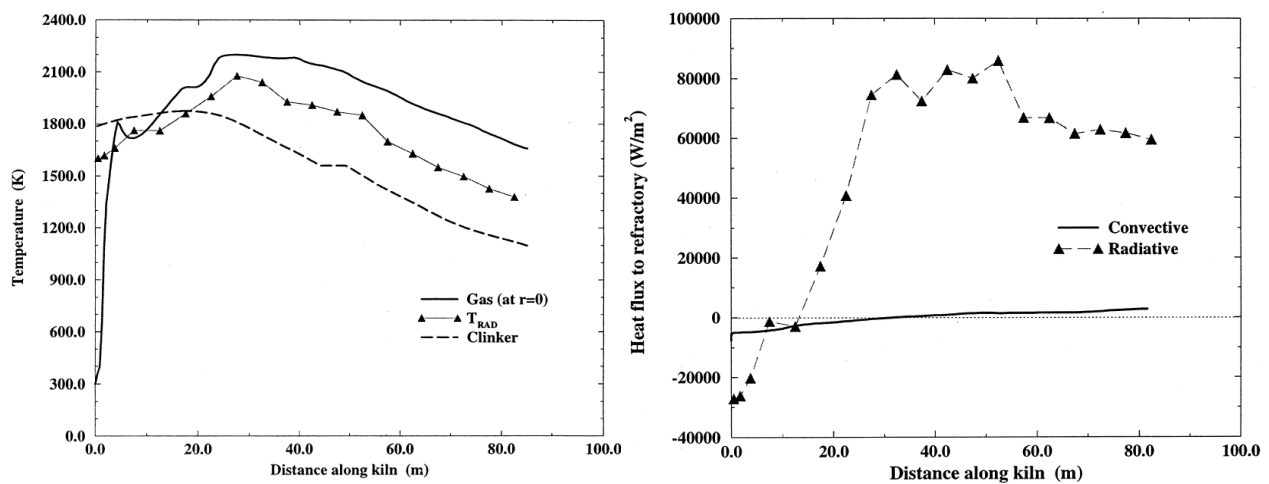
Figure 2.35: Axial distributions of the gas temperature, the fictitious temperature TRAD, and the clinker temperature (left),Axial distributions of the radiative and convective heat flux from the gas to the kiln-clinker system calculated by FLOW3D - RAD3D (right), [81].

Martins *et al.* [82] carried out one-dimensional mathematical model for the simulation of petroleum coke calcination in rotary kilns. The model is included of 14 ordinary differential equations derived from mass and energy conservation principles. The system of equations is solved by a fourth-order Runge-Kutta method. The model predicts, in the axial direction, temperature profiles for the bed of particles, the gas phase and the kiln internal wall as shown in Fig. 2.36[5]. It also predicts the composition profiles for the gas and solid phases. The simulation results of this study for the temperature profile of the solids bed and for the composition of the gas phase presented better agreement with measured industrial data (see Fig. 2.36).

---

[4]This figure is used based on license agreement between the author and Elsevier with license number of 2644160988305.

[5]This figure is used based on license agreement between the author and Elsevier with license number of 2644161275307.
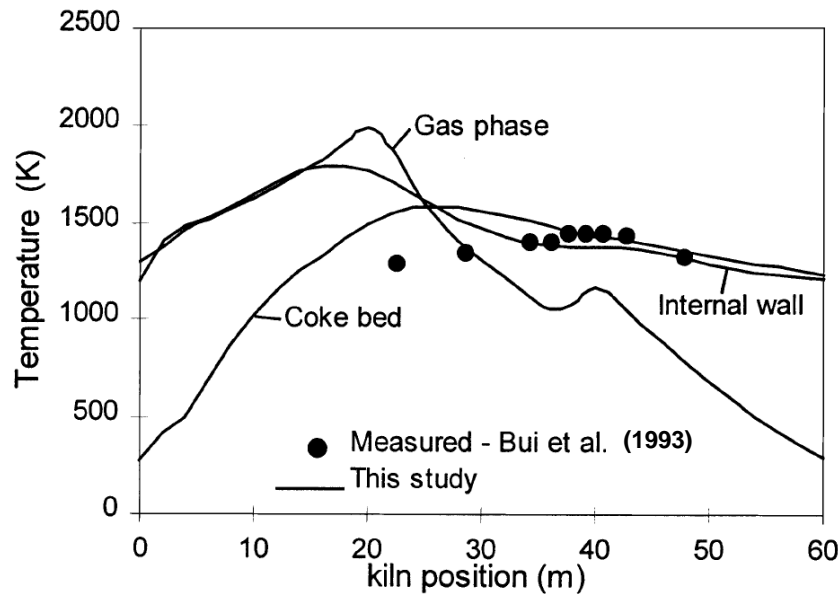
Figure 2.36: Temperature profiles for the solids bed, gas phase and internal wall [82].

Georgallis *et al.* [6] presented 3-D steady-state model to predict the flow and heat transfer in a rotary lime kiln. The model is based on a global solution of three sub models for the hot flow, the bed and the rotating wall/refractory. The overall model is validated using pilot kiln trials (5.5 m laboratory kiln, University of British Columbia, Canada). The numerical data (lines) capture the radial thermal gradients of the buoyant field as well as the correct difference between upper and lower inner wall temperatures.

Marias [83] presented a new development in the study of a rotary kiln incinerator. He described a possible coupling between $gPROMS^{TM}$ and $Fluent^{TM}$. The modelling of the furnace has been divided into two parts. On the one hand, a model describing the physico chemical processes which occur within the burning bed of municipal solid waste (50% of wood, 40% of cardboard and 5% of PVC (on a weight basis)) On the other hand, CFD has been used to describe the processes occurring within the gaseous phase of the kiln and of the post combustion chamber (turbulence, combustion, radiation) self incineration was not possible. This can be attributed to the smaller quantity of the incident radiation received by the bed of waste, which insufficiently ensures its complete pyrolysis within the kiln. Subsequently, it has been demonstrated that adding an extra burner, fed with methane, was a possible solution in order to achieve the complete pyrolysis of waste within the kiln. The model is able to predict the combustion of the volatile matter within the incinerator as well as the subsequent radiation received by its walls, and the thermal and chemical species contours. This data may be very interesting in order to check for the efficient running of the process and then possible enhancements in the design of the furnace.

Ma *et al.* [84] carried out a 3-D numerical simulation with CFX software on physical field of multi-air channel coal burner in rotary kiln. The effects of various operational and structural parameters on flame feature and temperature distribution were investigated. A thermal measurement was conducted on a rotary kiln (4.5 m in diameter, 90 m in length) with four-air channel coal burner as shown in Fig. 2.37 to determine the

boundary conditions and to verify the simulation results. The calculated results show that (1) the distribution of velocity near burner exit is saddle-like; (2) recirculation zones near nozzle and wall are useful for mixture primary air with coal and high temperature fume; (3) Adjusting the ratio of internal airflow to outer airflow is an effective and major means to regulate flame and temperature distribution in sintering region; (4) Large coal size can reduce high temperature region and result in coal combusting insufficiently; (5) Too much combustion air will lengthen flame and increase heat loss
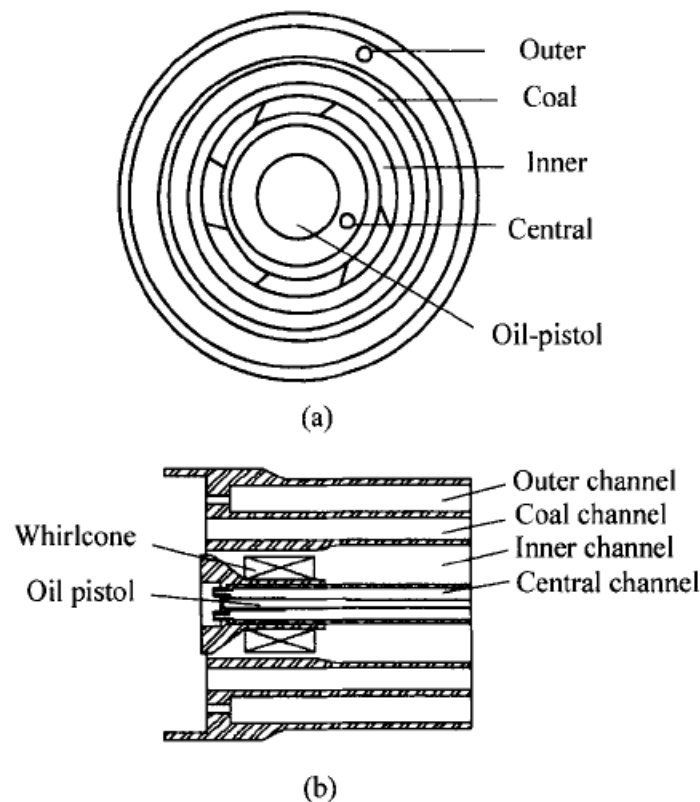
Figure 2.37: Sketch of four air channel burner (a)Radial section; (b) Axial section [84].

Torgunakov [85] developed and used IR systems for thermographic inspection of rotary kilns and for analysis of the temperature distribution in the radial and axial directions of a kiln's shell, on the inner surface of the lining layer, and in the kilned material. The operation of these systems is based on the application of the mathematical apparatus for solving the inverse thermal-conduction problem involving a simulated 3D model of thermal processes in a cement kiln. The model takes into account the radiative and convective heat exchange between the fuel flame and the inner wall of a kiln, heat exchange within the shell material, convective and radiative heat exchange on the outer surface, rotation of the frame, and movement of the kilned material (clinker). The shape of the thermal-radiation distribution is an important process parameter that significantly governs the efficiency of a thermal device. For each kiln, after ignition, there is an optimum shape of the thermal-radiation-distribution set, which should be maintained by the operator during the kiln's operation. Since the shape of the thermal-radiation distribution is mainly determined by the temperature of kiln gases, in the calculations based on the model, the author changes the temperature of kiln gases and study the resulting changes in other temperature fields. In the experiment, the length of this part is 85 meters. The first curve represents the

ideal shape of the thermal radiation distribution, which has been considered in many publications. The second and third curves show the maximum deviation of the thermal-radiation distribution from the ideal shape. The fourth distribution has the shape of a plateau (such a distribution will be referred to as flat). The fifth curve, characterized by two maxima in the thermal-radiation distribution, is often observed in practice when a solid dust like fuel is burnt.

Wang *et al.* [86] carried out a computational model for combustion process of coal under industrial operation conditions with the comprehensive model for a cement rotary kiln in the dry process cement product system, based on analysis of the chemical and physical processes of clinker formation, a heat flux function was introduced to take account of the thermal effect of clinker formation. Combining the models of gas-solid flow, heat and mass transfer, and pulverized coal combustion, a set of mathematical models for a full-scale cement rotary kiln were established. Using of commercial CFD code (FLUENT), the distributions of gas velocity, gas temperature, and gas components in a cement rotary kiln were obtained by numerical simulation of a 3000 t/d rotary kiln with a four channel burner. Figure 2.38 shows that; the average curves of the cross-section along the rotary kiln for gas temperature, CO, CO_2, and O_2 concentrations and also as is shown in the Figure, the average O_2 concentration of cross-section is 3%; the average CO and CO_2 concentration is 0.2% and 15%, respectively; and the burnout ratio reaches 97% at the inlet of the kiln feed.
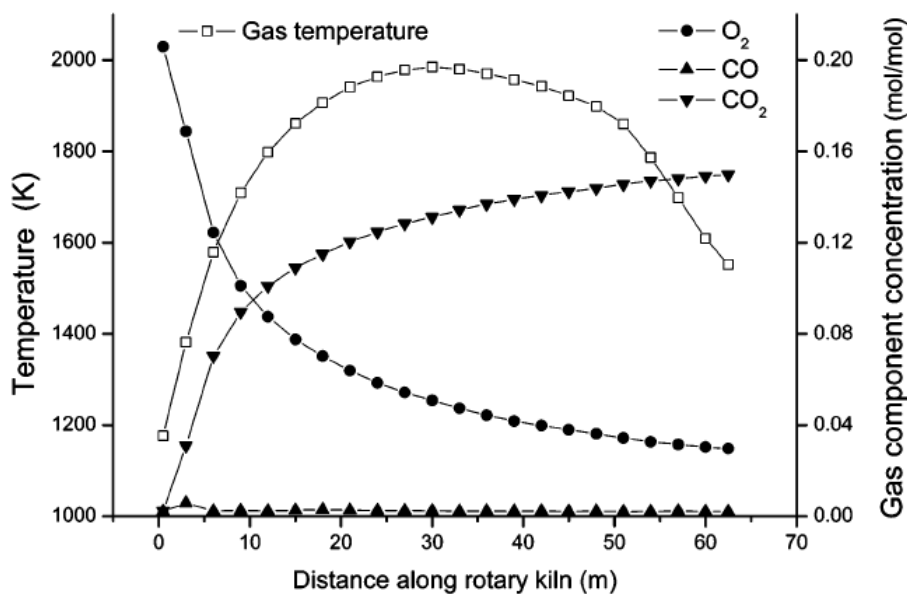
Figure 2.38: Average curves of cross-section along the kiln [86].

Mujumdar and Ranade [87] carried out one-dimensional reaction-engineering model to simulate reactions in bed region of rotary kiln along with heat transfer in the transverse plane of kilns. The model was also used to simulate performance of three industrial cement kilns. For simulation of industrial kilns, maximum temperature of freeboard gas was the adjustable parameter. By adjusting maximum flame temperature, the model was able to predict the mass fractions and temperature of solids at the solid exit reasonably well for three industrial kilns. The model was used to evaluate the kiln performance for

different operating conditions. Simulation results indicate that a better performance can be obtained by operating kilns at lower RPM, high solids flow rate and lower tilt. The model was further used to understand influence of temperature profile within the kiln on net energy consumption of cement kiln. It was observed that as position of maximum flame temperature moves closer to the solids entrance, the net energy consumption in the kiln decreases.

Mujumdar *et al.* [88] developed a comprehensive model to simulate complex processes occurring in pre-heater, calciner, kiln and cooler for clinker formation in cement industry. Complex heat transfer and reactions (solid-solid, gas-solid and homogeneous reactions in gas phase) in rotary kiln were modeled using three sub-models. The individual models were coupled with each other via mass and energy communication through common boundaries. The coupled model equations were solved iteratively. The integrated simulator was converted into simple to use GUI based software for cement industry, named as RoCKS. RoCKS was used to simulate performance of pre-heater, calciner, kiln and cooler for clinker formation. The simulation results indicated that operating kiln with higher solid loading, lower rpm, lower tilt and lower grate speed reduces energy consumption per unit production. The model was also able to predict kiln characteristics like maximum flame temperature and overall flame length for coals with different compositions. Detailed validation was unfortunately not possible since adequate industrial data could not be obtained. However, the model predictions agreed reasonably with industrial observations. RoCKS was used to understand influence of various design and operating parameters on overall performance. Fig. 2.39[6] shows gas and solid temperature profiles across pre-heaters, calciner, kiln and cooler in a cement clinker process.
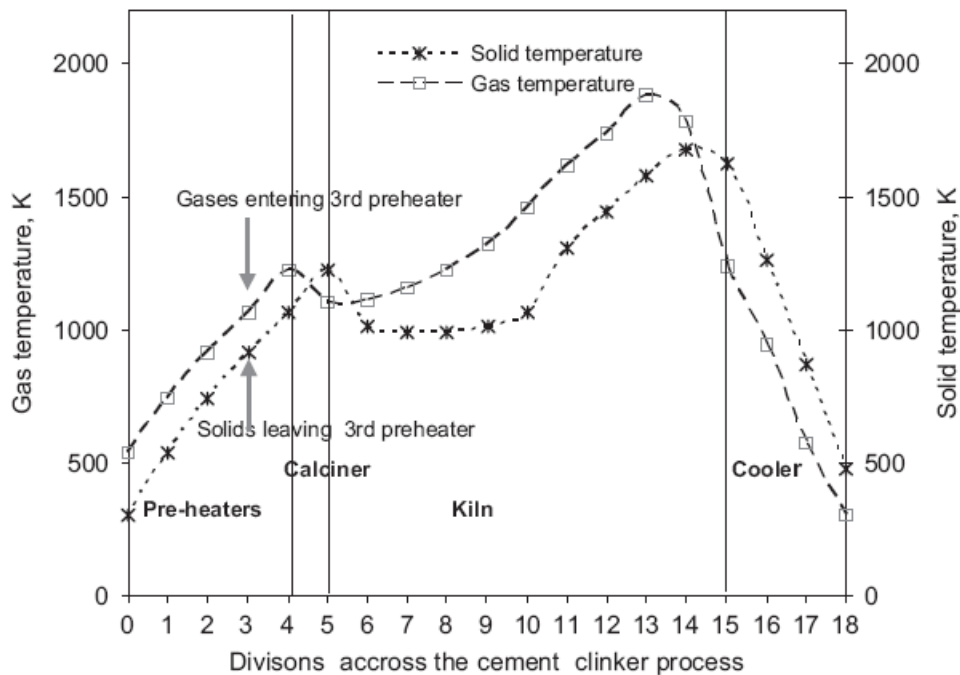
Figure 2.39: Gas and solid temperature profiles across pre-heaters, calciner, kiln and cooler in a cement clinker process, [88].

---

[6]This figure is used based on license agreement between the author and Elsevier with license number of 2644170912908.

Küssel *et al.* [89] carried out one dimensional modeling of rotary kilns used for calcinations of limestone as an application. The model is designed and numerically integrated within the Dymola modeling environment. The set up is depicted in the Figure 2.40. The flows of gas and bed phase are counter current. The rotary kiln itself consists of isolation and a steel shell. Chemical reactions in the bed and in the gas phase are considered. Heat and mass transfer between the bed and the gas phase are implemented. Results are compared with computational fluid dynamic simulations. Figure 2.41 shows the temperature profiles of the gas phase for Dymola and CFD simulation. The results show that the comparison to CFD simulation data confirms these results from Dymola modeling, and the errors are small enough to allow for application in observer based model. In addition, the modeling approach has a lower computational capacity.
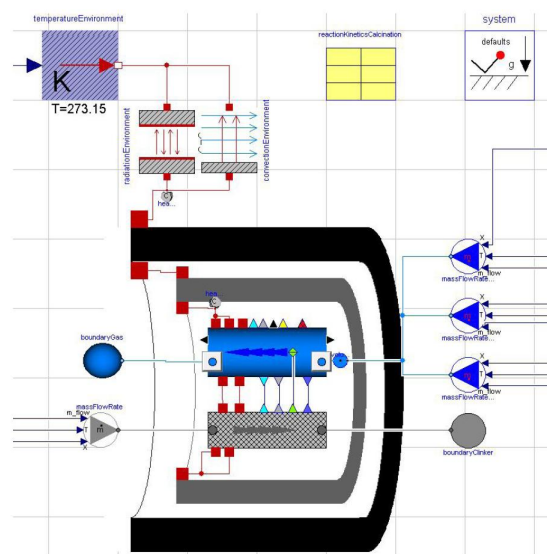
Figure 2.40: Dymola model of a rotary kiln [89].
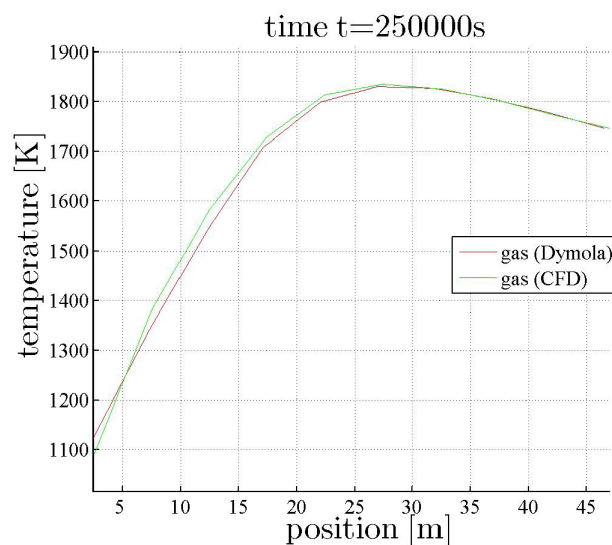
Figure 2.41: Comparison of gas phase temperature [89].

Bhad *et al.* [90] carried out CFD modelling for a full scale rotary cement kiln with multi channel coal burner using commercial CFD code Fluent-6.3.26. The study included developing and combining the models of gas-solid flow, modelling of pulverized coal combustion and heat transfer from flue gas to the reacting mass and surroundings. RNG $k - \varepsilon$ model for turbulence, eddy dissipation model for coal combustion and P1 radiation model were used in the CFD model. Four different cases have been studied where the vane angles of the swirler of the burner were varied from 22.5° to 45° and influence of swirler angle on flame profile, temperature distribution and species concentration were predicted. Results indicate that lowering the vane angle from 30° to 22.5° leads to contraction of higher temperature zone radially, which is desirable. With higher vane angle 37.5° & 45°, length of the flame reduces; however, higher temperature zone spreads radially towards the refractory wall. Centerline temperatures along the kiln length for the four cases studied (with different vane angles) are presented in Fig. 2.42 and a summary of mass weighted average mole fractions of components along the kiln length has been presented in Fig. 2.43.
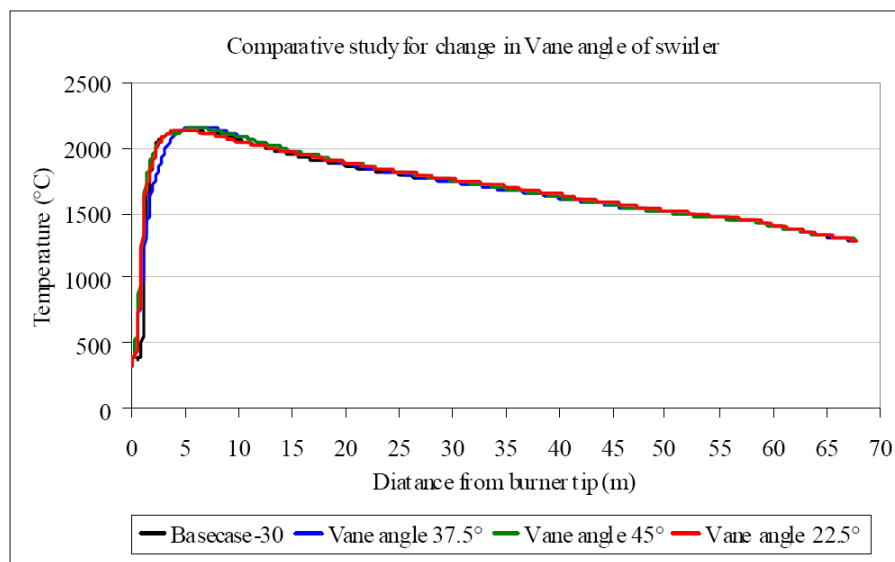
Figure 2.42: Centerline temperature of the kiln for different vane angles [90].

Macphee *et al.* [91] used Computational fluid dynamics (CFD) has been used to investigate the combustion processes occurring within a large-scale rotary lime kiln. In this preliminary study and because the main interest is the flame characteristics, the effects of the reacting limestone bed have been ignored. Numerical results were validated against experimental data from the International Flame Research Foundation's (IFRF) Furnace No.1. The validation study focused on comparisons between the finite rate and mixture fraction/PDF approaches to combustion chemistry, and different methods for defining coal particle size distributions. The aerodynamics and effects of varying the coal flow rate have been investigated for the rotary lime kiln. The results show that (1) the recirculation in the rotary kiln is affecting the temperature profile; (2) the effects of coal flow rate on temperature with a 13% difference in mass flow found to have little effect on the centre line temperature profile; (3) the validation experiments showed the finite rate model to produce a better representation of combustion characteristics than the mixture
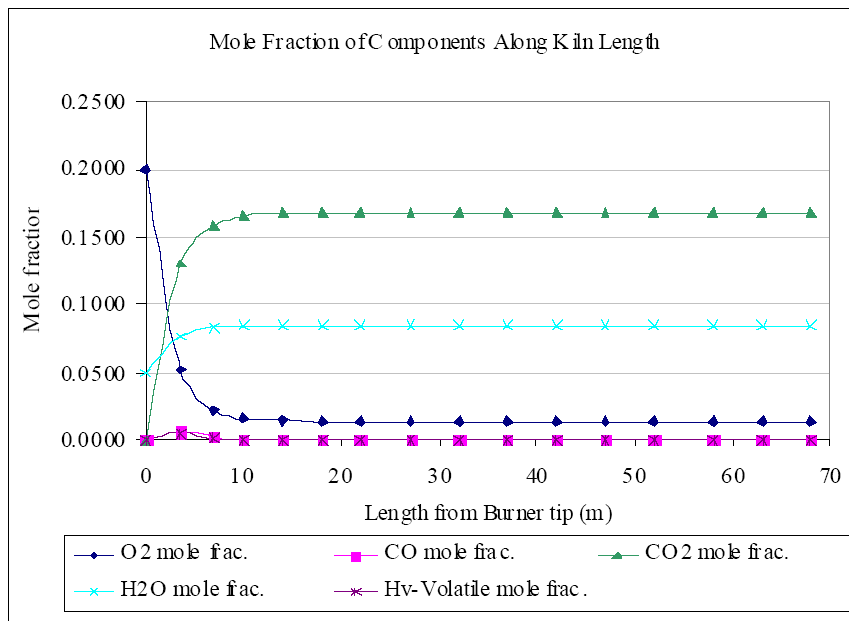
Figure 2.43: Species concentration along the kiln length [90].

fraction/PDF approach to combustion chemistry ; (4) the validation case also demonstrated that multiple uniform sized injections provide more accurate results than a single injection with a Rosin-Rammler particle size distribution.

Davies *et al.* [92] presented CFD modeling using ANSYS-CFX package and experimental studies of the flow characteristics within a rotating cylinder containing a rolling bed of sand. The axis of the cylinder was horizontal and there was no axial bulk flow of particles. The velocity field of the gas flowing through the cylinder was measured by hot-wire anemometry. The measurements indicate that the velocity field is asymmetric with respect to a diameter perpendicular to the granular bed. CFD calculations confirm this finding. The gas velocity profiles are very important in determining heat transfer from gas to solid. Fig. 2.44[7] shows measurements in a cylinder rotating at 7.2 *rpm*. In this case, measurements were taken on a 0.5 x 0.5 *cm* grid. The data show asymmetry with respect to a diameter perpendicular to the granular bed surface, in contrast to the case with no rotation: the velocities are lower near the lower part of the active bed surface than in the upper part of the active bed surface. Fig. 2.44 shows computed axial velocity contours over a cross section 0.10 *m* from the cylinder exit. As with the experimental measurements of the velocity profile, flow asymmetry is apparent, with a region of slower flows near the foot of the rolling bed. The experimental and computational results clearly show that the assumption that the air flow pattern in the cylinder is similar to that in a duct is not valid. Estimates of the gas-wall and gas-bed heat transfer coefficients based on pipe flow correlations are likely to under predict these parameters.

Stadler *et al.* [93] used a first principles model of a cement kiln is used to control and optimize the burning of clinker in the cement production process. The model considers heat transfer between a gas and a feed state via convection and radiation. Furthermore,

---

[7]This figure is used based on license agreement between the author and Elsevier with license number of 264425010671 2.
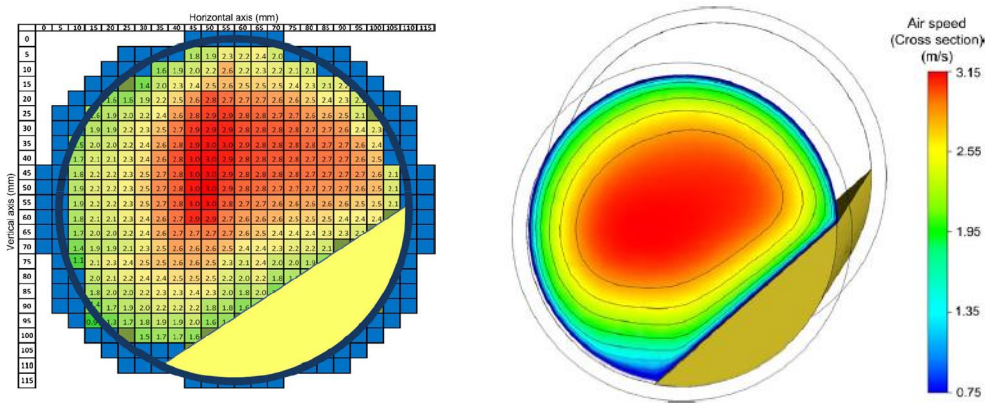
Figure 2.44: Axial velocity in (m/s) over a cross-section $0.1\,m$ from the air outlet end of the cylinder.Maximumbed depth, measured normal to the bed surface, $0.025\,m$. Air flow rate $0.0162\,m^3/s$. Rotation $7.2\,rpm$, measured (lift), computed (right) [92].

it contains effects such as chemical reactions, feed transport, energy losses and energy input. A model predictive controller is used to stabilize a temperature profile along the rotary kiln, guarantee good combustion conditions and maximize production. The temperature profile as shown in Fig. 2.45[8] cannot be measured because along the rotary kiln temperature sensors are not available. Hence, estimating the temperature profile is an important issue and needs to be considered in the model design. And also as shown the figure the system is divided into compartments corresponding to the zones to simplify the overall thermodynamic modeling of the process.
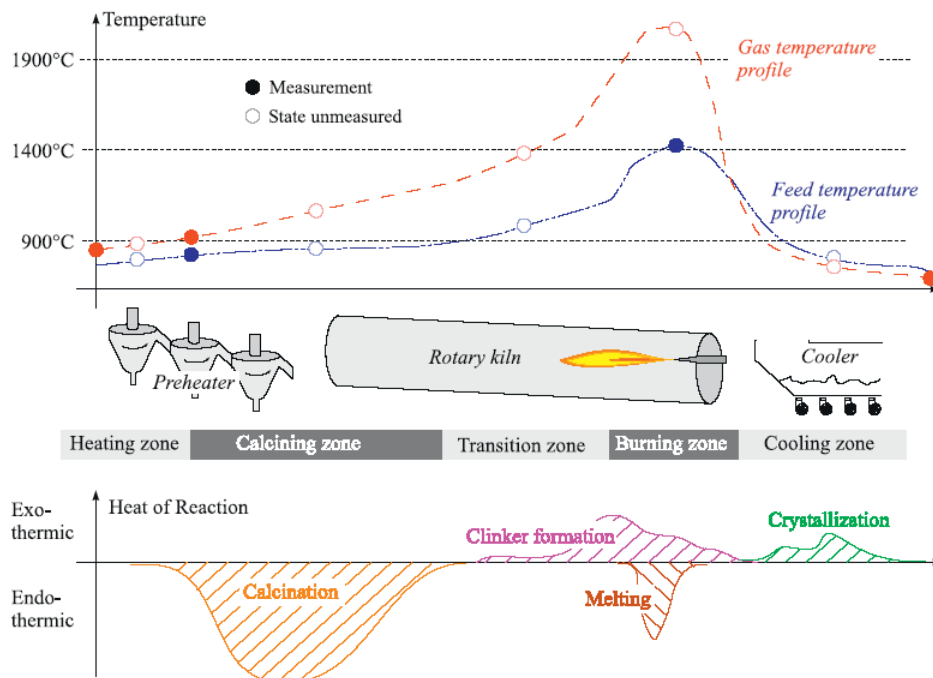
Figure 2.45: Temperature profile and the qualitative profile of the heat of reaction of the feed along the clinker production unit [93].

---

[8]This figure is used based on license agreement between the author and Elsevier with license number of 264250405073.

2.8 Concluding remarks

The review of the previous work presented in the previous sections of this chapter had been conducted in order to provide an extensive background and clear direction for the present study. It has been noticed that a huge amount of previous investigations related to heat transfer processes in rotary kilns has been conducted for radiation and convection in free board region to exposed wall and bed surfaces. Although extensive investigations have been performed for free jet diffusion flame including empirical and theoretical flame length correlations under different operating conditions, researches on the confined flame jet lengths under different operating parameters and flow field (aerodynamics) are still not completely solved, especially for rotary kilns.

The present literature review revealed that the information related to flame patterns (shape, length) and flow visualization inside rotary kilns, are still not completely studied. Studies of the effects of the inlet air conditions (air inlet temperature and air swirl number), excess air number, air inlet diameter, radiation effect, size and location of primary air, kiln burner geometry and power on the flame behavior and thermal distributions a long the kiln are quit limited. Such information and studies are necessary for the designer of such kilns. In a trial to fill a part of the gap existing in this field, the present work carries out numerical simulation on the flame in rotary kilns using commercial CFD code (FLUENT 6.3) using gas fuels. The effects of the above parameters on the thermal distribution along the rotary kiln were investigated and presented. Such parameters were varied to regulate the flame length which deals the processes inside the kiln and controls the product quality.

Chapter 3

Computational Methodology

3.1 CFD modeling overview

Computational fluid dynamics is a virtual prototyping that guides in building accurate flow models by solving transport equations. The features of combustion flows can be analyzed in detail with CFD. In particular, mixing, temperature, flow velocity, flame stability, and concentration of combustion species can accurately be computed for different geometry. CFD modeling of gas flow inside the rotary kiln chamber provides 2-D and 3-D analyses of the general flow pattern by mapping the pressure field and velocity vectors that show recirculation zones, mixing, and resident time within the chamber and further provides temperature and species concentration of the combustion products. It therefore makes it possible to evaluate useful operational parameters of interest for design optimization prior to prototyping, or troubleshooting an existing design for operational performance [47].

The physical and chemical phenomena of the reacting flow may be simulated by numerically solving a set of generalized conservation equations for flow (Navier Stokes equations), and an associated set of equations involving enthalpy, combustion, and so on. A fundamental method for the numerical simulation of the governing equations is the finite-difference or finite-element approximations. The formal steps involved in the application of the methods follow four steps [94]: (i) the domain of the problem is covered by a simple mesh, (ii) values of the numerical solution are labeled at the intersections or nodes of the mesh, (iii) a finite-difference or finite element approximation to the differential equation is formulated in each node resulting in a system of algebraic finite-difference or finite-element equations, and (iv) the system of equations approximating the problem is solved to produce a numerical solution. This process generally involves solving numerically large systems of linear algebraic equations and the corresponding computer algorithms are those of numerical linear algebra. Until recently when computer power improved, it was not possible to apply CFD modeling to industrial rotary kilns because of the large aspect ratio and the large number of mesh points involved to accurately represent the problem. A typical 3m diameter by 30m long rotary kiln (L/D =10) may require a couple million mesh points for the calculation domain and require several days or even weeks to execute the program depending on the power of the computer used. However, several CFD providers have improved their modeling capabilities and CFD has become a powerful tool in modeling the complex rotary kiln phenomena including combustion and flames. CFD solves the conservation equations

involving mass, momentum, combustion, and enthalpy equations within the boundaries of the kiln. The two-phase flow nature of pulverized fuel combustion requires tracking of the particles as localized sources and brings an added complexity to CFD modeling of such operations. To model the combustion in kilns, mathematical expressions are required for the turbulent reactive flow, coal pyrolysis or devotalization, homogeneous volatile combustion, heterogeneous char reaction, particle dispersion, radiation, and pollutant emission. There are several CFD providers that offer software packages for the simulation of rotary kiln processes. They all treat the mathematical expressions and the numerical schemes required for their solution slightly differently. We will present some of the generalized equations that are common to combustion modeling. The flow in a rotary kiln is typically gas solid turbulent flow with chemical reactions, mainly combustion. The building blocks behind the user-defined functions (UDF) in commercial CFD codes applied to rotary kiln combustion modeling consist of "renormalization group" (realizable) $k - \epsilon$ turbulent model for gas phase and, in the case of pulverized combustion particles, the statistical (stochastic) trajectory model for homogeneous volatile and heterogeneous solid-phase char combustion [47]. The fundamental equations are discussed in the next sections .

There are many commercial CFD packages for modeling and analyzing system involving fluid flow, heat transfer and dissociated phenomena such as chemical reaction. Some popular CFD packages include: FLUENT, CFX, PHOENICS and ANSYS. All these commercial CFD codes contain three main elements: Preprocessor, Solver and Post-processor (see Fig. 3.1). This study concentrates on the use of FLUENT software package to simulate the flow and mixing behaviour especially for chemical and thermal industrial applications. But comparisons with some of experimental and other analytical data were also necessary to be made in order to verify the results made by FLUENT CFD code.
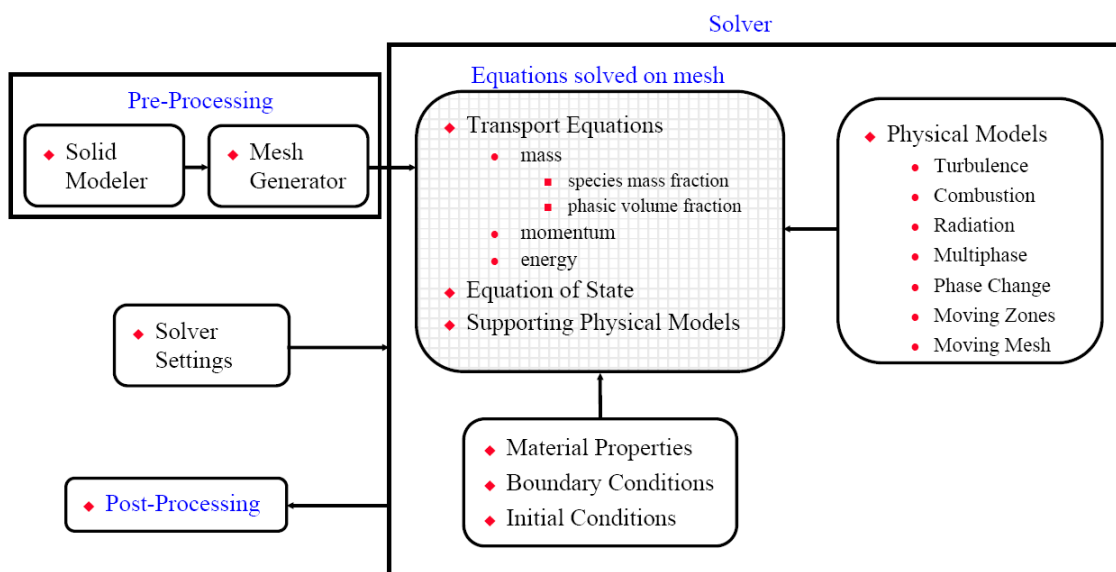
Figure 3.1: Structure of CFD code [95].

3.2 Gas-phase governing equations used in CFD modeling

The set of conservation equations that are solved in most CFD analyses are as presented earlier but expanded to include the stress generation as in the following equations [86].
Continuity:

$$\frac{\partial \rho}{\partial t} + \frac{\partial}{\partial x_i}(\rho u_i) = S_p \tag{3.1}$$

where the variable in the continuity equation represents a source term typical to fuel injection or combustion of particles in a control volume. The components of velocity in a three-dimensional coordinate system are represented by the momentum equation
Momentum:

$$\frac{\partial}{\partial t}(\rho u_i) + \frac{\partial}{\partial x_i}(\rho u_i u_j) = -\frac{\partial p}{\partial x_j} + \frac{\partial \tau_{ij}}{\partial x_j} + \rho g_i + F_i + S_p \tag{3.2}$$

which includes pressure, turbulent shear stresses, gravitational force, that is, buoyancy effects, and the source terms arising from gas-solid interactions. The τ_{ij} term in Equation (3.2) represents Reynolds stress as

$$-\overline{\rho \tilde{u_i} \tilde{u_j}} = \mu_t \left(\frac{\partial u_i}{\partial x_j} + \frac{\partial u_j}{\partial x_i} \right) - \frac{2}{3}\delta_{ij} \left(\rho k + \mu_t \frac{\partial u_i}{\partial x_i} \right) \tag{3.3}$$

In order to include temperature distribution, the Navier Stokes equations are accompanied by an energy equation that solves for enthalpy ($h = CpT$). The balance equation for **Enthalpy** is

$$\frac{\partial}{\partial t}(\rho h) + \frac{\partial}{\partial x_i}(\rho u_i h) = \frac{\partial}{\partial x_j} \left(\Gamma_h \frac{\partial h}{\partial x_j} \right) + S_h \tag{3.4}$$

The source term, S_h, includes combustion, that is, the heat source and the heat transfer within the system that affect temperature. In rotary kilns, the dominant heat transfer mode is radiation and there are several models to evaluate its value, some of which will be examined in detail later.

CFD providers treat gas-phase combustion by using a mixture fraction model [86]. The model is based on the solution of the transport equations for the fuel and oxidant mixture fractions as scalars and their variances. The combustion chemistry of the mixture fractions is modeled by using the equilibrium model through the minimization of the Gibbs free energy, which assumes that the chemistry is rapid enough to assure chemical equilibrium at the molecular level. Therefore, individual component concentrations for the species of interest are derived from the predicted mixture fraction distribution [47].

3.3 FLUENT software package

FLUENT was developed by Fluent Inc. and is a state-of-the-art computational tool that uses the finite volume method to solve fluid flow problems. It is a robust, reliable

comprehensive CFD package. The FLUENT user interface consists of a Graphical User Interface (GUI) with pull-down menus and a Text User Interface (TUI) where commands can be specified to perform certain operations, such as saving a file, reading it back, and modifying the memory properties defined in the FLUENT manual [95].

The FLUENT [95] package includes a solver (FLUENT), preprocessors (GAMBIT, T Grid, G/TURBO), and filters/translators (for importing meshes from other packages such as NASTRAN and AutoCAD). The organization of the above components and the interactions among them are shown in Figure (3.2).
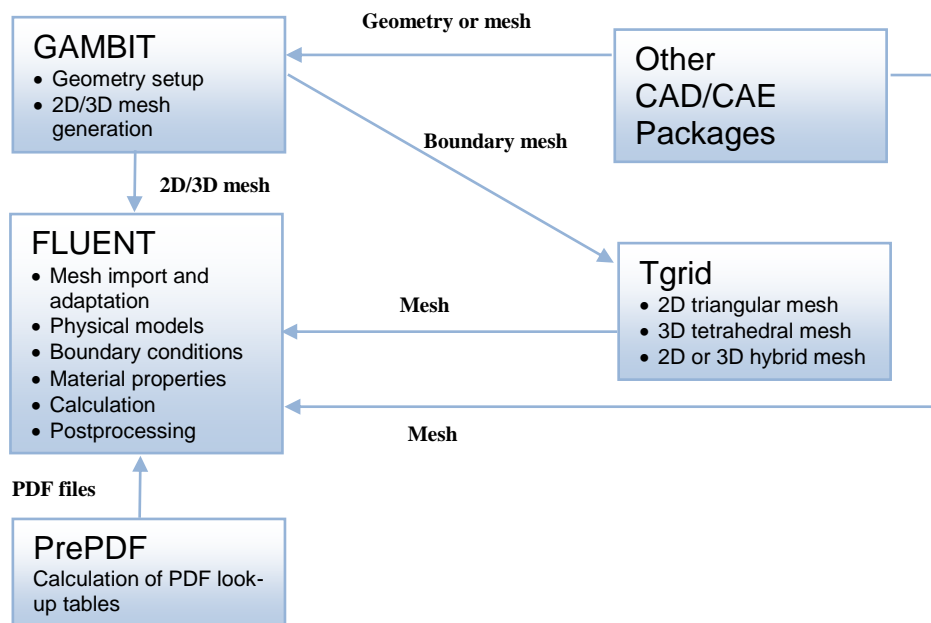
Figure 3.2: Basic program structure of fluent packages [95].

The computational domain must be created before solving a problem. GAMBIT supports both 2D and 3D geometries and is used to create the geometry and define boundary types. Supported mesh types include 2D triangular/quadrilateral, 3D tetrahedral, hexahedral, pyramid, wedge, and mixed i.e. hybrid meshes (see Fig. 3.3) and body-fitted, block-structured meshes. It uses unstructured meshes in order to reduce the amount of time you spend generating meshes. The mesh can also be refined or adapted depending on the problem requirement in FLUENT. The geometry is created and meshed, dividing the domain into discrete units. The discretized computational domain is then exported to FLUENT where the models and process parameters are chosen. The standard interface may not meet the needs of all the problems, so user defined functions (UDF's), which are programs written by the user, can be hooked to FLUENT. In the example of a flow through a pipe, FLUENT allows the user to specify the inlet velocity. UDF's are used in this example if the flow is to be started after a certain amount of time or if the flow follows a specific profile. FLUENT solvers are based on the finite volume method; the domain is discretized into a finite set of control volumes or cells as shown in Fig. 3.4. FLUENT solves general conservation (transport) equation for mass, momentum, energy, etc. which is applied in each cell (see equation 3.5)
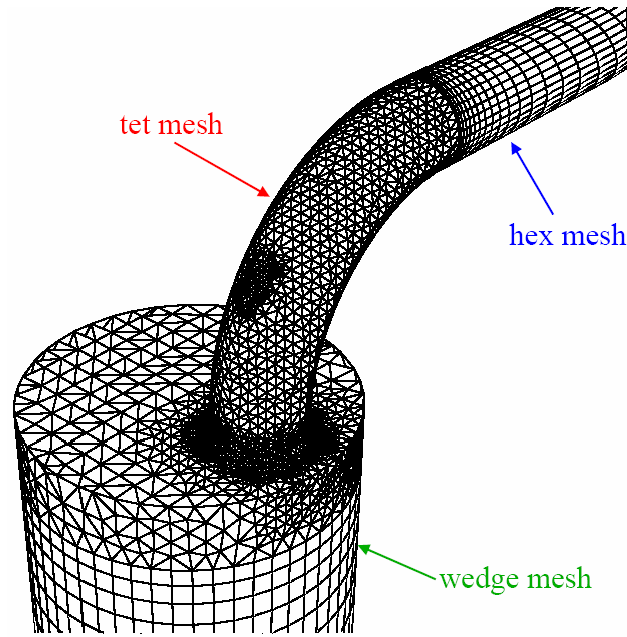
Figure 3.3: Structure of CFD code [95].
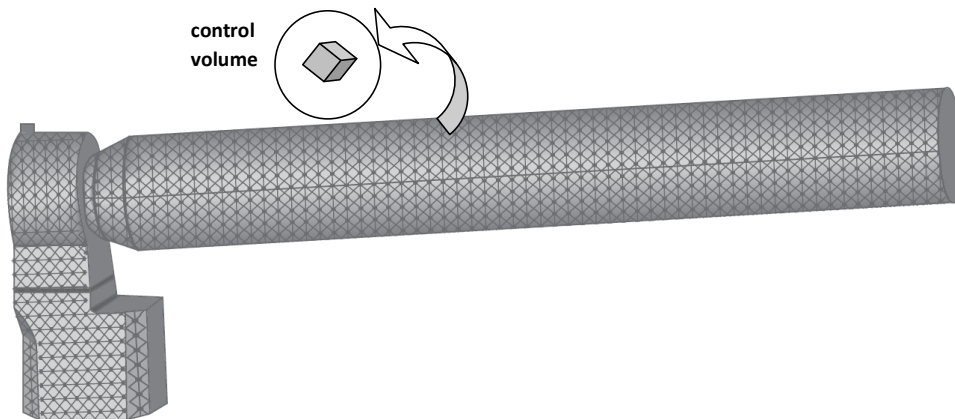
Figure 3.4: Structure of CFD code [95].

$$\frac{\partial}{\partial t}\int_v \rho\phi.dV + \oint_A \rho\phi V.dA = \oint_A \Gamma\nabla\phi.dA + \int_V S_\phi.dV \qquad (3.5)$$

Where ϕ is a quantity which is l for continuity equation, u for x-momentum equation, v for y- momentum equation, and h for energy equation. On the left side of Eqn. 3.5, the first part of the equation is to account for an unsteady condition and second part is to account for a convective behaviour. On the right side of the Equation 3.5, the first part is to account for a diffusive behaviour, and the second part is to account for generation of quantity (ϕ) inside the cell. Each transport equation is then discretized into algebraic form, while partial differential equations are discretized into a system of algebraic equations. All algebraic equations are then solved numerically to represent the solution field i.e. the discretized equations require field data (material properties, velocities, etc.) which are stored at cell centers, and also require face values which are interpolated in terms of local and adjacent cell values. The equation is written out for

every control volume in domain resulting in an equation set. The set of equations are then solved to represent the flow field. Having determined the important features of the problem to be solved, then the following basic procedural steps should be followed to solve a problem in FLUENT.

1. Create the model geometry and grid in the Gambit.

2. Start the fluent by selecting the appropriate solver for 2D or 3D modeling.

3. Import the grid.

4. Check the grid.

5. Select the solver formulation.

6. Choose the basic equations to be solved: laminar or turbulent, chemical species or reaction, heat transfer models, etc. Identify additional models needed: fans, heat exchangers, porous media, etc.

7. Specify material properties.

8. Specify the boundary conditions.

9. Adjust the solution control parameters, initialize the flow field and calculate a solution by iteration.

10. Examine and write the results.

11. If necessary, refine the grid or consider revisions to the numerical or physical model.

Fluent has two major numerical solvers; namely, Segregated solver and Coupled solver - Implicit and Explicit. In either of these methods, fluent will solve the governing integral equations for the conservation of mass and momentum, and energy (when appropriate) and other scalars such as turbulence and chemical species and in both cases a control-volume-based technique is used. For this work segregated solver was used.

3.4 Turbulent modeling using FLUENT

Turbulent flows are characterized by fluctuating velocity fields. These fluctuations mix transported quantities such as momentum, energy, and species concentration, and cause the transported quantities to fluctuate as well. Since these fluctuations can be of small scale and high frequency, they are too computationally expensive to simulate directly in practical engineering calculations. Instead, the instantaneous (exact) governing equations can be time-averaged, ensemble-averaged, or otherwise manipulated to remove the small scales, resulting in a modified set of equations that are computationally less expensive to solve. However, the modified equations contain additional unknown variables, and turbulence models are needed to determine these variables in terms of known quantities.

It is an unfortunate fact that no single turbulence model is universally accepted as being superior for all classes of problems. The choice of turbulence model will depend on considerations such as the physics encompassed in the flow, the established practice

for a specific class of problem, the level of accuracy required, the available computational resources, and the amount of time available for the simulation. To make the most appropriate choice of model for your application, you need to understand the capabilities and limitations of the various options. The purpose of this section is to give an overview of realizable $k - \epsilon$ turbulence model which used to carry out this work.

3.4.1 Realizable k-ϵ model overview

The realizable k-ϵ model [96] is a relatively recent development and differs from the standard k-ϵ model in two important ways:

- The realizable k-ϵ model contains a new formulation for the turbulent viscosity.

- A new transport equation for the dissipation rate, ϵ, has been derived from an exact equation for the transport of the mean-square vorticity fluctuation.

The term "realizable" means that the model satisfies certain mathematical constraints on the Reynolds stresses, consistent with the physics of turbulent flows. Neither the standard k-ϵ model nor the RNG k-ϵ model is realizable. An immediate benefit of the realizable k-ϵ model is that it more accurately predicts the spreading rate of both planar and round jets. It is also likely to provide superior performance for flows involving rotation, boundary layers under strong adverse pressure gradients, separation, and recirculation [95]. Both the realizable and RNG k-ϵ models have shown substantial improvements over the standard k-ϵ model where the flow features include strong streamline curvature, vortices, and rotation. Since the model is still relatively new, it is not clear in exactly which instances the realizable k-ϵ model consistently outperforms the RNG model. However, initial studies have shown that the realizable model provides the best performance of all the k-ϵ model versions for several validations of separated flows and flows with complex secondary flow features. One of the weaknesses of the standard k-ϵ model or other traditional k-ϵ models lies with the modeled equation for the dissipation rate ϵ. The well-known round-jet anomaly (named based on the finding that the spreading rate in planar jets is predicted reasonably well, but prediction of the spreading rate for axisymmetric jets is unexpectedly poor) is considered to be mainly due to the modeled dissipation equation [95].

3.4.1.1 Transport equations

$$\frac{\partial}{\partial t}(\rho k) + \frac{\partial}{\partial x_j}(\rho \, k \, u_j) = \frac{\partial}{\partial x_j}\left[\left(\mu + \frac{\mu_t}{\sigma_k}\right)\frac{\partial k}{\partial x_j}\right] + P_k + P_b - \rho \, \epsilon - Y_M + S_k \qquad (3.6)$$

$$\frac{\partial}{\partial t}(\rho \epsilon) + \frac{\partial}{\partial x_j}(\rho \, \epsilon \, u_j) = \frac{\partial}{\partial x_j}\left[\left(\mu + \frac{\mu_t}{\sigma_\epsilon}\right)\frac{\partial \epsilon}{\partial x_j}\right] + \rho \, C_1 \, S \, \epsilon - \rho \, C_2 \, \frac{\epsilon^2}{k + \sqrt{\nu \, \epsilon}} +$$

$$C_{1 \, \epsilon}\frac{\epsilon}{k}C_{3\epsilon}P_b + S_\epsilon \qquad (3.7)$$

where

$$C_1 = \max\left[0.43, \frac{E}{E + 5}\right], \qquad E = S\frac{k}{\epsilon}, \qquad S = \sqrt{2S_{ij} \, S_{ij}} \qquad (3.8)$$

where S is the modulus of the mean rate of strain tensor.

In these equations, P_k represents the generation of turbulence kinetic energy due to the mean velocity gradients, calculated as follows:

$$P_k = \mu_t S^2 \tag{3.9}$$

P_b is the generation of the turbulence kinetic energy due to buoyancy, negligible for our applications:

$$P_b = \beta g_i \frac{\mu_t}{Pr_t} \frac{\partial T}{\partial x_i} \tag{3.10}$$

where Pr_t is the turbulent Prandtl number for energy and g_i is the component of the gravitational vector in the ith direction. The default value of Pr_t is 0.85.

The cofficient of thermal expansion, β is defined as:

$$\beta = -\frac{1}{\rho}\left(\frac{\partial \rho}{\partial T}\right)_P \tag{3.11}$$

3.4.1.2 Modelling turbulent viscosity

As in other k-ϵ models, the eddy viscosity is computed from

$$\mu_t = \rho \, C_\mu \, \frac{k^2}{\epsilon} \tag{3.12}$$

While C_μ is constant in the standard k-ϵ model, in the Realizable k-ϵ model this coefficient is calculated as follows:

$$C_\mu = \frac{1}{A_0 + A_s \frac{kU^*}{\epsilon}} \tag{3.13}$$

$$U^* = \sqrt{S_{ij} \, S_{ij} + \tilde{\Omega}_{ij} \, \tilde{\Omega}_{ij}} \tag{3.14}$$

$$\tilde{\Omega} = \Omega - 2\epsilon_{ijk} \, \omega_k \tag{3.15}$$

and

$$\Omega = \overline{\Omega}_{ij} - \epsilon_{ijk} \, \omega_k \tag{3.16}$$

where $\overline{\Omega}_{ij}$ is the mean rate of rotation viewed in a rotating reference frame with the angular velocity ω_k. The model constants A_0 and A_s are given by:

$$A_0 = 4.04, \quad A_s = \sqrt{6}\cos\phi \tag{3.17}$$

where

$$\phi = \frac{1}{3} \, \arccos(\sqrt{6} \, W) \tag{3.18}$$

$$W = \frac{S_{ij} \, S_{jk} \, S_{ki}}{\tilde{S}} \tag{3.19}$$

$$\tilde{S} = \sqrt{S_{ij} \, S_{ij}} \tag{3.20}$$

$$S_{ij} = \frac{1}{2} \left(\frac{\partial u_j}{\partial x_i} + \frac{\partial u_i}{\partial x_j} \right) \tag{3.21}$$

Model Constants

$$C_{1\epsilon} = 1.44, \quad C_2 = 1.9, \quad \sigma_k = 1.0, \quad \sigma_\epsilon = 1.3 \tag{3.22}$$

This model has been extensively validated for a wide range of flows [28, 96], including rotating homogeneous shear flows, free flows including jets and mixing layers, channel and boundary layer flows, and separated flows. For all these cases, the performance of the model has been found to be substantially better than that of the standard k-ϵ model. Especially noteworthy is the fact that the realizable k-ϵ model resolves the round-jet anomaly; i.e., it predicts the spreading rate for axisymmetric jets as well as that for planar jets.

3.5   Combustion modeling using FLUENT

FLUENT provides five approaches for modeling gas phase reacting flow which are: generalized finite-rate model, non-premixed combustion model, premixed combustion model, partially premixed combustion model, composition probability density function (PDF) transport model. Fig. 3.5 shows the aspects of reaction modeling. In the non-premixed combustion model, the individual transport equations are not solved. Instead, transport equations for one or two conserved scalars (the mixture fraction) are solved and individual component concentrations are derived from the predicted mixture fraction distribution. Here the reacting system is treated using flame sheet (mixed is burned) approach or chemical equilibrium calculations.

The composition PDF transport model simulates realistic finite-rate chemistry in turbulent flames. Arbitrary chemical mechanism can be imported into FLUENT and kinetic effects such as non-equilibrium species and ignition/extinction can be captured. This model is applicable to premixed, non-premixed, and partially premixed flames. But one must note that this model is computationally expensive.

The first step in solving any problem involving species transport and reacting flow is to determine which model is appropriate. For cases involving the mixing, transport, or reaction of chemical species, or reactions on the surface of a wall or particle (e.g., chemical vapor deposition), the generalized finite-rate model can be used. For reacting systems involving turbulent diffusion flames that are near chemical equilibrium where the fuel and oxidizer enter the domain in two or three distinct streams, use the non-premixed combustion model.
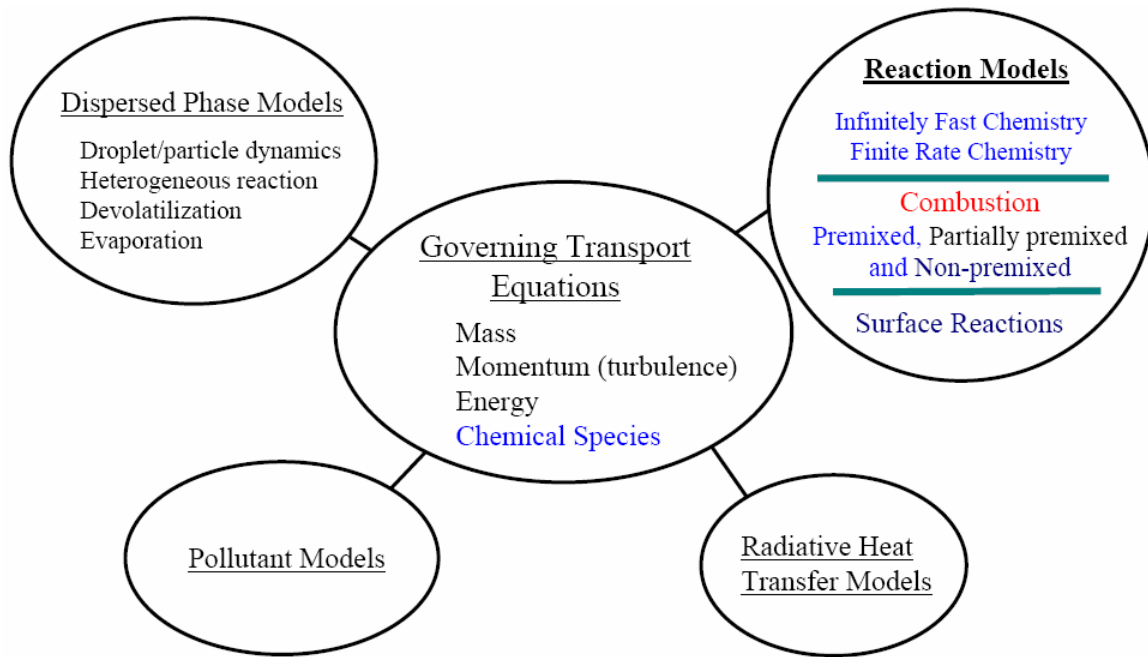
Figure 3.5: Aspects of reaction modeling [95].

3.5.1 Non-premixed combustion modeling

Turbulent non premixed flames are encountered in a large number of industrial systems for two main reasons. First, compared to premixed flames, burners are simpler to design and to build because a perfect reactant mixing, in given proportions, is not required. Non-premixed flames are also safer to operate as they do not exhibit propagation speeds and cannot flashback. Accordingly, turbulent non premixed flame modeling is one of the most usual challenges assigned to combustion codes in industrial applications.

In non-premixed combustion, fuel and oxidizer enter the reaction zone in distinct streams. This is in contrast to premixed systems, in which reactants are mixed at the molecular level before burning. Examples of non-premixed combustion include pulverized coal furnaces, diesel internal-combustion engines and pool fires. Under certain assumptions, the thermochemistry can be reduced to a single parameter: the mixture fraction. The mixture fraction, denoted by f, is the mass fraction that originated from the fuel stream. In other words, it is the local mass fraction of burnt and unburnt fuel stream elements ($C, H, etc.$) in all the species ($CO_2, H_2O, O_2, etc.$). The approach is elegant because atomic elements are conserved in chemical reactions. In turn, the mixture fraction is a conserved scalar quantity, and therefore its governing transport equation does not have a source term. Combustion is simplified to a mixing problem, and the difficulties associated with closing non-linear mean reaction rates are avoided. Once mixed, the chemistry can be modeled as being in chemical equilibrium with the Equilibrium model, being near chemical equilibrium with the Steady Laminar Flamelet model, or significantly departing from chemical equilibrium with the Unsteady Laminar Flamelet model.

The non-premixed modeling approach has been specifically developed for the simulation of turbulent diffusion flames with fast chemistry. For such systems, the method

offers many benefits over the eddy-dissipation formulation. The non-premixed model allows intermediate (radical) species prediction, dissociation effects, and rigorous turbulence-chemistry coupling. The method is computationally efficient in that it does not require the solution of a large number of species transport equations. When the underlying assumptions are valid, the non-premixed approach is preferred over the eddy-dissipation formulation [95].

3.5.2   Mixture fraction and PDF model

Non-premixed modeling involves the solution of transport equations for one or two conserved scalars (the mixture fractions). Equations for individual species are not solved. Instead, species concentrations are derived from the predicted mixture fraction fields. The thermochemistry calculations are preprocessed in prePDF and then tabulated for look-up in FLUENT. Interaction of turbulence and chemistry is accounted for with an assumed-shape Probability Density Function (PDF).

The basis of the non-premixed modeling approach is that under a certain set of simplifying assumptions, the instantaneous thermochemical state of the fluid is related to a conserved scalar quantity known as the mixture fraction f. It can be defined as the ratio of mass of material having its origin in the fuel stream to mass of mixture [95].

$$f = \frac{Mass\ of\ Material\ having\ its\ origin\ in\ the\ fuel\ stream}{Mass\ of\ mixture} \qquad (3.23)$$

$$f = \frac{Z_i - Z_{i,ox}}{Z_{i,fuel} - Z_{i,ox}} \qquad (3.24)$$

where, Z_i is elemental mass fraction for element i. The subscript ox denotes the value at the oxidizer stream inlet and the subscript fuel denotes the value at the fuel stream inlet. The mixture fraction f is a special kind of mass fraction formed as a combination of fuel, oxidizer and product mass fractions. Mass fraction is unity i.e. $f = 1$, in the fuel stream and zero in the oxidizer stream; and within the flow field it takes a value between 1 and 0.

$$1\ kg\ fuel\ +\ L\ kg\ oxidizer\ \rightarrow\ (1+L)\ kg\ product \qquad (3.25)$$
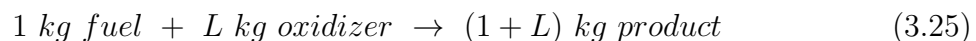
where L is the stoichiometric air-to-fuel ratio on a mass basis. Denoting the equivalence ratio as ϕ,
where

$$\phi = \frac{(air/fuel)_{stoichiometric}}{(air/fuel)_{actual}} \qquad (3.26)$$

Under more general mixture, Eqn. 3.25 can be written as

$$\phi\ fuel\ +\ L\ oxidizer\ \rightarrow\ (\phi + L)\ product \qquad (3.27)$$
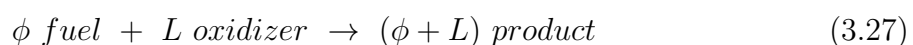
Mixture fraction for the whole combustion system can be deduced to be

$$f = \frac{\phi}{\phi + L} \tag{3.28}$$

All thermochemical scalars (species mass fraction, density, and temperature) are uniquely related to the mixture fraction(s). The instantaneous mixture fraction value at each point in the flow field can be used to compute the instantaneous values of individual species mole fractions, density, and temperature. For a single-mixture-fraction problem, the following steps were performed in prePDF:

1. Define the chemical species to be considered in the reacting system model and choose the chemical description of the system. The equilibrium chemistry option was used, because in this approach the concentration of species of interest is determined from the mixture fraction using the assumption of chemical equilibrium. Besides, the effects of intermediate species and dissociation reactions can be included to producing more realistic predictions of flame temperatures in combustion models

2. Indicate whether the problem is adiabatic or non adiabatic. The case here is non adiabatic case.

3. Choose the PDF (probability density function) shape that will be used to describe the turbulent fluctuations in the mixture fraction. The Beta PDF is selected because its shape matches experimental observations of f fluctuations much better than the double-delta function.

4. Compute the look-up table, containing mean (time-averaged) values of species mass fractions, density, and temperature as a function of mean mixture fraction, mixture fraction variance, and enthalpy. The contents of this look-up table will reflect the preceding inputs describing the turbulent reacting system.

3.6 Radiation modeling using FLUENT

3.6.1 Overview

In the flame region of a rotary kiln, radiative heat transfer is about three times more significant than heat transfer by turbulent diffusion (Stefan number=3) and therefore an accurate prediction of the thermal field is highly dependent on the accurate modeling of radiative transfer. Due to the importance and difficulties of the accurate prediction of radiation heat transfer in industrial furnaces, there are a many number of radiation models developed. FLUENT provides five radiation models which allow you to include radiation, with or without a participating medium, in your heat transfer simulations: Heating or cooling of surfaces due to radiation and/or heat sources or sinks due to radiation within the fluid phase can be included in your model using one of the following radiation models.

- Discrete Transfer Radiation Model (DTRM)

- P-1 Radiation Model

- Rosseland Radiation Model

- Surface-to-Surface (S2S) Radiation Model

- Discrete Ordinates (DO) Radiation Model

The P-1 model has several advantages, it is easy to solve with little CPU demand. The model includes the effect of scattering. For combustion applications where the optical thickness is large, the P-1 model works reasonably well. In addition, the P-1 model can easily be applied to complicated geometries with curvilinear coordinates. So, in order to study effect of radiation on the flame length, the P-1 approximation model was selected in my simulation.

3.6.2 Radiative Transfer Equation

The radiative transfer equation (RTE) for an absorbing, emitting, and scattering medium at position $\vec{r}$ in the direction $\vec{s}$ is

$$\frac{dI(\vec{r}, \vec{s})}{ds} + (a + \sigma_s)I(\vec{r}, \vec{s}) = an^2\frac{\sigma T^4}{\pi} + \frac{\sigma_s}{4\pi}\int_0^{4\pi} I(\vec{r}, \vec{s}')\Phi(\vec{s}.\vec{s}')d\Omega' \qquad (3.29)$$

where,

$\vec{r}$= position vector
$\vec{s}$= direction vector
$\vec{s}'$= scattering direction vector
s= path length
a= absorption coefficient
n= refractive index
σ_s= scattering cofficient
σ= Stefen-Boltzmann constant $(5.672 \times 10^{-8}\,W/m^2.K^4)$
I= radiation intensity, which depends on position $(\vec{r})$ and direction $(\vec{r})$
T= local temperature
Φ= phase function
Ω'= solid angle

$(a + \sigma_s)$ is the optical thickness or opacity of the medium.

The refractive index n is important when considering radiation in semi-transparent media. Figure 3.6 illustrates the process of radiative heat transfer.

The P-1 radiation model requires the absorption coefficient a as input. a and the scattering coefficient σ_s can be constants, and a can also be a function of local concentrations of H_2O and CO_2, path length, and total pressure. FLUENT provides the weighted-sum-of-gray-gases model (WSGGM) for computation of a variable absorption coefficient. The discrete ordinates implementation can model radiation in semi-transparent media. The refractive index n of the medium must be provided as a part of the calculation for this type of problem.

3.6.3 The P-1 Model Equations

The P-1 radiation model is the simplest case of the more general P-N model, which is based on the expansion of the radiation intensity I into an orthogonal series of spherical
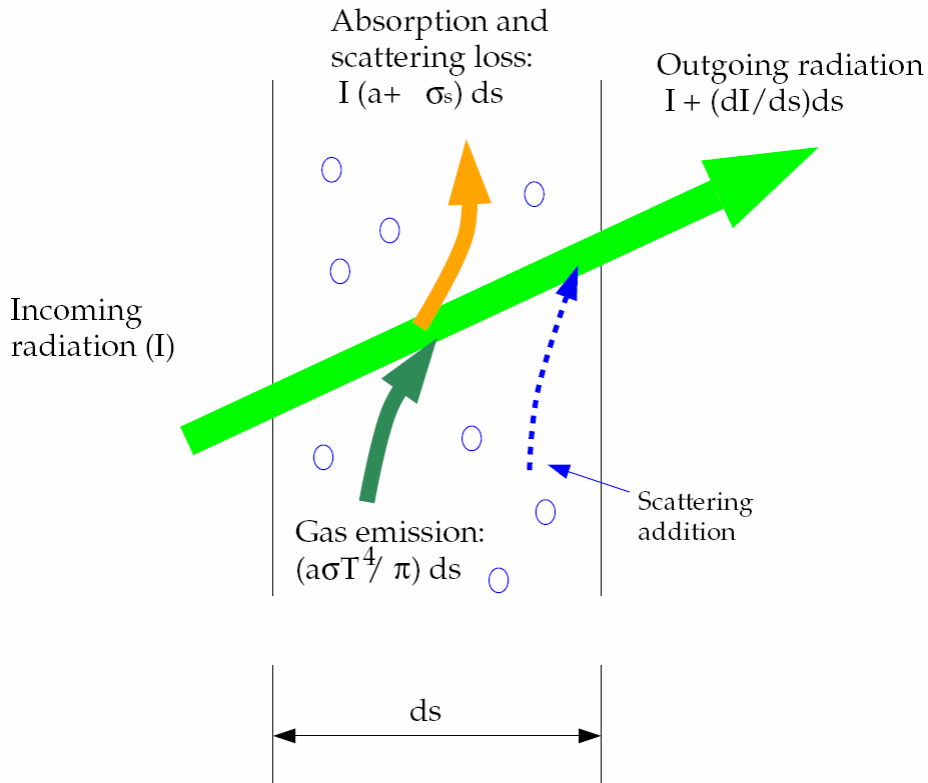
Figure 3.6: Radiative heat transfer process [95].

harmonics. If only four terms in the series are used, the following equation is obtained for the radiation flux q_r:

$$q_r = -\frac{1}{3(a + \sigma_s) - C\sigma_s} \nabla G \tag{3.30}$$

where a is the absorption coefficient, σ_s is the scattering coefficient, G is the incident radiation, and C is the linear-anisotropic phase function coefficient, described below. After introducing the parameter

$$\Gamma = -\frac{1}{(3(a + \sigma_s) - C\sigma_s)} \tag{3.31}$$

Equation (3.30) simplifies to

$$q_r = -\Gamma \nabla G \tag{3.32}$$

The transport equation for G is

$$\nabla.(\Gamma \nabla G) - a + 4a\sigma T^4 = S_G \tag{3.33}$$

where σ is the Stefan-Boltzmann constant and S_G is a user-defined radiation source. FLUENT solves this equation to determine the local radiation intensity when the P-1 model is active. Combining Equations (3.35) and (3.32), the following equation is obtained:

$$- \nabla . q_r = aG - 4a\sigma T^4 \tag{3.34}$$

The expression for $-\nabla . q_r$ can be directly substituted into the energy equation to account for heat sources (or sinks) due to radiation [95].

3.7 CFD simulation of this work

3.7.1 The major assumptions

The following assumptions applied on my research cases, including free jet flame, confined jet flame, and rotary kiln flame simulations.

1. Steady state problems; although, in practice, many of variables such as air and fuel velocities will fluctuate with the time, but it is assumed to have no significant effect on the flame patterns.

2. The problems assumed to be axi-symmetry, although some of the kiln burners are offset from the center, which makes the flow field asymmetric about the kiln axis. Also the hood geometry may affect the symmetry of the secondary air flow profile around the primary jet, so asymmetric effect is assumed to be insignificant. When the flame is symmetric, the heat transfer to the surroundings is symmetric.

3. Incompressible flow; although some of the kiln burner operates at subsonic flows, Mach number ~ 0.6 [31], so the flow may be treated as incompressible.

4. Negligible buoyancy effect. In practice, many of rotary kilns operate at high primary jet momentum and with preheated secondary air, where the Richardson number equals 1×10^{-3}; this typical value is assumed to prevent buoyancy from having a significant effect on the flame dynamics [31].

5. In case of rotary kiln problem; rotation speed, and bed percent fill have insignificant effect on the flame aerodynamics (shape and turbulence). The typical rotation speed of rotary kilns is about 1 RPM [31], the axial velocities are orders in magnitude higher than the tangential velocities. So, the rotation speed has no significant effect of the flame behavior. In most rotary kilns, the bed percent fill is about 15% or less [31], this value is assumed to have no effect on the internal geometry of the kiln and consequently has no effect on the flame aerodynamics. "Many investigators of the rotary kiln flame found that ignoring the physical presence of the bed is a reasonable simplifying practice" [31].

6. The wall is assumed to be adiabatic, i.e. no heat loss through the wall in case of confined flame jet and rotary kiln flame simulation.

3.7.2 Geometry, boundaries and mesh generation

The main goal of this part is to explain the different burner geometries used in simulation of free jet flame, different confinement shapes which used for confined flame jet simulation and rotary kiln flame geometry. All domains dimensions and boundaries types were stated in the following sections. Mesh generation and mesh types are also demonstrated for all cases which stated in my simulation.

3.7.2.1   2D free jet flame

Figure 3.7 shows the principle schematic diagrams for three proposed burner geometries which used in free jet flame simulation. The free jet flame simulation was used to select the best turbulence model and also to validate it, this will be explained in the next sections. In addition to free jet simulation was used as a basic step to measure the free jet flame length, furthermore it was considered as a preliminary step to demonstrate the effect of confinement on the confined jet flame length; this will explain and discuss in Chapter 4.

The first burner geometry is shown in Fig. 3.7 (a), it is a pilot plain tube burner which consists of a nozzle with $50\,mm$ diameter and thermal power range $(2.31 - 6.56\,MW)$ according to the kind of fuel. The fuel flows at a uniform axial velocity of $100\,m/s$. in this case three fuels were proposed to study; Methane (CH_4), Carbon monoxide (CO), and Biogas $(50\,\%\ CH_4$ and $50\,\%\ CO_2)$. The second burner geometry was presented in Fig. 3.7 (b), it is considered a pilot annulus tube burner. In this type, only Methane fuel was used with $30\,m/s$ axial uniform velocity $(1.97\,MW$ burner thermal power) and $50\,mm$ fuel nozzle diameter. The annulus diameter changed with different values to show the effect of annulus geometry on the flame length. The last burner geometry was similar to the last burner with adding supported walls to annulus burner type (see Fig 3.7 (c)). In this type, Methane fuel was used with $30\,m/s$ axial uniform fuel velocity $(1.97\,MW$ burner thermal power) and with $50\,mm$ fuel nozzle diameter. This kind of burner was suggested to study the effects of supported wall and annulus air swirl on the flame behavior (shape and length).

The fuel and air inlet conditions, burner thermal power and ranges of annulus diameters for three burner geometries were depicted in table 3.1. While, the physical and thermal properties for three simulated fuels $(CH_4$, CO, and $Biogas)$ were tabulated in Table 3.2.

Table 3.1: Boundary conditions of free jet flame simulation for three burners geometries.

Burner type	Fuel kind	q_o (MW)	u_o (m/s)	T_{air} (°C)	T_o (°C)	$\dot{m}_o$ (kg/s)	d_o (mm)	$\frac{d_p}{d_o}$	S_n
Burner (a)	CH_4, CO, $Biogas$	2.31→ 6.56	100	20→ 1000	20	0.131→ 0.228	50	—	—
Burner (b)	CH_4	1.97	30	20	20	0.0393	50	3.7→ 31.1	—
Burner (c)	CH_4	1.97	30	20	20	0.0393	50	3.7→ 31.1	0→ 1

Figure 3.8 shows 2D domain geometry and mesh for free jet flame simulations. The full domain geometry of the free jet problems was considered as a big symmetrical cylinder $(20\,m$ length and $10\,m$ in diameter) to simulate a large space and to avoid the wall effects on the flame behavior. As shown in Fig. 3.8 (a), half portion of the cylinder has been taken for simulations as a studied domain to minimize the simulation time, by considering the fact that the flame and space are cylindrical and symmetrical. The mesh generated in GAMBIT 2.2.30 package as a preprocessing program with 40400 cells, structured and
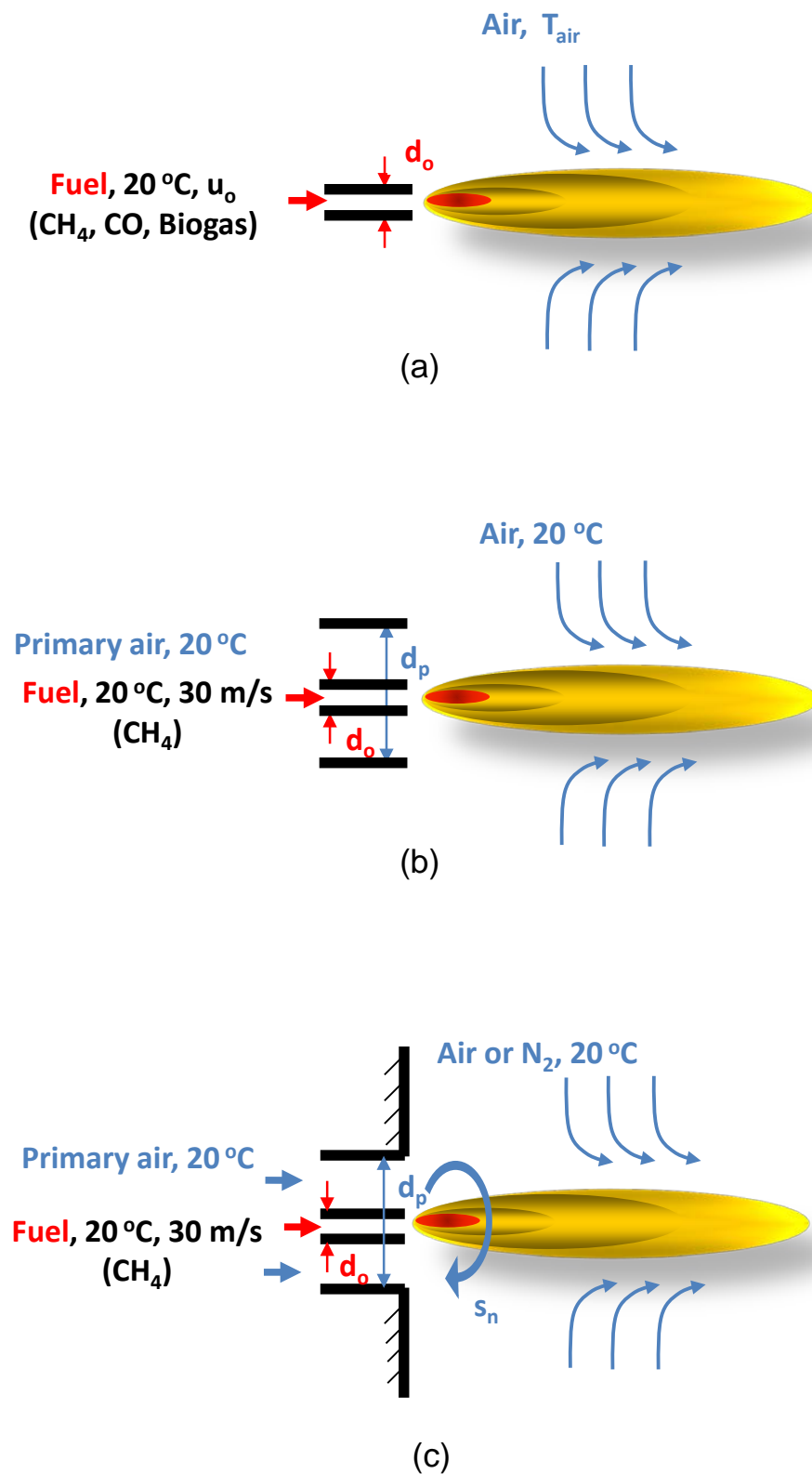
Figure 3.7: Showing different burner geometries: (a) plain tube, (b) annulus tube, (c) annulus tube with supported wall.

Table 3.2: physical and thermal properties of fuels.

Fuel kind	L (kg_{air}/kg_o)	ρ_o (20°C) (kg/m^3)	h_u (net) (MJ/kg_o)	M_o $(kg/kmol)$	$\tilde{L}$ (m^3_{air}/m^3_o)	f_{st}	k $(W/m.K)$
CH_4	17.3	0.668	50	16	9.5	0.055	0.035
Biogas	5.45	1.248	20.5	30	4.76	0.155	0.0295
CO	2.46	1.165	10.1	28	2.38	0.289	0.024

quadrilateral mesh type with quality of worst element of 1.3 e-10 for (EquiSize Skew) and 6.35 for (Aspect ratio) in mesh exam. The mesh was adjusted to be more condense near the burner, this because the importance of the flame region in my study. The boundary types and continuum were also defined in the same package. Fig. 3.8 (b) explains mesh and boundary types generated by GAMBIT 2.2.30, the inlet for the fuel is defined as *velocity inlet* and air inlet is defined as *pressure inlet* because the inlet pressure is known but the flow rate and/or velocity inlet is unknown and the outlet of combustion gases is defined as *pressure outlet*.

3.7.2.2   2D confined jet flame

Figure 3.9 shows the principle schematic diagrams for three proposed confined flame geometries which used in confined jet flame simulation. These different confined flame geometries were used to study the effects of geometrical parameters (confinement shape) and operational parameters on the flame aerodynamics (flow field) and flame lengths. For more explanation see Chapter 5.

The first confined flame geometry is shown in Fig. 3.9 (a), it is a simple tube burner with variable air inlet area size ($A_{a,i}$) which controlled by changing air inlet diameter ($d_{a,i}$). The burner consists of a nozzle with $50\,mm$ diameter and thermal power ranges ($0.69 - 1.97\,MW$) according to the kind of fuel. The fuel flows at a uniform axial velocity of $30\,m/s$, in this case three fuels were proposed to study; Methane (CH_4), carbon monoxide (CO) and Biogas (50% CH_4 and 50% CO_2). The second confined flame geometry was presented in Fig. 3.9 (b), it is considered a pilot annulus tube burner with fully opened cylinder for secondary air. In this type, only Methane fuel was used with $30\,m/s$ axial uniform velocity ($1.97\,MW$ burner thermal power) and $50\,mm$ fuel nozzle diameter. The annulus diameter (d_p) changed to show the effect of annulus geometry on the flame length. The last confined burner geometry was the same last one but with fully closed cylinder for secondary air(see Fig. 3.9 (c)). The influence of annulus air swirl on the flame length was studied in last two confined flame geometries and compared with each other as we will see in details in Chapter 5. Boundary conditions and geometrical ranges of three confined flame geometries for different fuels were presented in Table. 3.3.

Fig. 3.10 shows 2D domain geometry and mesh of confined jet flame simulation. The full domain geometry of the confined jet flame simulation was considered as a symmetrical cylinder ($20\,m$ length and $2.6\,m$ in diameter) to simulate a confined jet flame and to present the wall effect on the flame behavior. As shown in Fig. 3.10 (a), half portion of the cylinder has been taken for simulations as a studied domain to minimize the simulation time by considering the fact that the flame and surrounding are cylindrical and symmetrical. The

(a)

(b)
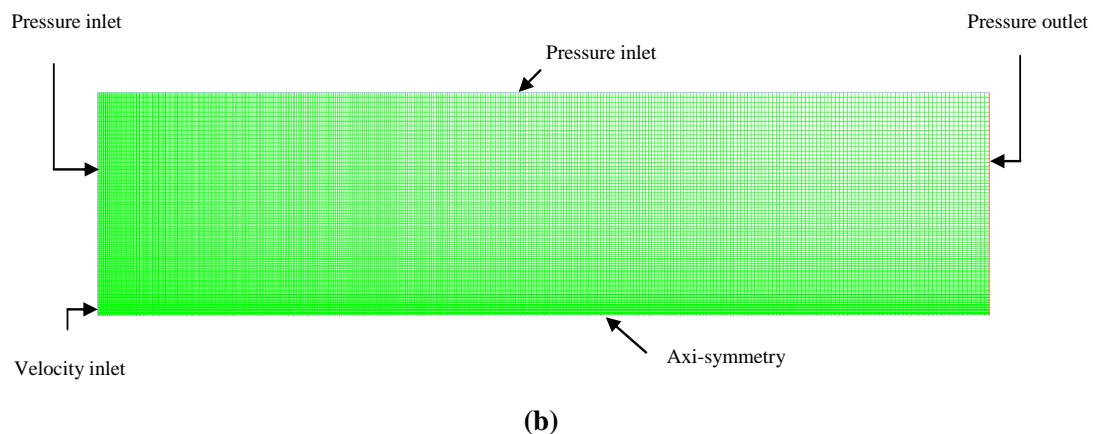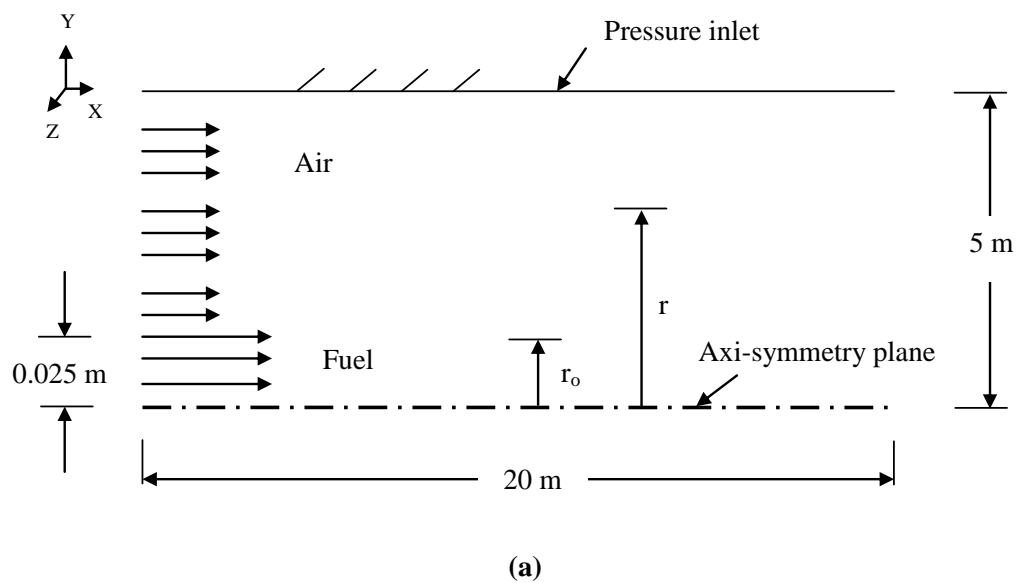
Figure 3.8: 2D domain of investigated free jet flame model: (a) geometry, (b) mesh.

mesh generated in GAMBIT 2.2.30 package as a preprocessing program with 30000 cells, structured and quadrilateral mesh type with quality of worst element of $1.3\,e-10$ for (EquiSize Skew) and 5.7 for (Aspect ratio) in mesh exam. The mesh was adjusted to be more condense near the burner, this because the importance of the flame region in my study. The boundary types and continuum were also defined in the same package. Fig. 3.10 (b) explains mesh and boundary types which generated by GAMBIT 2.2.30, the inlets for both fuel and air are defined as *velocity inlet*, the cylinder surface is defined as *wall* and the outlet of combustion gases is defined as *pressure outlet*.

3.7.2.3   3D rotary kiln flame

Figure 3.11 shows the 3D principle schematic model for full scale rotary kiln geometry. The burner geometry as well known is an important parameter which affects the flame behavior (i.e., the flame shape). Therefore, two burners configurations (burner (A) and burner (B))
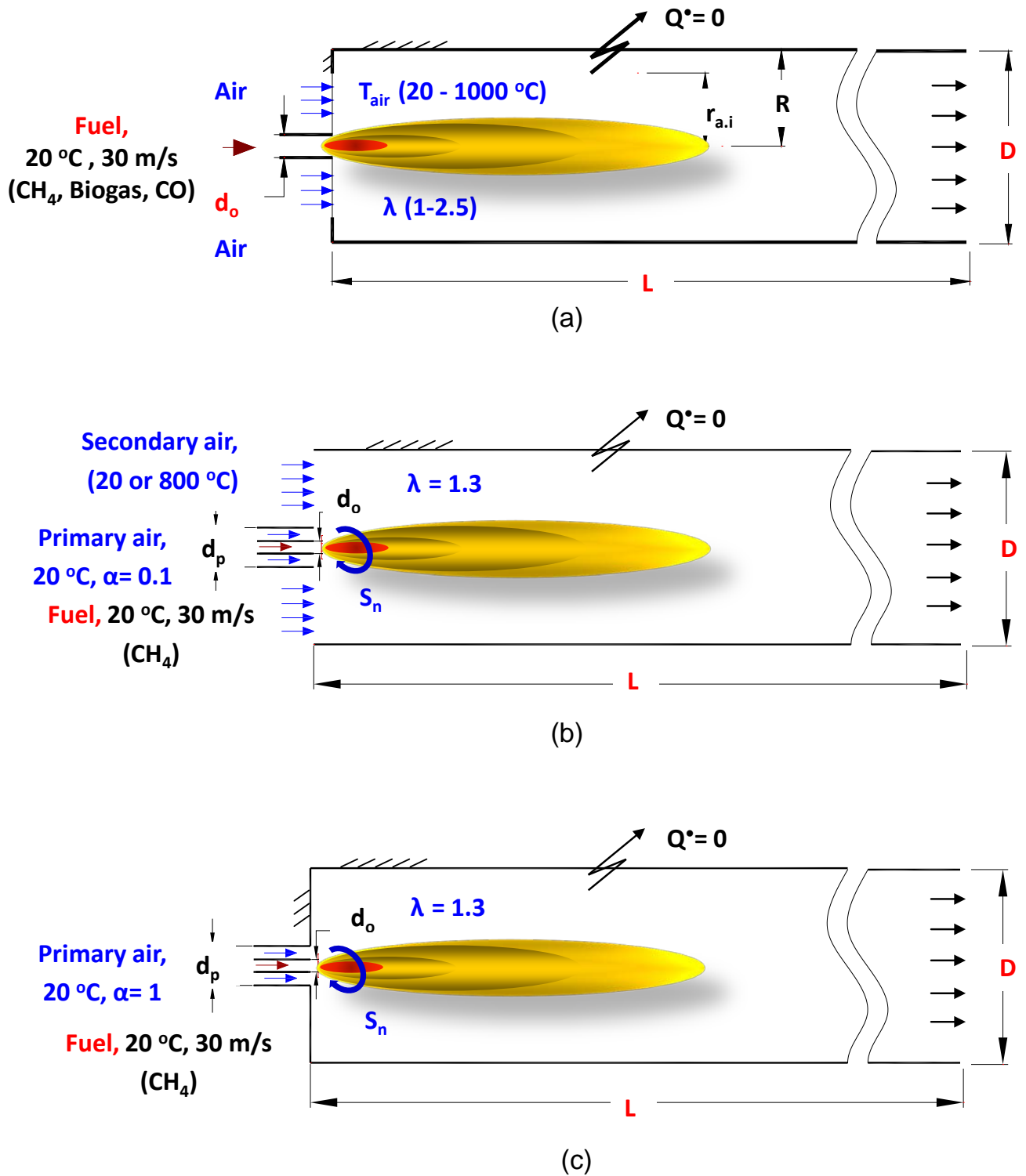
Figure 3.9: Showing different confinement shapes; (a) variable inlet air area (plain tube burner), (b) fully opened cylinder (annulus tube burner), and (c) fully closed cylinder (annulus tube burner).

Table 3.3: Boundary conditions of confined jet flame simulation for three confined burners shapes.

Burner type	Fuel kind	q_o (MW)	u_o (m/s)	T_{air} (°C)	T_o (°C)	$\dot{m}_o$ (kg/s)	d_o (mm)	$\frac{d_p}{d_o}$	$\frac{d_{a,i}}{D}$	λ	S_n
Burner (a)	CH_4, CO, Biogas	0.69→ 1.97	30	20→ 1000	20	0.0393 → 0.0686	50	—	0.06	1 → 2.5	—
Burner (b)	CH_4	1.97	30	20 & 800	20	0.0393	50	2.3 & 5	—	1.3	0 → 1
Burner (c)	CH_4	1.97	30	20	20	0.0393	50	2.3 → 5	—	1.3	0 → 1

were assumed to explain the effect of fuel nozzle diameter and primary air location and size on the flow field (i.e, flow visualization) and thermal distribution inside the kiln. The simulated kiln has a diameter of 4 meters and length of 40 m (see Fig. 3.11 (b)). Burner configuration (A) consists of a 50 mm ID fuel nozzle diameter surrounded by a primary air annulus of 100 mm ID and 200 mm OD. For burner configuration (B), the fule nozzle diameter is 100 mm and the primary jet annulus is 360 mm ID and 440 mm OD (see Fig. 3.11 (c)). To minimize the numerical effect of the inlet conditions, the inlet boundaries are set at 2 m upstream the burner outlet (see Fig. 3.11 (a)). Methane fuel was proposed to carry out the kiln flame simulation with two thermal burner power of 10 MW and 40 MW according to the burner power, the fuel velocity is 152.5 m/s and 610 m/s for burner (A), respectively and 38.12 m/s and 152.48 m/s for burner (B), respectively. Concerning the boundaries types, the inlet conditions for both fuel and primary air and secondary air are defined as *velocity inlet* and cylinder surface is defined as *wall* and the outlet of combustion gases is defined as *pressure outlet*. The influence of burner configuration, primary air ratio, burner power on the kiln flame behavior were performed and discussed in details in Chapter 6.

Fig. 3.12 shows 3D computational domain and mesh for rotary kiln flame simulation. The full scale kiln geometry is considered as a symmetrical cylinder (40 m length and 4 m in diameter). Therefore, one eighth of the total kiln volume has been taken for simulations as a computational domain, this to minimize the simulation time by considering the fact that the flame and surrounding are cylindrical and symmetrical (see Fig. 3.12 (a)). The mesh generated in GAMBIT 2.2.30 package as a preprocessing program with 122,324 cells for burner (A) and 122,962 cells for burner (B). The mesh is unstructured and tetrahedron mesh type (see Fig. 3.12 (b)). The quality of worst element is 0.85 (EquiSize Skew) and 0.83 (EquiAngle Skew) for burner (A) and 0.89 (EquiSize Skew) and 0.81 (EquiAngle Skew) for burner (B) in mesh exam.
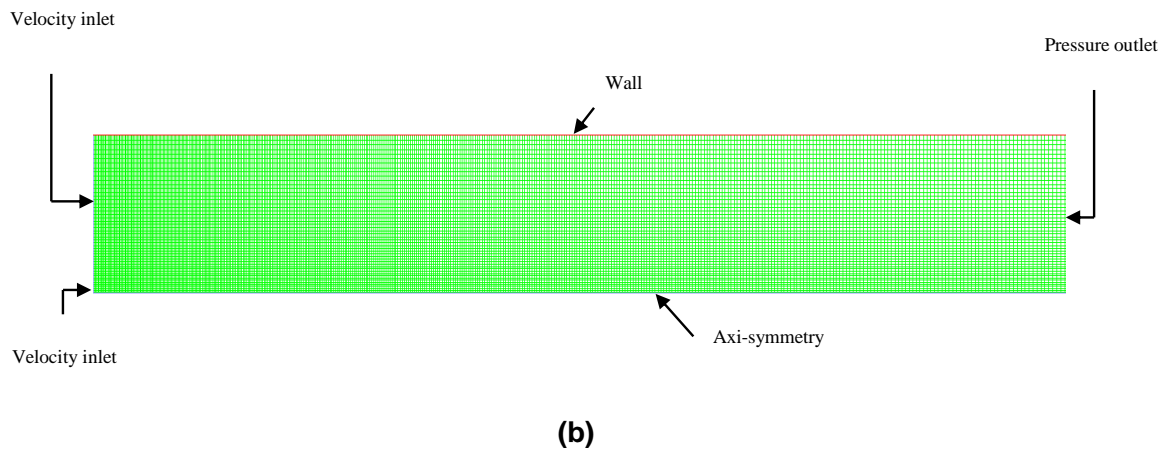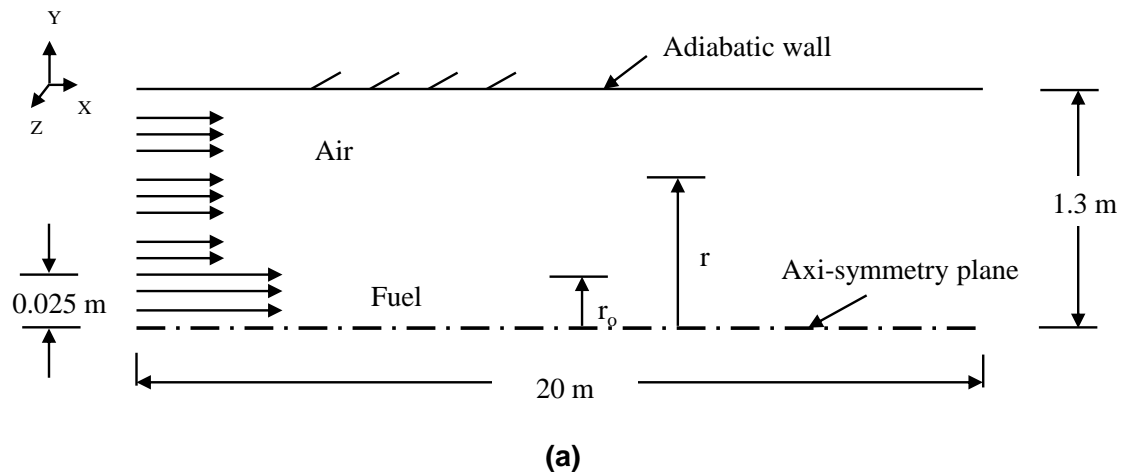
Figure 3.10: 2D domain of investigated confined jet flame model: (a) geometry, (b) mesh.

3.7.3 Grid independence study

For free jet flame simulation, first I created a number of 2D meshes with increasing in the density and quality to perform a mesh independence study to make sure that the flame length converges as the mesh size increases. As shown in Fig. 3.13 the mesh number varied from 5,270 to 99,660 cells, where the coarsest grids are associated with large variation of the dimensionless flame length. On the other side, the utilizing grids more than 40,400 cells lead to a relative variation in dimensionless flame length, less than 0.3 %. So to minimize CFD cost and time, the grade of 40,400 cells has been selected to carry out all free jet flame simulation in the present work. Corresponding results are shown in Fig. 3.14 many different 2D dimensional grids of increasing in density and quality, changed from 3,000 to 100,000 cells have been tested to calculate dimensionless flame length for confined jet flame. It was observed that the grids which more than 30,000 cells lead to small variation less than 0.2 % in dimensionless flame length. So this number of cells was recommended for further calculations concerning the confined flame jet flame simulations.
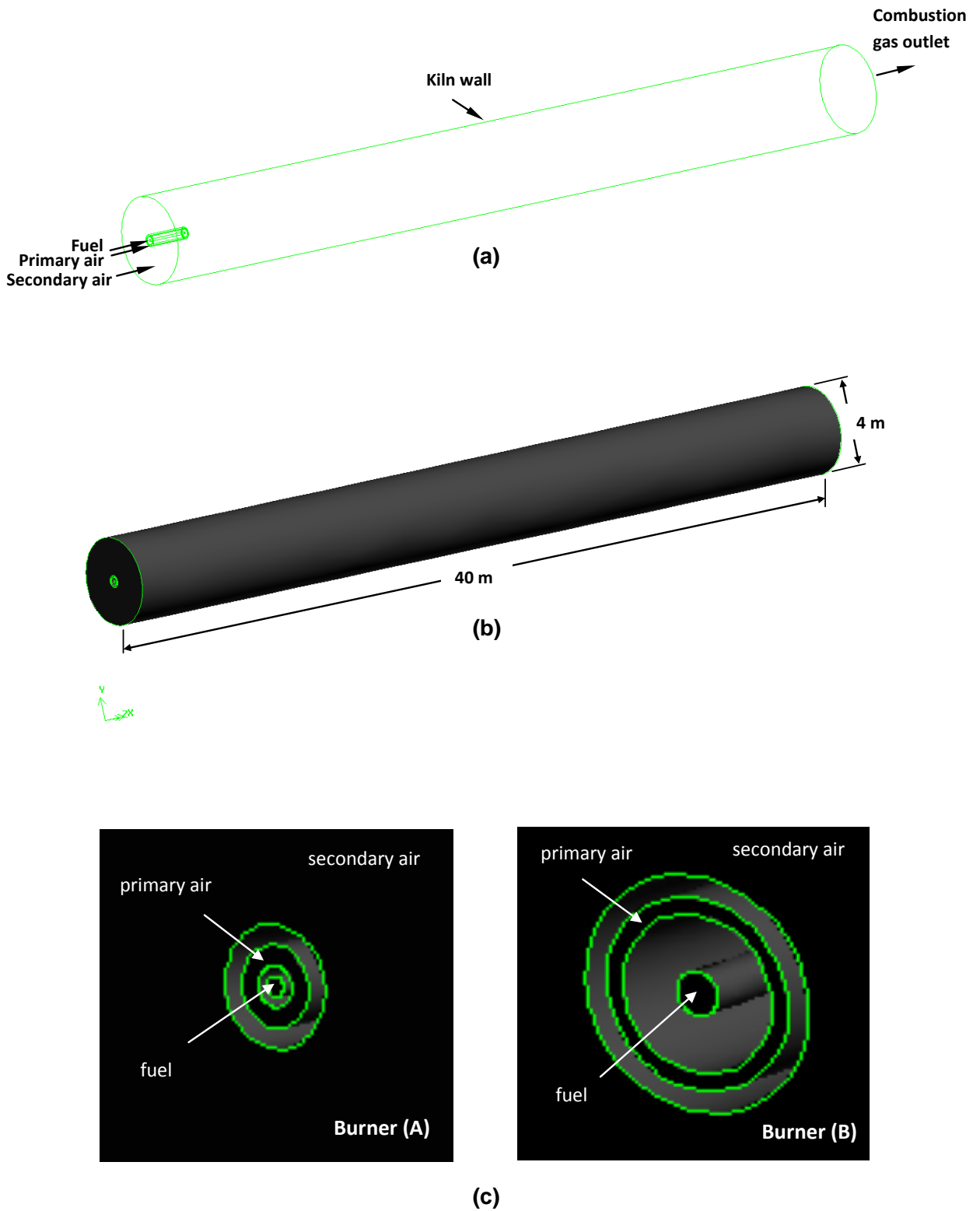
Figure 3.11: 3D full scale kiln geometry: (a) rotary kiln boundaries, (b) rotary kiln dimensions, (c) burner configurations.
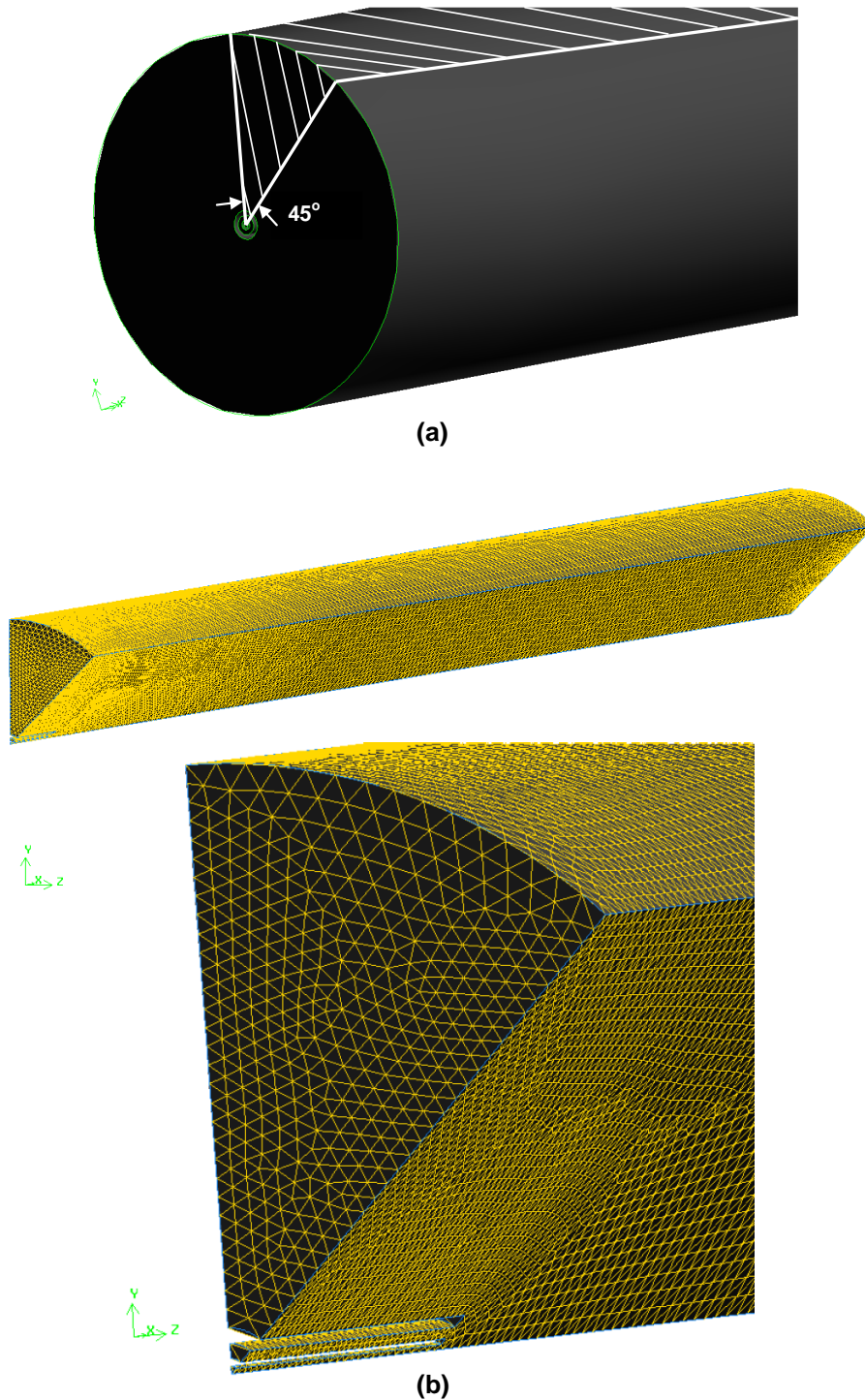
Figure 3.12: 3D rotary kiln flame model: (a) computational domain, (b) mesh.

According to the results presented in Fig. 3.15 for both burner (A) and burner (B). Many different 3D grids changed from 50,732 to 243,554 cells for burner (A), and from 48,572 to 251,207 for burner (B) have been tested to compute the kiln flame length in dimensionless form. From the study, we found that the grids which more than 122,324, and 122,962 give small variation less than $1.2\,\%$ and $0.33\,\%$ for burner (A) and burner (B), respectively. Therefor these numbers were recommended for further simulations of rotary kiln flame.
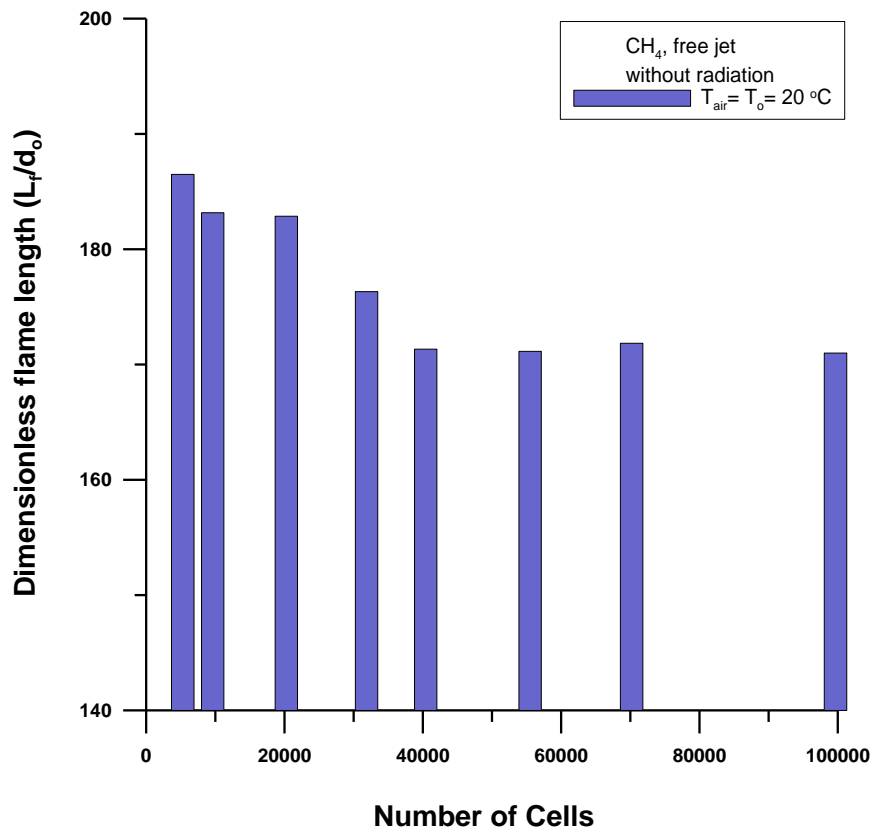
Figure 3.13: Grid independence study for free jet dimensionless flame length.
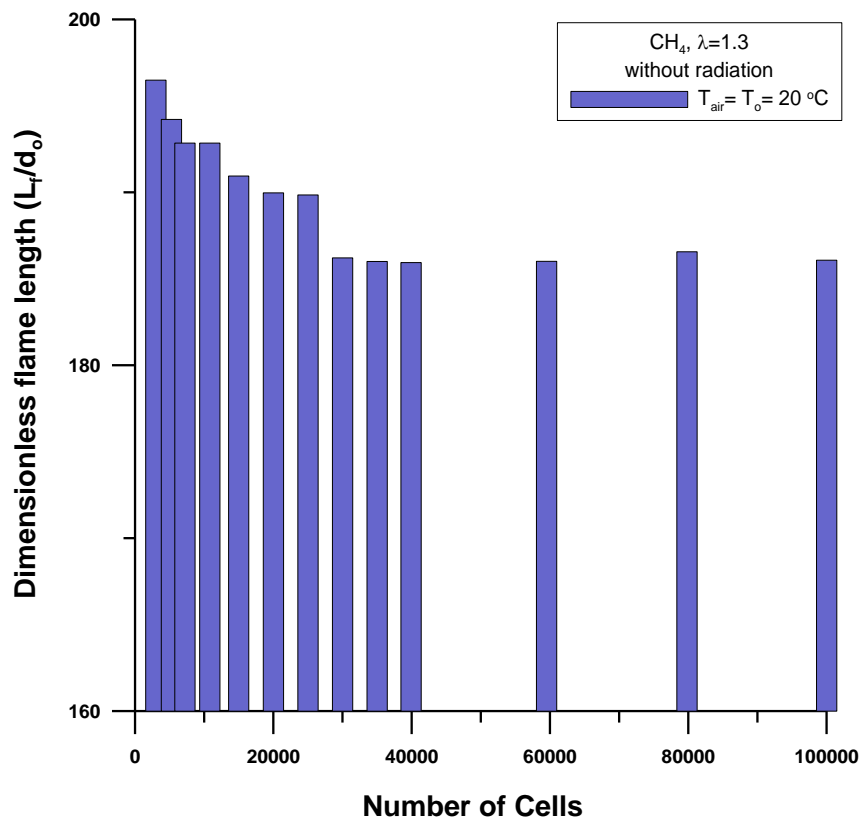
Figure 3.14: Grid independence study for confined jet dimensionless flame length.
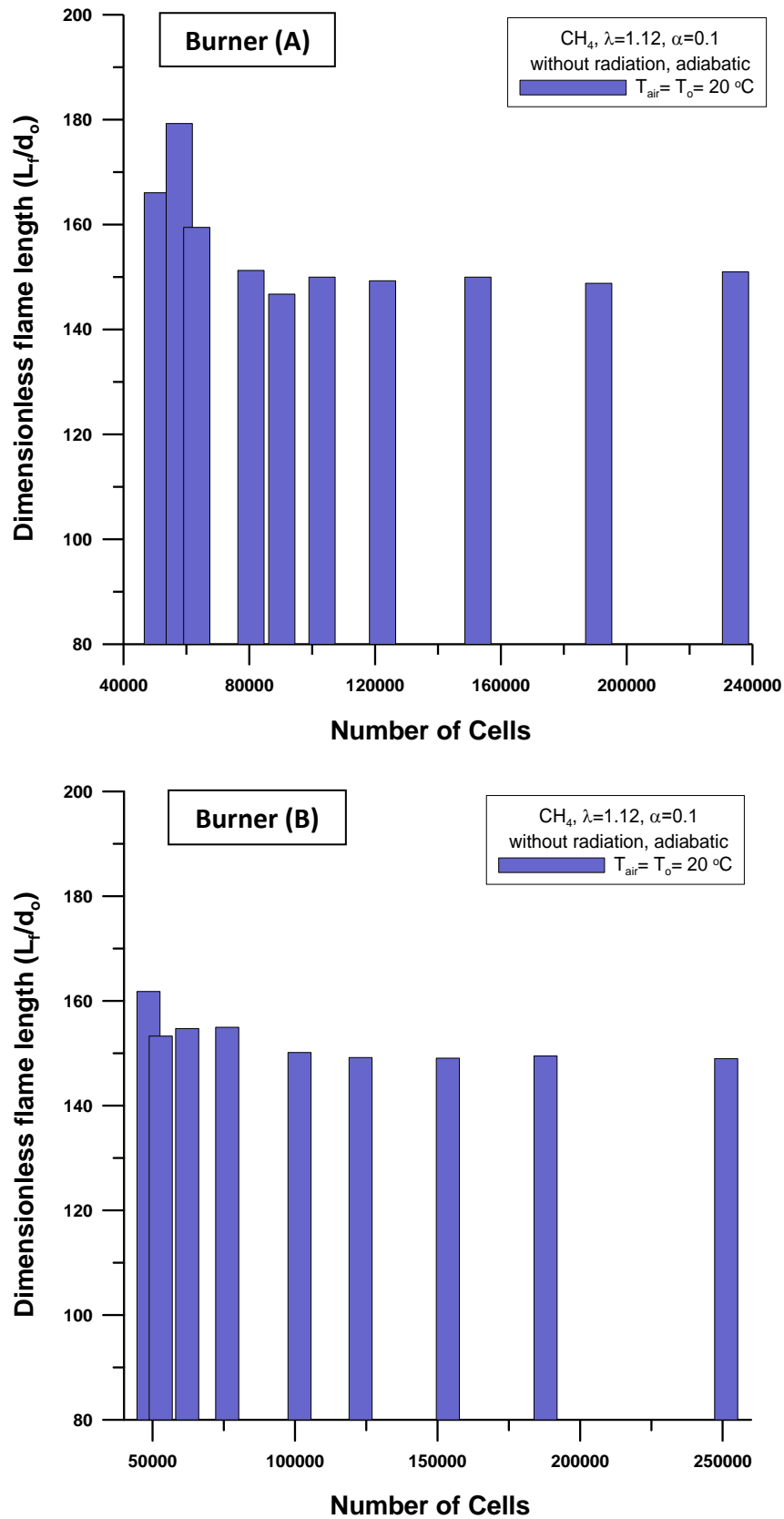
Figure 3.15: Grid independence study for rotary kiln dimensionless flame length: burner (A) and burner (B)

3.7.4 Solution strategies in FLUENT

3.7.4.1 Non-premixed flame simulation

The following procedure is recommended by FLUENT company for best solution of non-premixed gas combustion problems by using FLUENT package:

1. Initialize the solution with mixture fraction = 0, there is no need to patch any high temperature.

2. First, use about 300-400 iterations to establish the flow.

3. Check the flow and temperature field. If everything looks fine, change the following URF (under relaxation factors);

   - Increase pressure URF to 0.5 and lower momentum URF to 0.2
   - Set the energy, mixture fraction, and temperature URF to 1
   - If there are any stability problems, reduce the URF for energy and mixture fraction (for example 0.99)

4. Run the case further ($\sim$200-300 iterations), then check the solution again (flow, temperature, species...).

5. If everything looks fine at this point, switch on radiation (if required), P-1 model was recommended, and then set the absorption coefficient to WSGGM-domain based.

6. Once the fist order solution has been converged, switch to high-order discretization to improve the accuracy by;

   - Select PRESTO for pressure
   - Select second-order upwind for momentum, energy and mean mixture fraction (I do not always use second-order for turbulence and NEVER for radiation)

3.7.4.2 Axi-symmetric swirling flame simulation

For simulation of free jet and confined jet flame involving swirl, the following step-by-step procedure make the problems to be easier to solve. The following approach allows to establish the field of angular momentum, then leave it fixed while you update the velocity field, and then finally to couple the two fields by solving all equations simultaneously. In this procedure, I will use the **Equations** list in the **Solution Controls** panel to turn individual transport equations **on** and **off** between calculations.

1. Begin by solving the flow without swirl effects. That is, enable the Axisymmetric option instead of the Axisymmetric Swirl option in the Solver panel, and do not set any rotating boundary conditions. The resulting flow field data can be used as a starting guess for the full problem.

2. Enable the Axisymmetric Swirl option and set all swirling boundary conditions.

3. Begin the prediction of the swirling flow by solving only the momentum equation. This is the Swirl Velocity listed in the Equations list in the Solution Controls panel. Let the rotation "diffuse" throughout the flow field, based on your boundary condition inputs. Leave the turbulence equations active during this step. This step will establish the field of rotation throughout the domain.

4. Turn off the momentum equations describing the circumferential motion (Swirl Velocity). Leaving the velocity in the circumferential direction fixed, solve the momentum and continuity (pressure) equations (Flow in the Equations list in the Solution Controls panel) in the other coordinate directions. This step will establish the axial and radial flows that are a result of the rotation in the field. Again, you should leave the turbulence equations active during this calculation.

5. Turn on all of the equations simultaneously to obtain a fully coupled solution.

3.7.5 Turbulence model selection and validation

All flame simulations presented in this study based on software ANSYS-FLUENT version 6.3. The flow variables and all turbulent quantities are descetized in a finite-volume formulation using a second-order upwind scheme. All numerical procedure especially, the employed turbulence model should be compared and validated with published experimental results or analytical derivations. Fig. 3.16 shows a comparison between different turbulence models and analytical solution of axial velocity distribution for free jet flame which presented by Jeschar and Alt (1997) [97], the derived equation by the authors is given by.

$$\frac{u_a}{u_o} = \frac{1}{\sqrt{2\sqrt{\pi}}.k_u} \cdot \frac{d_o}{x} \cdot \sqrt{\frac{\rho_o}{\rho}} \qquad (3.35)$$

Where K_u is the experimental factor and equals 0.076 for CH_4, and ρ_o & ρ are the fuel and average jet density (kg/m^3), respectively. The influence of the turbulence model is shown in Fig. 3.16 on the axial velocity profile, as shown in the Figure, the results of CFD demonstrate that the best turbulence model fit with analytical solution is realizable k-ϵ, so, this turbulence model gives good agreement in the comparison with analytical solution. Similar study was performed but in this time with published experimental results. The influence of the turbulence model on the axial mixture fraction and axial temperature profiles is shown in Fig. 3.17(a) and (b). These results demonstrate again that, the realizable k-ϵ is the best one fit and gives good agreement with experimental data measured by Sandia and DLR which presented by Meier et al. (2000) [98]. Also it is observed from comparison study as in Fig. 3.17, the Reynolds-Stress-Model (RSM) has approximately the same behavior of realizable k-ϵ but we prefer to use the later because RSM leads to longer computational time. Fig. 3.18 shows many comparisons between CFD results using realizable k-ϵ turbulence model and experimental results measured by Sandia and DLR which presented by Meier et al. (2000). As shown in the Figure the comparisons include radial distribution for both temperature and mixture fraction and axial mass fraction distribution for species including CH_4, H_2, O_2, H_2O, CO, $and\,CO_2$. As a result, realizable k-ϵ shows good agreement in comparison with analytical solutions and also with published experimental results, so that, realizable k-ϵ was selected to carry out all my simulation work (free jet, confined jet and rotary kiln flame simulation).
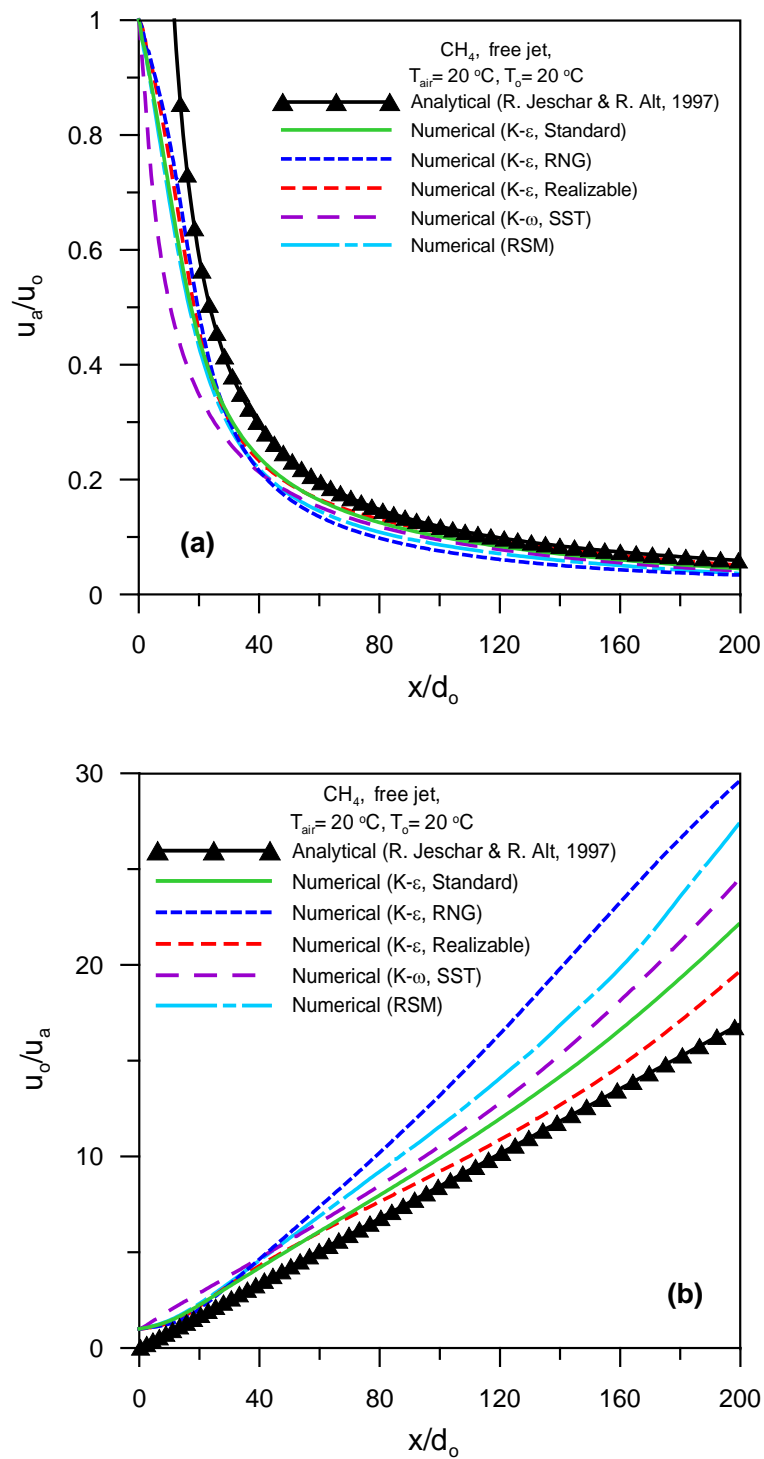
Figure 3.16: Turbulence model comparisons and validations: (a) axial to fuel velocity ratio, (b) fuel to axial velocity ratio, all turbulence models compared to analytical solution for free jet flame presented by R. Jeschar & R. Alt (1997) [97].
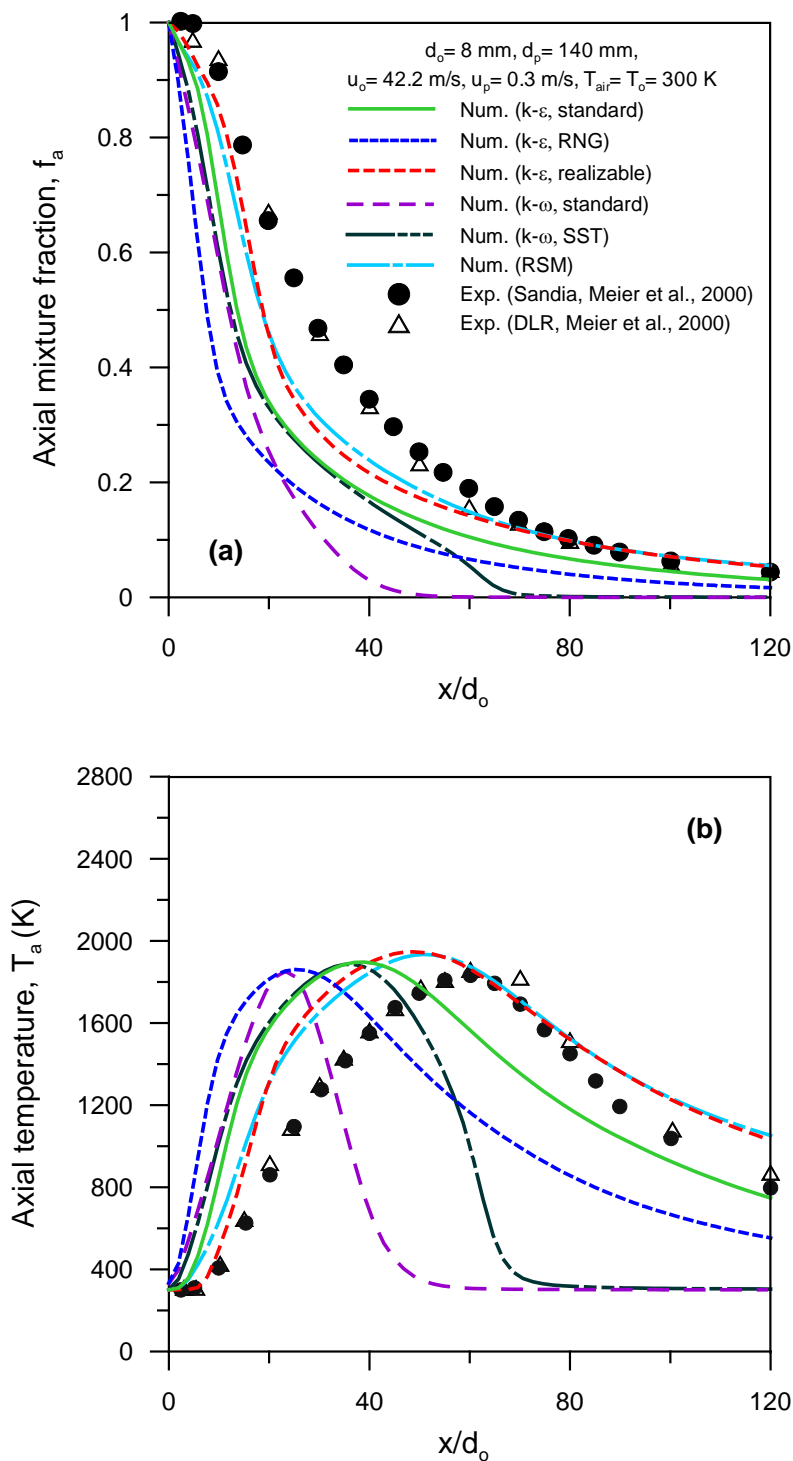
Figure 3.17: Turbulence model comparisons and validations: (a) axial mixture fraction, (b) axial temperature, all turbulence models compared to published experimental results measured by (Sandia & DLR) for free jet flame which presented by Meier et al. (2000) [98].
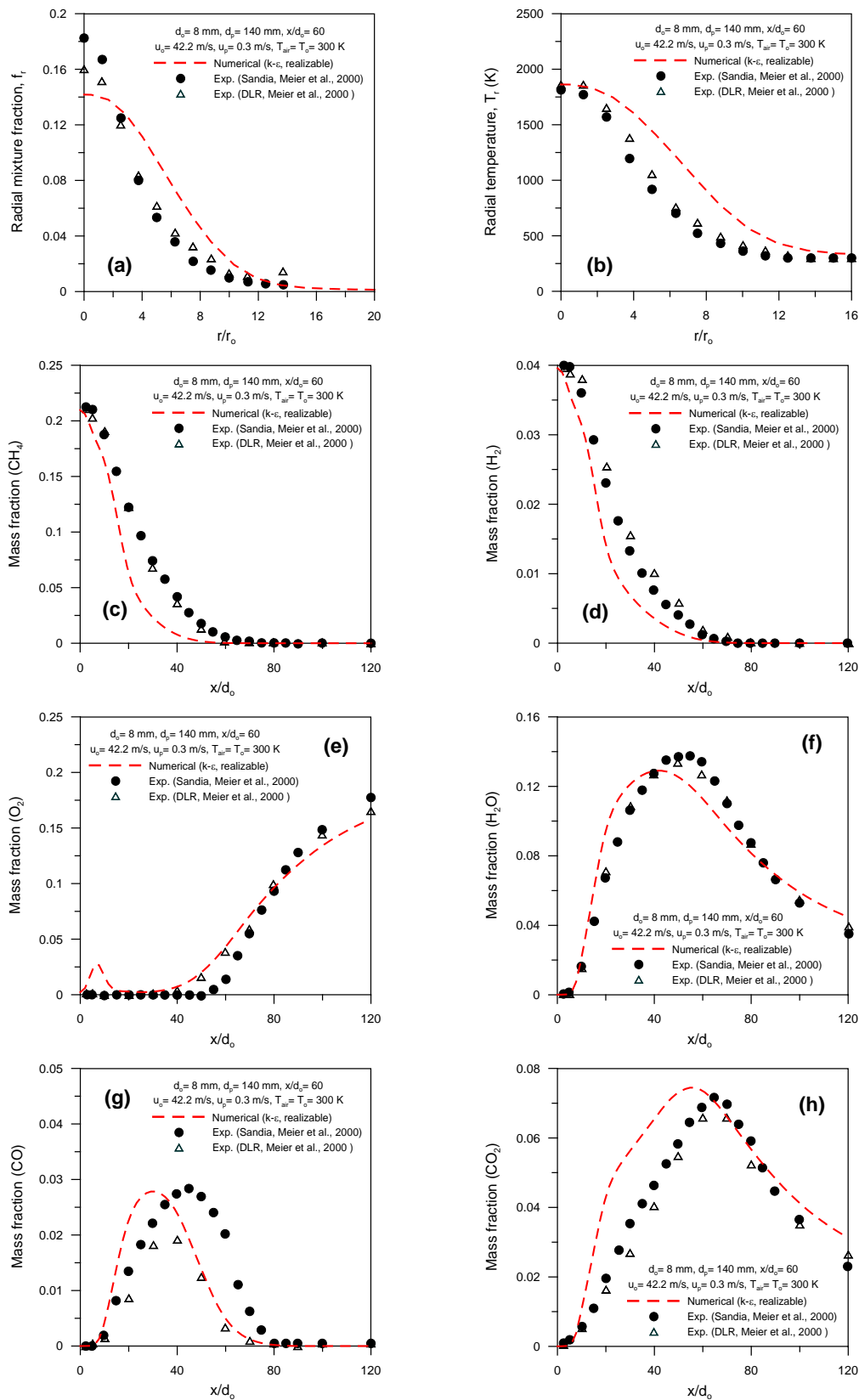
Figure 3.18: Validation of computational model, comparison of realizable $k - \epsilon$ turbulence model with published experimental results measured by (Sandia & DLR) for free jet flame and presented by Meier et al. (2000) [98]: (a) radial mixture fraction, (b) radial temperature, (c) CH_4 mass fraction, (d) H_2 mass fraction, (e) O_2 mass fraction, (f) H_2O mass fraction, (g) CO mass fraction, (h) CO_2 mass fraction.

Chapter 4

2D-Free Jet Flame Simulation: Results and Discussions

The present computational work was carried out to establish better understanding of the fee jet flame behavior and its characteristics, as a basic and reference step for confined jet flame simulation, as we see in details in the next chapter. The results of this chapter were divided to three main sections according to the proposed burner configurations; simple tube burner, annulus tube burner, and annulus tube burner with supported wall. The results were presented to investigate the effects of influencing parameters including operating and geometrical parameters such as fuel velocity, air temperature, radiation, burner annulus size, wall-supported burner and annulus air swirl on the flame length.

In this chapter the effects of the operating conditions and burner geometrical parameters on the centerline axial velocity, axial temperature, axial density, and mean mixture fraction profiles were presented and investigated. Also temperature and mean mixture fraction contours were used to visualize the flame. A useful burner design guidelines and useful design correlations of dimensionless parameters that characterize the flame length were obtained and presented.

4.1   Simple tube burner

Plain tube with 50 mm in diameter was used as a simple case (see Fig. 4.1), three gases were proposed to study CH_4, $Biogas$, and CO. The results in this section include the species distributions in axial and radial directions, effects of inlet fuel velocity, effects of air temperature, and effects of radiation on the flame characteristics, especially on the flame length which is the scope of this research. Also this section includes fuel comparisons between three studied gases. Finally, prediction of velocity and flame length correlations in dimensionless forms were obtained and validated with experimental and analytical correlations.

4.1.1   Species distributions

Figure 4.2 (a) shows the typical mass fraction profiles of individual species along the flame centerline, during combustion of Methane fuel without radiation effects under the simplified reaction scheme. As shown in the figure the mass fraction of Methane reduces along the axis of the flame, where the flame end not achieved, since the convert of CO to CO_2 is
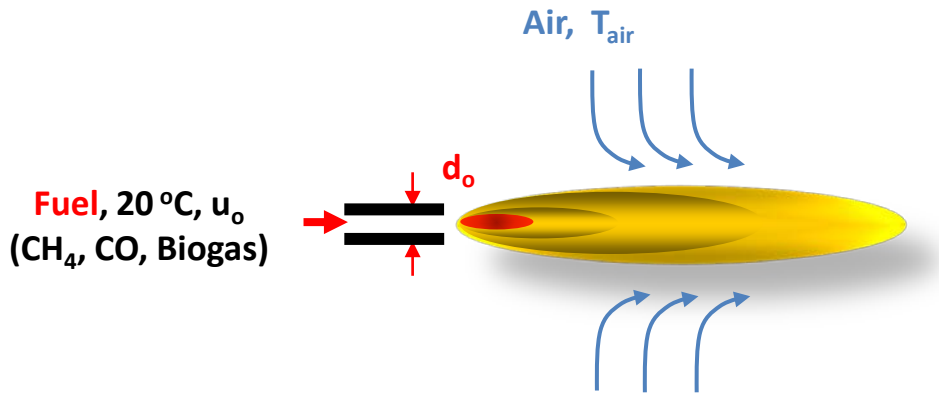
Figure 4.1: Schematic diagram of simple tube burner configuration.

still react. Accordingly, the flame end of hydrocarbons flames is to be expected where no CO is present on the axis. Also the radial profiles of mass fraction of individual species were illustrated at $x/do = 30$ in Figure 4.2 (b). Clearly the formation of the reaction zone can be seen, since the oxygen and Methane coexist.

4.1.2 Effects of fuel velocity

Figures 4.3 and 4.4 show the influence of the fuel velocity on the centerline axial temperature profiles and centerline inverted axial mean mixture fraction, respectively, using Methane fuel at $20\,°C$ and air temperature at $20\,°C$ without radiation and the fuel velocity varies (30-150 m/s). As shown in Fig.4.3, the flame temperature increases along the flame axis to reach peak temperature ($\sim 1800\,°C$) at ($x/d_o \simeq 170$) and after that reduces with the flame axis, this trend is the same at any fuel velocity. Also the figure illustrated that the inlet fuel velocity has no effect on the axial flame temperature profiles. Fig. 4.4 presented the inverted axial mean mixture fraction along the flame axis. As shown in the Fig. 4.4, the flame length is measured using a conserved scalar quantity; mean mixture fraction. The flame length ends at a point where the simulated mean fraction is the same as the stoichiometric mean mixture fraction. The values of studied gases stoichiometric mean mixture fraction are given in Table 3.2, the corresponding flame length for Methane fuel for free jet is at $x/d_o = 174$. Also Fig. 4.4 demonstrated that the flame length is independent of the fuel velocity and consequently the burner thermal power.

4.1.3 Effects of air temperature

The effects of air temperature on the axial velocity profiles, axial temperature profiles, axial mean mixture fraction profiles, temperature and mean mixture fraction contours and density profiles versus mean mixture fraction are shown in Figs. (4.5, 4.6, 4.7, 4.8, 4.9 and 4.10). Three gases were presented to study (CH_4, $Biogas$, and CO) at 100 m/s fuel velocity and 20°C fuel temperature. In this case the radiation model (P1) doesn't use (without radiation).

Figure 4.5 shows influence of air temperature (20, 250, and 1000°C) on dimensionless axial velocity profiles along the flame for different fuels (CH_4, $Biogas$, and CO). As shown in the Figure, the axial velocity decreases along the flame axis. The trend is the same at any air temperature and for any fuel, also as illustrated in the Figure, the
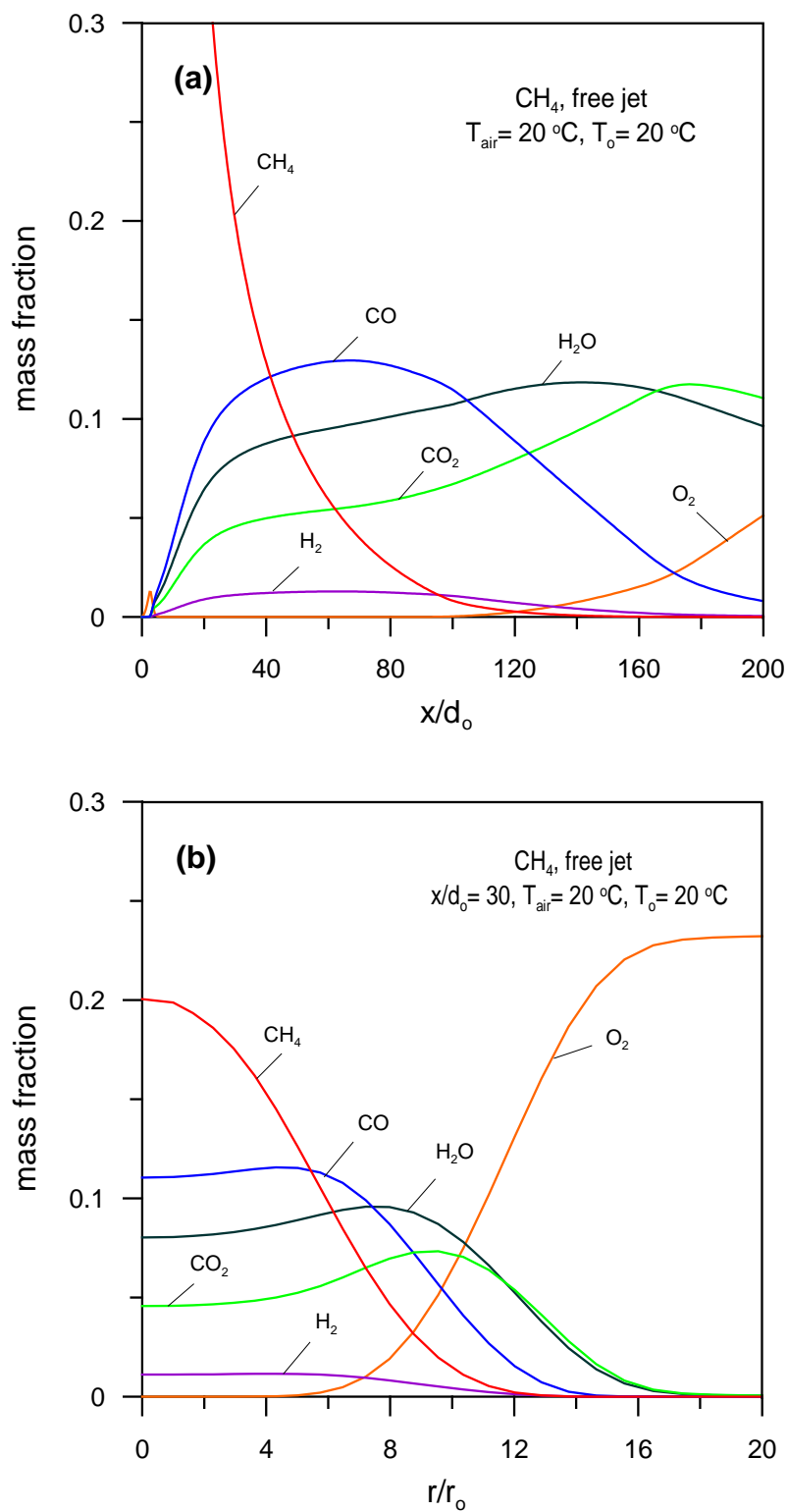
Figure 4.2: Species mass fraction distributions: (a) axial distribution, (b) radial distribution.
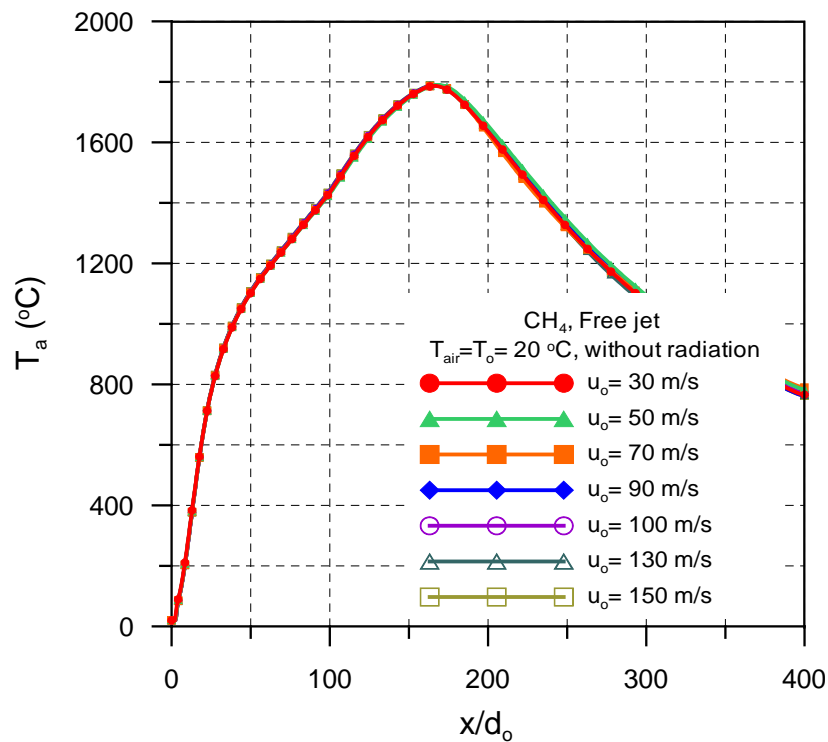
Figure 4.3: Influence of fuel velocity on axial temperature distribution.
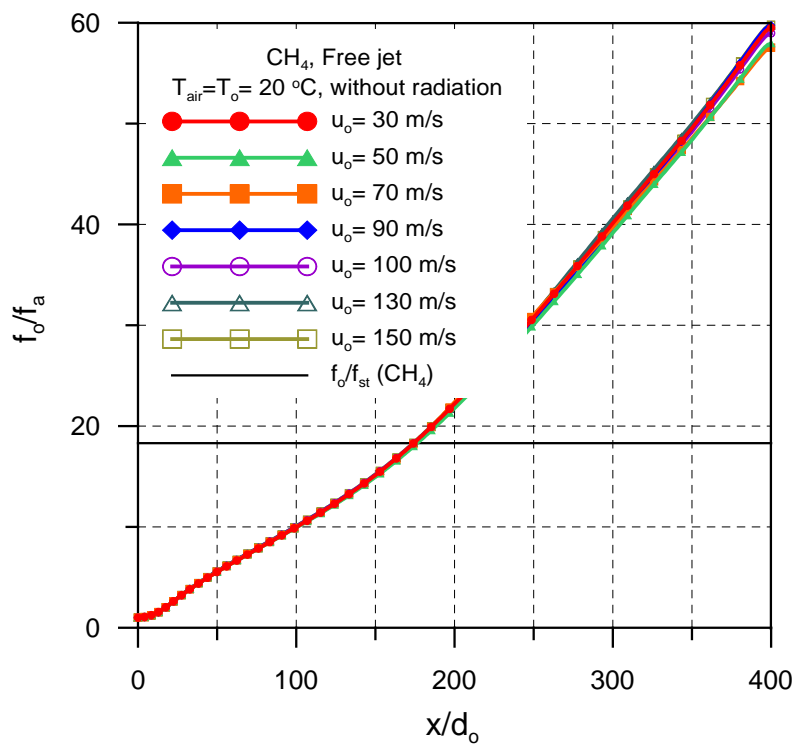
Figure 4.4: Influence of fuel velocity on inverted axial mean mixture fraction.

air temperature has a small effect on the velocity profile, while the axial velocity profile increases with increasing the air temperature and this effect is the same for all fuels, and this effect increases slightly from fuel Methane to Carbon monoxide (i.e., this effect appears with fuels which have higher stoichiometric mean mixture fraction values).

Figure 4.6 display the influence of air temperature (20, 250, 500, 750, and 1000°C) on the axial temperature profiles along the flame for different fuels (CH_4, $Biogas$, and CO). As demonstrated in the Figure, the air temperature has a significant effect on the axial temperature profile (i.e., the axial temperature profiles increases with increasing the air temperature), the trend is the same for any fuel. This can be attributed to the increase in air temperature as an oxidizer tends to increase the mixing temperature and consequently an increase in flame temperature. The results also show that an increase in air temperature from 20 to 1000°C increases the peak flame temperature by ∼28 %, ∼30 %, and ∼15 % for CH_4, $Biogas$, and CO, respectively.

The effect of air temperature (20, 250, 500, 750, and 1000°C) on the free jet flame length for different fuels (CH_4, $Biogas$, and CO) was presented in Fig. 4.7. As shown in the figure the flame length ends at a point where the simulated mean fraction is the same as the stoichiometric mean mixture fraction. The results show that the flame length increases with increasing the air temperature and this trend is the same for any fuel. This is due to, as the air temperature increased, the mass flux by turbulent mixing reduced because a decrease of air density. The low density at higher temperature causes less diffusion of oxidant into the fuel flow. Less penetration of air into the fuel jet results in an increase in the flame length. The same investigation had been done by [71]. Also as shown in Fig. 4.7, the increasing in the flame length with temperature is reasonable for Methane and Biogas fuels. These fuels (lower stoichiometric mean mixture fraction) and this effect decreases with CO fuel (high stoichiometric mean mixture fraction). Where, the results demonstrated that an increase in air temperature (from 20 to 1000°C) increases the the dimensionless flame length by ∼18 %, ∼21 %, and ∼15 % for CH_4, $Biogas$, and CO, respectively. Figures 4.8 and 4.9 show the influence of air temperature on temperature and mean mixture fraction contours for Methane fuel. The contours proof what I explained and discussed above; the air temperature has a reasonable effect on the peak flame temperature and flame length.

The variation of the density profiles against mean mixture fraction with different air temperatures for different fuels (CH_4, $Biogas$, and CO) was depicted in Fig. 4.10. As shown in the Figure, the density decreases with increasing mean mixture fraction to reach the lowest value at stoichiometric mean mixture fraction value, then increases with mean mixture fraction. The trend is the same at any air temperature and for all simulated fuels. This can be attributed to, as the mean mixture fraction is increased, the flame temperature is increased until the peak flame temperature (stoichiometric mean mixture fraction), this because the fuel convergence is increased. In consequence the density reduces to reach the minimum value at peak flame temperature (stoichiometric mean mixture fraction). After peak flame temperature; the flame temperature decreases with the increase of mixture fraction and consequently the density increases again. Also as presented in Fig. 4.10 the density profile against the mean mixture fraction decreases with the increase of the air temperature, this effect is reasonable at low mixture fraction and slight at high mixture fraction values, and this effect is the same for all fuels.
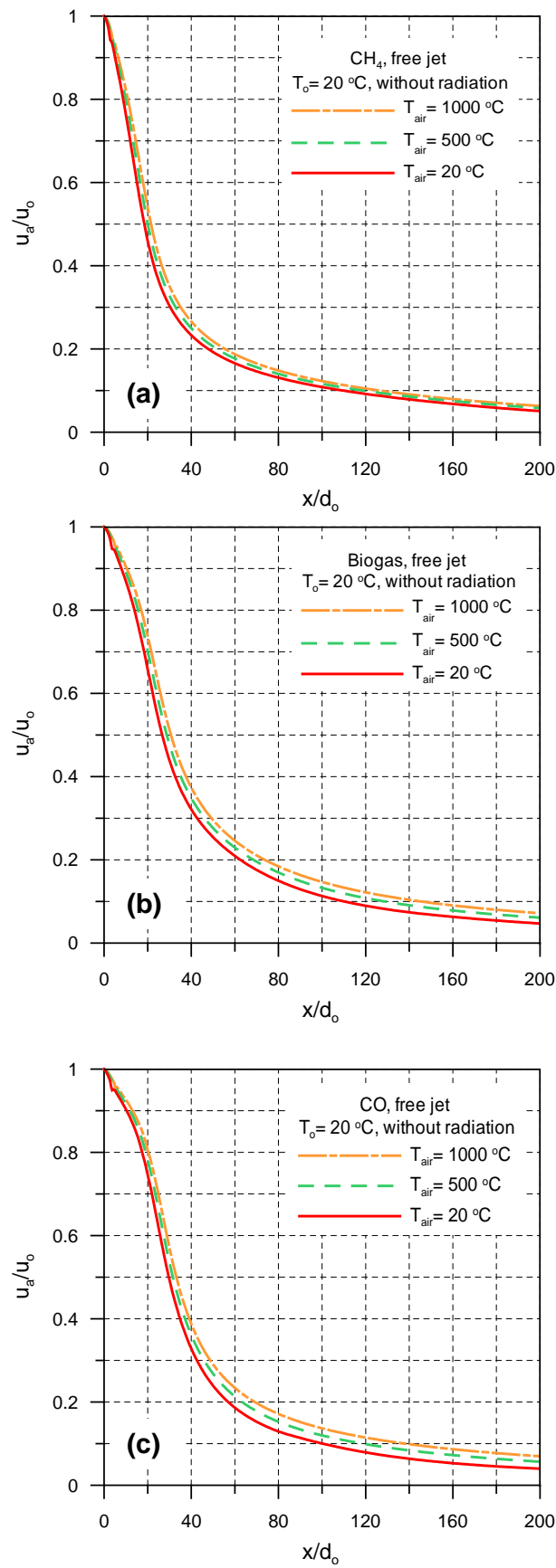
Figure 4.5: Influence of air temperature on dimensionless axial velocity profiles along the flame: (a) CH_4, (b) *Biogas*, (c) *CO*.
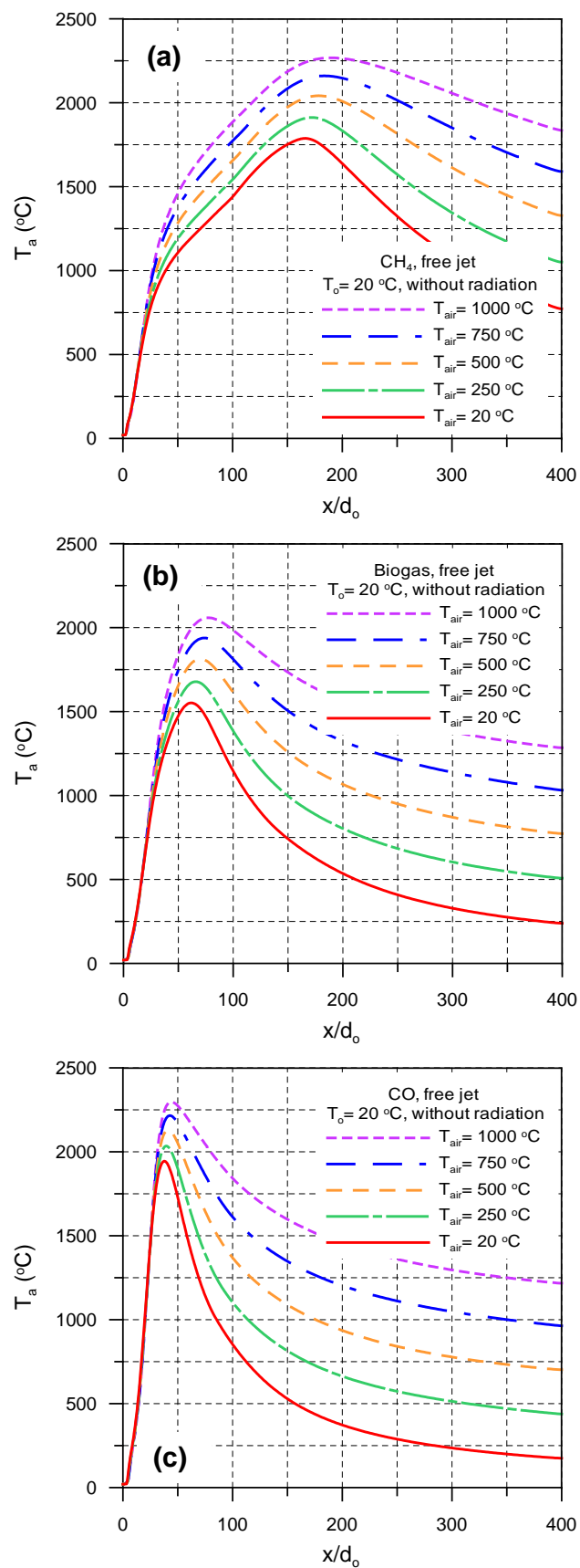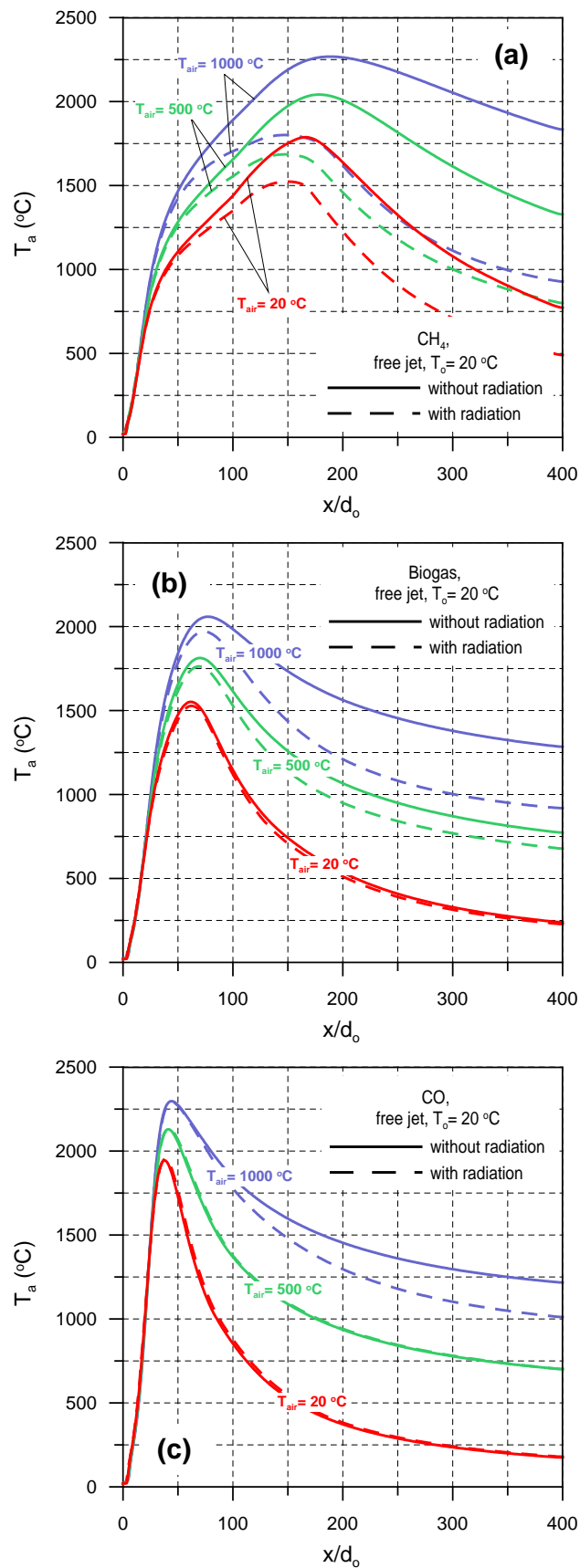
Figure 4.6: Influence of air temperature on axial temperature profiles along the flame: (a) CH_4, (b) *Biogas*, (c) *CO*.
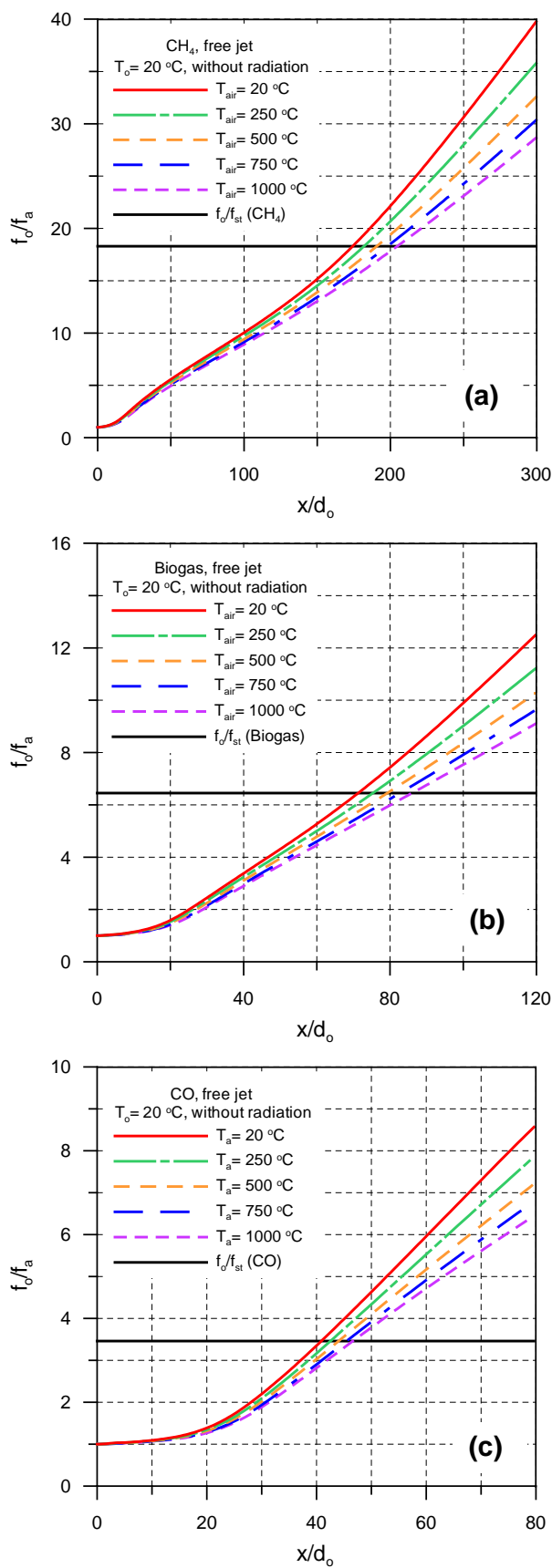
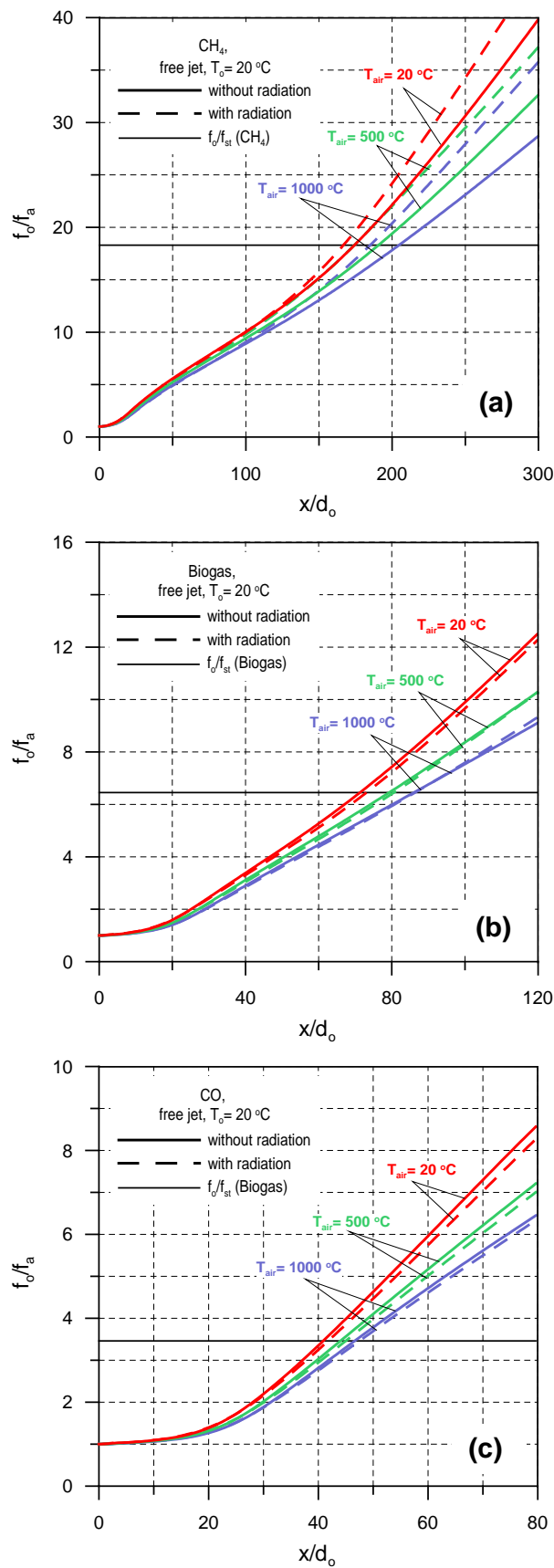Figure 4.7: Influence of air temperature on inverted dimensionless axial mixture fraction profiles along the flame: (a) *CH$_4$*, (b) *Biogas*, (c) *CO*.
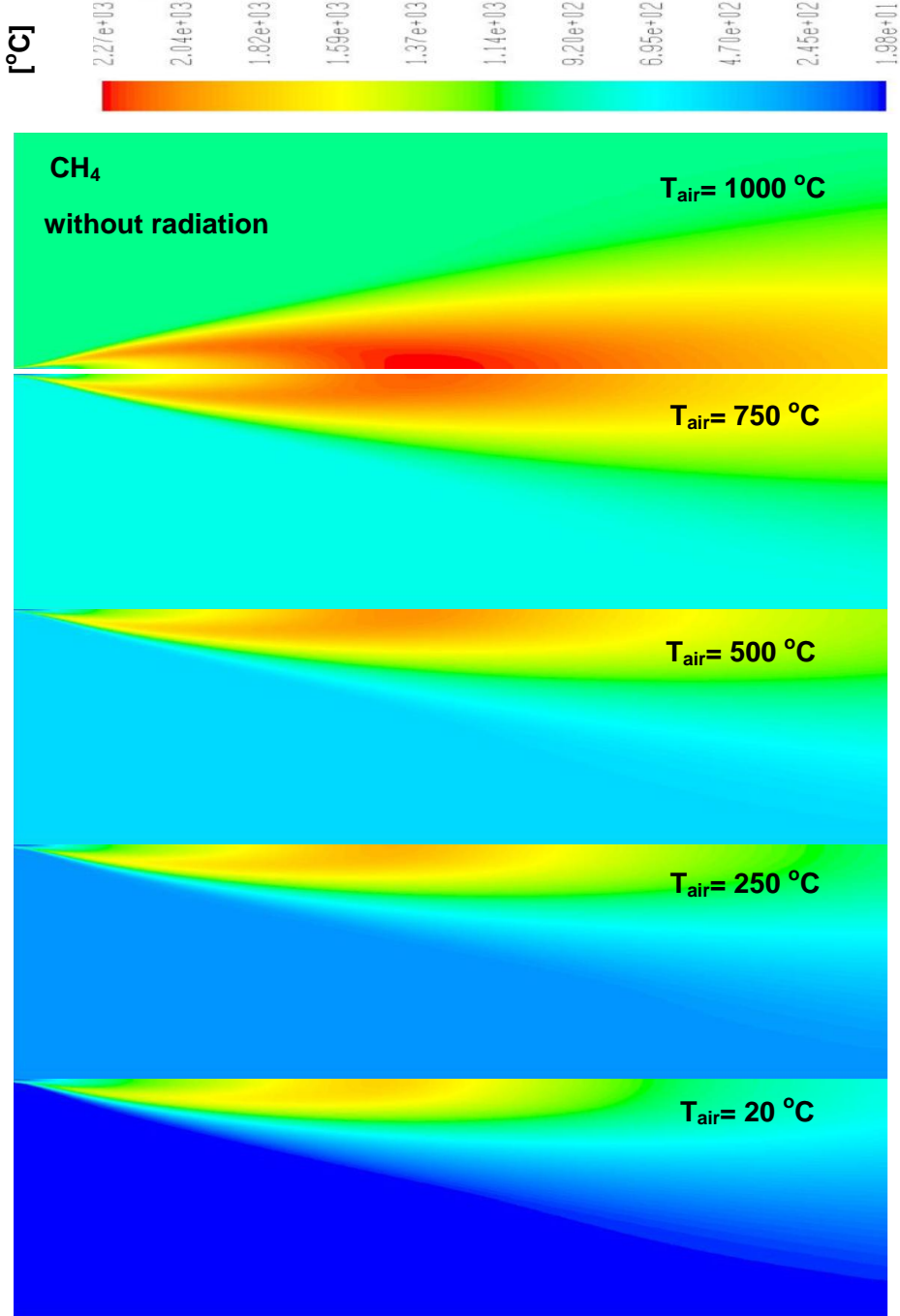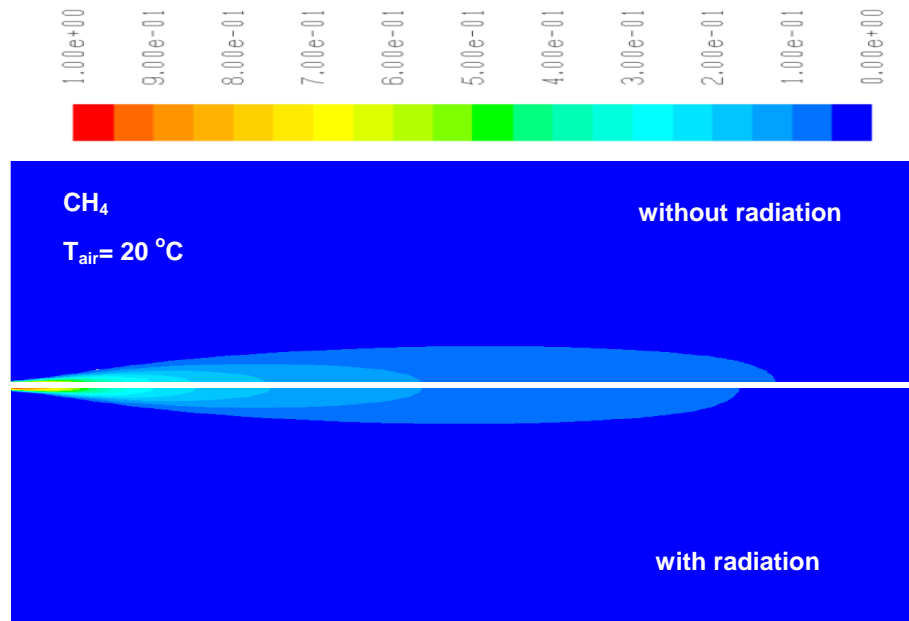
Figure 4.8: Influence of air temperature on temperature contours along the flame for Methane fuel (CH_4).
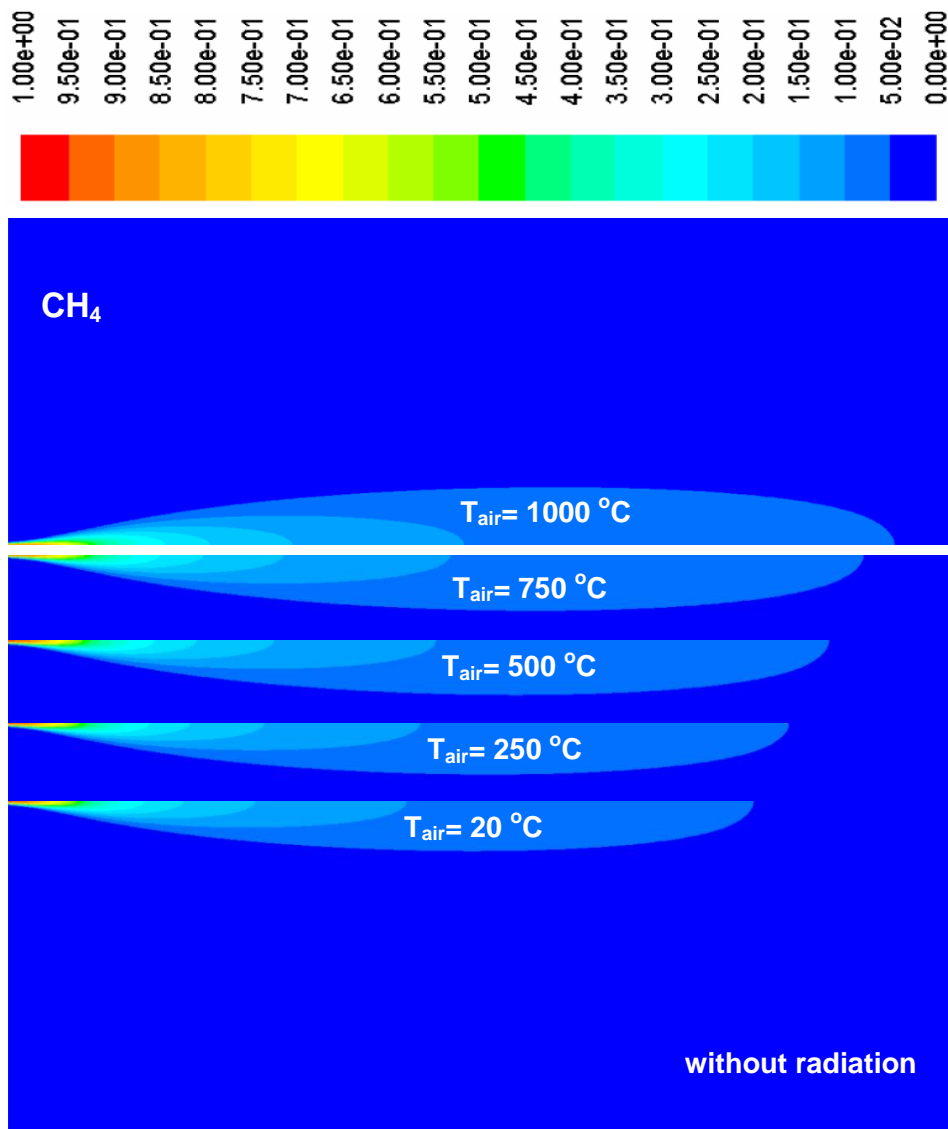
Figure 4.9: Influence of air temperature on mixture fraction contours along the flame for Methane fuel (CH_4).
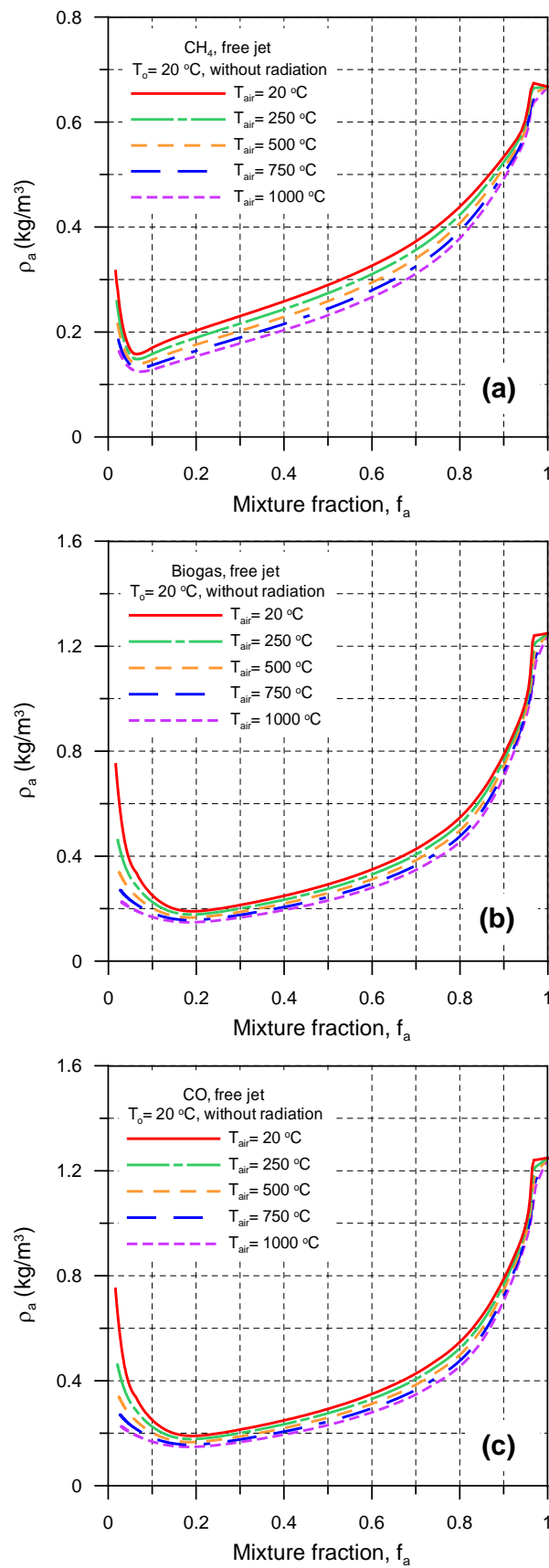
Figure 4.10: Influence of air temperature on axial density versus axial mixture fraction along the flame: (a) CH_4, (b) $Biogas$, (c) CO.

4.1.4   Effects of radiation

The influence of radiation on the axial temperature profiles, axial density profiles, axial mean mixture fraction profiles, temperature and mean mixture fraction contours is presented in Figs. (4.11−4.16). Three gases were simulated to study (CH_4, $Biogas$, and CO) at 100 m/s fuel velocity and 20°C fuel temperature. In this case the radiation model (P1) was used (with radiation) and the results were presented and compared with the case of without radiation modeling.

Figure 4.11 shows the influence of radiation on the axial temperature profiles with the air temperature (20, 500, and 1000°C) as a parameter for different gases (CH_4, $Biogas$, and CO). As shown in the Figure, at any fuel and at any air temperature, the temperature profile along the flame and corresponding its peak flame temperature decreases with radiation effect (i.e., with radiation calculation). This can be attributed to, part of heat released by radiation added to the total heat released from the flame, this amount of heat released by radiation cools the flame and consequently drops the temperature profile along the flame. Also as shown in the Fig. 4.11 the effect of radiation on the flame temperature is significant at high air temperature and slight at low air temperature. Also as displayed in the Figure the influence of radiation diminishes at 20°C air temperature for both $Biogas$ and CO. This is as a result of the part of heat transfer by radiation, from low heating value gases at low air temperature is very small part, so the radiation hasn't effect the flame temperature profile. Fig. 4.12 presented the flame temperature contours for Methane fuel at 20°C air temperature to show the Influence of radiation on the flame temperature. As shown in the Figure the lower temperature flame zone is associated with radiation consideration.

The effect of radiation on the centerline axial density profiles with air temperature (20, 500, and 1000°C) as a parameter is shown in Fig. 4.14 for (CH_4, $Biogas$, and CO) fuels. As shown in the Figure, at any fuel and at any air temperature, the density profile along the flame shifted up with radiation effect. This because of the presence of radiation calculation which decreases the flame temperature and consequently increases the flame density. Also as shown in the Figure, the effect of radiation on density profiles diminishes at 20°C air temperature for $Biogas$ fuel and at 20°C and 500°C for CO fuel. This can be attributed to the radiation consideration has no effect on the temperature profiles of low heating value gases with high air temperatures, and in consequence radiation hasn't effect on the density profiles of low heating value gases with high air temperatures. Fig. 4.13 shows the influence of radiation on the flame density contours for Methane fuel at 20°C air temperature. As depicted in the Figure, the flame has higher density zone in case of radiation consideration than without radiation.

Figure 4.15 presents influence of radiation on the inverted dimensionless axial mean mixture fraction profiles to determine the flame length. As shown in the Figure, radiation has approximately no effect on the flame lengths for high stoichiometric mixture fraction gases (low air demand) like $Biogas$ and CO fuels, but has a smaller effect on the flame length of Methane, CH_4. As illustrated in Fig. 4.15 the flame length of Methane fuel decreases by ∼4 %, ∼9 %, and ∼10 % for 20, 500, and 1000°C air temperature, respectively in case of radiation consideration. Fig. 4.16 shows the influence of radiation on the flame mean mixture fraction contours for Methane fuel at 20°C air temperature. As depicted in the Figure, the radiation has a small effect on flame length reducing.

Figure 4.11: Influence of radiation on axial temperature profiles along the flame: (a) CH_4, (b) *Biogas*, (c) *CO*.
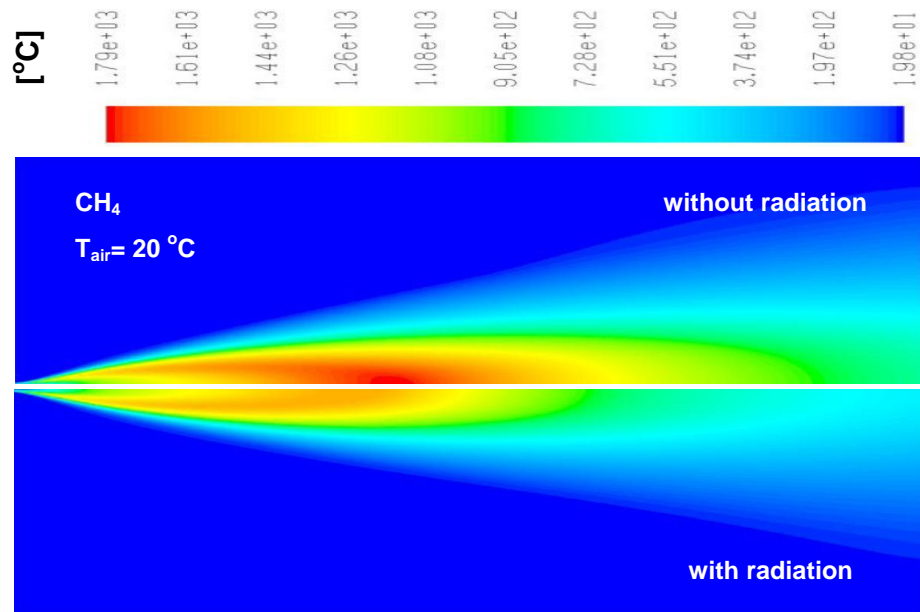
Figure 4.12: Influence of radiation on temperature contours for Methane fuel (CH_4).
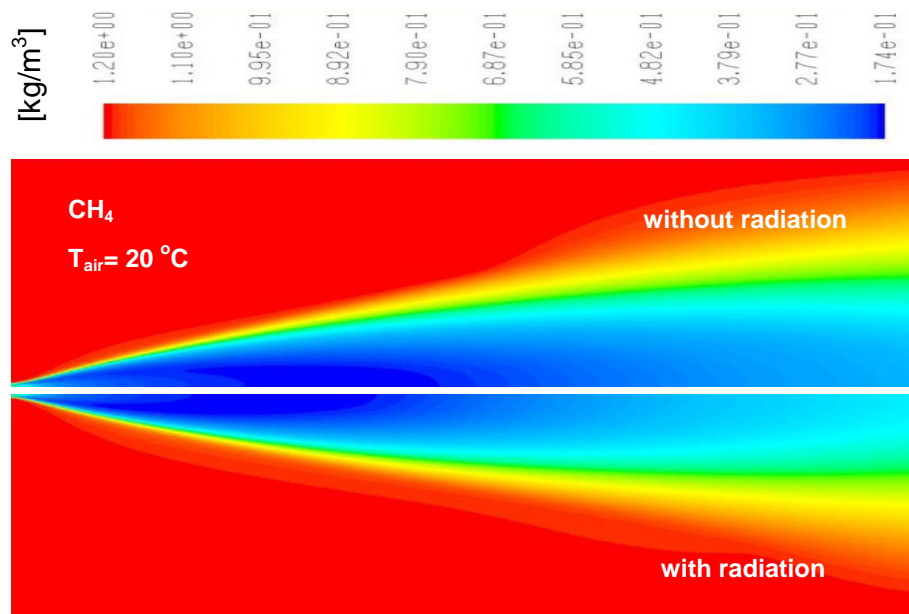
Figure 4.13: Influence of radiation on density contours for Methane fuel (CH_4).
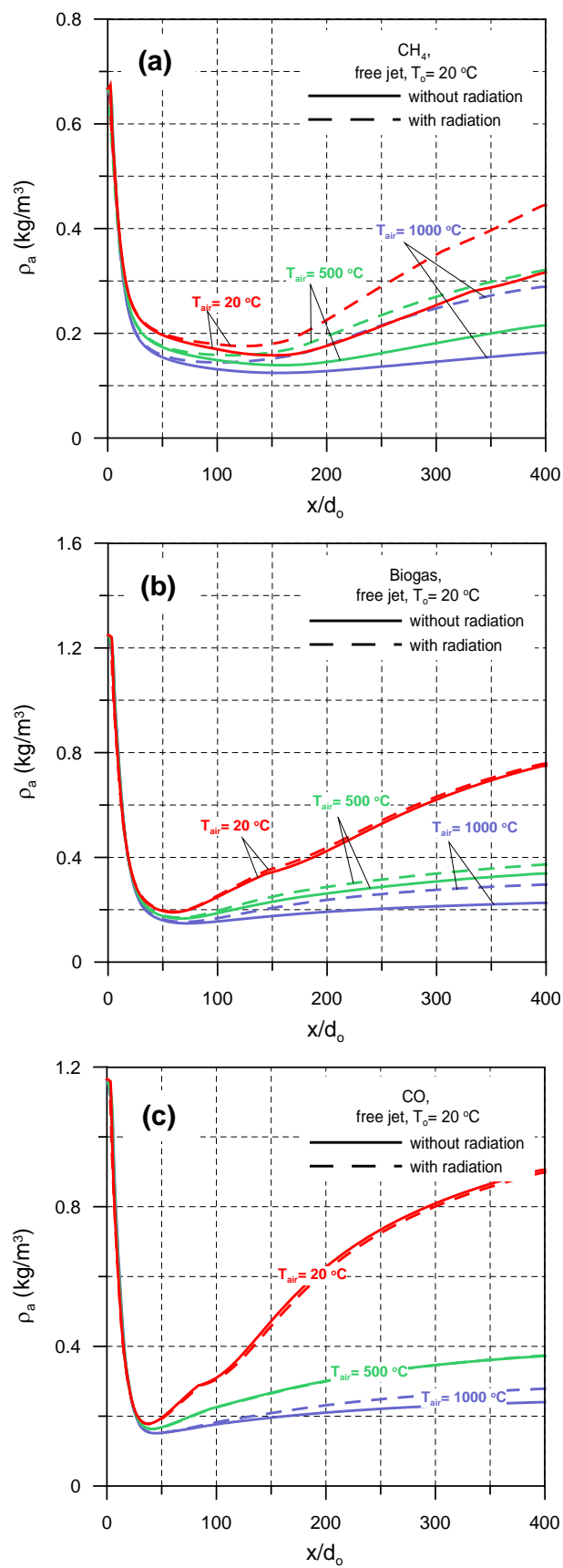
Figure 4.14: Influence of radiation on axial density profiles along the flame:(a) CH_4, (b) *Biogas*, (c) *CO*.

Figure 4.15: Influence of radiation on inverted dimensionless axial mixture fraction profiles along the flame:(a) CH_4, (b) $Biogas$, (c) CO.

Figure 4.16: Influence of radiation on mixture fraction contours for Methane fuel (CH_4).

4.1.5 Fuels comparisons

The comparisons between different gases (CH_4, $Biogas$, and CO) at 100 m/s fuel velocity and 20°C fuel temperature on the flame behavior were presented and discussed in the following paragraphs. The Figures from 4.17 to 4.25 show influence of kind of fuel on axial velocity profiles, axial temperature profiles, mixture fraction profiles, temperature contours, and mean mixture fraction contours, last two figures presented a comparison between Numerical and analytical results for flame length and velocity profiles in radial direction.

Figure 4.17 shows dimensionless axial velocity profiles for CH_4, $Biogas$, and CO at 100 m/s fuel velocity and 20°C fuel temperature. As shown in the Figure, the axial velocity decreases along the flame, the trend is the same for all gases. Also as presented in the Figure, up to $x/d_o \approx 40$, CO has the upper velocity profile, while the CH_4 has the lower one. This is due to that the velocity variation depend on the density of the fuel (see Table 3.2). Whereas, the higher the fuel density, the higher axial velocity profile. Therefore CO is higher velocity profile than CH_4, while $Biogas$ has intermediate velocity profile and close to CO profile due to its density which is closer to CO than CH_4. Also we can find that, after $x/d_o \approx 100$, the fuel kind has slight effect on the velocity profiles.

The comparisons of axial temperature profiles for CH_4, $Biogas$ and CO at 100 m/s fuel velocity and 20°C fuel temperature with and without radiation consideration were presented in Fig. 4.18 at air temperature of 20, 500, and 1000°C. As displayed in the Figure, the temperature profiles shifted up with increasing air temperature for all fuels in both cases (with and without radiation). As discussed before, the higher air temperature, the higher flame temperature profile. Also the figure displays that, CO has the highest peak flame temperature at $x/d_o \approx$ (41-47) according to the air temperature and effect of radiation, while $Biogas$ has the lowest peak flame temperature at $x/d_o \approx$ (71-86), and CH_4 has intermediate peak flame temperature at a location of $x/d_o \approx$ (166-205). That
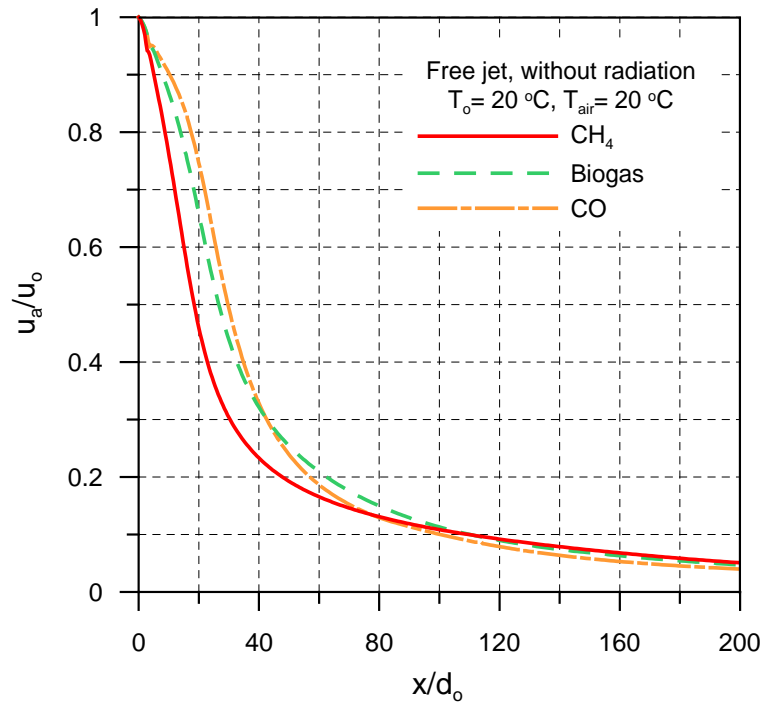
Figure 4.17: Comparison of axial velocity profiles along the flame for CH_4, $Biogas$ and CO.

means, the flame of CO has the highest peak flame temperature, highest heat flux and consequently has the shortest flame length. Vice versa for CH_4, but $Biogas$ in between of them.

According to the previous discussion, Fig. 4.19 shows the axial temperature profiles for CH_4, $Biogas$, and CO fuels at 100 m/s fuel velocity and 20°C fuel temperature along the flame length, with and without radiation simulation as a parameter for different air temperatures of 20, 500, and 1000°C. As shown in the Fig. 4.19, the peak flame temperature locates at or near the flame end. This result is the same for all fuels at any air temperature for both cases (with and without radiation). Therefore, the final result is, the flame length ends at or near the peak flame temperature location, where the mean mixture fraction is stoichiometric value. The temperature contours of three simulated gases (CH_4, $Biogas$, and CO) at 20°C air temperature (without radiation) were depicted in Fig. 4.20. As shown in the Figure, CO has the highest peak flame temperature and smallest flame hot zone area. $Biogas$ has the lowest peak flame temperature and intermediate flame hot zone area, while CH_4 has the biggest flame hot zone area and intermediate peak flame temperature. In other words, the higher the fuel heating value, the bigger the flame volume.

Figure 4.21 displays the inverted dimensionless axial mean mixture fraction profiles a long the flame for CH_4, $Biogas$, and CO fuels at 100 m/s fuel velocity and 20°C fuel temperature, with and without radiation simulation as a parameter for different air temperatures of 20, 500, and 1000°C. As shown in the Figure, according to the method of flame length calculation, the flame length ends at the point where the simulated mean mixture fraction equals to the stoichiometric value. Therefore, the lower the fuel stoichiometric mean mixture fraction, the longer the flame, and vice versa (see Table

3.2). From the figure; CH_4 has the longest flame length, CO has the shortest flame length, and $Biogas$ in between of them, this result is the same at any air temperature and for both cases (with and without radiation). As well Fig. 4.22 shows the axial mixture fraction profiles for CH_4, $Biogas$, and CO fuels at 100 m/s fuel velocity and 20°C fuel temperature along the flame length, with and without radiation simulation as a parameter for different air temperatures of 20, 500, and 1000°C. The mean mixture fraction contours for the three gases (without radiation) were depicted in Fig. 4.23 at 20°C air temperature. As shown in the figure, the flame length of Methane gas is greater than Biogas, and CO gases by ∼59 %, and ∼76 %, respectively.

The flame length in dimensionless form versus air temperature was illustrated in Fig. 4.24 for CH_4, $Biogas$, and CO fuels at 100 m/s fuel velocity and 20°C fuel temperature with and without radiation simulation. The comparison of the analytical flame length derivation presented by Specht [99] ($L_f/d_o = 1/(f_{st} \tan 9^o)(\sqrt{\rho_o/\rho})$) and simulated free jet flame length (with and without radiation) was conducted and presented. As shown in the figure the simulated free jet flame lengths give good agreement with analytical solution for $Biogas$ and CO fuels, but for CH_4 fuel the analytical solution is greater than the numerical solution by ∼12 %. This difference can be attributed to the modeling assumptions and numerical approximations. Also a comparison between numerical and analytical radial dimensionless velocity profiles presented by Giese [100] was conducted and presented in Fig. 4.25. The radial velocity profiles were simulated at different distance from burner tip (x/d_o=10, 30, 50, 100, and 200), using Methane fuel at 20°C air temperature and fuel temperature 20°C. The figure shows good agreement between analytical solution and numerical simulations.

4.1.6 Prediction of velocity and flame length correlations

The inverted dimensionless axial velocity correlation with axial distance from burner tip, nozzle diameter, average jet flame density, and fuel density can be obtained from the simulated results of the present study using regression analysis as follows:

$$\frac{u_o}{u_a} = 0.1597 \frac{x}{d_o} \sqrt{\frac{\rho}{\rho_o}}$$
(4.1)

Where ρ is the mean centerline jet density along the flame. Equation 4.1 was obtained from data in the following ranges: 20°C≤T_{air}≤1000°C; 10≤ x/d_o≤200; and T_o= 20°C. The prediction of this equation is shown in Fig. 4.26, the correlation can describe 85 % of the numerical results within error ±15 %.

The free jet flame length in dimensionless form in terms of stoichiometric air demand (mass basis) can be deduced from the computed results of the present study using regression analysis as follows:

$$\frac{L_f}{d_o} = 14.14(1 + L)^{0.86}$$
(4.2)

Equation 4.2 was obtained from data in the following ranges: 2.46≤L≤17.3; T_{air}= 20°C; and T_o= 20°C. The prediction of this equation is shown in Fig. 4.27, the correlation can predict 100 % of the numerical results within error ±0.73 %.
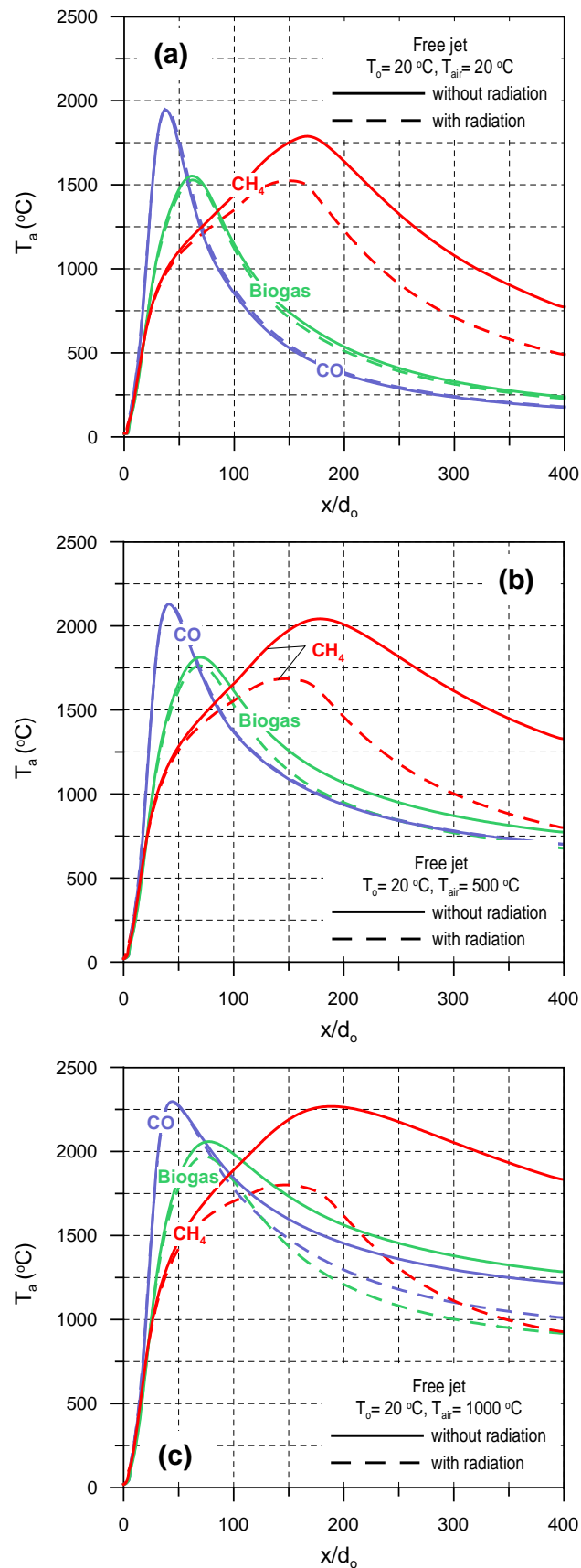
Figure 4.18: Comparison of axial temperature profiles along the flame for CH_4, $Biogas$ and CO fuels with and without radiation at different air temperature: (a) T_{air}=20°C, (b) T_{air}=500°C, (c) T_{air}=1000°C.
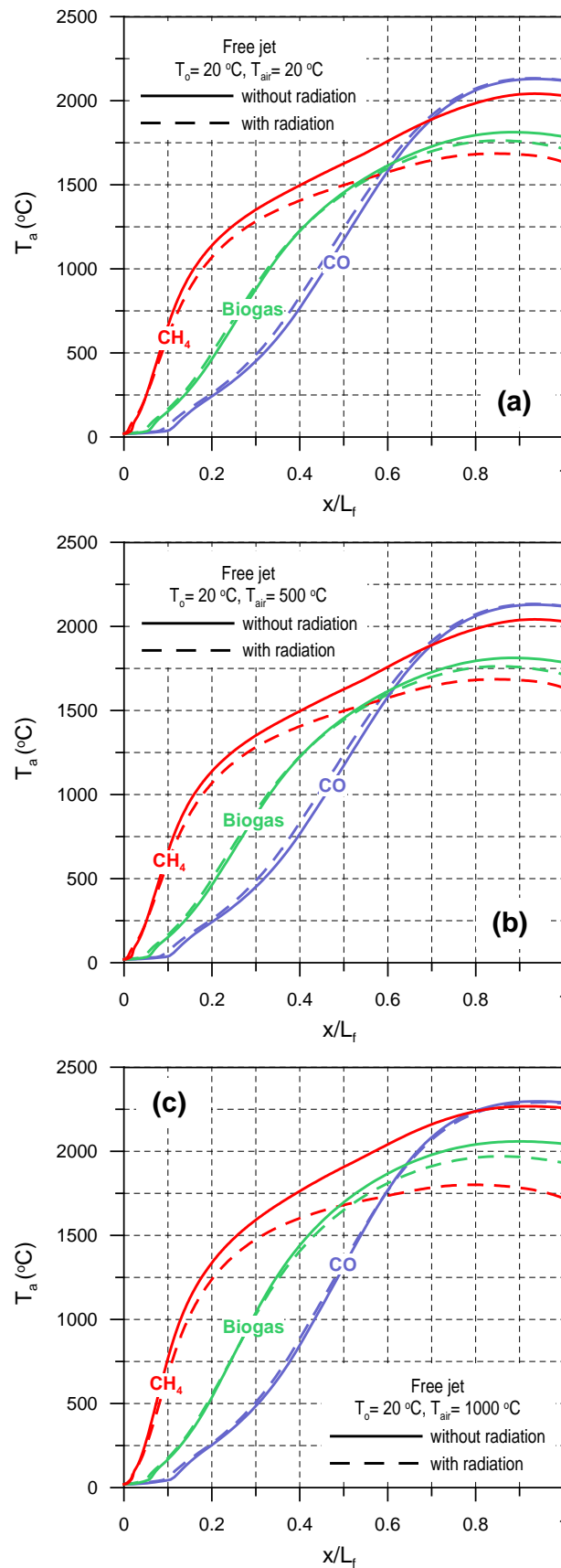
Figure 4.19: Comparison of axial flame temperature corresponding to flame length for CH_4, *Biogas* and CO fuels with and without radiation at different air temperature: (a) T_{air}=20°C, (b) T_{air}=500°C, (c) T_{air}=1000°C.
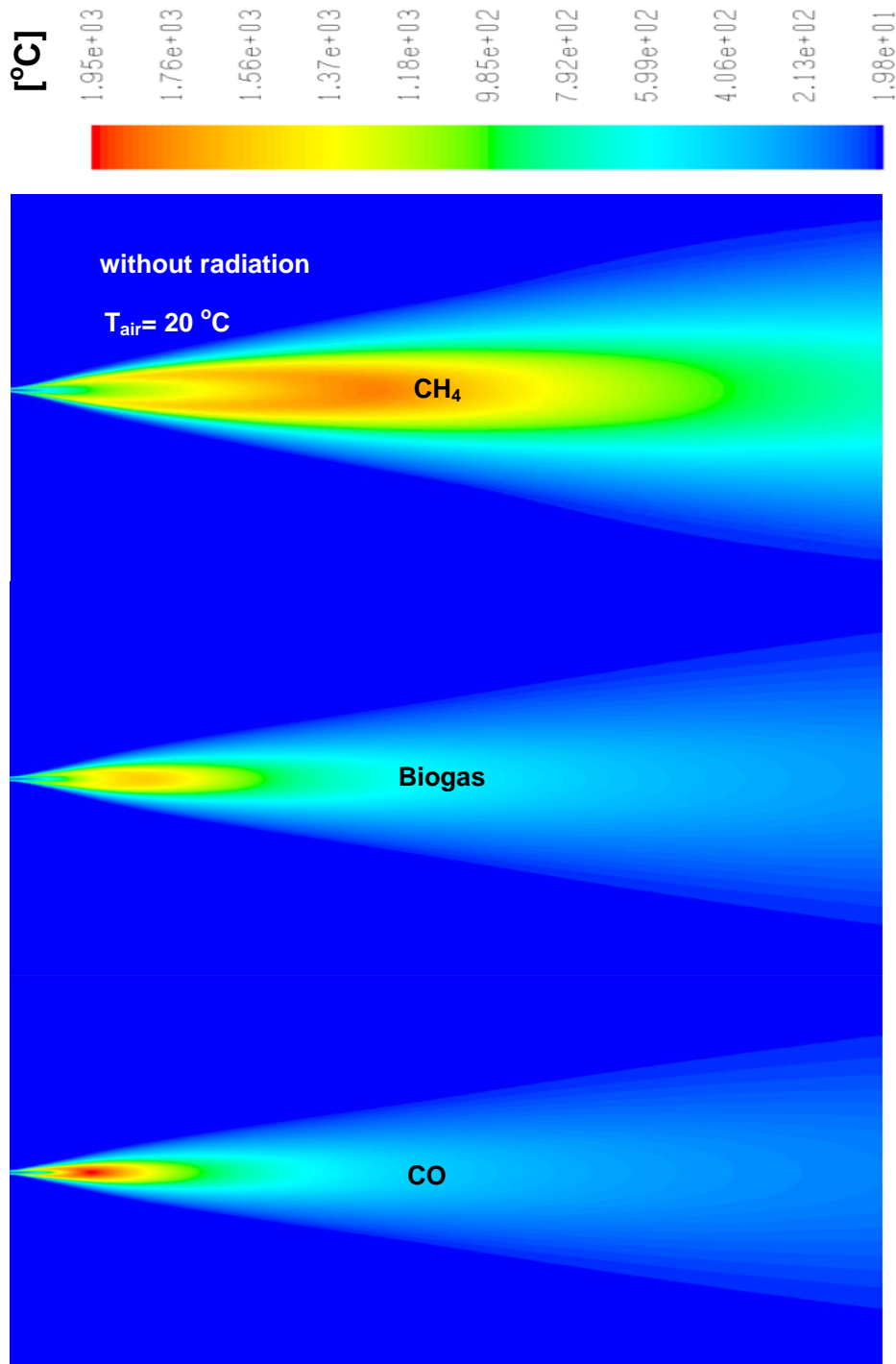
Figure 4.20: Comparison of free jet flame temperature contours for CH_4, $Biogas$ and CO fuels without radiation at T_{air}=20°C, u_o= 100 (m/s).
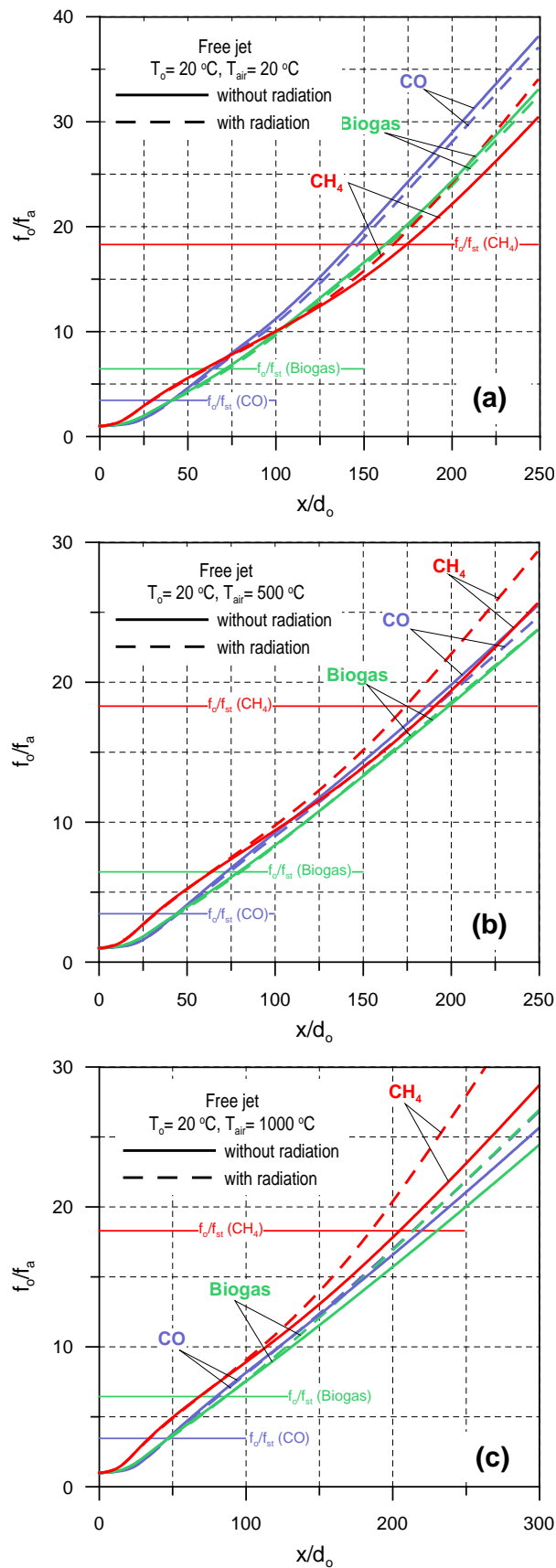
Figure 4.21: Comparison of inverted dimensionless axial mixture fraction for CH_4, $Biogas$ and CO fuels with and without radiation at different air temperature: (a) T_{air}=20°C, (b) T_{air}=500°C, (c) T_{air}=1000°C.
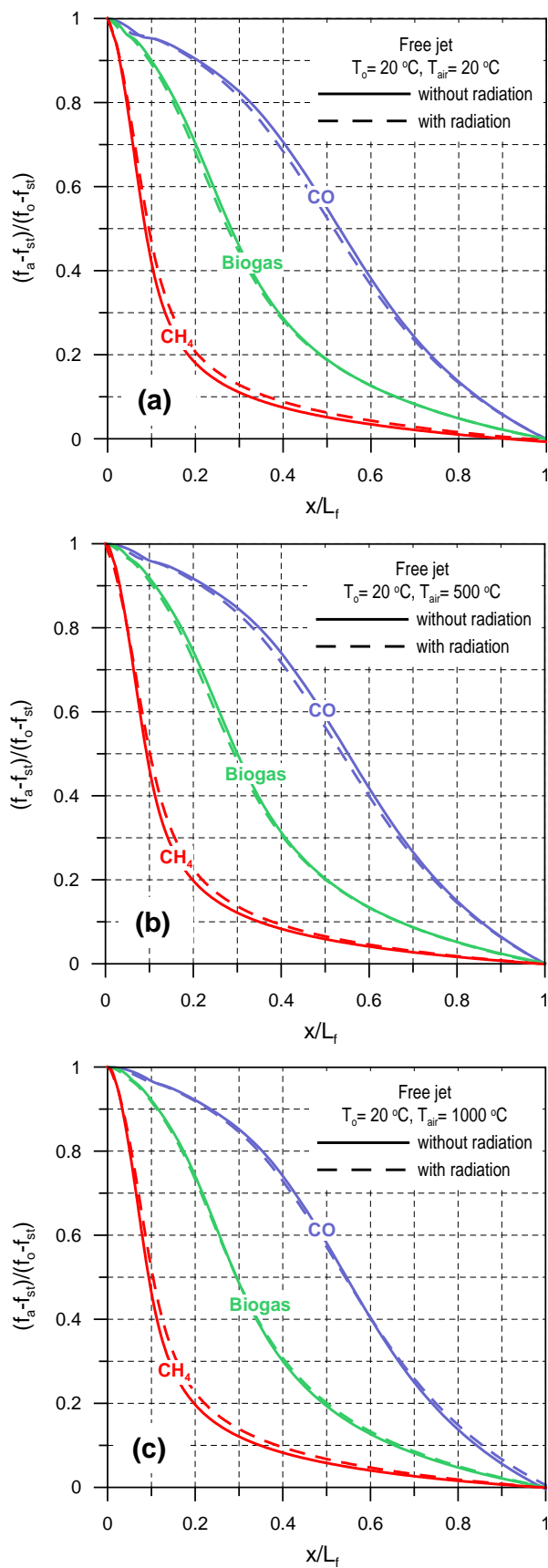
Figure 4.22: Comparison of axial mixture fraction corresponding to flame length for CH_4, $Biogas$ and CO fuels with and without radiation at different air temperature: (a) T_{air}=20°C, (b) T_{air}=500°C, (c) T_{air}=1000°C.
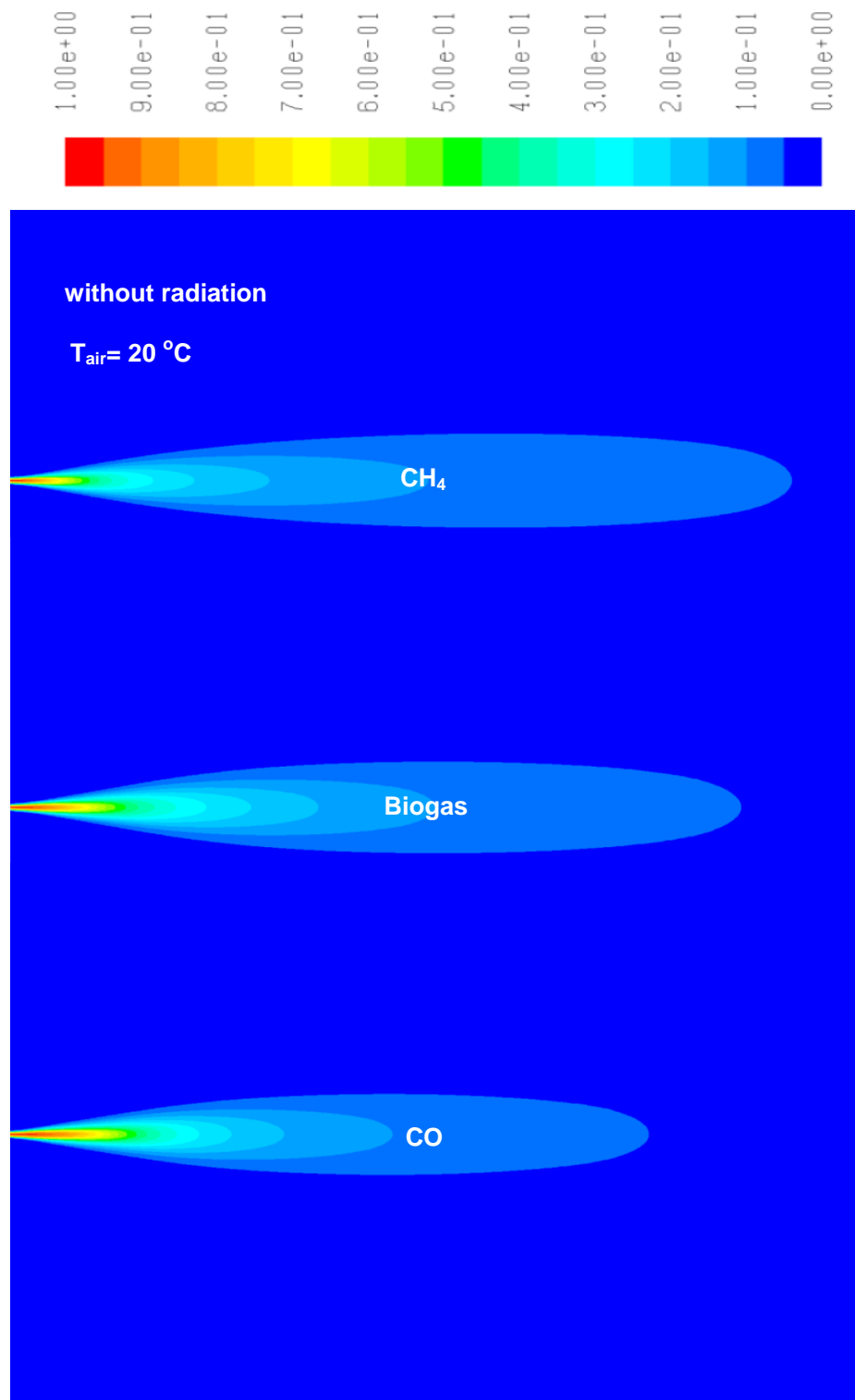
Figure 4.23: Comparison of free jet flame mixture fraction contours for CH_4, $Biogas$ and CO fuels without radiation at T_o=20°C, u_o= 100 (m/s).
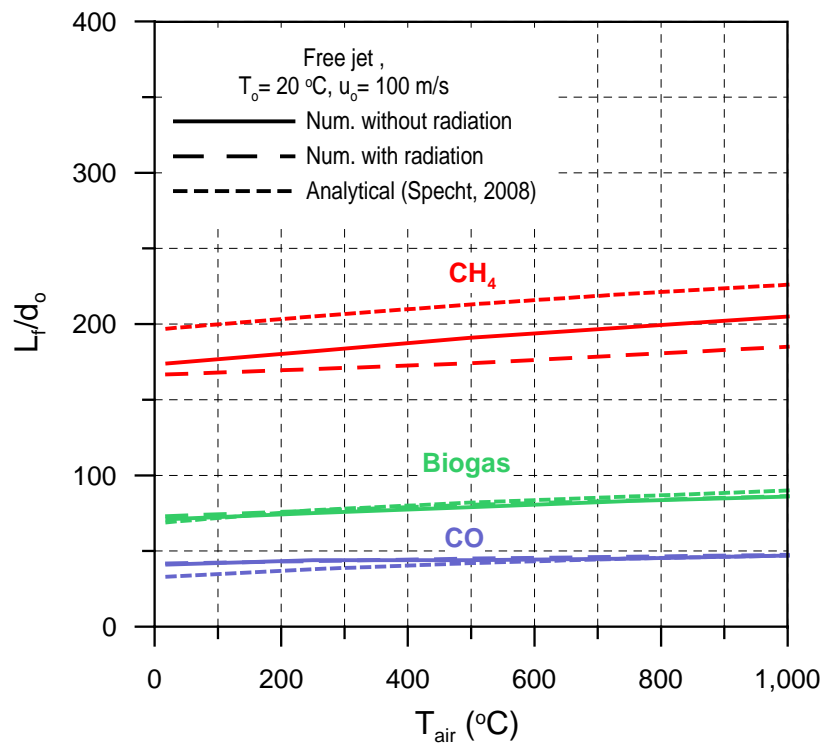
Figure 4.24: Influence of air temperature on the flame length for CH_4, $Biogas$ and CO fuels.
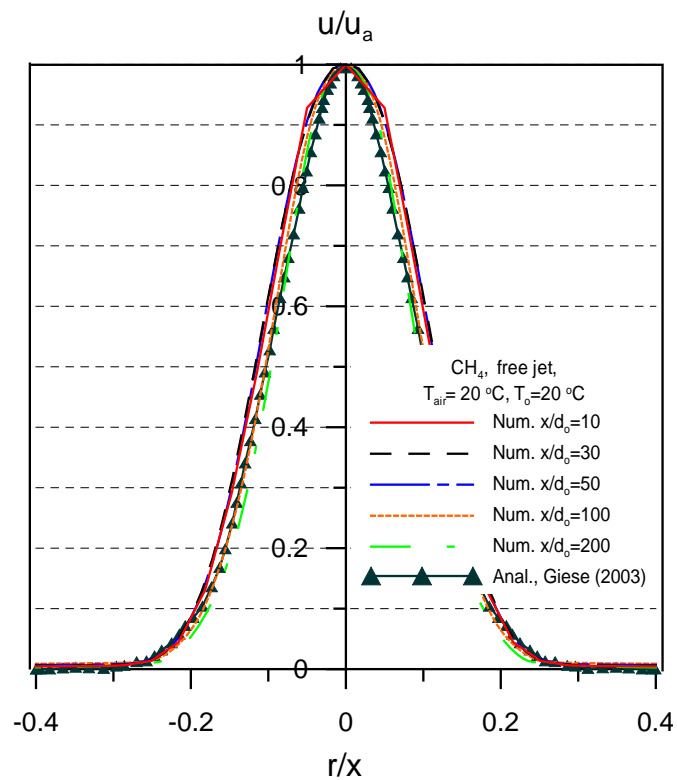
Figure 4.25: Comparison of numerical and analytical radial dimensionless velocity profiles for CH_4 fuel at T_{air}=20°C, u_o= 100 (m/s).
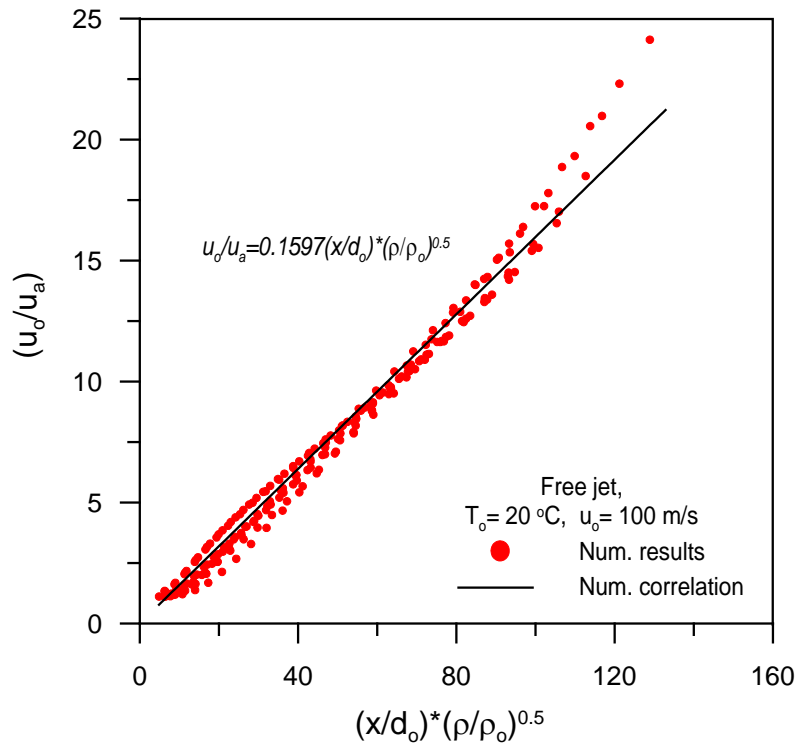
Figure 4.26: Prediction of inverted dimensionless axial velocity correlation for free jet - CH_4, $Biogas$, CO fuels without radiation.

Another flame length correlation was correlated for a wide range of air temperature. The flame length in dimensionless form as a function in stoichiometric mean mixture fraction, fuel density, and stoichiometric density (density of combustion gas at stoichiometric mixture fraction) can be correlated from the computed results of the present study using regression analysis as follows:

$$\frac{L_f}{d_o} = \frac{4.8}{f_{st}} \left(\frac{\rho_o}{\rho_{st}} \right)^{1/2} \qquad (4.3)$$

Equation 4.3 is valid for data in the following ranges: $0.055 \leq f_{st} \leq 2.89$; $20°C \leq T_{air} \leq 1000°C$; and $T_o = 20°C$. The prediction of this correlation is shown in Fig. 4.28, the correlation can predict 100 % of the numerical results within error ± 9.5 %. As an approximation for the flame length Eqn. 4.3, we can set the molecular weight at stoichiometric mixture equals to that of Nitrogen [29], thereby estimating the density ratio ρ_o/ρ_{st} from

$$\frac{\rho_o}{\rho_{st}} = \frac{M_o}{M_{N_2}} \frac{T_{st}}{T_o} \qquad (4.4)$$

Here T_{st} is the combustion gas temperature at stoichiometric mixture, so it is assumed the maximum flame temperature. Where, T_{st} equals 2061 K, 1825 K and 2217 K for CH_4, $Biogas$ and CO, respectively at $T_{air} = 20°C$ and $T_o = 20°C$. The maximum deviation obtained between numerical correlation 4.3 and its approximation using Eqn. 4.4 is ± 8 %.
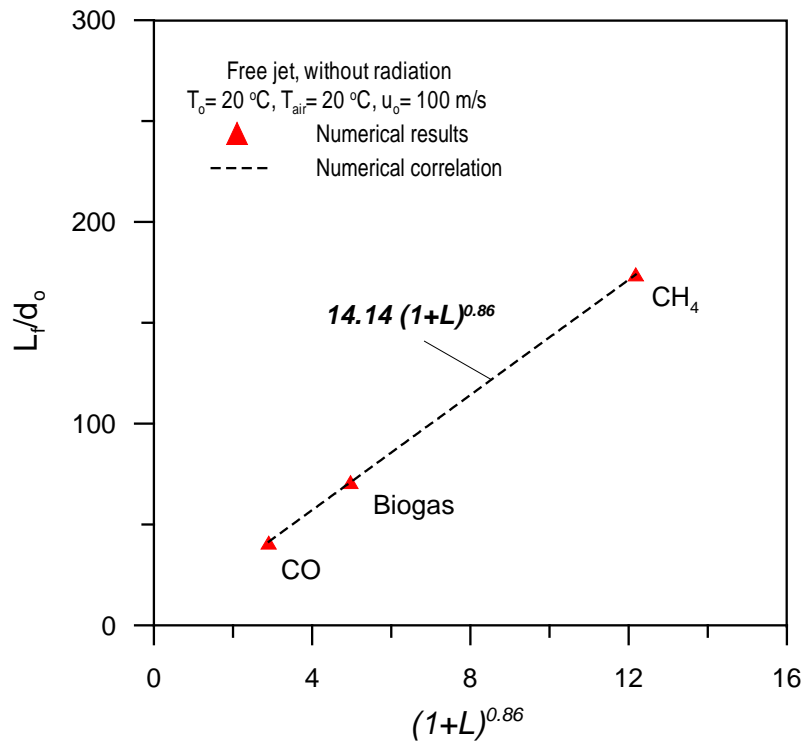
Figure 4.27: Prediction of dimensionless free jet flame length correlation in terms of stoichiometric air demand (L) at $T_{air} = 20°C$.
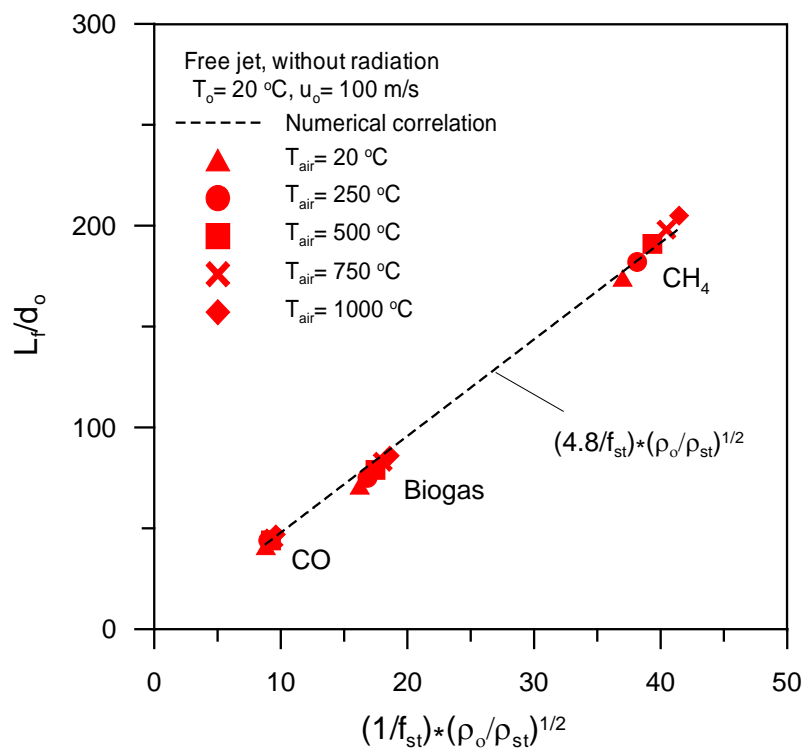
Figure 4.28: Prediction of dimensionless free jet flame length correlation in terms ρ_o, ρ_{st}, and f_{st}.

4.1.7 Comparisons with literature

Comparison between experimental correlation reported by Hawthorne et al., [21] and present numerical correlation (Eqn. 4.3) is presented in Fig. 4.29. As shown in the figure the experimental flame length values are larger than the simulated values, but no significant differences are observed. This is because of the difference of definitions of the flame length for both simulated and measured values (refer to section 2.1). Also the difference between experimental and computed results owing to inherent simplifying assumptions in the turbulence and combustion models and due to experimental measurements uncertainty. The maximum deviation observed between experimental correlation (Hawthorne et al., 1949) and numerical correlation (Eqn. 4.3) is $\pm 9.4\%$.
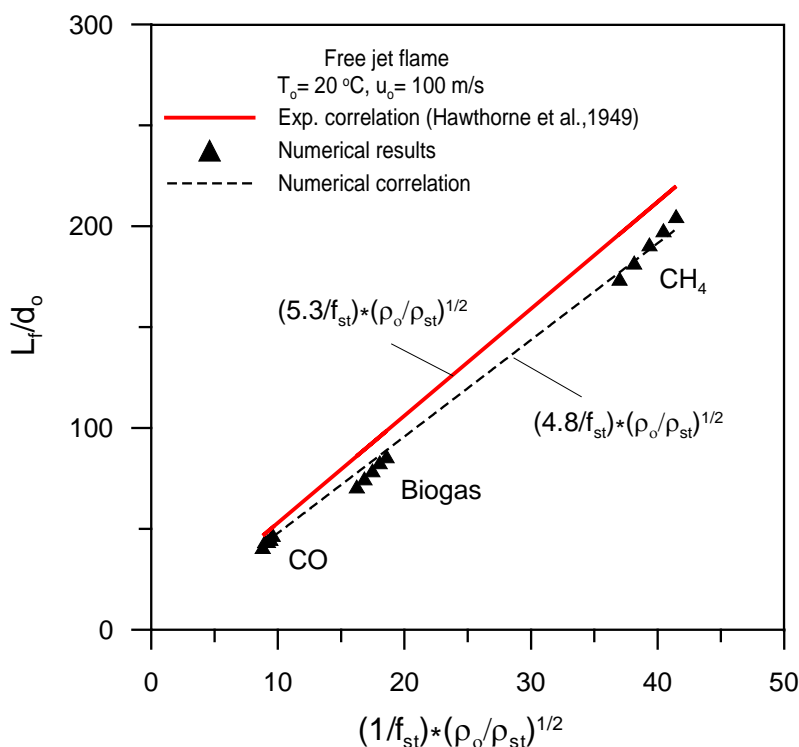
Figure 4.29: Comparison between experimental correlation presented by Hawthorne et al. [21] and numerical dimensionless free jet flame length correlation.

4.2 Annulus tube burner

Most of industrial burners are concentric type burners (i.e., annulus type) are used for flame stability. Therefore it is important to study like this burner geometry on the flame behavior especially, the annulus diameter. In this section the influence of annulus diameter on the flame temperature and flame length will be presented and discussed. Annulus tube burner with constant fuel nozzle diameter of 50 mm, and different annulus diameters in dimensionless form (3.7, 5.1, 7.4, 10.6, 15.9 and 31.1) were proposed to study (see Fig. 4.30). In this section only Methane fuel was simulated at 30 m/s fuel velocity, 20°C fuel temperature, and 20°C air temperature. The primary excess air number (λ_p) is constant and equals 1.1 and the radiation effect wasn't considerd in this section.
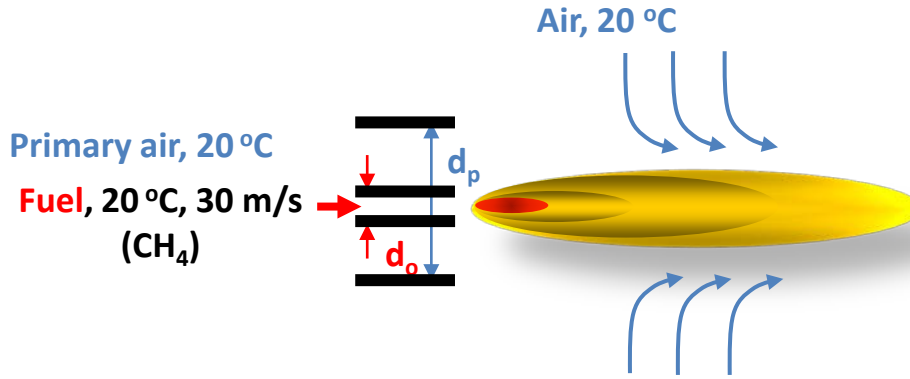
Figure 4.30: Schematic diagram of annulus tube burner configuration.

4.2.1　Effects of annulus diameter

The effects of annulus diameter on centerline axial temperature profiles, inverted dimensionless axial mean mixture fraction profiles, temperature contours, and mean mixture fraction contours are shown in Figs. (4.31, 4.33 and 4.32). The relation between flame length in dimensionless form with annulus diameter and annulus velocity in dimensionless shape were illustrated in Figs. (4.34 and 4.35). In this case, *Methane* gas was used for the flame simulation at 30 m/s fuel velocity, 20°C fuel temperature, 20°C air temperature and primary excess air number (λ_p) is constant and equals 1.1. The primary air to fuel velocity ratio (u_p/u_o) changes from 0.829 to 0.011 according to variation of d_p/d_o, which varied from 3.7 to 31.1 (see Table.4.1). The radiation model (P1) wasn't considered in this part.

Table 4.1: primary air to fuel velocity ratio at different annulus diameters

d_p/d_o	u_p/u_o
3.7	0.829
5.1	0.415
7.4	0.196
10.6	0.094
15.9	0.042
31.1	0.011

Figure 4.31 displays the variation of centerline axial temperature profile along the flame axis with different annulus diameter as a parameter, compared with simple tube burner (see section 4.1). As shown in the Figure, the axial temperature distribution a long the flame increases with increasing the annulus diameter . Also the temperature profile shifted up and close to simple tube burner case with increasing the annulus diameter. Whereas, the temperature profile has approximately the same temperature profile of simple tube burner case at $d_p/d_o = 31.1$. Also the peak flame temperature increases by ∼30 % and shifted to right by ∼270 % with the increase of annulus diameter from 3.7 to 31.1. This is because increasing the annulus diameter increases the interface area between combustion air and fuel (i.e., bigger reaction zone). Increasing the mixing area increases the flame volume, and consequently increases the flame temperature. On the
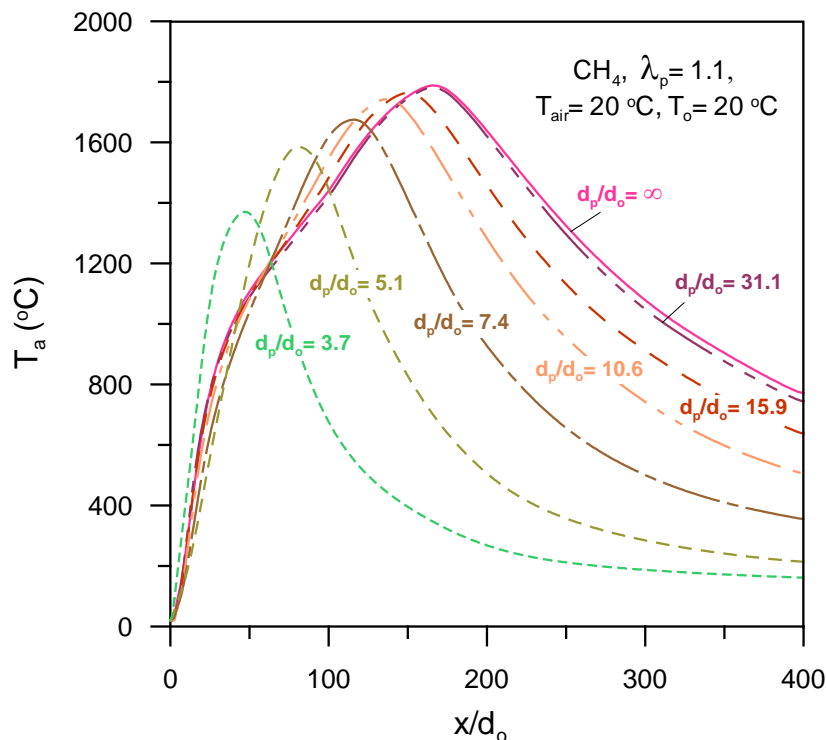
Figure 4.31: Influence of annulus diameter on axial temperature distribution along the flame for Methane fuel (CH_4).

other hand, reducing the annulus diameter increases the annulus air velocity. Increasing the annulus air velocity improves the mixing between air and fuel, so the combustion process completes in short distance from the burner tip, which results in a decrease in flame volume and in consequence the peak flame temperature closes to the burner tip (see Fig. 4.32).

The influence of annulus diameter on the inverted dimensionless axial mean mixture fraction profiles to determine the flame length was presented in Fig. 4.33. As shown in the Figure, the annulus diameter has a significant effect on the mixture fraction profiles and consequently on the flame length, where the flame length increases by ~270 % with the increase of annulus diameter from 3.7 to 31.1. Also as shown in the Figure the mixture fraction profile converges to the simple burner case with increasing the annulus diameter and has approximately the same profiles at $d_p/d_o = 31.1$ (i.e., the same flame length). The results show that the smaller the annulus diameter, the shorter the flame. As we discussed above the small annulus diameter leads to high annulus air velocity which improve the mixing between fuel and air and complete the combustion in short distance. The final result is the flame length increases with the increase of annulus diameter.

The final computed results of flame length in dimensionless form versus dimensionless annulus diameter and dimensionless annulus air velocity were prepared and presented in Figs. 4.34 and 4.35, respectively. As shown in the Figures the flame length is direct proportional with the annulus diameter and reverse proportional with annulus air velocity. Both of them were discussed above.
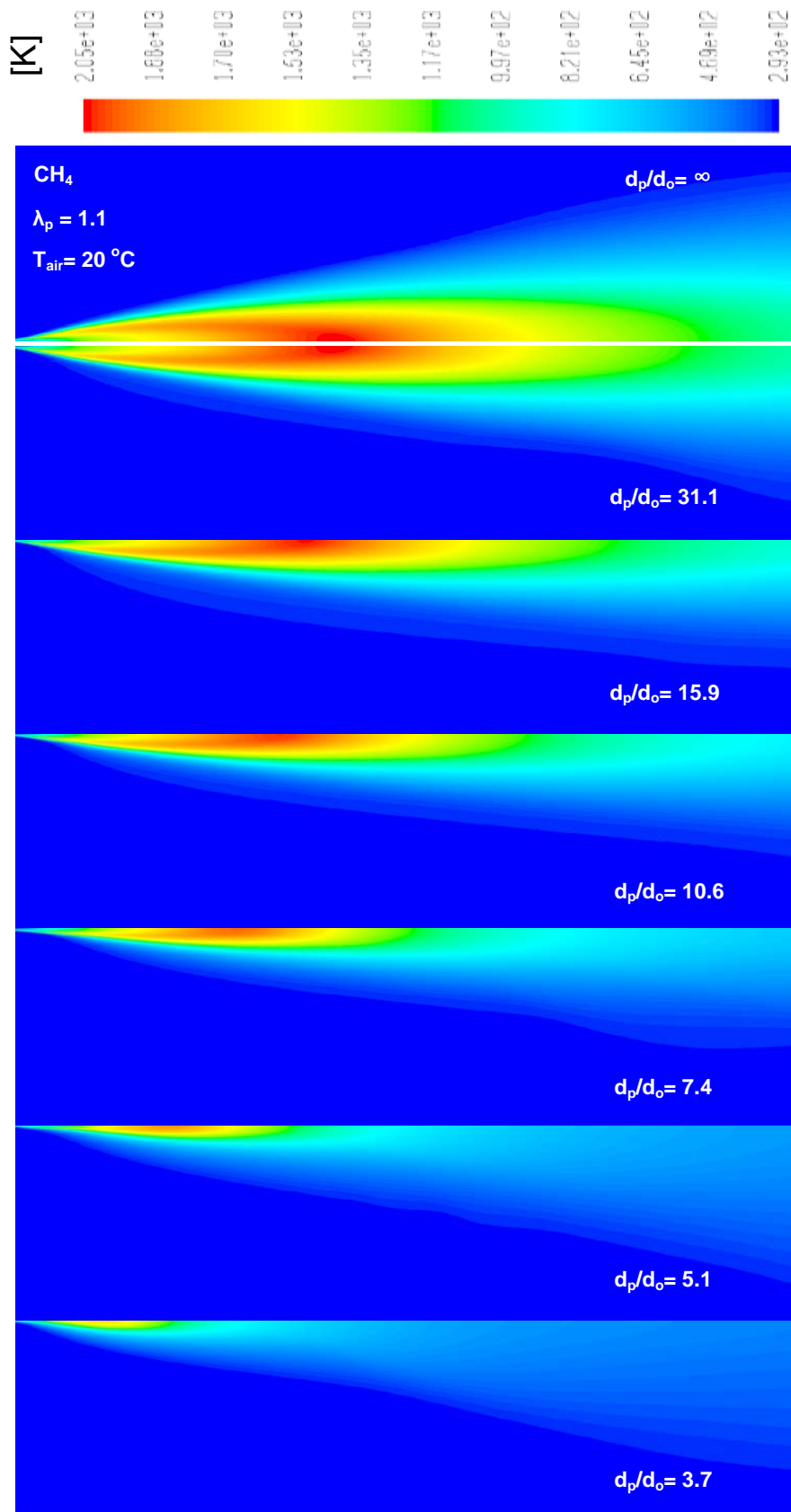
Figure 4.32: Influence of annulus diameter on temperature contours for Methane fuel (CH_4).
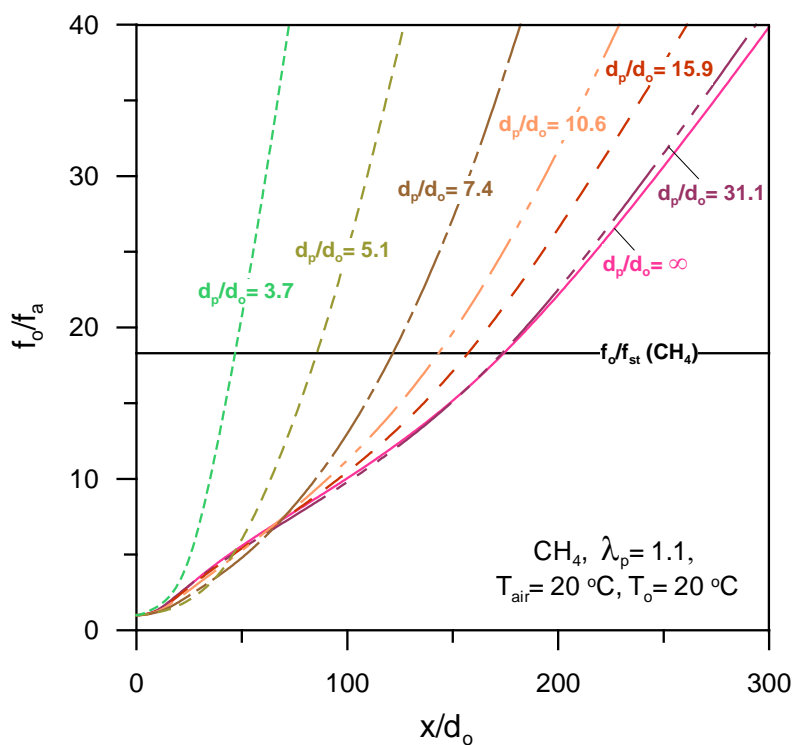
Figure 4.33: Influence of annulus diameter on inverted dimensionless axial mixture fraction profiles along the flame for Methane fuel (CH_4).
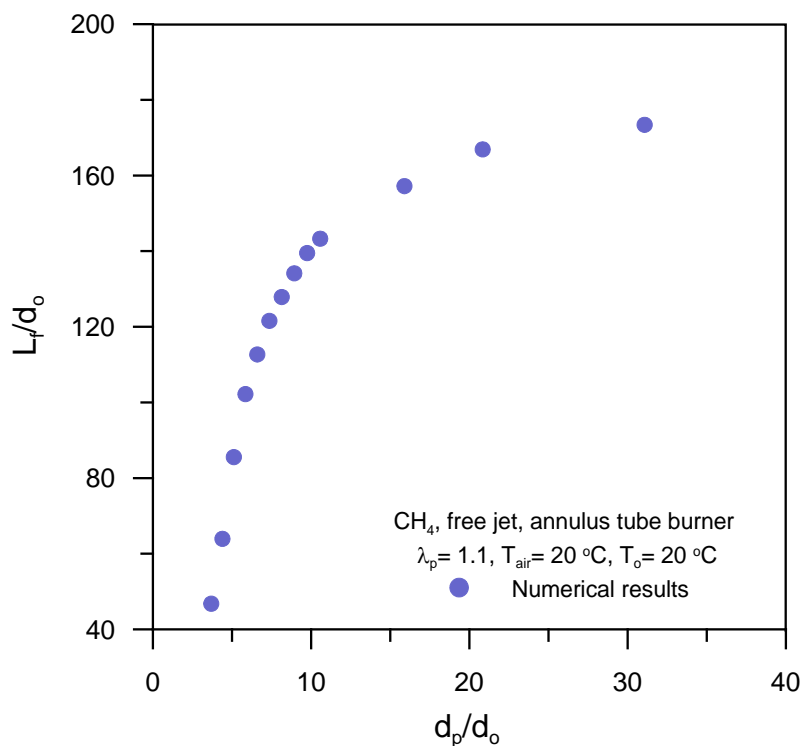
Figure 4.34: Influence of annulus diameter on flame length for Methane fuel (CH_4).
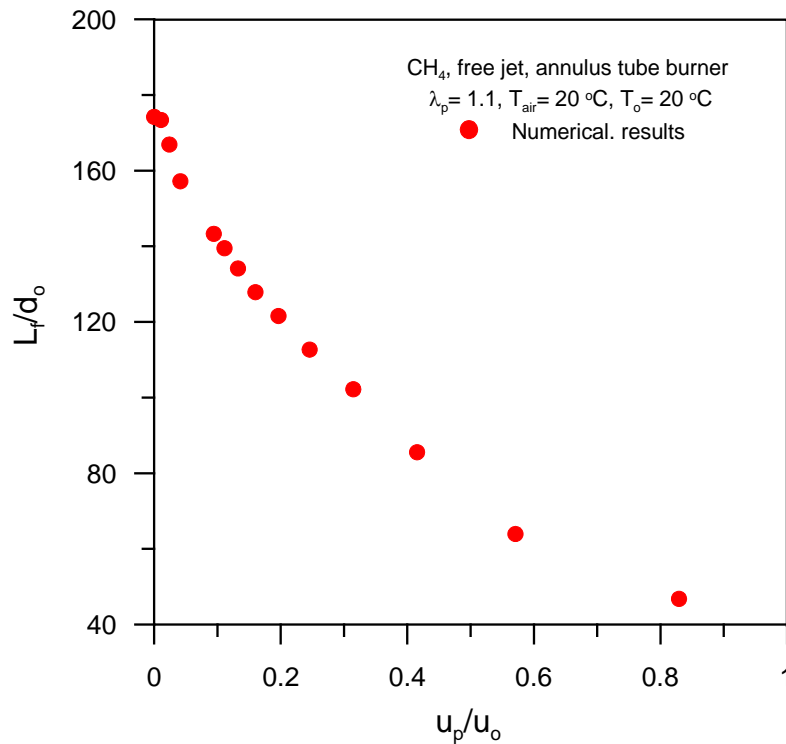
Figure 4.35: Influence of dimensionless annulus velocity ratio on flame length for Methane fuel (CH_4).

4.3 Wall-supported annulus tube burner

In practice most of industrial burners were supported by walls. Therefore annulus tube burner with constant fuel nozzle diameter of 50 mm, and different annulus diameters in dimensionless form (7.4, 10.6, and 31.1) was modified by supported wall and presented here in this section to study (see Fig. 4.36). In this section, only Methane fuel was simulated at 30 m/s fuel velocity, 20°C fuel temperature, and 20°C air temperature. Two proposed values for primary excess air number (λ_p) are 1.1 and 1.3, the radiation effect wasn't considered in this section. The annulus air swirl number was changed and simulated (S_n= 0, 0.3, 0.5, 0.7, 1, 1.6 and 2.3).
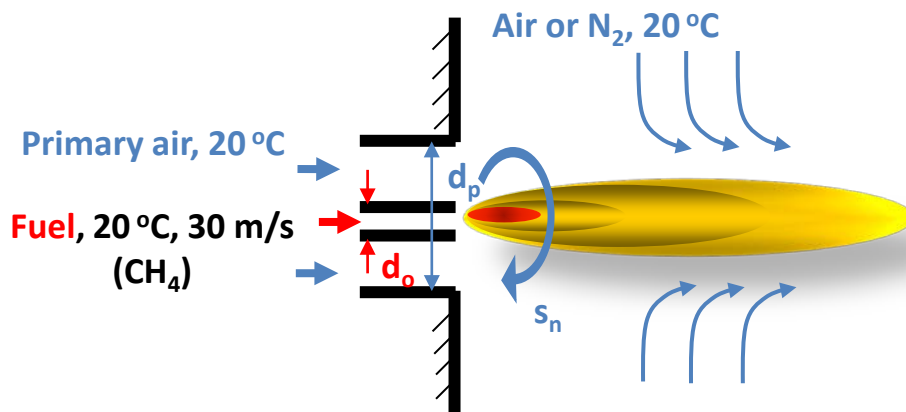
Figure 4.36: Schematic diagram of wall supported annulus tube burner.

4.3.1 Influence of supported wall

Figs. 4.37 and 4.38 show the effects of supported wall at different annulus diameters in dimensionless form (d_p/d_o = 7.4, 15.9, and 31.1) on the centerline axial temperature profiles and inverted dimensionless axial mean mixture fraction profiles, respectively. As shown in the Figures, the supported wall hasn't approximately effect on the temperature profiles along the flame and flame length. This effect is the same for any annulus diameter.
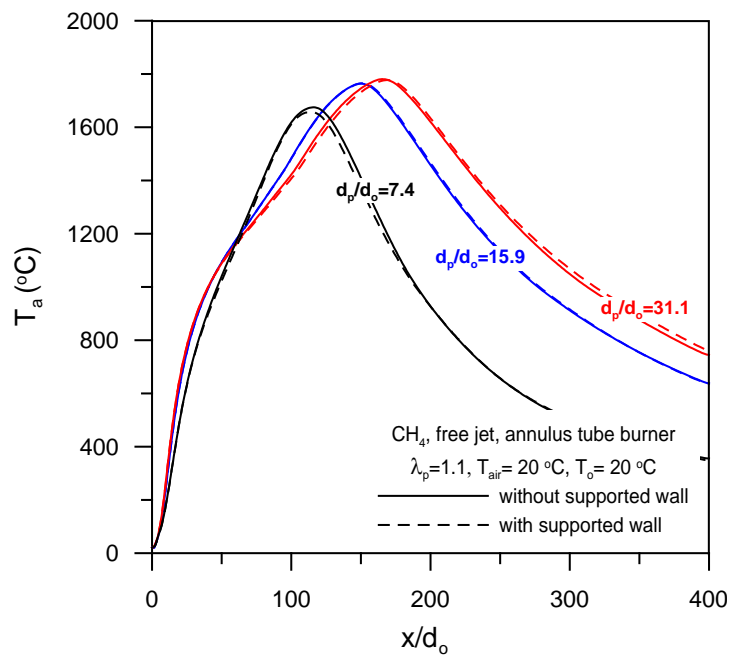
Figure 4.37: Influence of supported wall on the axial flame temperature profiles.
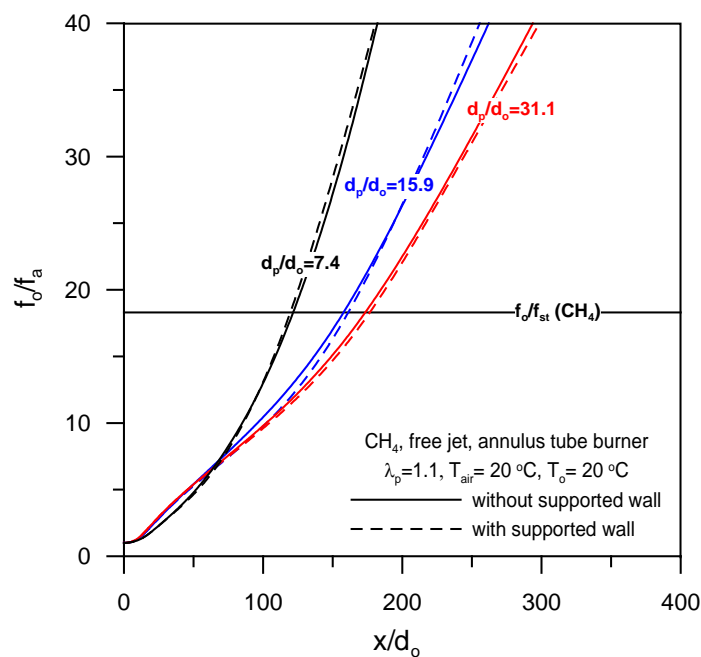
Figure 4.38: Influence of supported wall on the inverted dimensionless mixture fraction profiles.

4.3.2 Effects of N_2 as a recycled gas

Low combustion temperatures, short retention time at high temperature, and low Oxygen concentration are important conditions to reduce the NO formation (Specht [101]). Flue gas recirculation is one from the important methods to restrict the formation of NO_x from combustion. The flue gas recirculation decreases the temperature of the flame and reduces the O_2 concentration in the supplied combustion air. Therefore, the influence of N_2 as a recycled gas (see Fig. 4.36) on the axial flame temperature, temperature contours, axial mean mixture fraction, velocity vectors colored by temperature were performed and presented in Figs. $(4.39 - 4.42)$. The last but not the least, a comparison between Air and N_2 as a surrounding gases around the flame was conducted and presented in Figs. $(4.43, 4.44, \text{ and } 4.45)$.

Figures. $(4.39 \text{ and } 4.41)$ show the temperature profiles and temperature contours, respectively for different annulus diameters (d_p/d_o= 7.4, 10.6 and 31.1) at Nitrogen temperature of 20°C and primary excess air number (λ_p) equals 1.1. As shown in Fig. 4.39, the axial temperature profile shifted up and the peak flame temperature increases by ∼45 % with the increase of annulus diameter from 7.4 to 31.1. Also as depicted in Fig. 4.41 the flame volume and the area of high temperature zones increases with increasing annulus diameter, for more details refer to Section 4.2. On the same manner, Figs. $(4.40 \text{ and } 4.42)$ display the inverted axial mean mixture fraction profiles to determine the flame length and velocity vectors colored by temperature, respectively for different annulus diameters (d_p/d_o= 7.4, 10.6, and 31.1) at Nitrogen temperature of 20°C. From the Figures and as described in previous section, the flame length increases with the increase of the annulus diameter, vice versa. The reasons were discussed in details in section 4.2. As it is observed in Fig. 4.40, the flame length increases by ∼86 % with the increase of annulus diameter from 7.4 to 31.1.

A comparison of N_2 and Air as a surrounding gases around the flame was performed and presented in Figs.$(4.43 - 4.45)$. Figs. 4.43 and 4.44 present the temperature profiles and temperature contours, respectively for Air and Nitrogen as a surrounding gases around the flame. The comparison was performed at Nitrogen temperature of 20°C and primary excess air number (λ_p) equals 1.1 and d_p/d_o=7.4. As depicted in Fig. 4.43, the axial temperature distribution in case of Air is higher than that in case of Nitrogen, and the peak flame temperature in case of Air much higher than of Nitrogen by ∼45 % and shifted to right by ∼30 %. This can be attributed to the N_2 reduces the Oxygen concentration in combustion air. The reduction in Oxygen concentration in combustion air reduces the combustion gas temperature, and consequently the flame temperature profiles and peak flame temperature drops. Vice versa in case of using Air as a surrounding gas. The temperature contours for both cases (i.e., Air and Nitrogen) were depicted in Fig. 4.44, as shown in the Figure, the greater flame volume and higher temperature zone area are related with the Air case. On the same way,

Fig. 4.45 shows the influence of Nitrogen on the flame length compared with Air as surrounding gases. As shown in the Figure, the flame length in case of Air is longer than that in case of Nitrogen by ∼30 %. This is because, in case of Air, the reaction zone and interface area between diffused air and fuel is bigger, so the combustion completed in long distance from the burner tip, vice verse in case of Nitrogen.
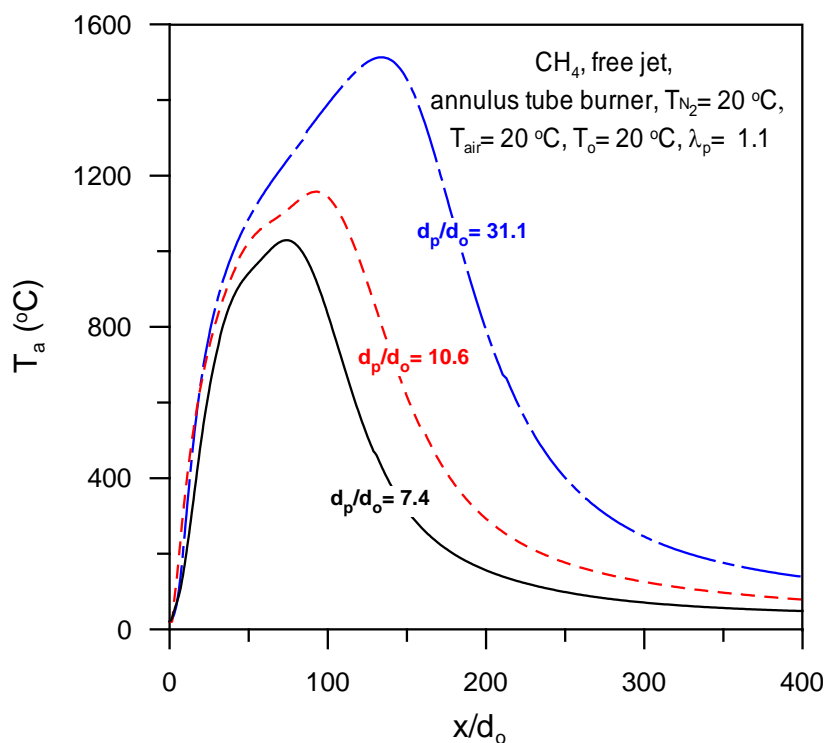
Figure 4.39: Influence of dimensionless annulus diameter ratio on axial flame temperature for Methane fuel (CH_4).
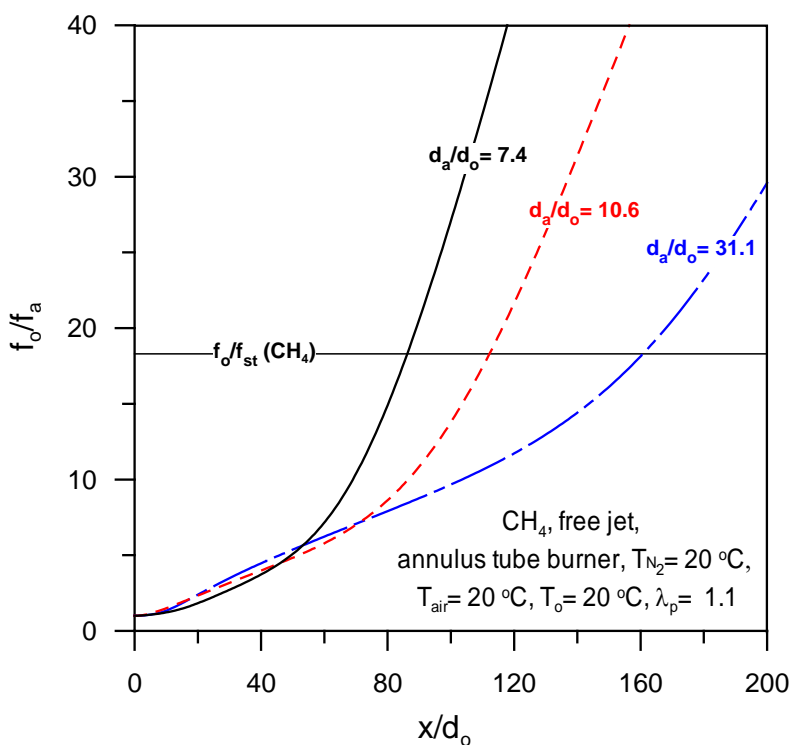
Figure 4.40: Influence of dimensionless annulus diameter ratio on axial mixture fraction profiles for Methane fuel (CH_4) using N_2 as recycled gas.
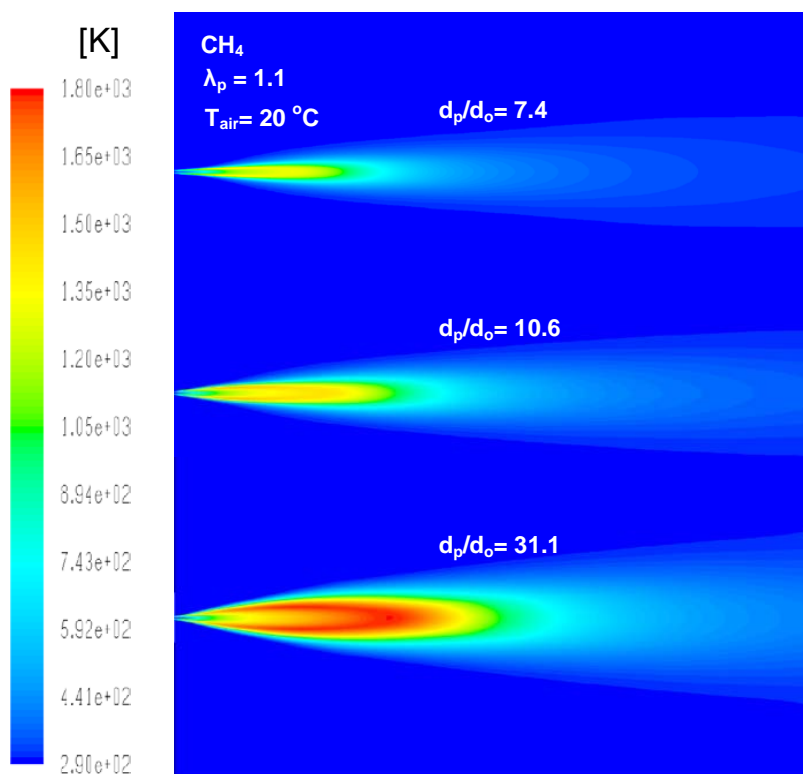
Figure 4.41: Influence of dimensionless annulus diameter ratio on temperature contours for Methane fuel (CH_4) using N_2 as recycled gas.
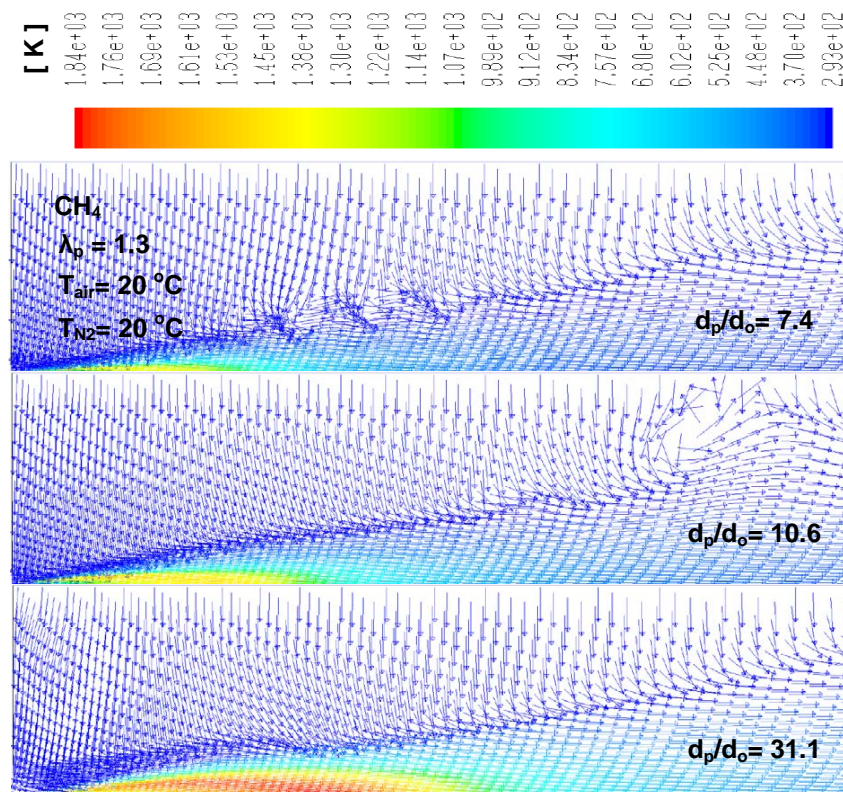
Figure 4.42: Influence of dimensionless annulus diameter ratio on velocity vectors colored by temperature for Methane fuel (CH_4) using N_2 as recycled gas.
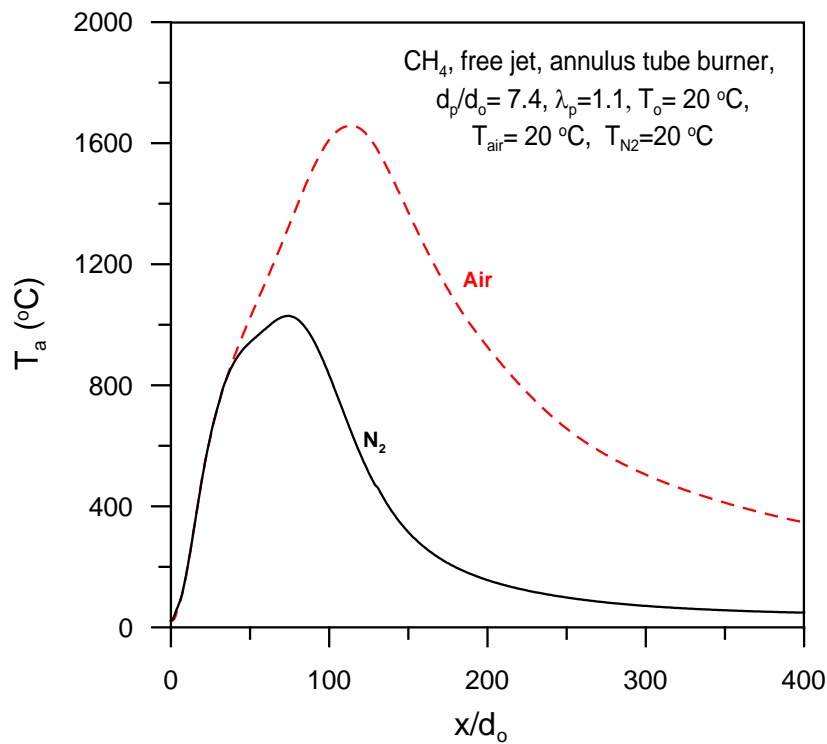
Figure 4.43: Comparison of Air and Nitrogen injection as a recycled gas on axial flame temperature profiles for Methane fuel (CH_4).
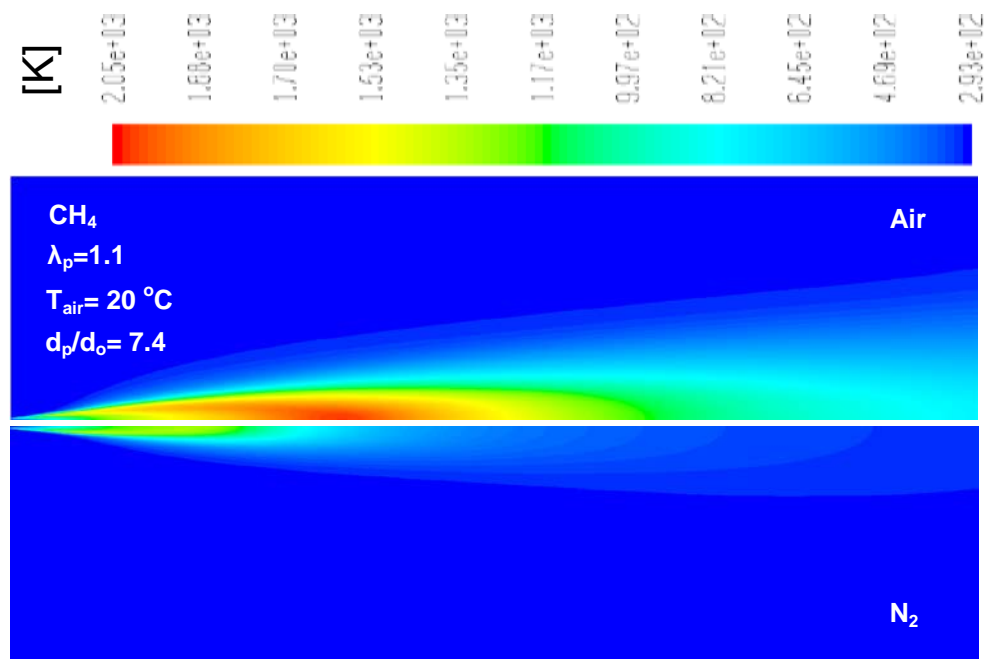
Figure 4.44: Comparison of Air and Nitrogen injection as a recycled gas on temperature contours for Methane fuel (CH_4).
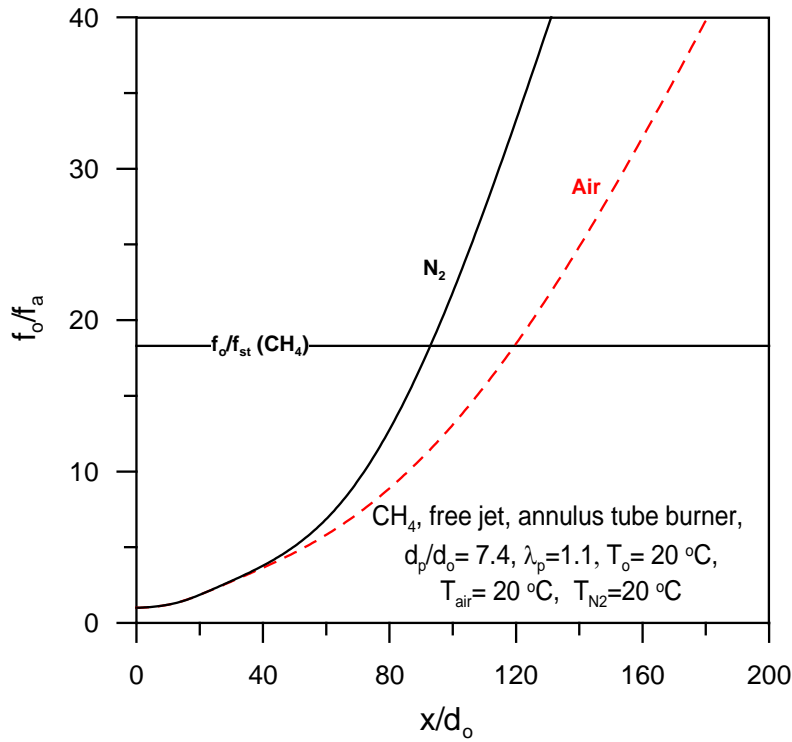
Figure 4.45: Comparison of Air and Nitrogen injection as a recycled gas on axial mixture fraction profiles for Methane fuel (CH_4).

4.3.3   Effects of annulus air swirl number

The burner swirl has a significant effect on the flame shape and consequently has an impact on the heat flux distribution from the flame. The flame stability is a very important aspect of the burner, the flame stability is enhanced by controlling the inlet swirl number. Swirl number (S_n) can be computed based on the ratio of angular momentum to the axial momentum. An equation for swirl number was presented by [102] as follows:

$$S_n = \frac{\int_0^r (wr)\rho u 2\pi r dr}{r \int_0^r u\rho u 2\pi r dr} \tag{4.5}$$

where, $w=$ tangential velocity, $u=$ axial velocity, $\rho=$ fluid density, and $r=$ burner radius.

As discussed, the swirl number can have a significant effect on the flame behavior and the approximate rules applicable for gas burners were presented by [102] as follows: $S_n{\sim}0.3$ (Moderate swirl), $S_n{>}0.6$ (Considerable swirl), $S_n{>}1$ (High swirl), and $S_n{>}2$ (Very high swirl). From the above discussion, the swirl is very important parameter affects the flame characteristics, so the influence of swirl number S_n ranges from 0 to 2.3 on the axial temperature profiles, inverted dimensionless axial mean mixture fraction profiles, temperature contours, velocity vectors colored by temperature and flame length are explained in Figs. $(4.46 - 4.48)$. In this case, *Methane* gas was used for the flame simulation at 30 m/s fuel velocity, 20°C fuel temperature, 20°C air temperature and primary excess air number (λ_p) is constant and equals 1.1, and d_p/d_o also constant and equals 7.4. The radiation model (P1) wasn't consider in this part.

Figure 4.46 shows the variation of centerline axial temperature profiles along the flame axis with different annulus air swirl number as a parameter, compared with the reference case; without swirl (i.e., $S_n = 0$). As observed in the Figure, the peak flame temperature shifted to right by $\sim 120\%$ and increased by $\sim 8\%$ with increasing the swirl number from 0 to 2.3. After the length of $X/d_o \approx 260$, it was observed that the temperature profile of combustion gas is slightly shifted up with the swirl number until $S_n = 0.7$ and other than it was strongly shifted up. This can be attributed to the increase of interface area between diffused air and fuel, hence this increases the reaction zone area with increasing the swirl number for open flame (i.e., free jet flame). As a result in, the flame volume and high temperature zone area increase with increasing the swirl number (see Fig. 4.49).

The influence of annulus air swirl on the inverted dimensionless axial mean mixture fraction profiles and velocity vectors colored by temperature, to estimate the effect of swirl on the flame length, was explained in Figs. 4.47 and 4.50, respectively. As presented in the Figures, the annulus air swirl number has a considerable effect on the mixture fraction profiles and consequently the flame shape (i.e., flame length). The results show that the flame length increases by $\sim 120\%$ with increasing the swirl number from 0 to 2.3. This is because, the increase of the swirl on the free jet flame reduces the diffused air to reach the fuel, hence the combustion can't complete in small length and volume, so that the flame must be dispersed to complete the reaction. The final result is an increase of the flame length with increasing the swirl number. The computed results of the flame lengths against the annulus air swirl number were presented in Fig. 4.48.
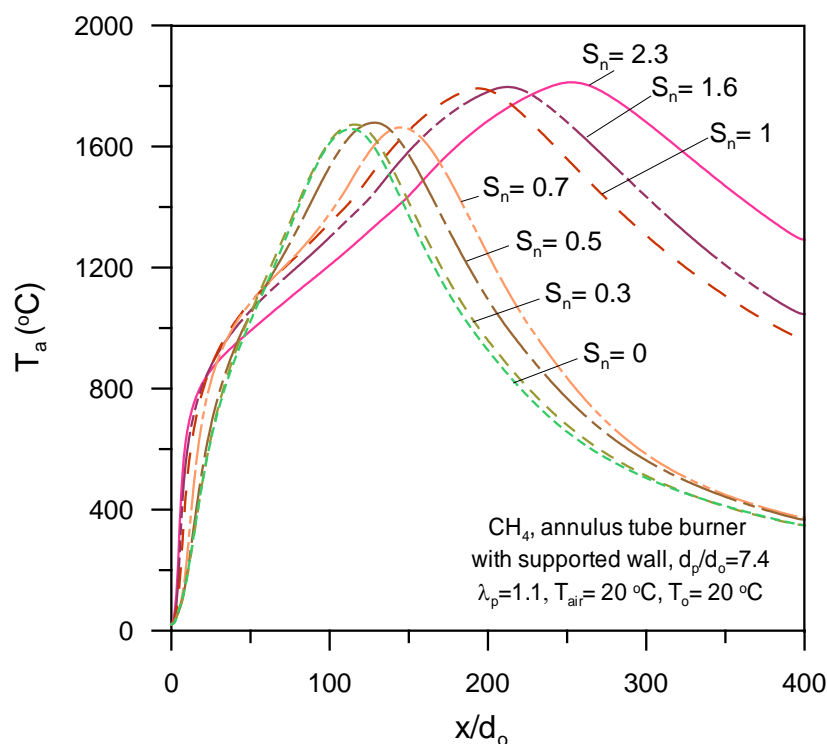
Figure 4.46: Influence of annulus air swirl number on axial flame temperature profiles for Methane fuel (CH_4).
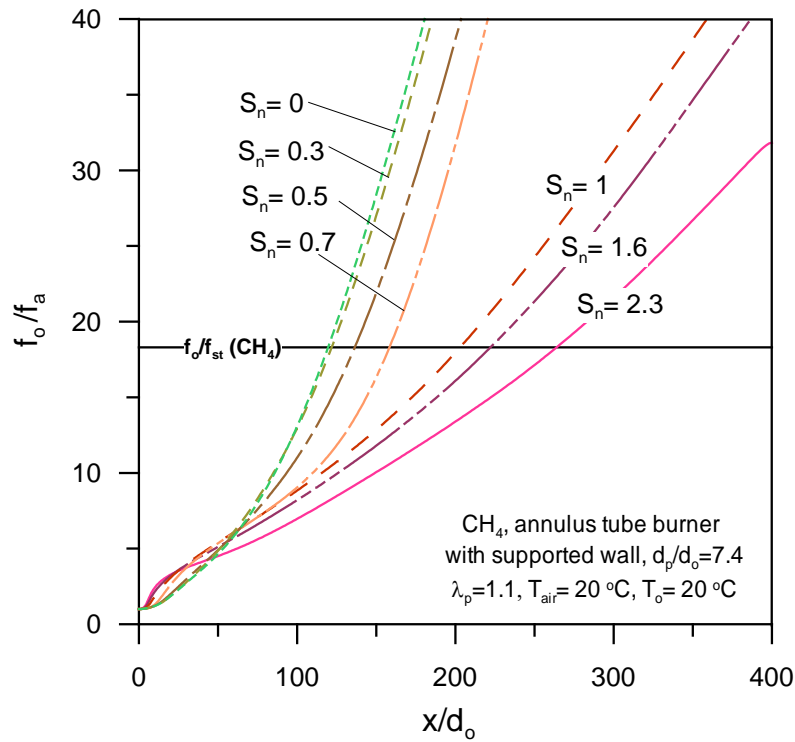
Figure 4.47: Influence of annulus air swirl number on axial mixture fraction profiles for Methane fuel (CH_4).
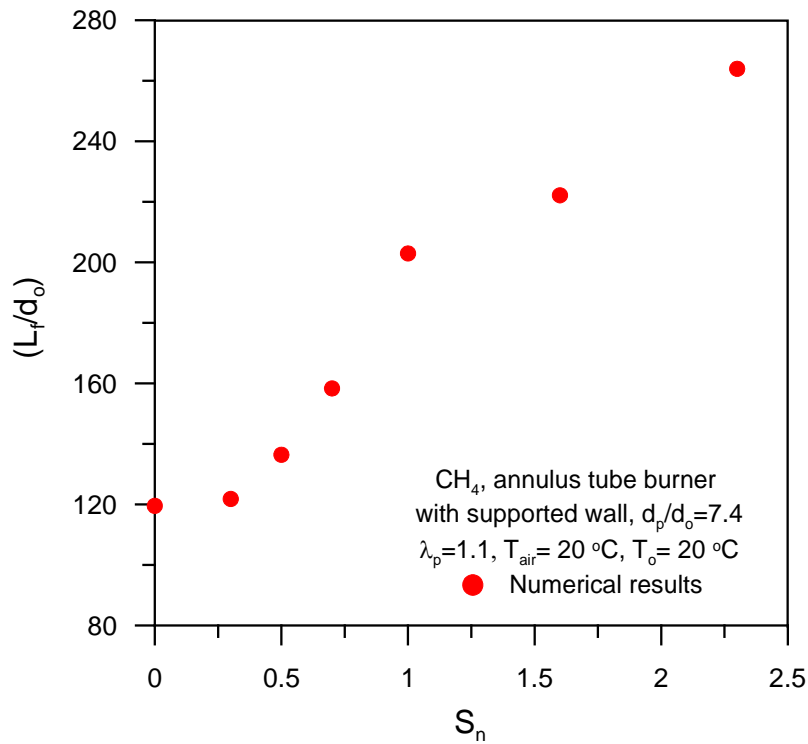
Figure 4.48: Influence of annulus air swirl number on the flame length for Methane fuel (CH_4).
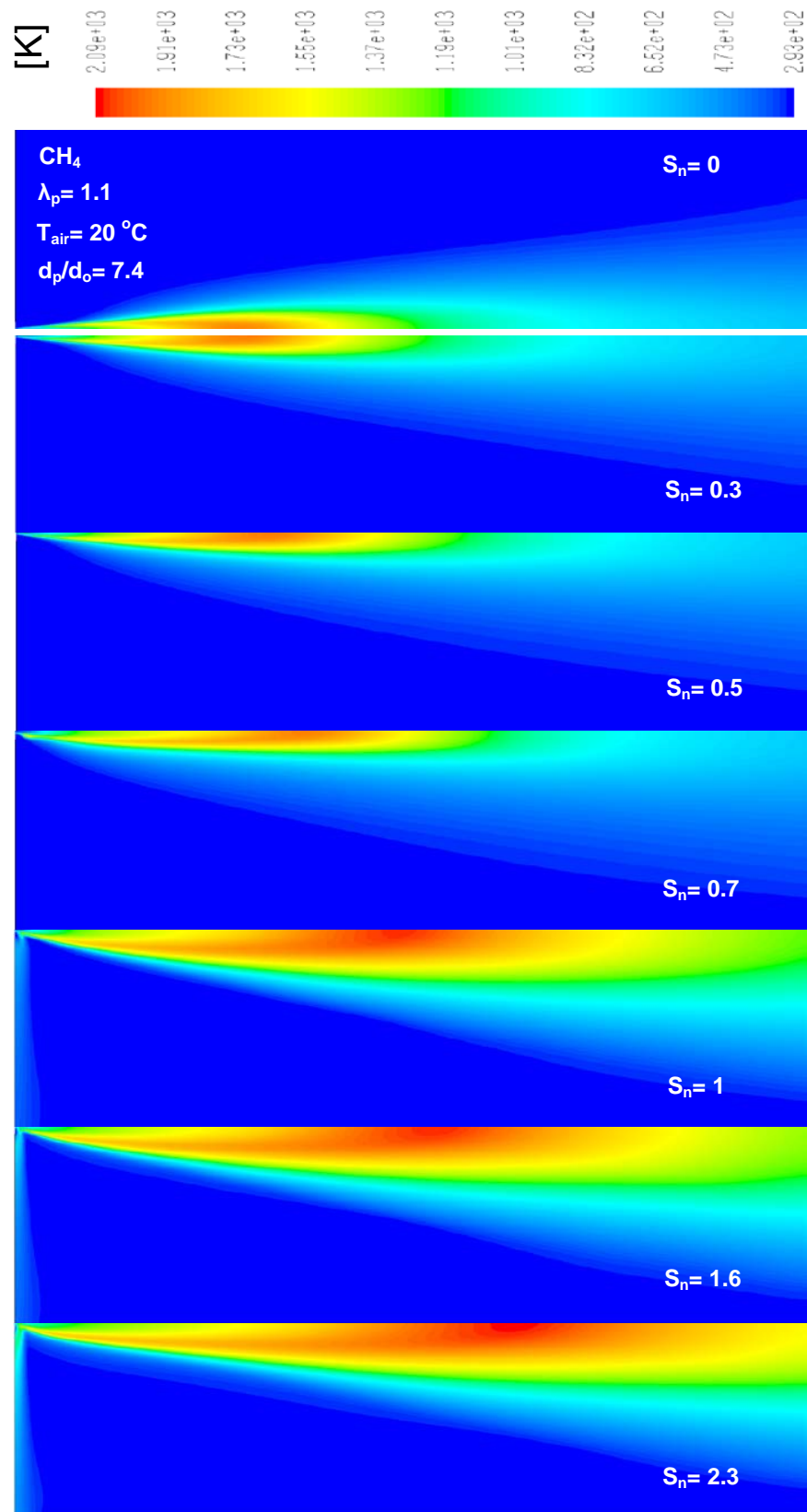
Figure 4.49: Influence of annulus air swirl number on flame temperature contours for Methane fuel (CH_4).
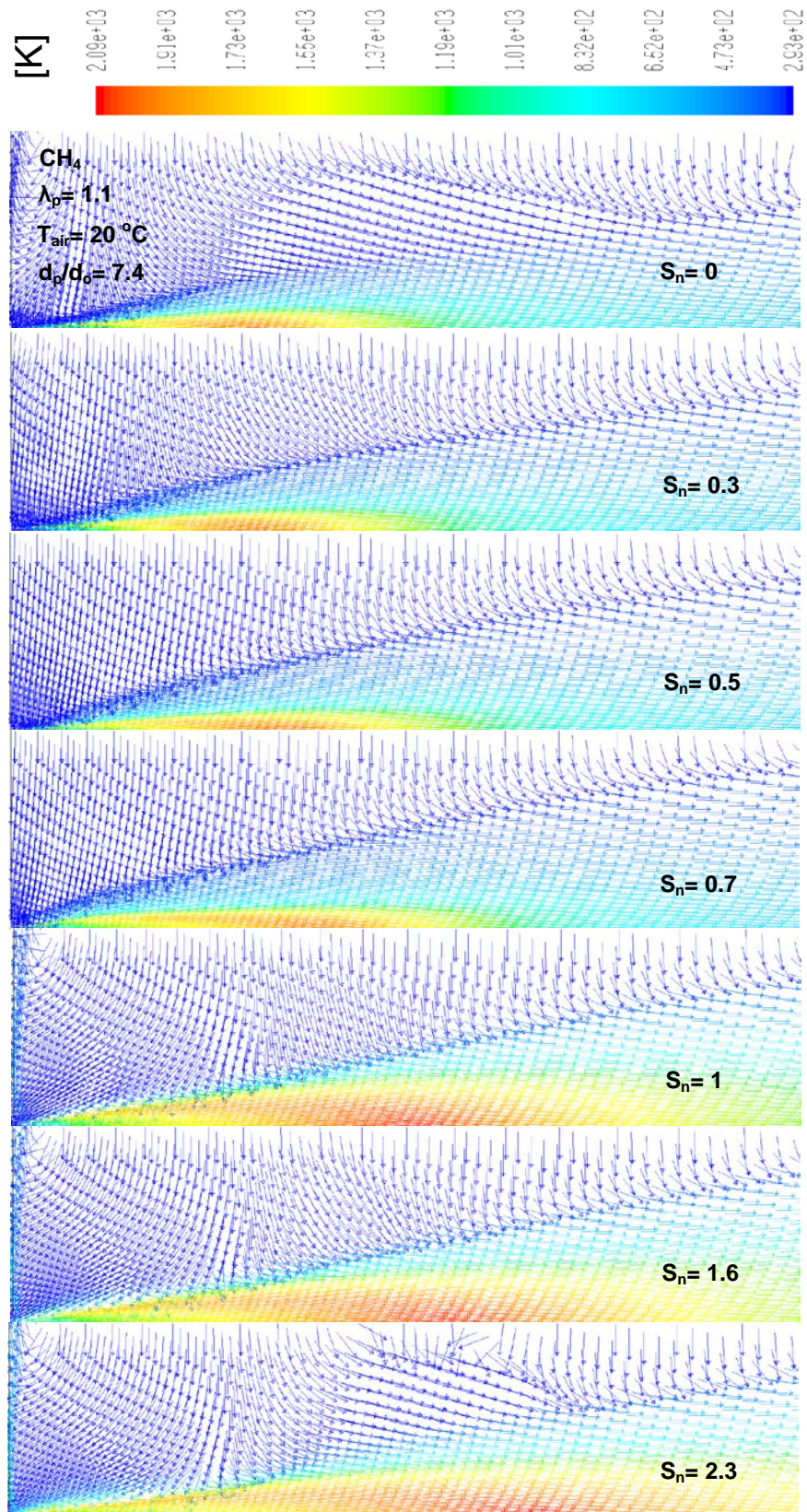
Figure 4.50: Influence of annulus air swirl number on velocity vectors colored by temperature for Methane fuel (CH_4).

Chapter 5

2D-Confined Jet Flame Simulation: Results and Discussions

Confined jets may differ from free jets for three reasons; First, the quantity of entrained fluid is limited. In practical combustion systems, it is usually controlled at a value corresponding to the stoichiometric ratio. Second, it is possible for the energy of the entrained air to contribute to mixing (e.g. preheat combustion air). And third, the presence of the enclosing walls of the mixing chambers limits the expansion of the jet and my give a rise to recirculation or back flow [103]. Figure 5.1 shows the velocity mass flow profiles in enclosed combustion chamber that have been proposed by Thring and Newby [103]. Thring and Newby proposed mass flow relation for enclosed jet flame as:

$$\frac{\dot{m}(x)}{\dot{m}_o} = 0.32 \frac{x}{d_o} \sqrt{\frac{\rho}{\rho_o}} \tag{5.1}$$

Where at recirculation point x_1:

$$\dot{m}(x) = \dot{m}_o + \dot{m}_1 \tag{5.2}$$

$$\frac{\dot{m}_o + \dot{m}_1}{\dot{m}_o} = 0.32 \frac{x_1}{d_o} \sqrt{\frac{\rho}{\rho_o}} \tag{5.3}$$

The end of mass recirculation is given by equation:

$$x_2 = \frac{D/2}{tan(\alpha/2)} \tag{5.4}$$

Where D is diameter of combustion chamber

This Chapter carried out 2D simulation for confined jet flame in order to understand the flame behavior under different flame confinements and burner configurations. Big cylinder with diameter of 2.6 m and 20 m length was proposed here to simulate the industrial kilns. Three different confinements and burner configurations were suggested to study; simple tube burner with variable air inlet diameter, annulus tube burner with fully opened cylinder for secondary air, annulus tube burner with fully closed cylinder for secondary air (see Fig. 3.9). Therefore, the results of this chapter were divided into three main sections according to the proposed confinements and burner configurations. The results here were used to investigate the effects of burner and flame confinement geometrical parameters and operating parameters on the flame

behavior (i.e., thermal distribution and flow visualization). The effects of excess air number, air inlet diameter, inlet air temperature, radiation, primary air swirl, annulus diameter, secondary air temperature, secondary air velocity profiles and air swirl side (primary air swirl and secondary air swirl) on the thermal distribution and flow visualization of confined jet flame were conducted and discussed here in the following sections.

The Influence of operational and geometrical parameters results were presented and explained in the form of centerline axial velocity profiles, centerline and wall axial temperatures profiles and axial mean mixture fraction profiles to estimate the flame length. In addition to mean mixture fraction and temperature contours were used to visualize the flame. A useful burner and confinement design guidelines and useful design correlations of dimensionless parameters that characterize the flame length were presented and compared with results of free jet flame which obtained from previous Chapter. Also a comparison between present results and previous experimental work was carried out as we see later.
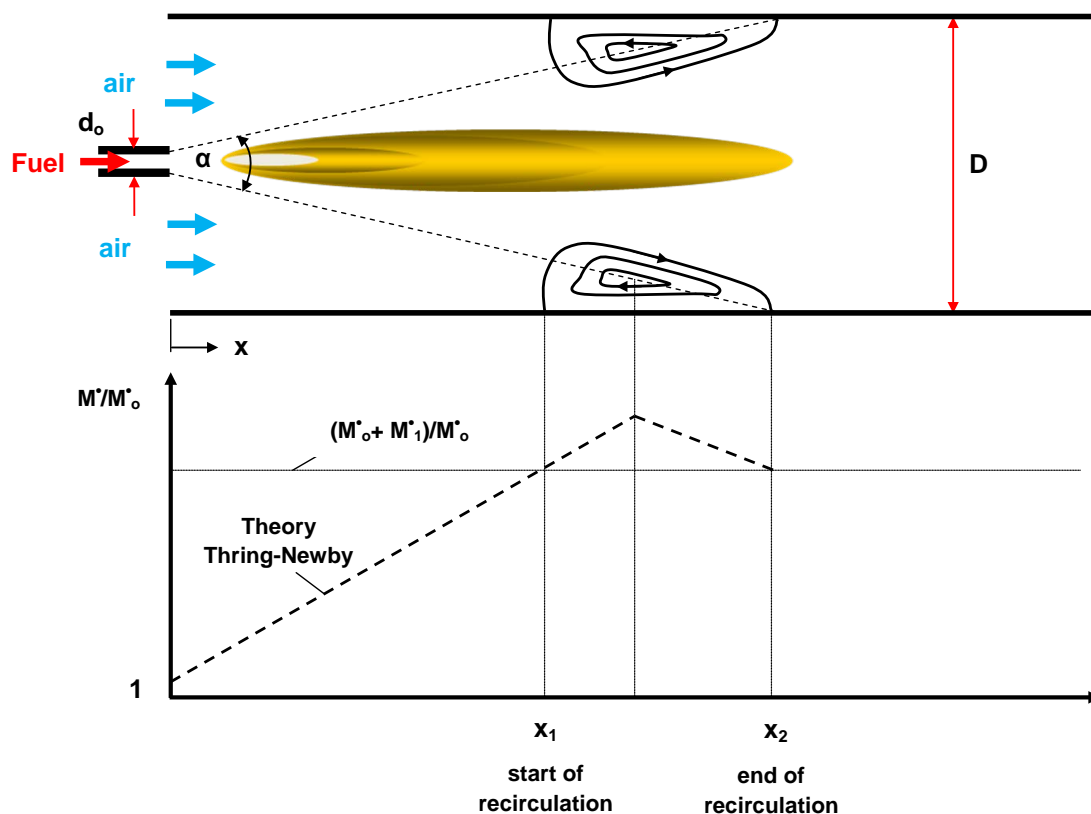
Figure 5.1: Recirculation and mass flow profiles in an enclosed combustion chamber [103].

5.1 Simple tube burner with variable air inlet diameter

Simple tube burner with diameter of 50 mm and cylinder with dimensionless air inlet diameter, $d_{a,i}/D$ changes from 0.06 to 1 (see Fig. 5.2), three gases were used in simulation; CH_4, $Biogas$ and CO. The results in this section include axial and radial species distributions, effects of excess air number, effects of inlet air temperature and effects of radiation on the flame behavior, especially, on the flame length which is the scope of this research. Also this section involves fuels comparisons between the simulated gases. Finally, prediction of flame length correlations in dimensionless form were obtained and presented, and also a comparison of numerical and experimental results were conducted.
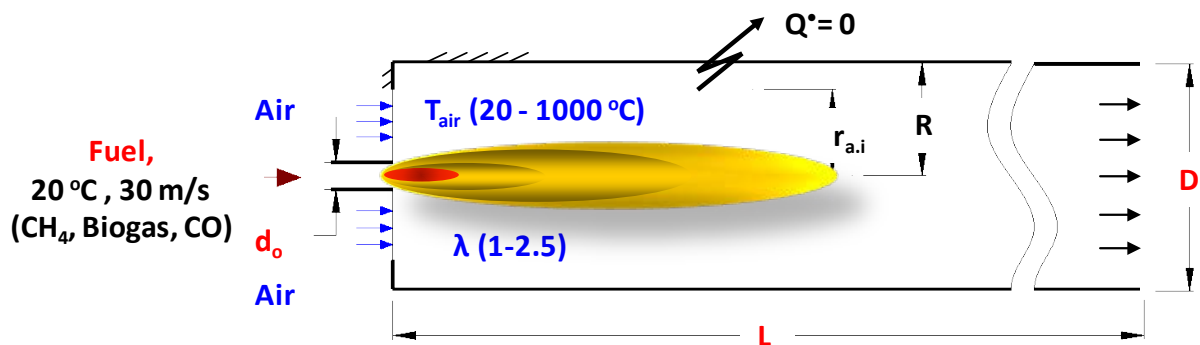
Figure 5.2: Schematic diagram of confined flame (simple tube burner with variable air inlet diameter).

5.1.1 Species distributions

Figure 5.3 (a) shows the typical mass fraction profiles of individual species of CH_4, CO, CO_2, H_2O, H_2, and O_2 along the centerline axis of confined flame, during combustion of Methane fuel without radiation at 1.3 excess air number under the simplified reaction scheme. As shown in the Figure, the individual species distribution in confined jet flame is similar to free jet flame, but mass fraction of O_2 is much higher in free jet flame at the end of calculated space than confined jet flame (see Fig. 4.2 (a)). This can be attributed to the free jet flame has an infinite excess air number and consequently this gives higher oxygen concentration at the end of computed space. Also as we see in the Figure, the mass fraction for both of CO_2 and H_2O at the end of confined jet flame is doubled than free jet flame. Figure 5.3 (b) explains the radial profiles of mass fraction of individual species which presented at $x/do = 30$. Clearly the mass fraction profiles of individual species in confined jet is typical to free jet flame (see Fig. 4.2 (b)), and the reaction zone has approximately the same, where the Methane and Oxygen coexist. Also as shown in the Figure the mass fraction of CH_4 is slightly higher in free jet flame than in confined jet flame.
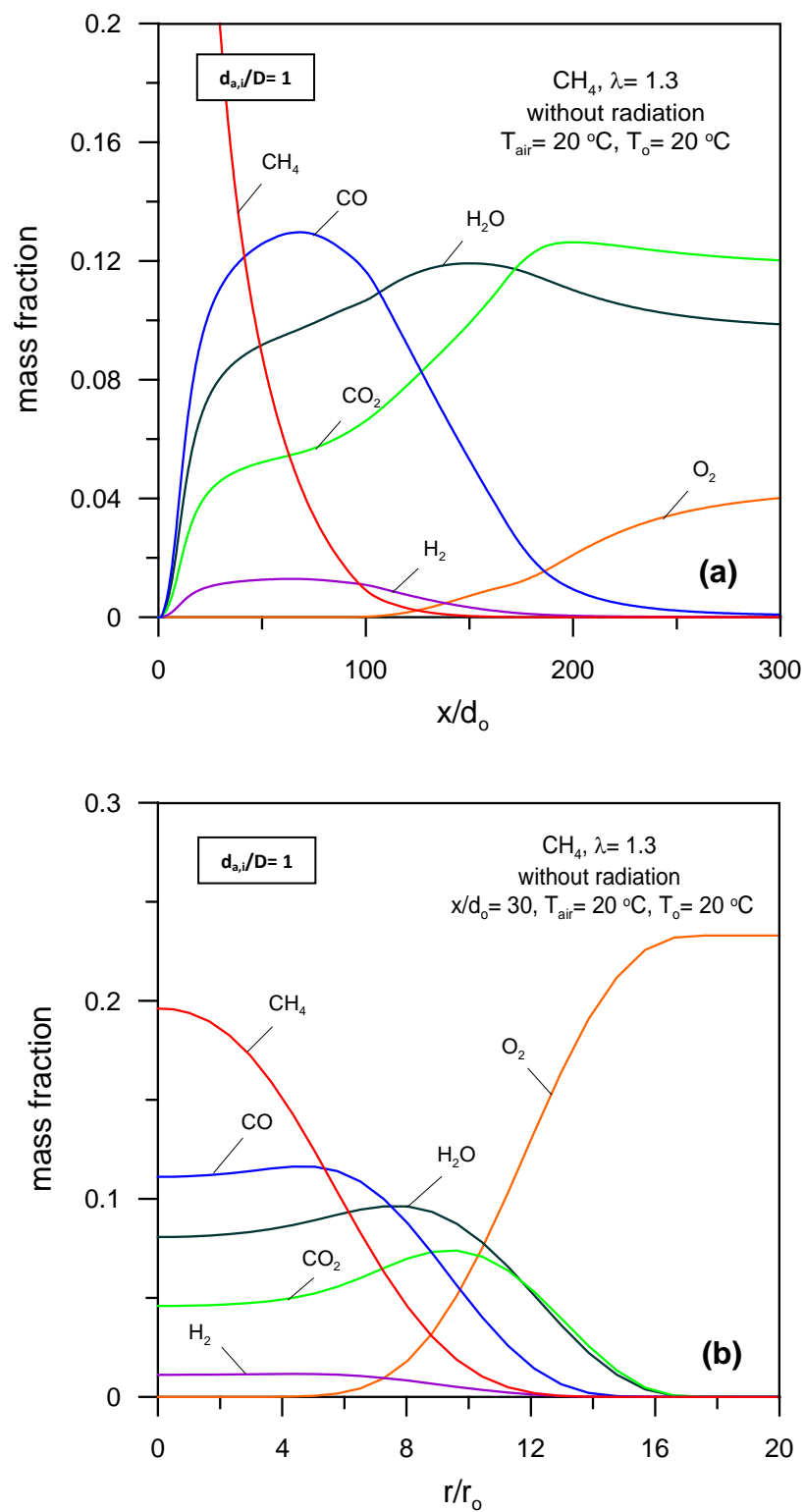
Figure 5.3: Species mass fraction distributions: (a) axial distribution, (b) radial distribution.

5.1.2   Effects of excess air number

The effects of excess air number changes (from 1 to 2.5) compared with free jet for three simulated gases (CH_4, $Biogas$, and CO) on the axial velocity profiles, axial temperature profiles, axial mean mixture fraction profiles, temperature and mean mixture fraction contours, and velocity vectors are shown in Figs (5.4−5.10).   The radiation wasn't considered (i.e., the radiation model (P1) wasn't used) and $d_{a,i}/D = 1$ in this section.

Figures 5.4 and 5.5 explain the influence of excess air number that varies from 1 to 2.5 on dimensionless axial velocity profiles and inverted dimensionless axial velocity profiles, respectively using different fuels (CH_4, $Biogas$, and CO). As shown in the Figures the axial velocity decays along the flame axis. This trend is the same at any excess air number and for any fuel. Also as we see in the Figures, the excess air number has a considerable effect on the axial velocity profiles. Where the axial velocity increases with increasing the excess air number, and this effect is the same for any fuel. This is due to that, the air axial velocity increases with increasing excess air number. Increasing the air axial velocity leads to higher axial velocity profiles. This effect not appear in the entrance region but it is reasonable in fully developed region. Also the Figures explain that the confinement has a significant effect on the velocity profiles when it compared with free jet profiles. This is because the confined flame axial velocity is controlled by axial air velocity according to amount of excess air number.

Figure 5.6 shows velocity vectors colored by temperature to explain the effect of excess air number on the outer recirculation zones for confined Methane jet flame. As shown in the Figure the recirculation appears at excess numbers of 1 and 1.1, and after that the recirculation diminishes with increasing the excess air number. This can be attributed to the ambient air momentum for low excess air number is less than that which the jet can entrain, so the recirculation introduced, but at higher excess air number (i.e., higher air momentum), the ambient air momentum is higher enough to fulfill the requirements for entrainment, so the jet will expand to attach the wall without recirculation (see sec. 2.4), and for more details refer to reference [41]. Also Fig. 5.7 displays comparisons between analytical solution based on Eqs. (5.3 and 5.4) and numerical calculations to estimate the the recirculation lengths (i.e., start and end points of recirculation eddies). As shown in the figure, the numerical solutions give the same trends with analytical solutions but differ in values. The discrepancies is due to that the analytical solution was derived for gases without combustion.

The influence of excess air number on the centerline axial temperature compared with free jet flame for different fuels (CH_4, $Biogas$, and CO) is shown in Fig. 5.8. As shown in the Figure the excess air number has a considerable effect on the axial temperature profiles. Whereas, the higher the excess air number the lower the peak flame temperature and product combustion gas temperature. The results explains that the temperature profile converges to free jet profile with increasing the excess air number. This trend is the same for any fuels, and the reason is due to the mixing temperature between fuel and air decreases with increasing the amount of excess air, and this causes drop in combustion gas temperature. Also as shown in the Figure, the influence of excess air number exhibits on the temperature profiles only after $X/d_o{\approx}170$, 60 and 35 for CH_4, $Biogas$, and CO, respectively. The effects of excess air number on the temperature contours in comparison with free jet flame are depicted in Fig. 5.9. As presented in the
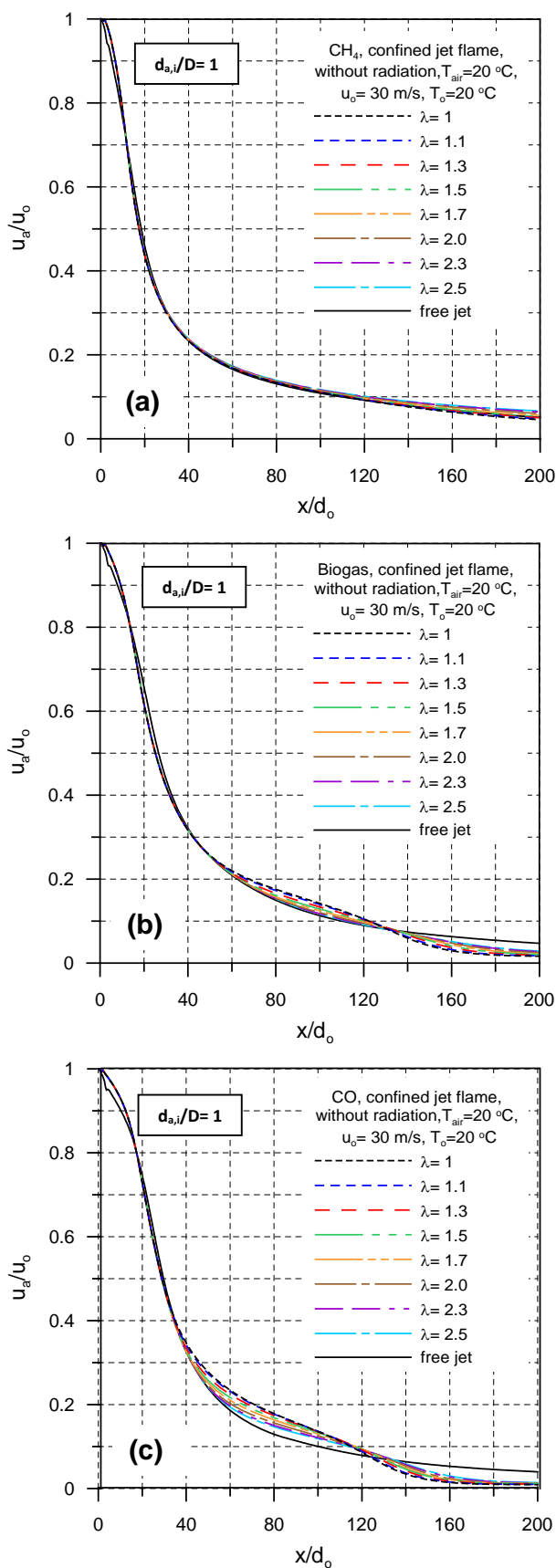
Figure 5.4: Influence of excess air number on dimensionless axial velocity profiles along the flame: (a) CH_4, (b) *Biogas*, (c) *CO*.
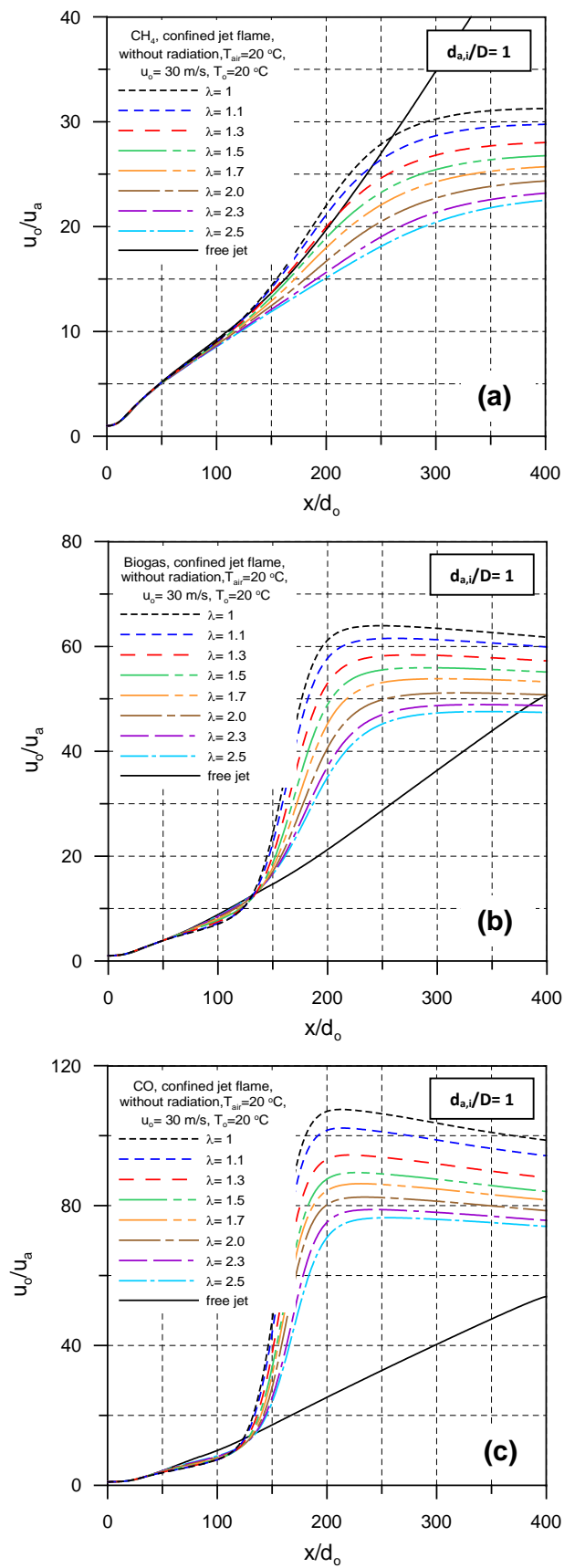
Figure 5.5: Influence of excess air number on inverted dimensionless axial velocity profiles along the flame: (a) CH_4, (b) $Biogas$, (c) CO.

Figure the high temperature zone area and flame volume decreases with the increase in excess air number and the confined flame jet shape closes to free jet flame shape and it seems the same at $\lambda = 2.5$. The possible explanation is that the lower amount of excess air leads to lower amount of oxidizer, hence the combustion can't complete in short distance and the flame must be dispersed to complete the reaction. Therefore the high temperature zone area and flame volume increase with decreasing the excess air number. To explain the effect of the excess air number on the flame length in comparison with free jet flame, Fig. 5.10 illustrates the influence of excess air number on inverted dimensionless axial mixture fraction profiles for different fuels (CH_4, $Biogas$, and CO). As shown in the Figure, the flame length decreases with increasing the excess air number and it becomes the same as in free jet at $\lambda = 2.5$. This is due to the higher the excess air number the higher amount of oxidizer, hence the combustion completed in small volume and consequently in short distance. The same investigation had been done by ref. [71]. The length of the flame tends to the same as in free jet with the highest value of excess air number ($\lambda = 2.5$). This means that the flame length reaches to the smallest possible value at the highest excess air number, and this effect is the same for all fuels (e.g., for CH_4 fuel the flame length shortens by $\sim 7\,\%$ with the increasing of λ from 1.3 to 2.5). As shown in Fig. 5.10 the mixture fraction resulting from combustion of all three gases can't reach to the stoichiometric value at $\lambda = 1$, therefore we can't compute the flame length for like these cases.

5.1.3   Effects of air inlet diameter

The principle diagram showing recirculation profiles of confined flame with variable air inlet diameters is shown in Fig. 5.11. On the other hand, Fig. 5.12 shows the effect of air inlet diameter in dimensionless form on the recirculation length, using Methane fuel at $\lambda = 1.3$, $u_o = 30$ m/s, $T_{air} = 20°C$ and $T_o = 20°C$. In the simulation, air inlet diameter in dimensionless form ($d_{a,i}/D$) changes from 0.06 to 1, and the radiation model (P1) wasn't used (i.e., without radiation effect). As shown in the figure the recirculation length decreases with increasing air inlet diameter, Also the figure shows that the numerical solutions give satisfactory agreement with analytical solutions based on the following correlation:

$$\frac{L_{Ra,i}}{D} = \frac{1 - \frac{da,i}{D}}{2tan\frac{\alpha}{2}} \approx 3(1 - \frac{d_{a,i}}{D}) \tag{5.5}$$

Where $\alpha \approx 19°$

Figures (5.13−5.22) show the influence of air inlet diameter in dimensionless form on the axial velocity profiles, velocity vectors, centerline axial temperature profiles, temperature contours, axial mean mixture fraction profiles and the flame length. Three gases were simulated in this section (CH_4, $Biogas$ and CO) at constant fuel velocity and constant thermal burner power, without radiation calculation (i.e., the radiation model (P1) wasn't used). In the simulation the dimensionless air inlet diameter, $d_{a,i}/D$ varies from 0.06 to 1 and excess air number changes from 1.05 to 2.5 as a parameter.

The effects of dimensionless air inlet diameter on the axial velocity and inverted axial velocity profiles in dimensionless form are shown in Figs 5.13 and 5.14, respectively at different excess air number, λ of 1.3, 1.5, 1.7, 2, 2.3 and 2.5. The results explain that

the axial velocity decreases along the jet flame axis, this trend is the same at any air inlet diameter, any excess air number and for any fuel. But at smallest values of $d_{a,i}/D$ (0.06 and 0.1) we see that, the axial velocity increases and then decreases along the jet axis. The possible explanation is that the axial air velocity around the jet is much higher than the fuel jet velocity, therefore the axial air affect on the fuel jet velocity by increasing the centerline axial velocity distribution until reach to the maximum value at $x/d_o \approx 25$ and $x/d_o \approx 10$ for $d_{a,i}/D = 0.06$ and $d_{a,i}/D = 1$, respectively, then the velocity decreases along the jet flame axis. Also as displayed in the Figures the air inlet diameter has a reasonable effect of the axial velocity profiles, whereas the axial velocity profiles shifted up with decreasing the inlet air diameter until the flow reaches to fully developed flow (at $x/d_o \approx 200$), and after that the effect of air inlet diameter diminishes. This can be attributed to the axial air velocity increases with decreasing the air inlet diameter (i.e, air inlet area), and consequently this cases an increase in the centerline axial velocity profile.

As we explained before, the strength and size of recirculation eddy affect both the stability and combustion length of the turbulent diffusion flame (refer to Sec. 2.4)and for more details see ref. [41]. Therefore, Figures (5.15, 5.16 and 5.17) display velocity vectors and pathlines colored by temperature to illustrate the influence of air inlet diameter on the outer recirculation zones for CH_4 and CO jet flame, respectively. As shown on the figures, the recirculation size decreases with increasing air inlet diameter, this is because of the air axial velocity decreases with increasing the air inlet area at the same excess air number, and in consequence the recirculation size decreases. In addition to the closed part at the air inlet helps to make a recirculation behind it.

The influence of the air inlet diameter on the axial temperature profiles was presented in Fig. 5.18. As shown in Figure, the axial temperature distribution and peak flame temperature increase with increasing inlet air diameter, this trend is the same at any excess air number. This can be attributed to the recirculation size increases with decreasing air inlet diameter, Which improves the mixing process between air and fuel, hence the combustion process can be completed in short distance (see Fig. 5.19).

The effect of the air inlet diameter on the inverted dimensionless axial mean mixture fraction profiles was presented in Fig. 5.20 in order to calculate the flame length using Methane fuel at different excess air number. As observed in the Figure the flame length increases with increasing the air inlet diameter (i.e., air inlet area) and vise versa. This trend is the same at any excess air number and for any fuel. This is due to the axial air velocity and recirculation eddy size increase with decreasing air inlet diameter size as we stated before, increasing the air velocity and recirculation size improve the mixing between the air and fuel, which result in a decrease in the flame length. Also as shown in the Figure the changing of $d_{a,i}/D$ from 0.06 to 0.4 has a significant effect on the flame length, other than it has a smaller effect on the flame length. For example, the flame length increases by $\sim 180\%$ with increasing of $d_{a,i}/D$ from 0.06 to 0.4 and by $\sim 6\%$ with increasing of $d_{a,i}/D$ from 0.4 to 1 in case of Methane fuel at $\lambda = 1.3$. Figures (5.21 and 5.22) display summarized curves to describe the relation between dimensionless flame length and dimensionless air inlet diameter for CH_4, $Biogas$, and CO without radiation at different excess air number as a parameter. These results will use to predicate the flame length correlations as we see later.
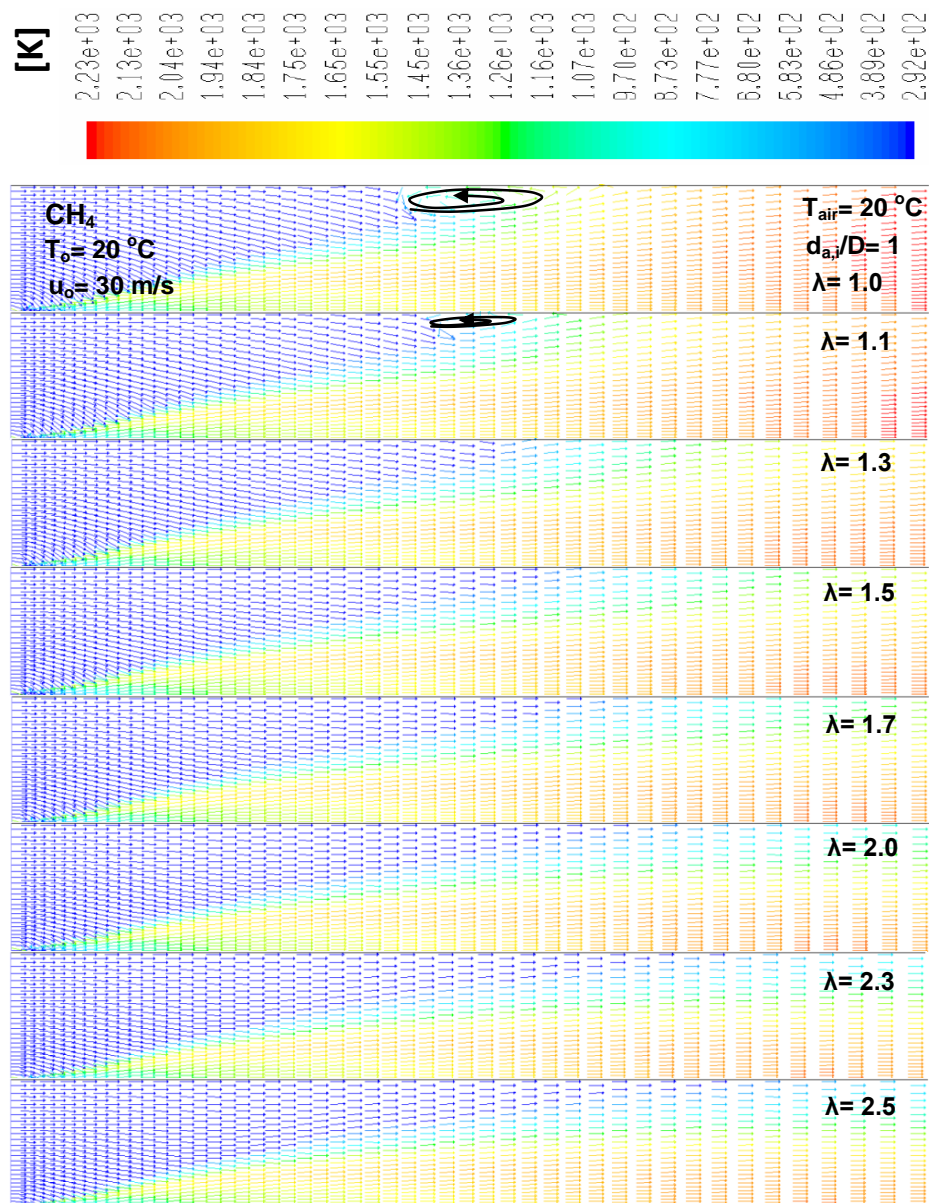
Figure 5.6: Influence of excess air number on recirculation zones presented by velocity vectors colored by temperature along the flame for Methane fuel (CH_4).
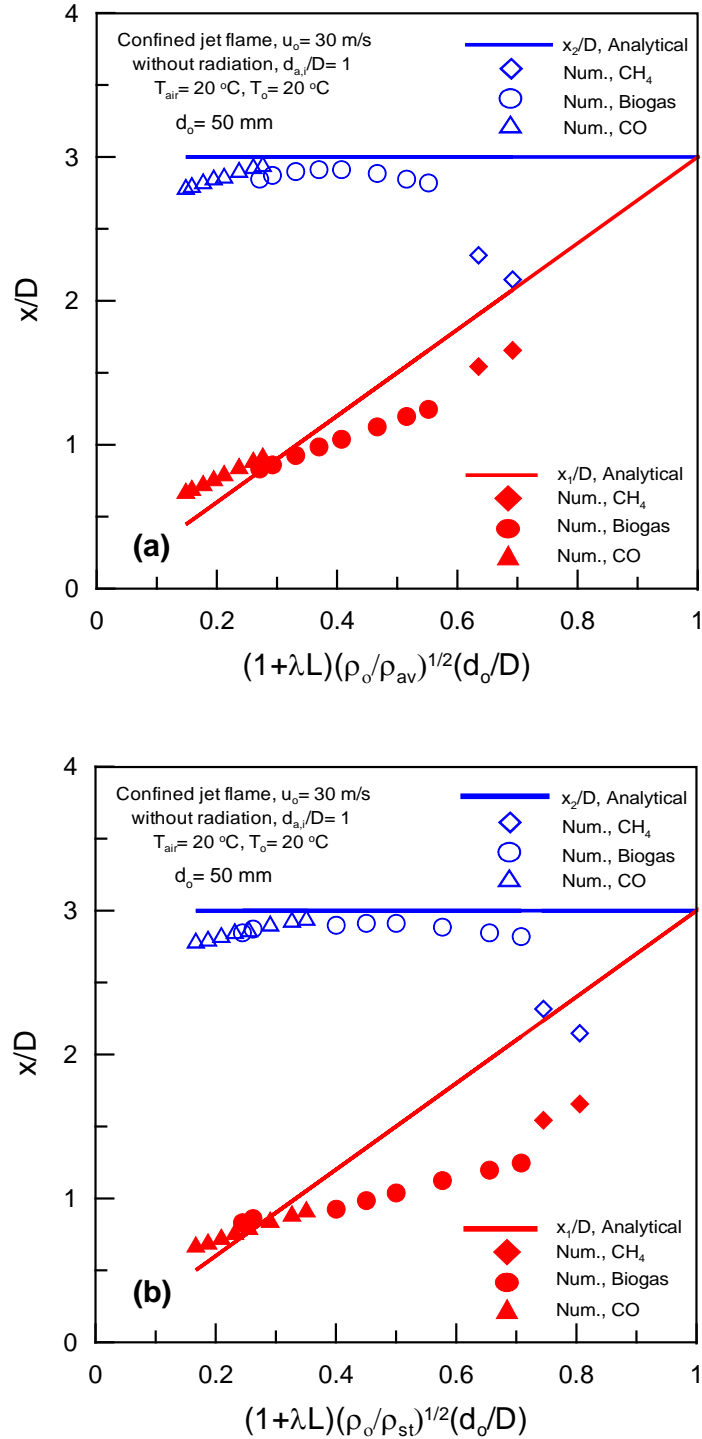
Figure 5.7: Influence of excess air number on recirculation lengthes comparing with analytical solution: (a) at average flame density, (b) at stoichiometric mixture density.
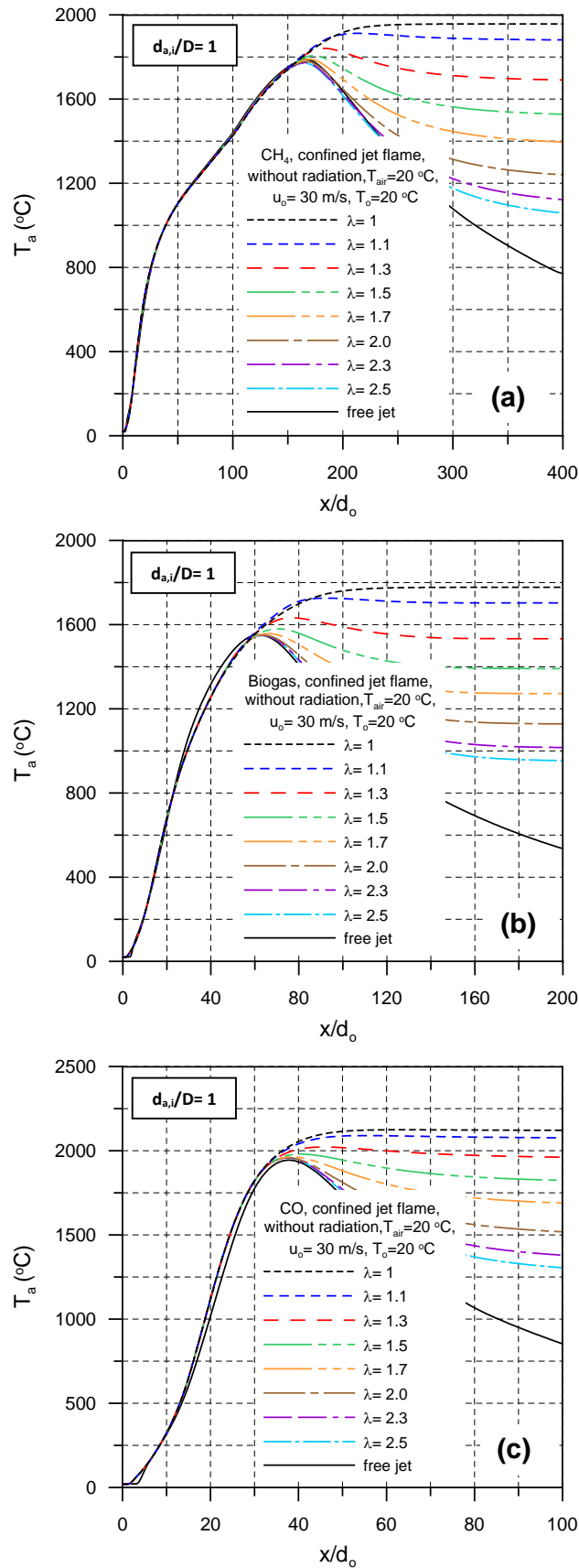
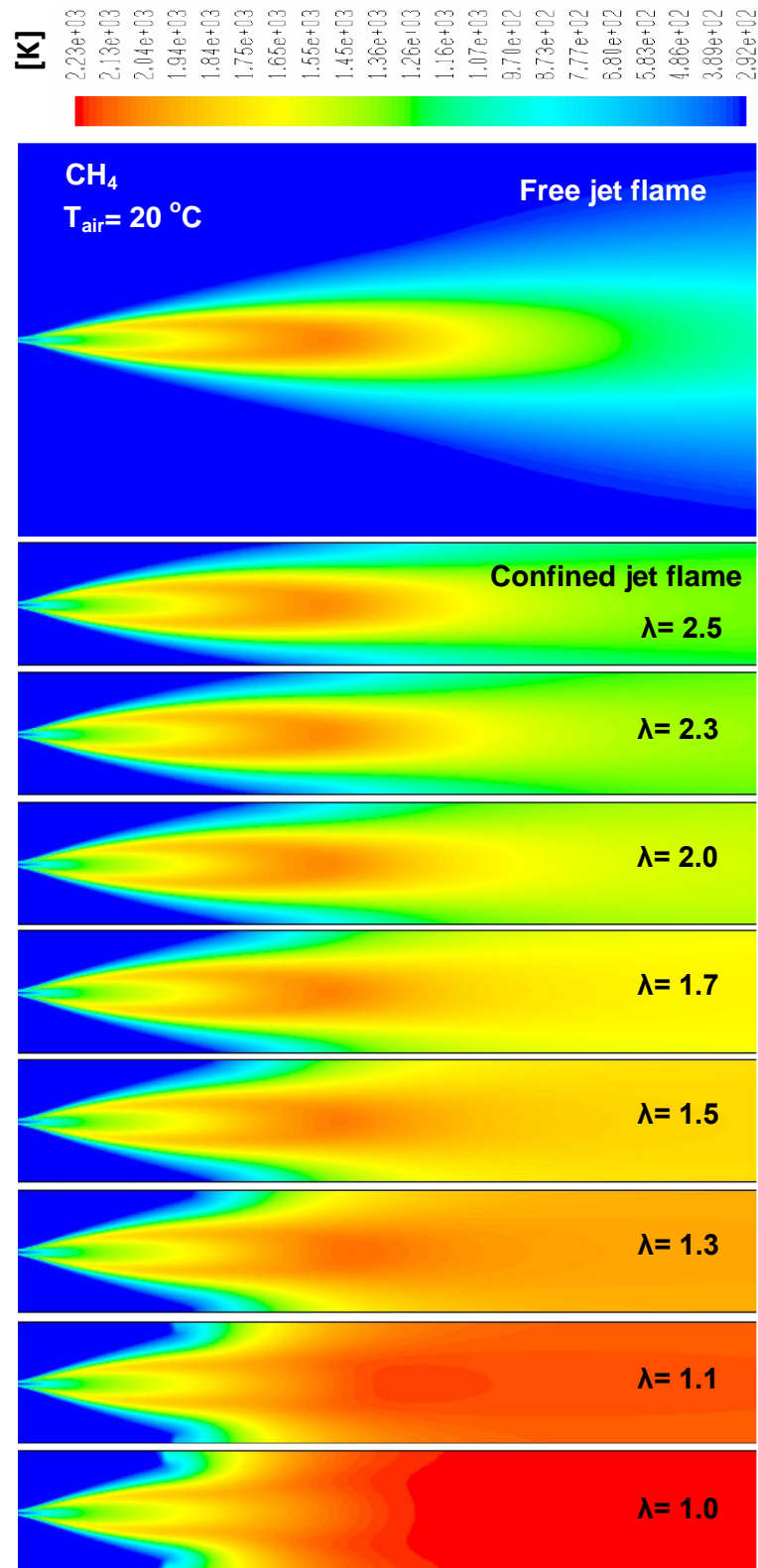Figure 5.8: Influence of excess air number on axial temperature profiles along the flame: (a) CH_4, (b) *Biogas*, (c) *CO*.

Figure 5.9: Influence of excess air number on temperature contours along the flame compared with free jet flame for Methane fuel (CH_4) at T_o= 20°C, u_o= 30 (m/s) and $d_{a,i}/D$=1.
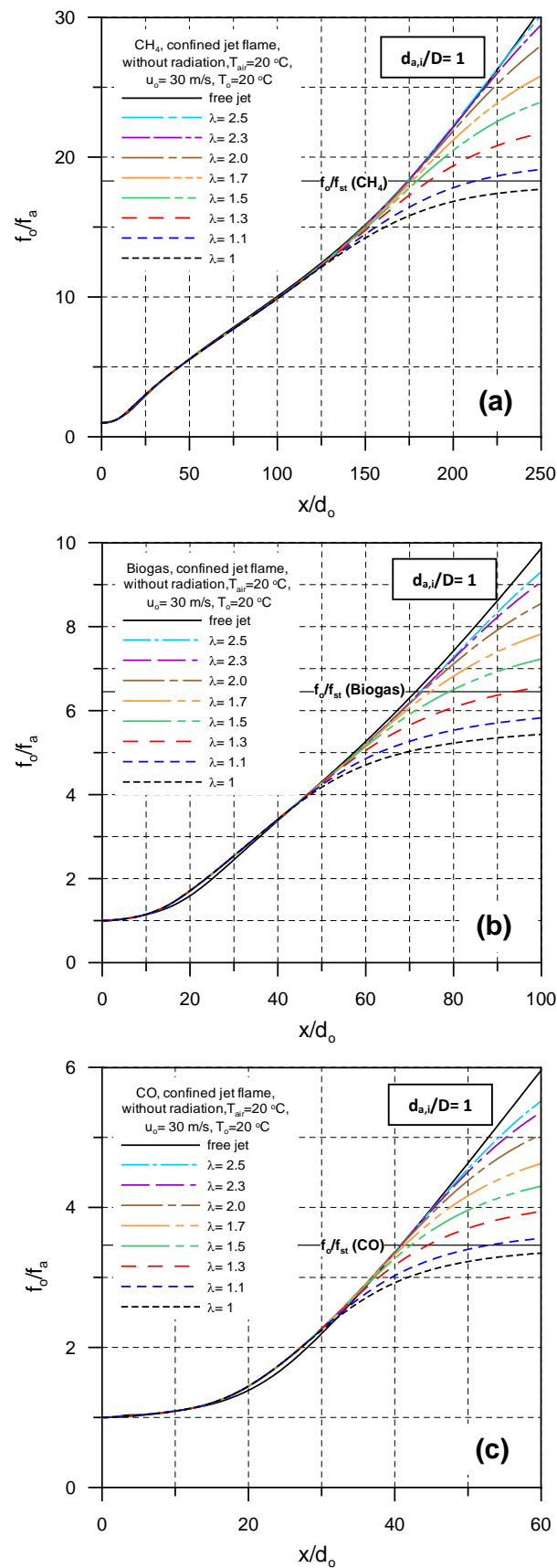
Figure 5.10: Influence of excess air number on inverted dimensionless axial mean mixture fraction profiles along the flame: (a) CH_4, (b) *Biogas*, (c) *CO*.
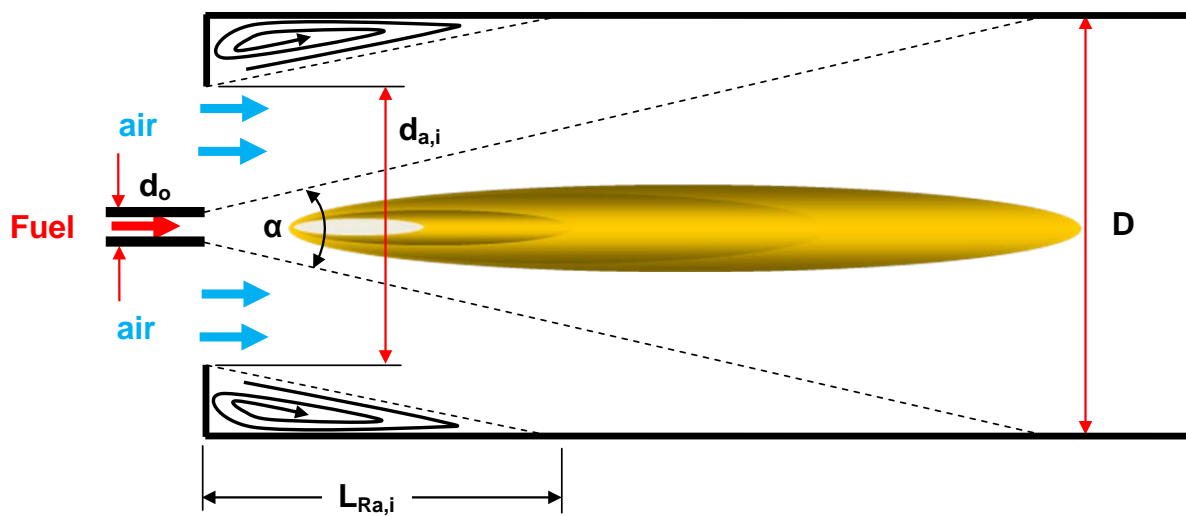
Figure 5.11: Schematic diagram showing recirculation profiles of confined flame (simple tube burner with variable air inlet diameter).
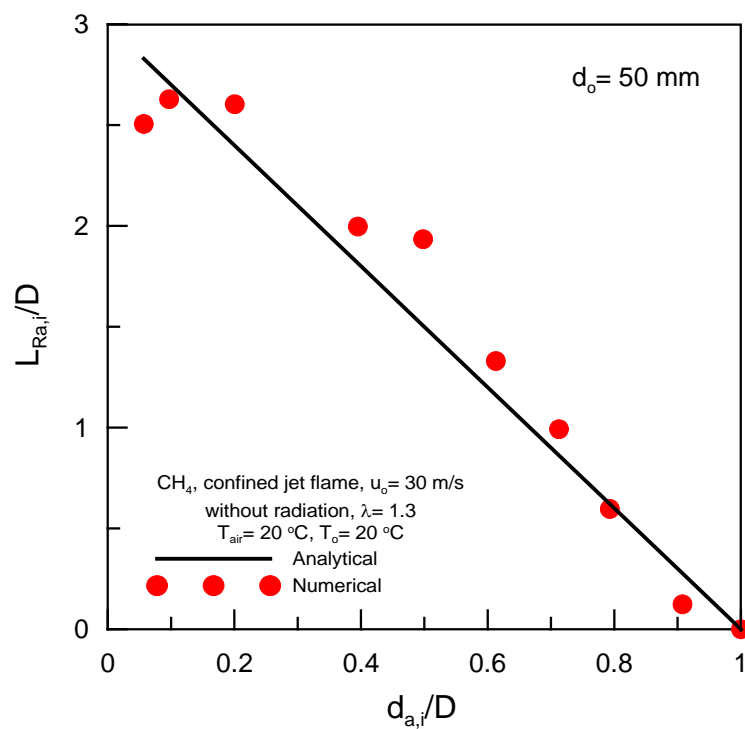
Figure 5.12: Recirculation length at different air inlet diameters.
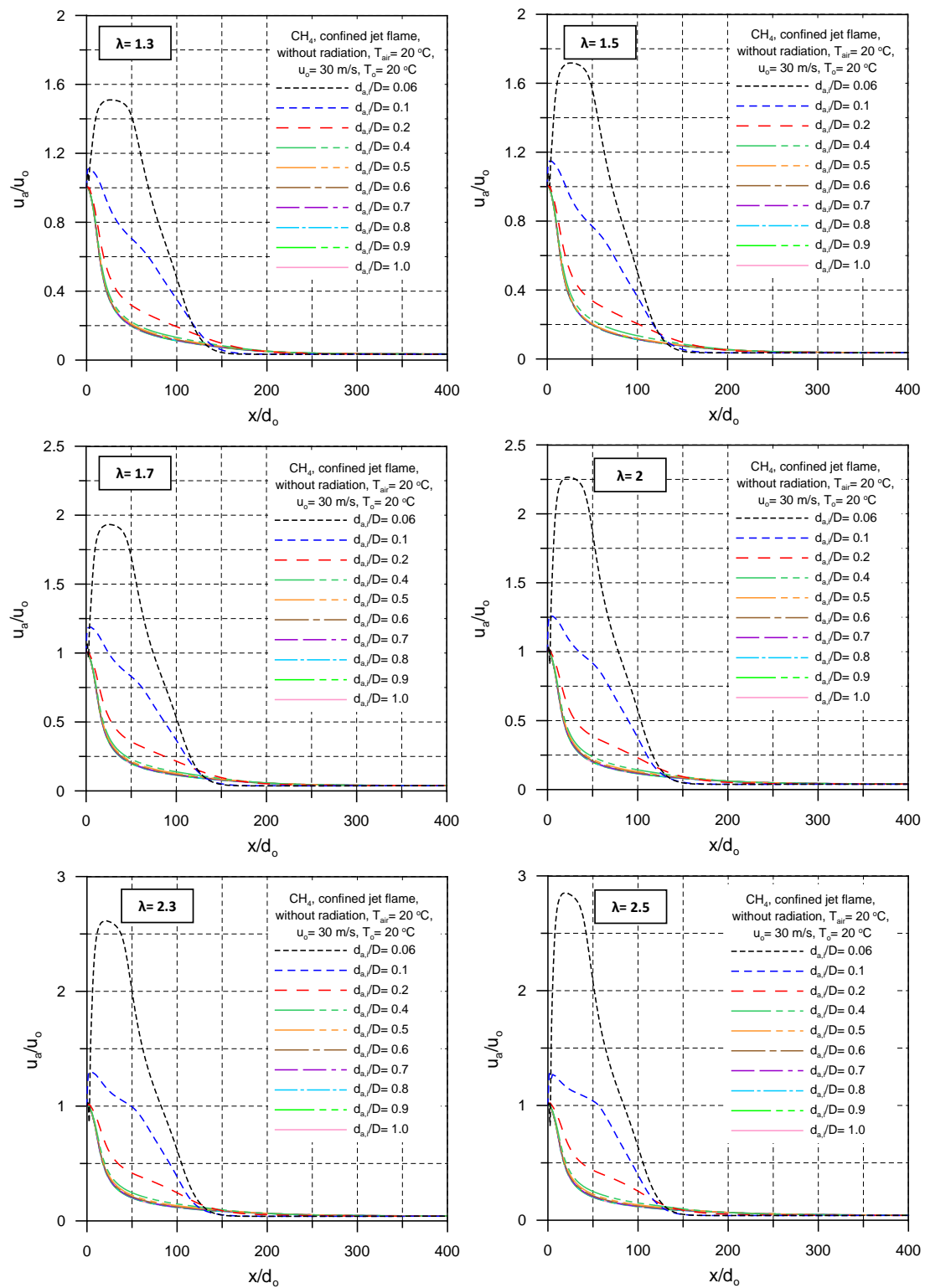
Figure 5.13: Influence of dimensionless air inlet diameter on dimensionless axial velocity profiles along the flame for different excess air number, λ using Methane fuel (CH_4).
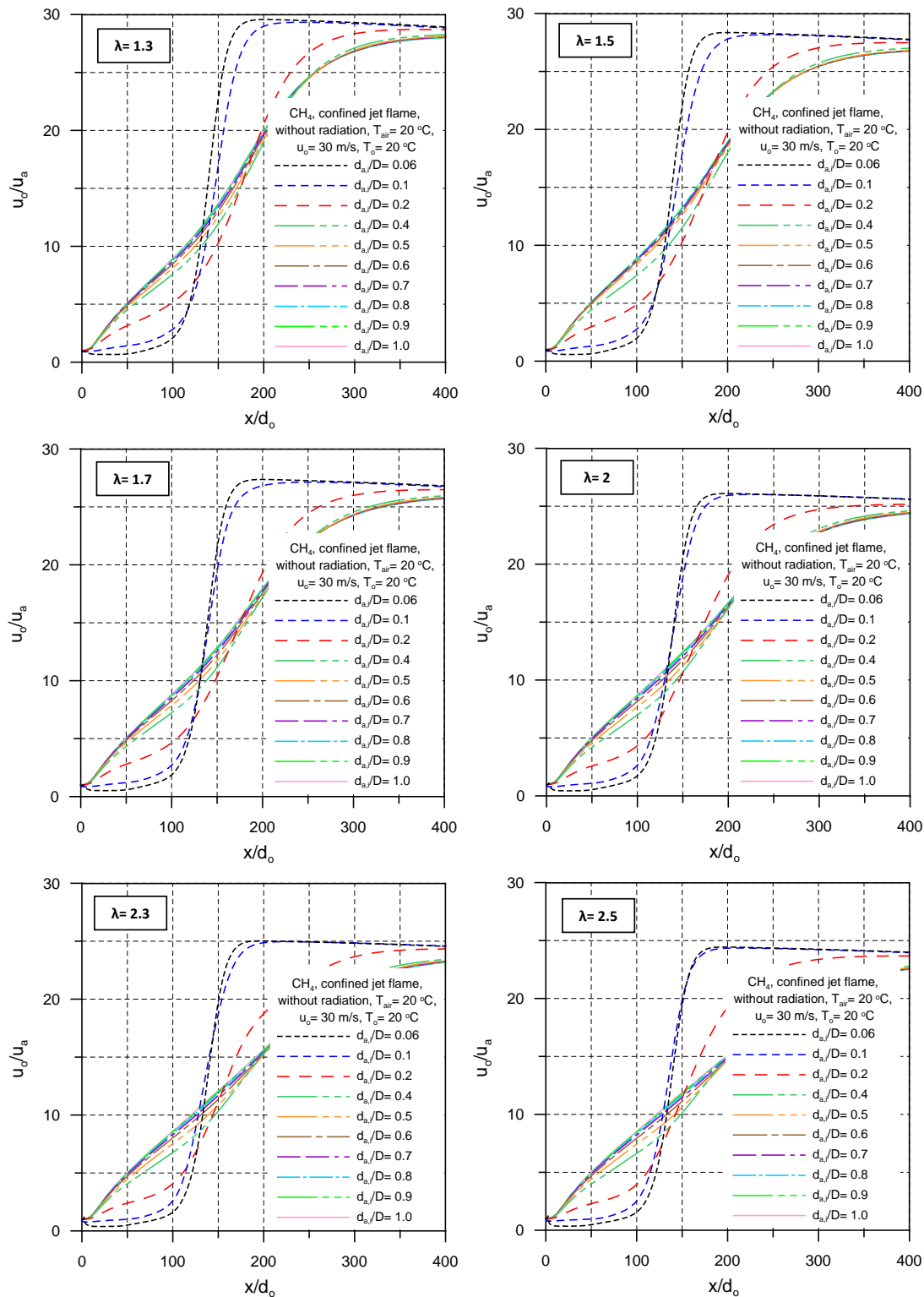
Figure 5.14: Influence of dimensionless air inlet diameter on inverted dimensionless axial velocity profiles along the flame for different excess air number, λ using Methane fuel (CH_4).
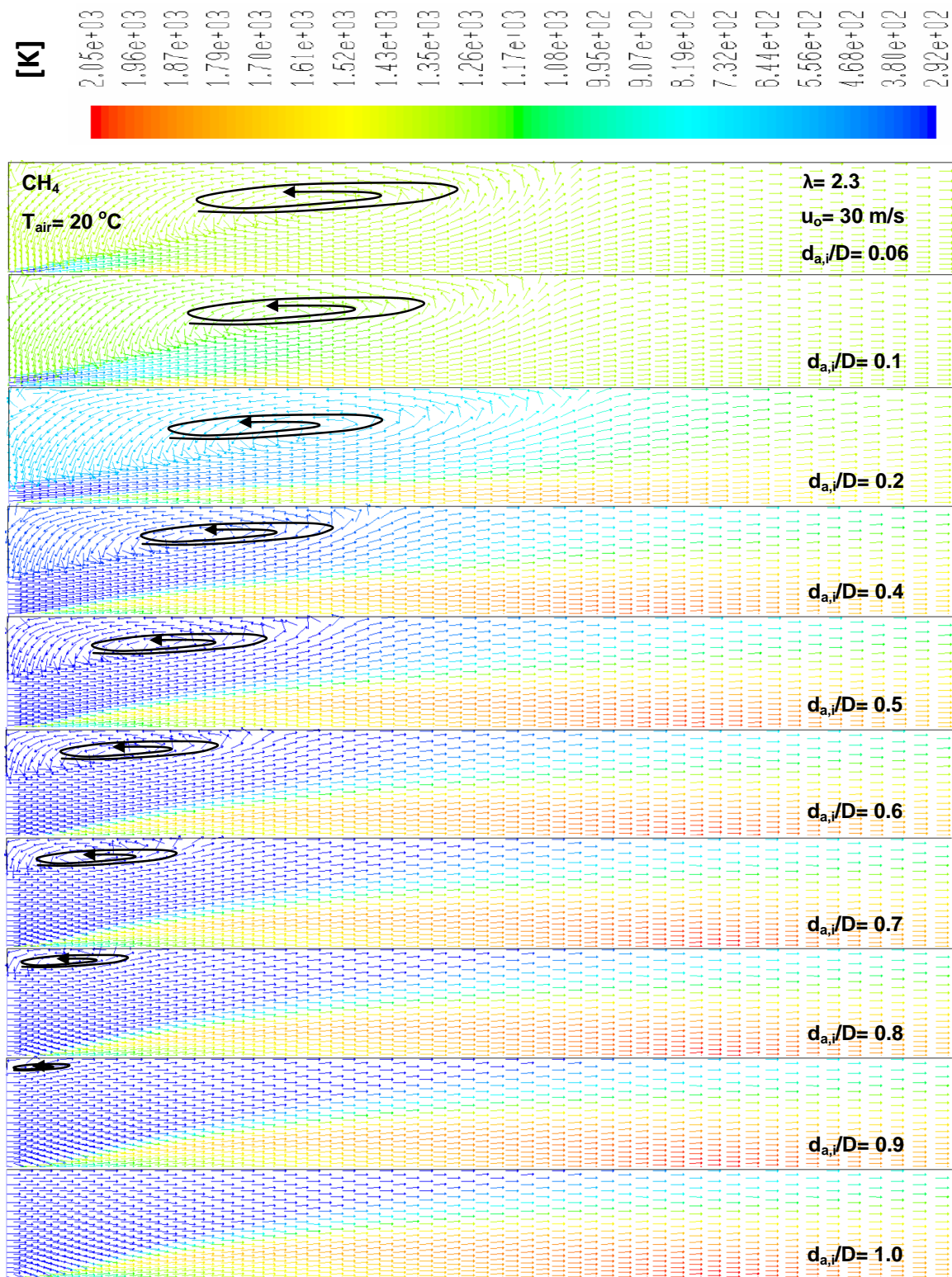
Figure 5.15: Influence of dimensionless air inlet diameter on recirculation zones presented by velocity vectors colored by temperature along the flame for Methane fuel (CH_4) at λ=2.3.
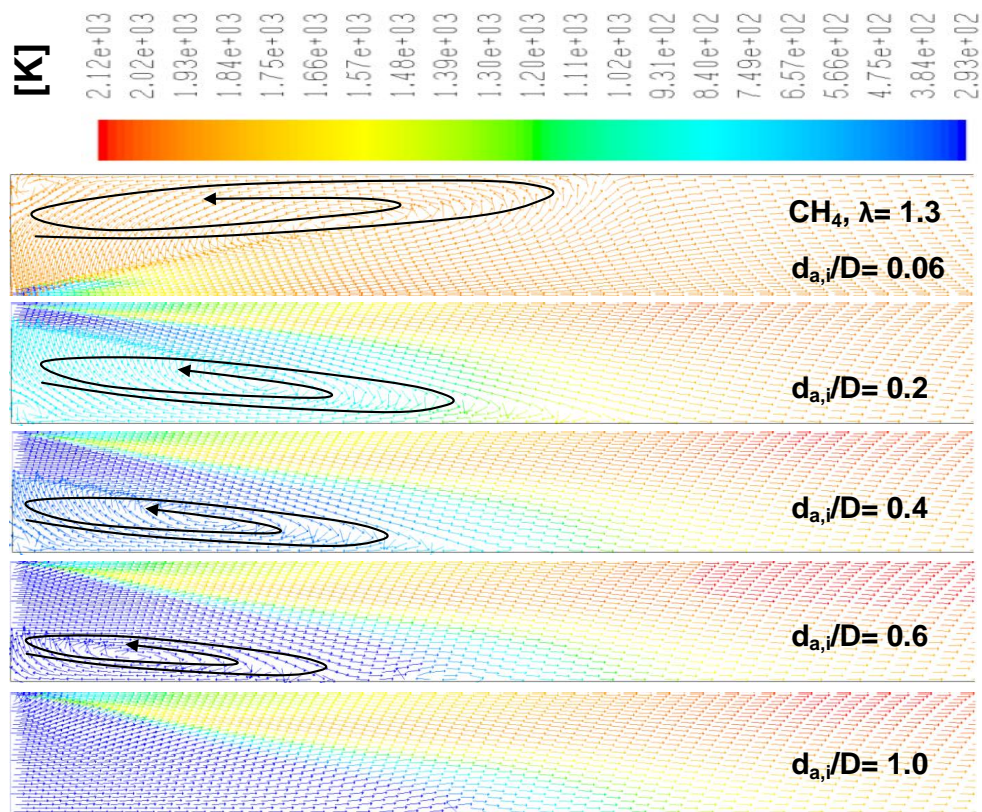
Figure 5.16: Influence of dimensionless air inlet diameter on recirculation zones presented by velocity vectors colored by temperature along the flame for CH_4 fuel at $\lambda=1.3$.
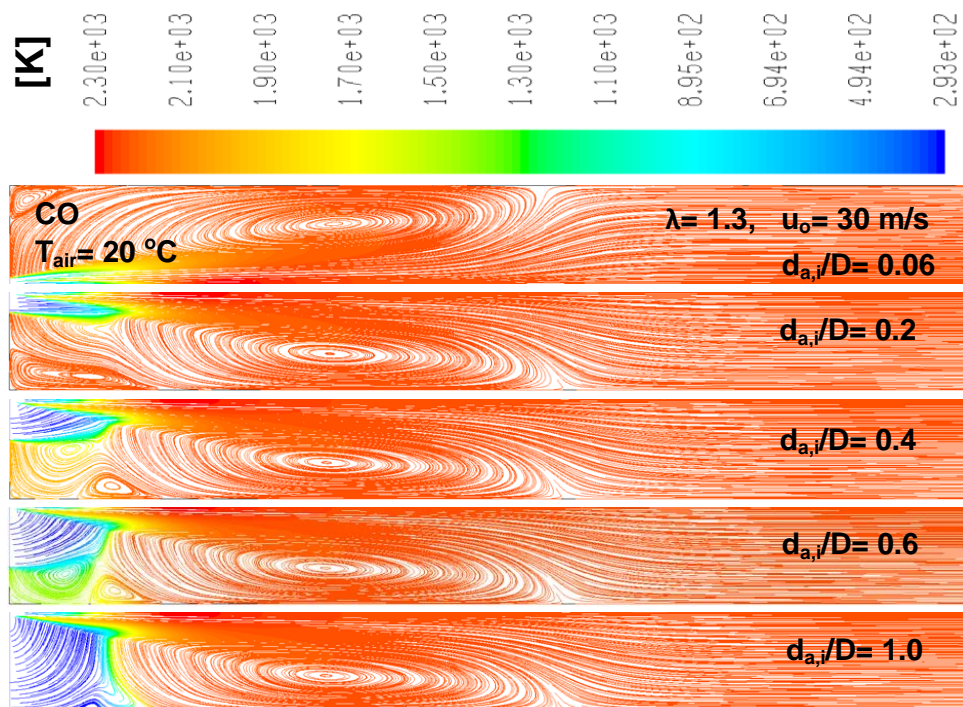
Figure 5.17: Influence of dimensionless air inlet diameter on recirculation zones presented by pathlines colored by temperature along the flame for CO fuel at $\lambda=1.3$.
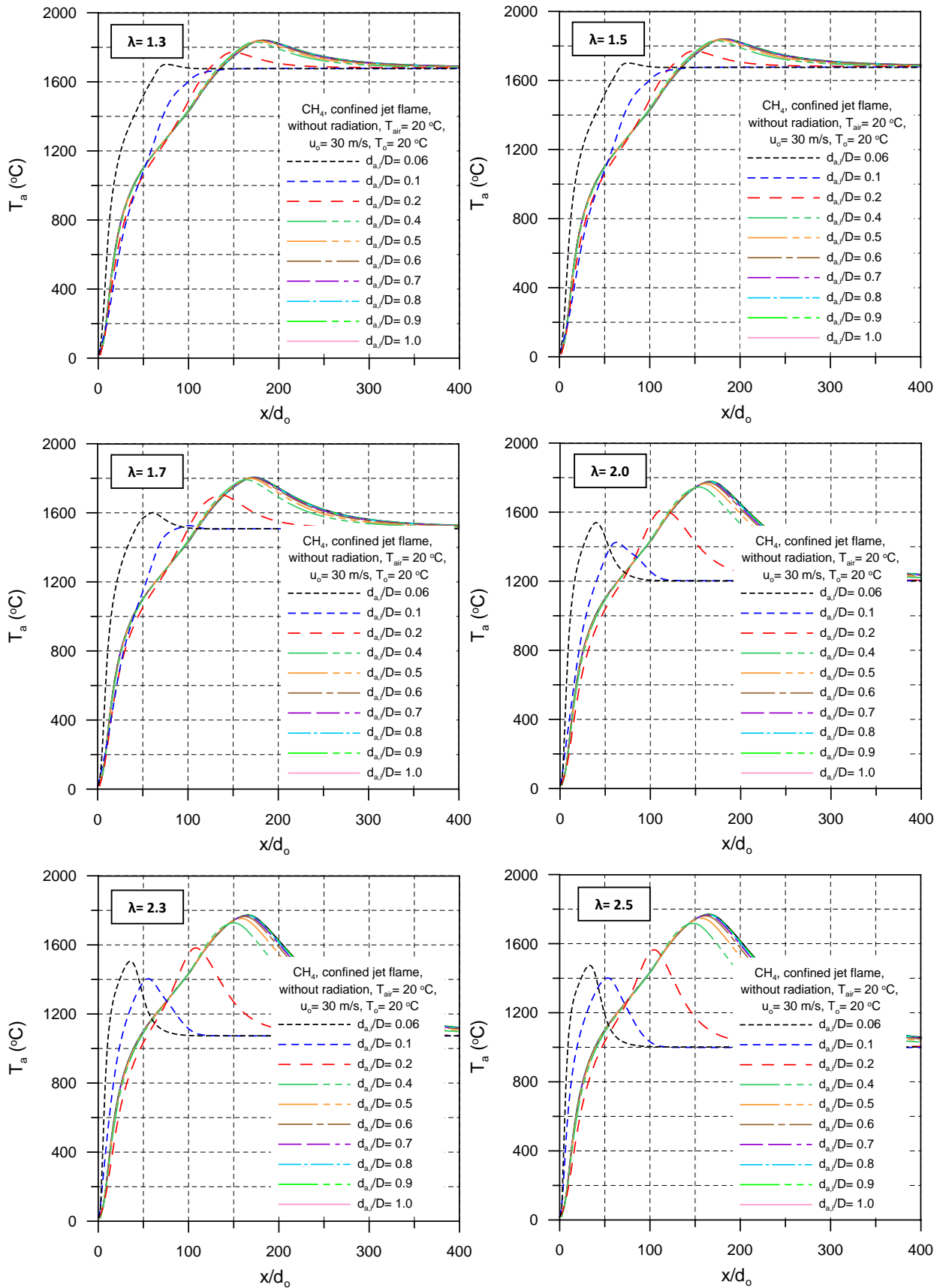
Figure 5.18: Influence of dimensionless air inlet diameter on axial temperature profiles along the flame for different excess air number, λ using Methane fuel (CH_4).
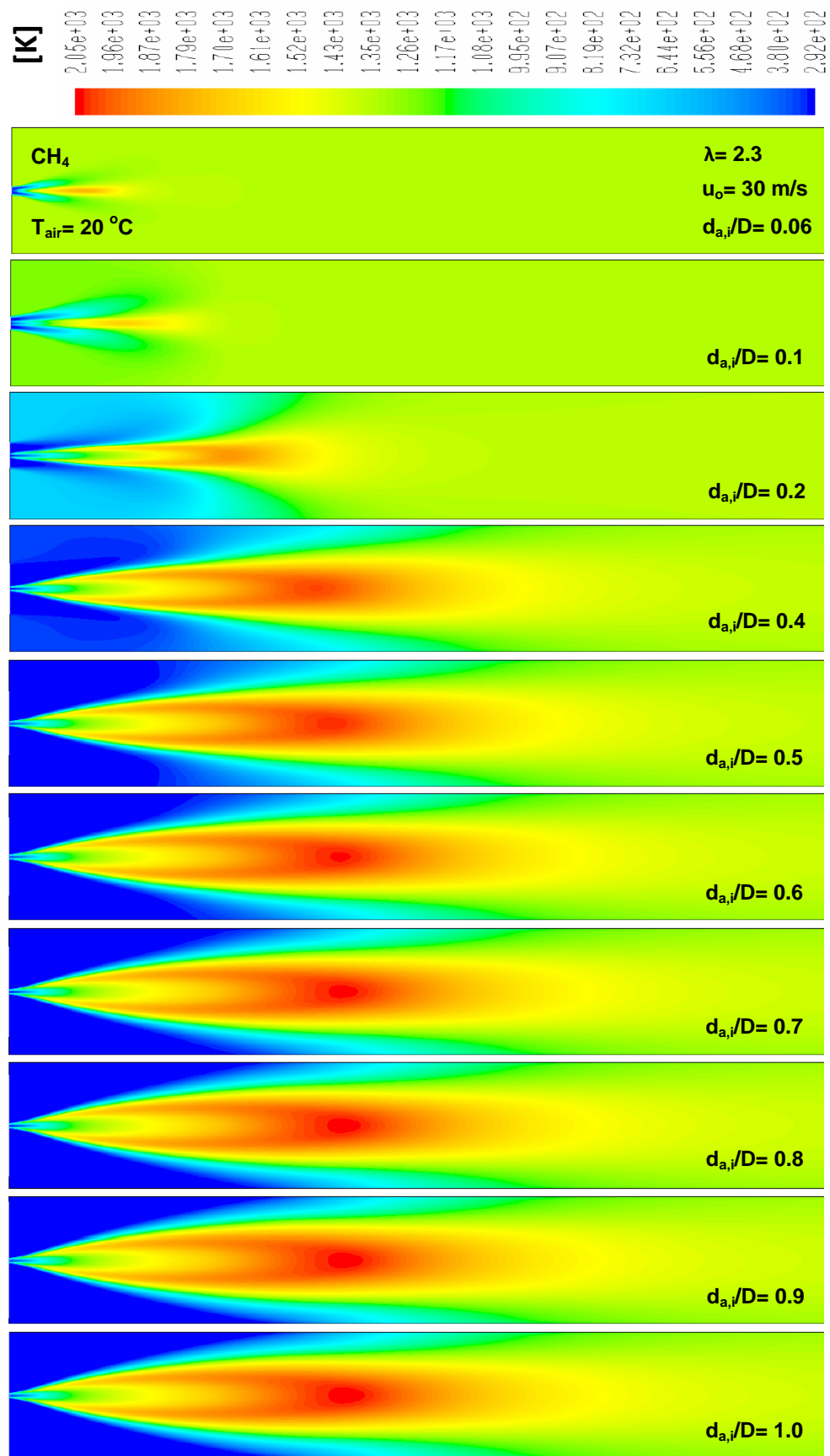
Figure 5.19: Influence of dimensionless air inlet diameter on temperature contours along the flame using Methane fuel (CH_4).
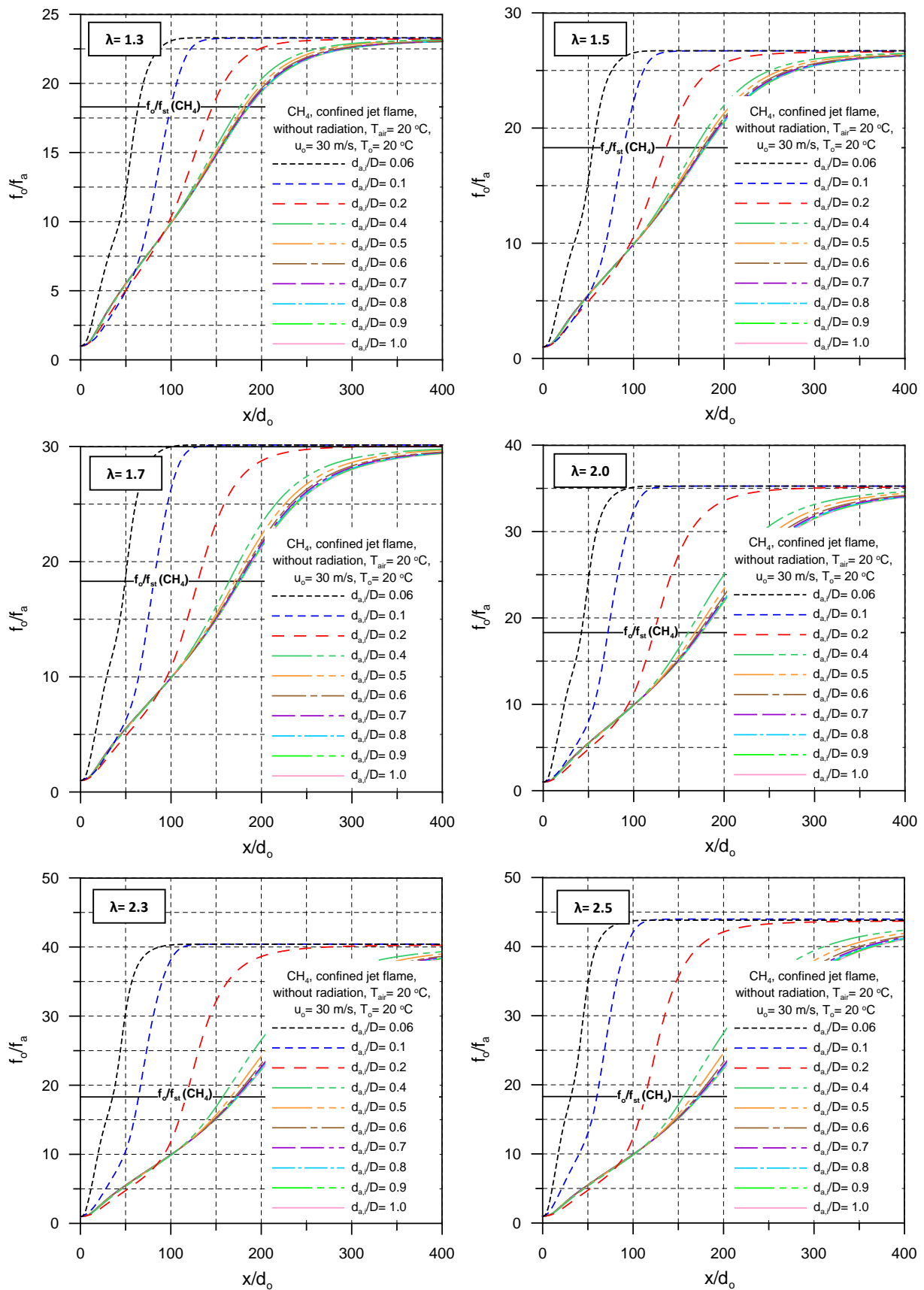
Figure 5.20: Influence of dimensionless air inlet diameter on inverted dimensionless axial mean mixture fraction profiles along the flame for different excess air number, λ using Methane fuel (CH_4).
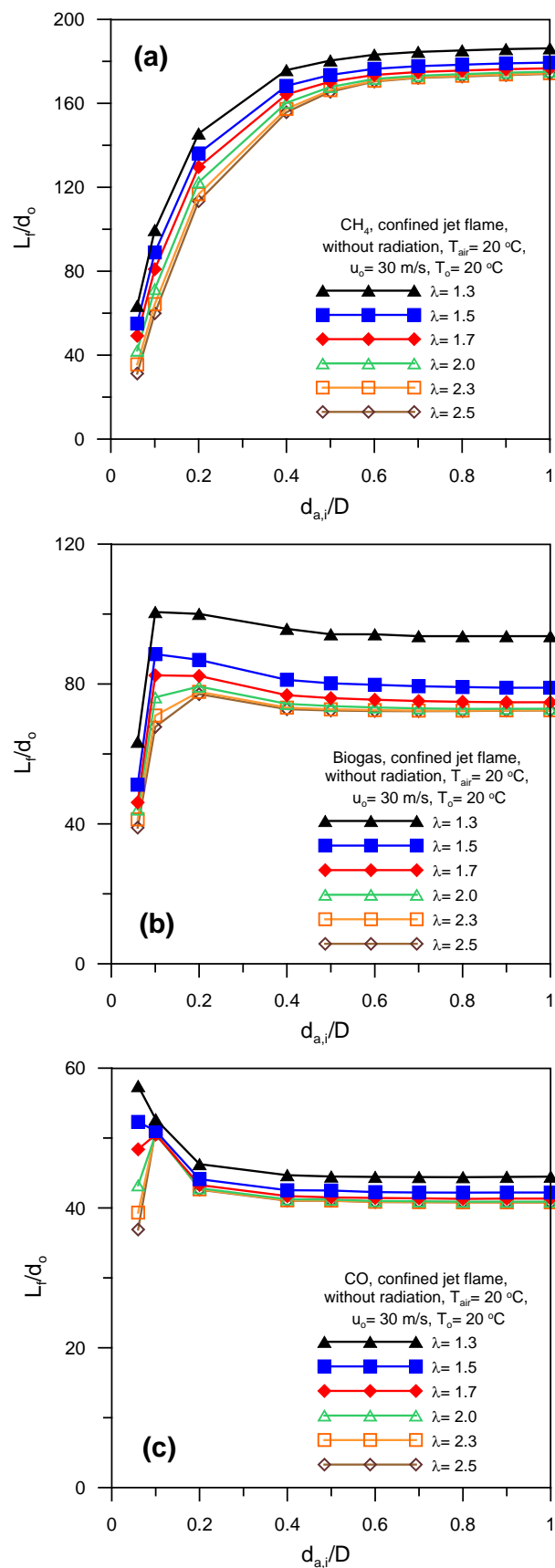
Figure 5.21: Influence of dimensionless air inlet diameter on the dimensionless flame length at constant fuel velocity: (a) CH_4, (b) *Biogas* and (c) *CO*.
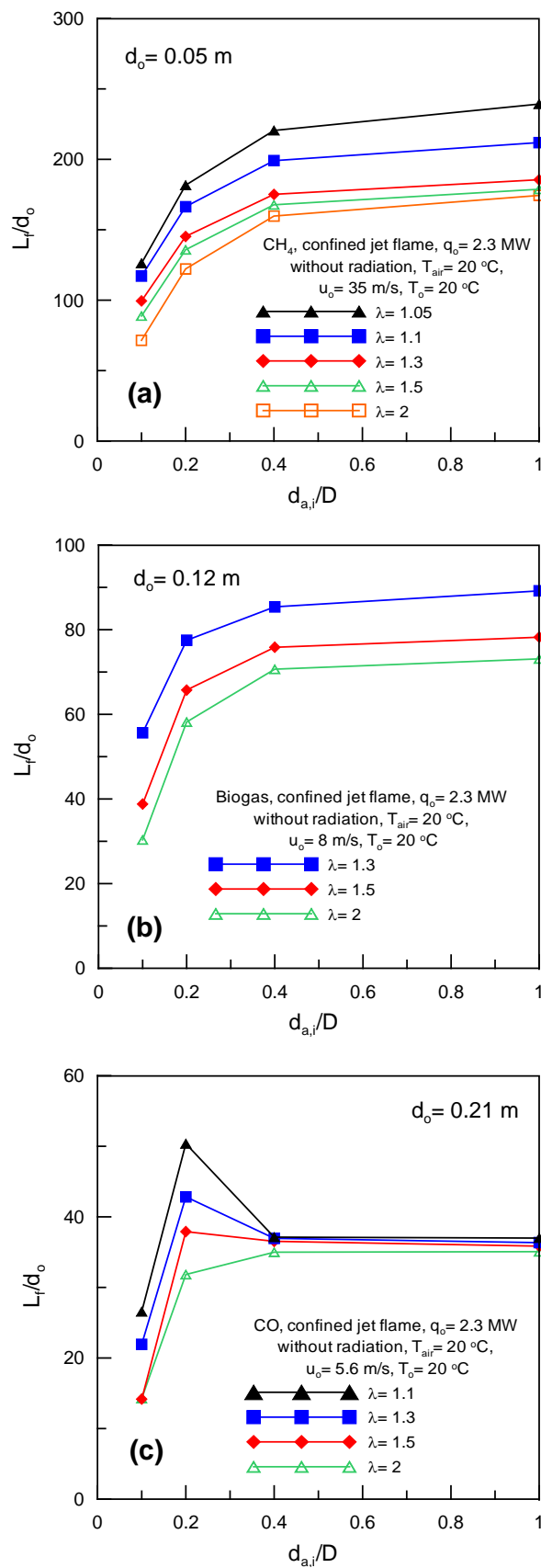
Figure 5.22: Influence of dimensionless air inlet diameter on the dimensionless flame length at constant thermal burner power: (a) CH_4, (b) *Biogas* and (c) *CO*.

5.1.4 Effects of inlet air temperature

Practically the preheated air temperature is common in the industrial furnaces for heat recovery to increase the furnace efficiency. Therefore the effects of air temperature on the centerline axial temperature profiles, axial wall temperature profiles and temperature contours are depicted in Figs. (5.23, 5.24, and 5.25). Methane fuel was proposed to carry out the simulation at $\lambda= 1.3$, $d_{a,i}/D=1$ and inlet air temperature varies from 20°C to 1000°C, and In this case the radiation model (P1) wasn't used (i.e., without radiation).

Figure 5.23 explains the influence of preheated air temperature (20, 250, 500, 750, and 1000°C) on the axial temperature profiles along the flame for CH_4 fuel at $\lambda= 1.3$. As illustrated in the Figure, the axial temperature distribution decreases with increasing the inlet air temperature, this trend observed up to $x/d_o \approx 120$, other than, in the range of (500−1000°C) the inlet air temperature has no effect on the axial profiles and in the range (20−250°C) the axial flame temperature increases with the inlet air temperature. The possible explanation is that the higher the air temperature the lower the air density and consequently less diffusion between the air and fuel. As a result, the high temperature zone areas concentrate near the wall away from the center (see Fig. 5.25). The wall temperature is important parameter because its effect on the life time of wall refractory. Therefore, Fig. 5.24 presents the influence of inlet air temperature on the axial wall temperature profiles. As shown in the Figure, the peak wall temperature increases and shifted to left with increasing the inlet air temperature. This because the higher air temperature the lower air density, and consequently less diffusion of combustion air into the fuel. The final result is the high temperature zone areas close to the inlet boundaries with increasing the inlet air temperature (see Fig. 5.25).
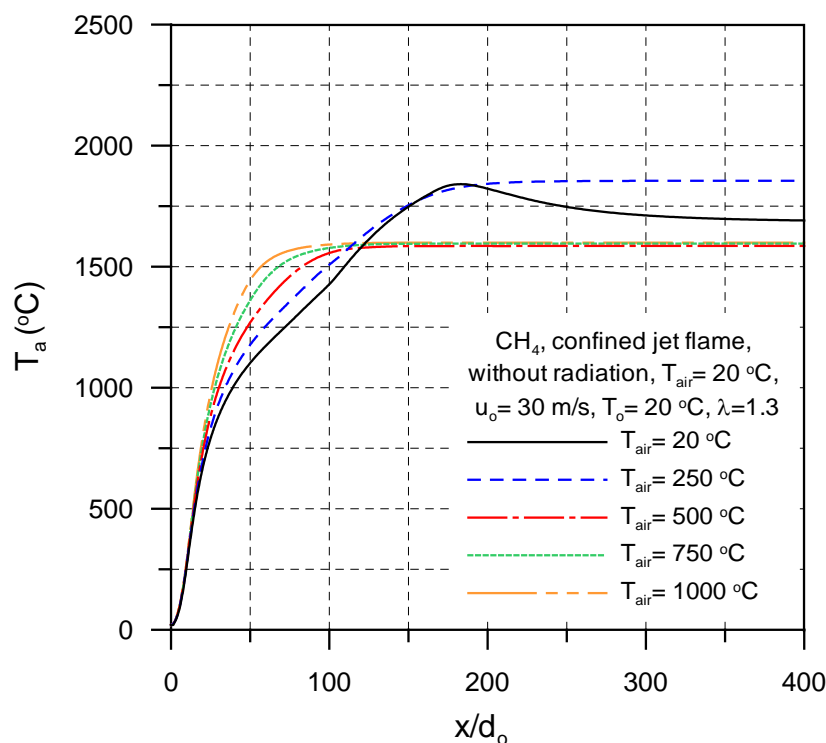
Figure 5.23: Influence of inlet air temperature on centerline axial temperature profiles using Methane fuel (CH_4) at $d_{a,i}/D=1$.
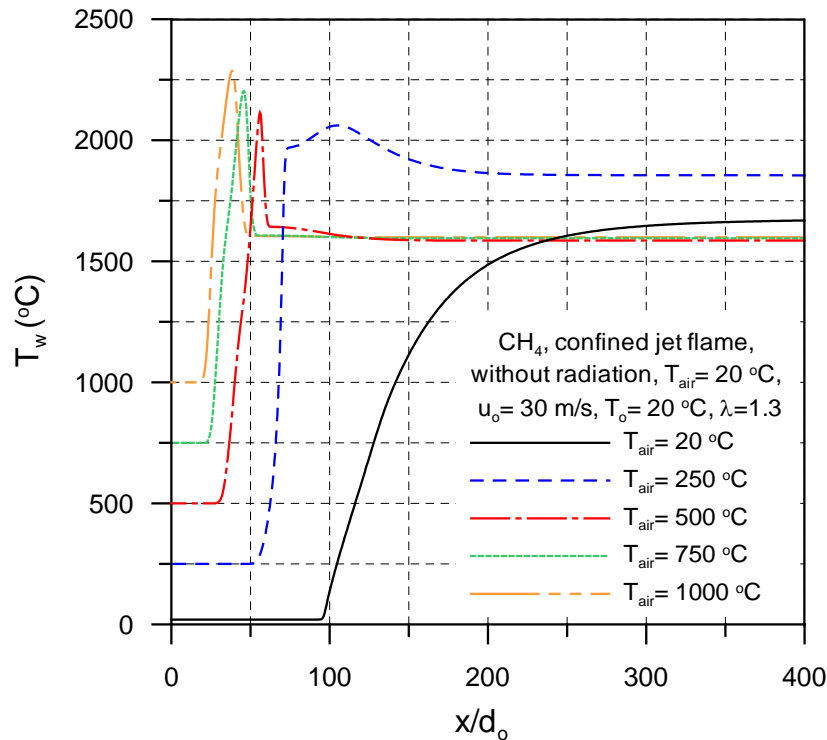
Figure 5.24: Influence of inlet air temperature on axial wall temperature profiles using Methane fuel (CH_4) at $d_{a,i}/D$=1.
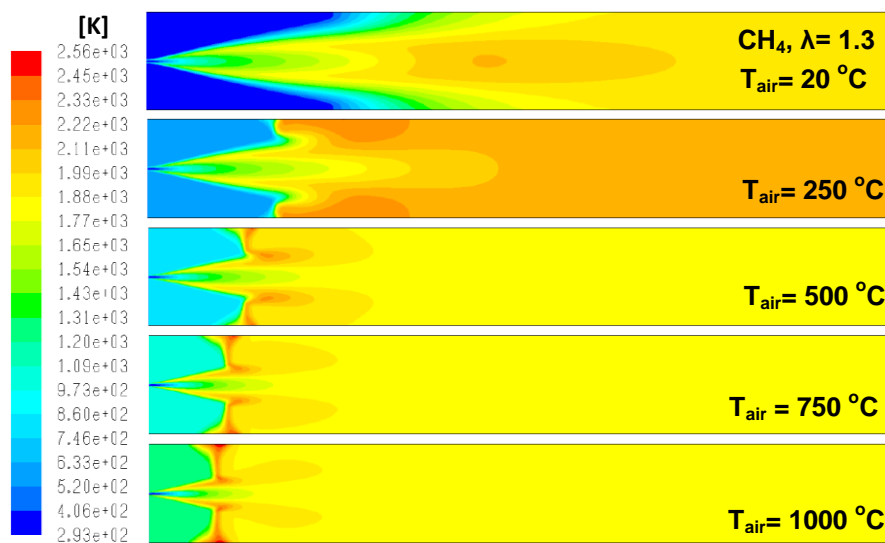

Figure 5.25: Influence of inlet air temperature on temperature contours at λ=1.3, $d_{a,i}/D$=1, T_o= 20°C, u_o= 30 (m/s) using Methane fuel (CH_4).

5.1.5 Effects of radiation

The influence of radiation on the axial temperature profiles, temperature contours, inverted dimensionless axial mean mixture fraction profiles, and mean mixture fraction contours is presented in Figs.(5.26− 5.29). Methane fuel was used to carry out the simulation for different excess air numbers (1.3, 1.7 and 2.3) at $d_{a,i}/D = 1$, the radiation model (P1) was used (i.e., with radiation calculation) and the results were presented and compared with the case of without radiation consideration.

Figure 5.26 shows the influence of radiation on the axial temperature profiles with the excess air number (1.3, 1.7, and 2.3) as a parameter for CH_4 fuel at $d_{a,i}/D = 1$. The peak flame temperature equals 1841°C, 1789°C and 1773°C for without radiation case and 1158°C, 1160°C and 1166°C for with radiation case at 1.3, 1.7 and 2.3 excess air number (λ), respectively. As we explained in free jet flame simulation, the excess air number reduces the peak flame and combustion gas temperatures, also the radiation reduces the peak flame temperature and shifted the temperature profile to down. This is due to the part of heat released by radiation added to the total heat released from the flame, hence the flame temperature drops. Also as shown in Fig. 5.26, the excess air number has a smaller effect on the temperature profiles in case of radiation presence. On the other hand the effect of excess air number is significant on the temperature profiles in case of without radiation consideration. The possible explanation is that the drop in the temperature profile due to released radiation overcome the drop in temperature profile due to increasing the excess air. So that the reduction in temperature profile due to increasing of excess air number is relatively small. Fig. 5.27 displays the flame temperature contours for Methane fuel at $\lambda = 2.3$, as we see, the lower flame temperature zones related with radiation consideration.

For confined jet flame, the radiation has a considerable effect on the flame length. Fig. 5.28 shows the influence of radiation on the inverted dimensionless axial mean mixture fraction profiles for Methane fuel at $d_{a,i}/D = 1$. As shown in the Figure the flame length shortens by ∼15 %, ∼13 %, and ∼12 % for (1.3, 1.7, and 2.3) excess air number, respectively in case of radiation consideration. These values of reduction in confined jet flame are much higher than the reduction in flame length in free jet Methane flame which was ∼4 % at 20°C air temperature. The effect of radiation on the mean mixture fraction contorts of methane fuel at $\lambda = 1.3$ is depicted in Fig. 5.29.

5.1.6 Effects of thermal burner power

The influence of of thermal burner power on the axial temperature profiles and temperature contours is shown in Figs.(5.30 and 5.31). Methane fuel was used to carry out the simulation for different thermal burner powers of 2.3 and 5 MW with burner diameters of 50 mm and 110 mm, respectively. The simulation was accomplished at 1.1 excess air number and $d_{a,i}/D = 1$, the radiation model (P1) was't used (i.e., without radiation calculation). As shown in the figures, the higher temperature profile and higher temperature zones are related with lower burner power ($d_o = 50mm$) and vice versa in case of higher burner power ($d_o = 110mm$). The possible explanation is that, the bigger the fuel nozzle diameter, the longer the flame length and consequently the lower flame heat flux distribution, then the lower axial temperature profile can be observed.
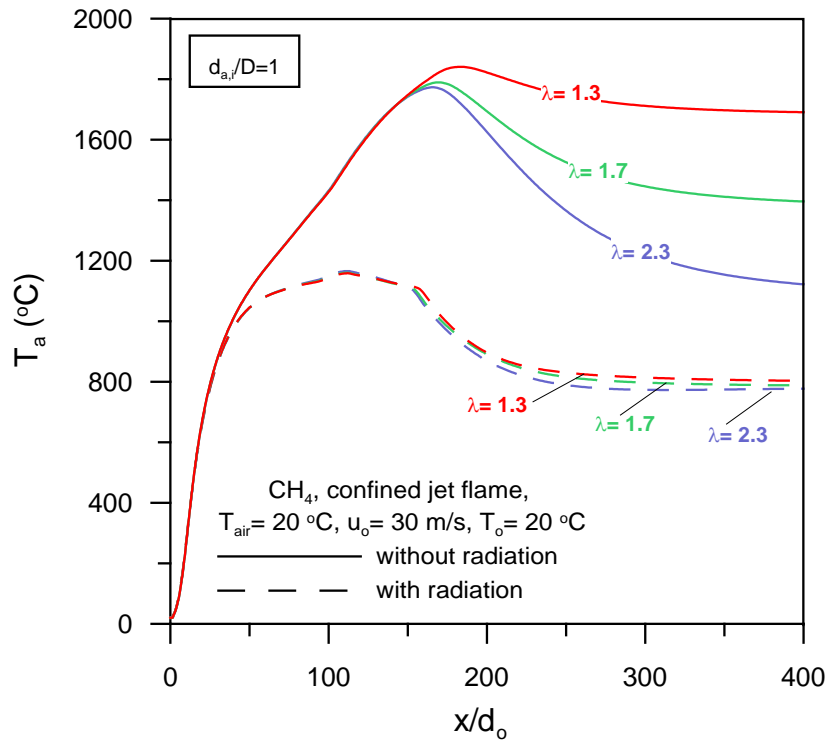
Figure 5.26: Influence of radiation on centerline axial temperature profiles at different excess air number, λ using Methane fuel (CH_4).
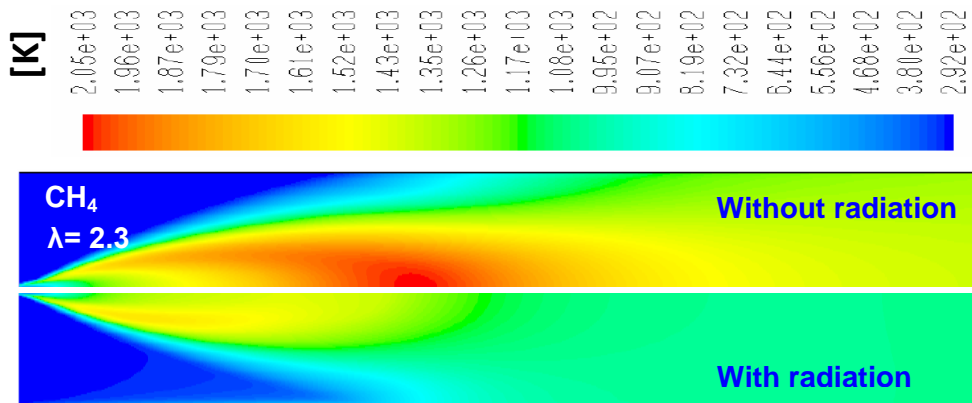

Figure 5.27: Influence of radiation on temperature contours along the flame using Methane fuel (CH_4) at different excess air number, T_{air}= 20°C, T_o= 20°C, u_o= 30 (m/s) and $d_{a,i}/D$=1.

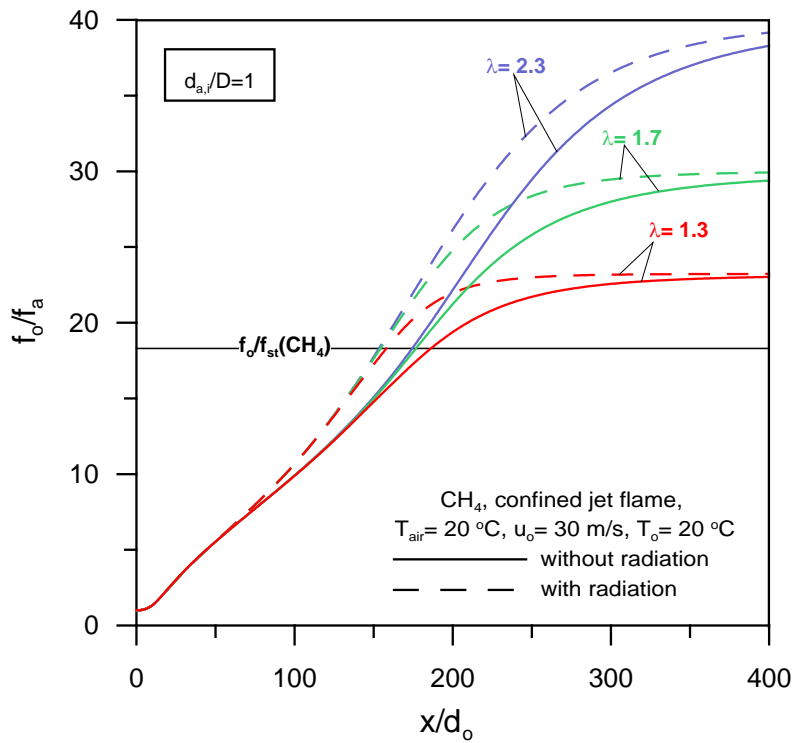Figure 5.28: Influence of radiation on inverted dimensionless axial mean mixture fraction profiles along the flame using Methane fuel (CH_4) at different excess air number.
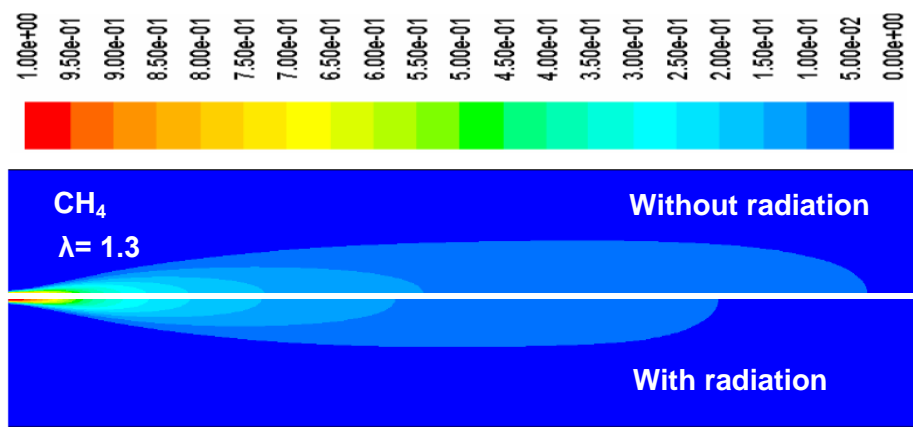
Figure 5.29: Influence of radiation on mean mixture fraction contours along the flame using Methane fuel (CH_4) at $\lambda= 1.3$, $T_{air}= 20°C$, $T_o= 20°C$, $u_o= 30$ (m/s).
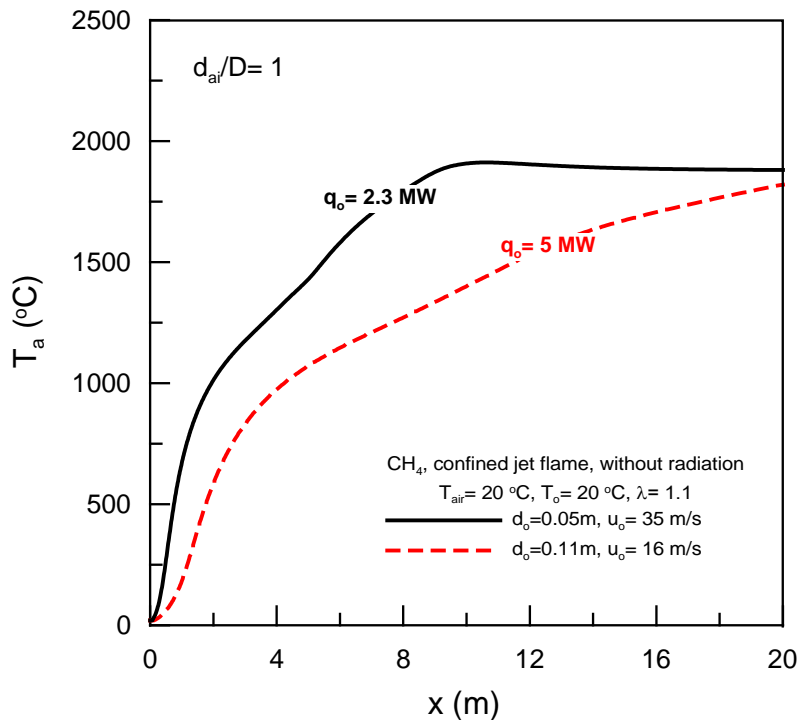
Figure 5.30: Influence of burner power on centerline axial temperature profiles at different burner diameters using Methane fuel (CH_4).
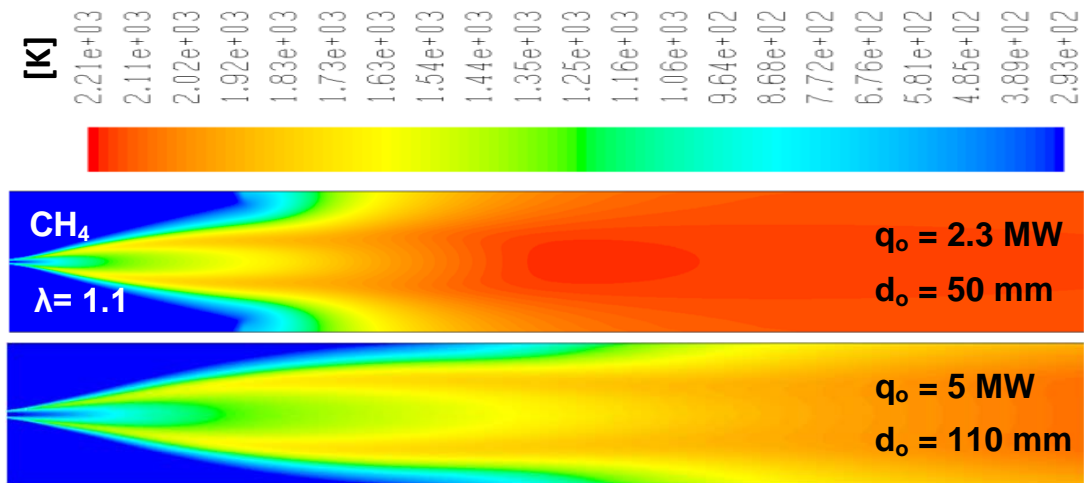
Figure 5.31: Influence of burner power on temperature contours along the flame using Methane fuel (CH_4) at different burner diameters, $T_{air}= 20°C$, $T_o= 20°C$ and $d_{a,i}/D=1$.

5.1.7 Fuels comparisons

As we explained in the previous Chapter, the flame length independent of the fuel velocity (refer to Sec.4.1), therefore the comparisons between three different gases were performed in two ways; constant fuel velocity and constant thermal burner power. From this situation, the comparison between three simulated gases (CH_4, $Biogas$, and CO) was carried out and presented at 30 m/s fuel velocity and at 2.30 MW thermal burner power and 20°C fuel temperature, in order to illustrate the flame behavior for different fuel gases as we see in the next paragraphs. Figures (5.32−5.39) explain the influence of kind of fuel on axial temperature profiles, temperature contours, axial mean mixture fraction profiles, mixture fraction contours, and the final Figures presents the effect of kind of fuel on the dimensionless flame length with excess air number as a parameter.

Figure 5.32 presents the comparisons of axial temperature profiles for CH_4, $Biogas$, and CO at $u_o=$ 30 (m/s), $\lambda=2.3$, $d_{a,i}/D=1$, and without radiation calculation. The results from the Figure show that the CO has the highest peak flame temperature $\sim$1950 °C at $x/d_o\approx41$, on the other hand $Biogas$ has the lowest peak flame temperature $\sim$1550 °C at $x/d_o\approx73$, whereas CH_4 has intermediate peak flame temperature $\sim$1800 °C at $x/d_o\approx174$. This results have approximately the same as free jet flame at 20°C air temperature. As depicted in Fig. 5.34 the CH_4 has the biggest flame volume and intermediate peak flame temperature, but the CO has the highest peak flame temperature and smallest flame volume, whereas the $Biogas$ has the lowest peak flame temperature and intermediate flame volume. The same conclusions were obtained from free jet flame (see Fig. 4.20).

Figure 5.36 explains the inverted dimensionless axial mean mixture fraction profiles a long the flame, in order to calculate the flame length for the same gases under the same previous conditions. As shown in the Figure, CH_4 has the longest flame length, CO has the shortest flame length, and $Biogas$ in between of them, this conclusion is similar as in free jet simulation (see Fig. 4.21).

The flame length in dimensionless form versus excess air number for CH_4, $Biogas$, and CO fuels at 30 m/s fuel velocity, $d_{a,i}/D=1$ and 20°C air temperature without radiation calculation is illustrated in Fig. 5.38. As shown in the Figure, CH_4 has the longest flame length profiles, then $Biogas$ after that CO. Also the results explain that the excess air number in the range from 1.1 to 1.5 has a considerable effect on the flame length, other than it has approximately no effect on the flame length.

Figures (5.33, 5.35, 5.37, and 5.39) present the comparisons between CH_4, $Biogas$, and CO at $q_o=$ 2.3 (MW), $\lambda=1.3$, $d_{a,i}/D=1$, and without radiation calculation. The results from these figures give the same conclusions and the same flame behavior which obtained form the case of constant fuel velocity comparisons.
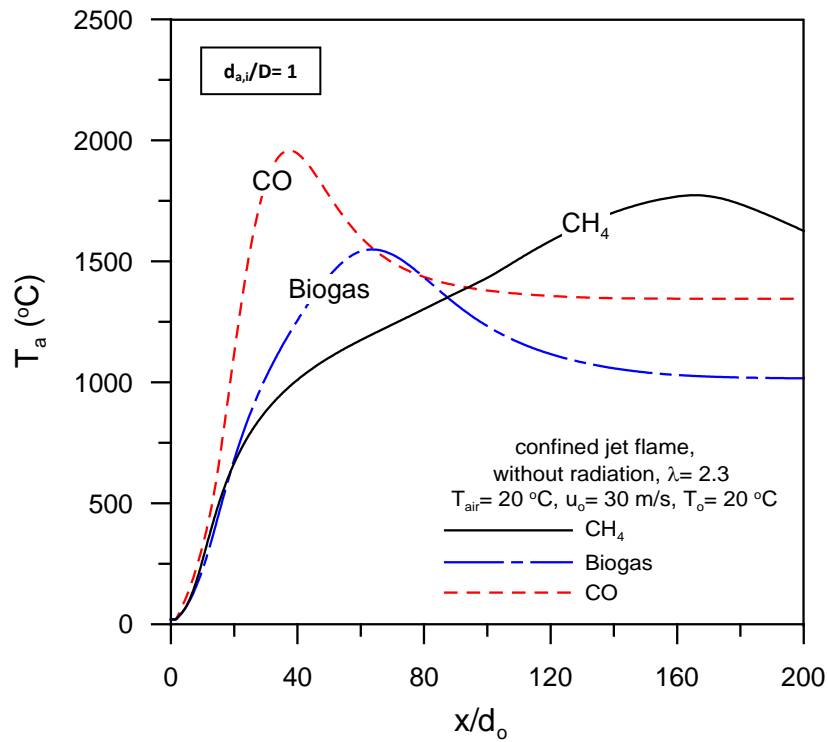
Figure 5.32: Comparison of centerline axial temperature profiles along the flame for different fuels (CH_4, $Biogas$ and CO) at constant fuel velocity.
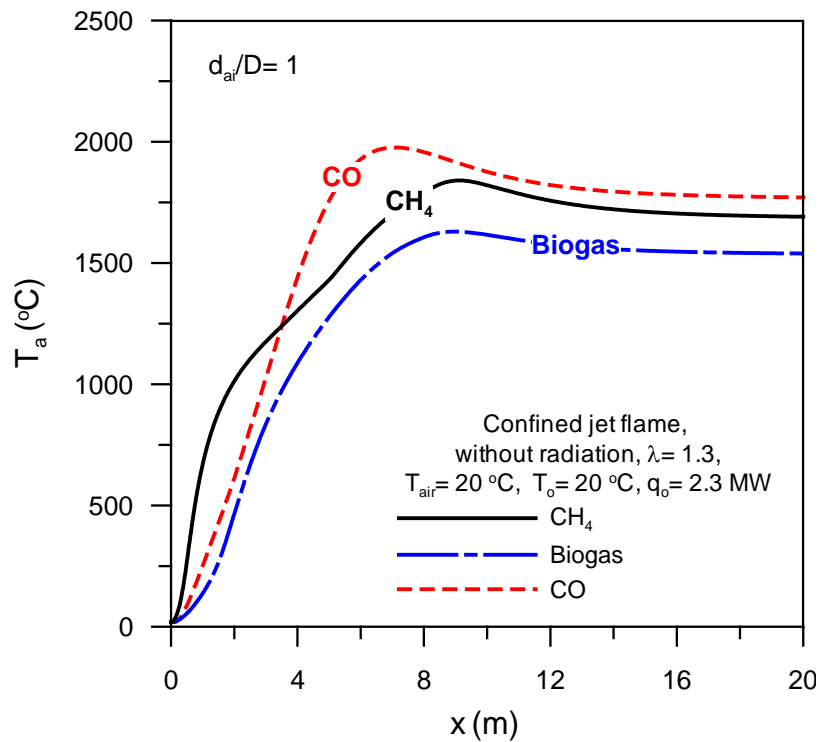

Figure 5.33: Comparison of centerline axial temperature profiles along the flame for different fuels (CH_4, $Biogas$ and CO) at constant thermal burner power.
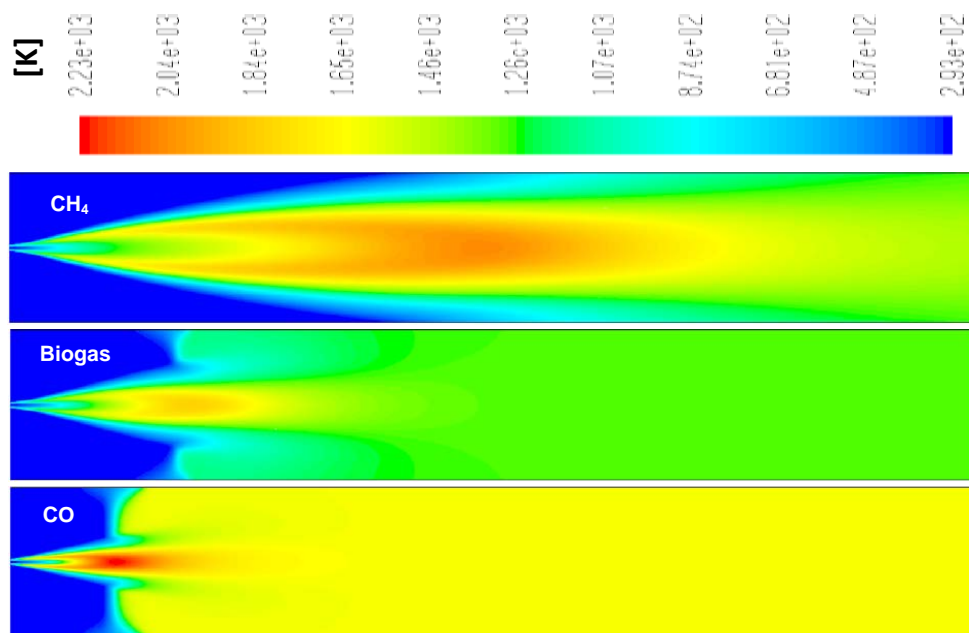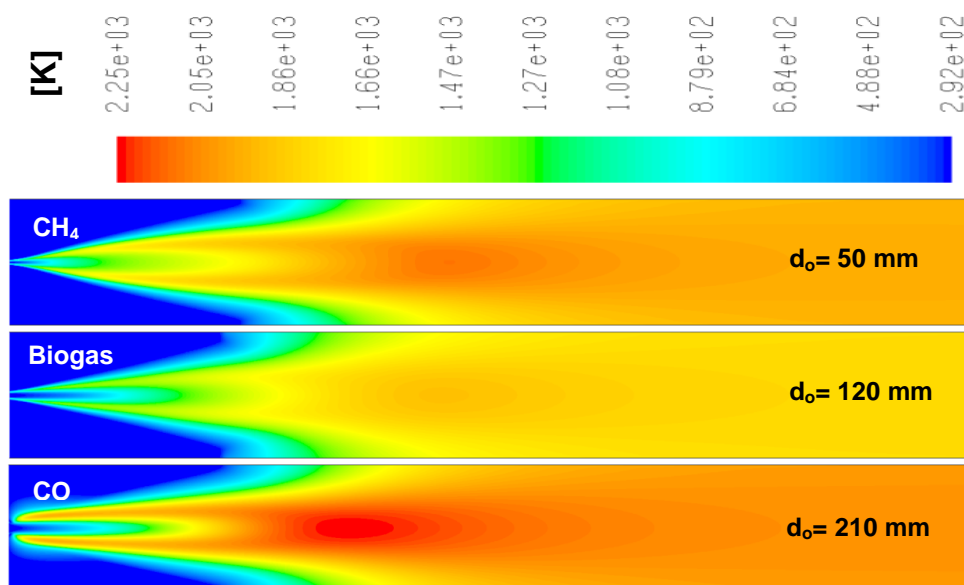
Figure 5.34: Comparison of temperature contours along the flame for different fuels (CH_4, *Biogas* and *CO*) at λ= 2.3, T_{air}= 20°C, T_o= 20°C, u_o= 30 (m/s) and $d_{a,i}/D$=1.

Figure 5.35: Comparison of temperature contours along the flame for different fuels (CH_4, *Biogas* and *CO*) at λ= 1.3, T_{air}= 20°C, T_o= 20°C, q_o= 2.3 (MW) and $d_{a,i}/D$=1.
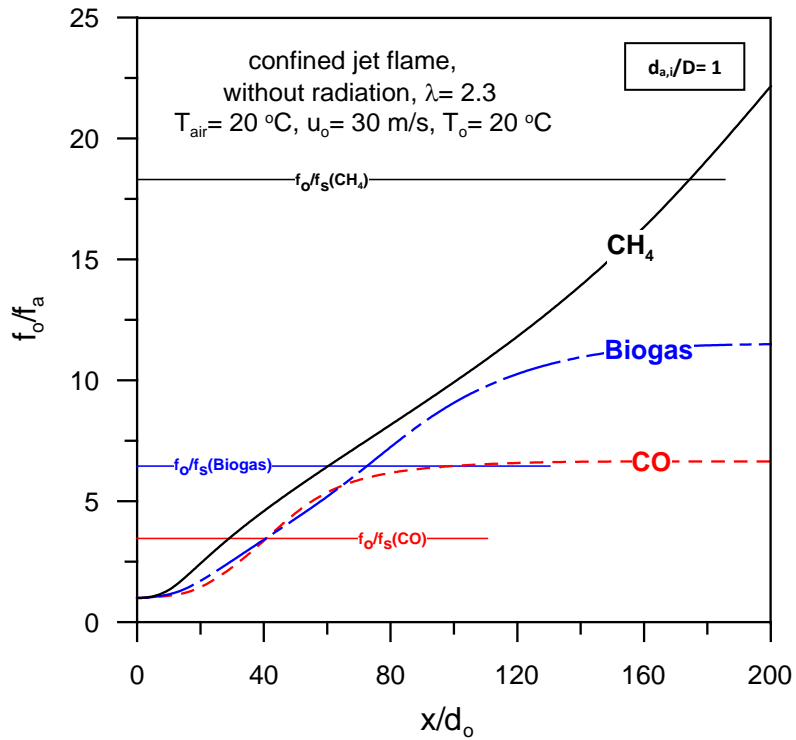
Figure 5.36: Comparison of inverted dimensionless axial mean mixture fraction along the flame for different fuels (CH_4, $Biogas$ and CO) at constant fuel velocity.
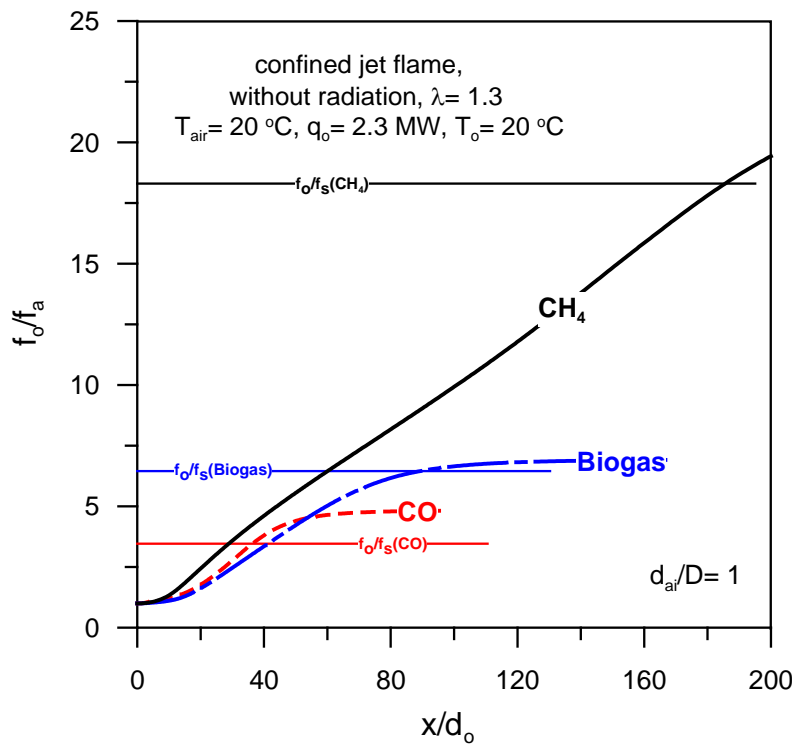
Figure 5.37: Comparison of inverted dimensionless axial mean mixture fraction along the flame for different fuels (CH_4, $Biogas$ and CO) at constant thermal burner power.
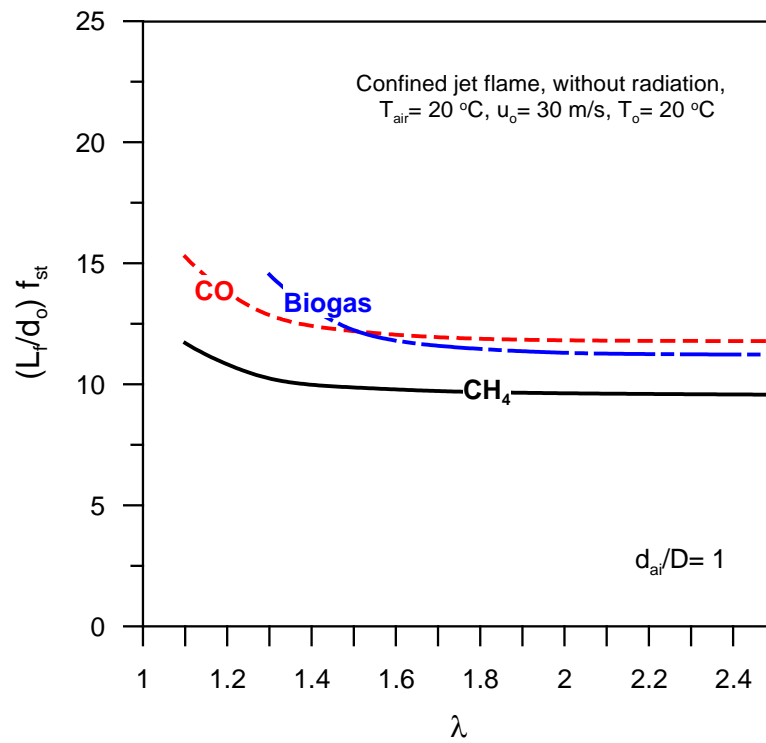
Figure 5.38: Comparison of flame length trends with excess air number for different fuels (CH_4, $Biogas$ and CO) at constant fuel velocity.
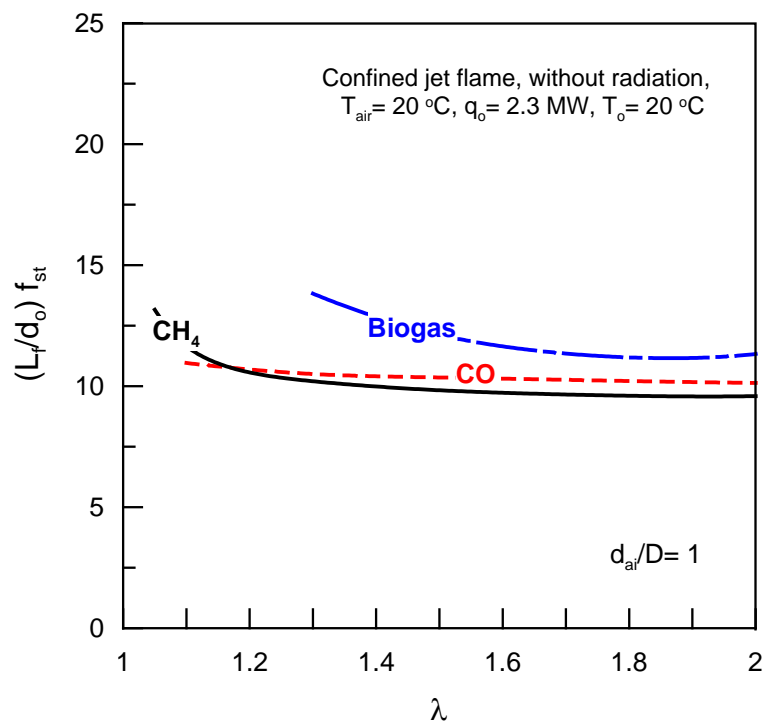

Figure 5.39: Comparison of flame length trends with excess air number for different fuels (CH_4, $Biogas$ and CO) at constant thermal burner power.

5.1.8 Prediction of flame length correlations

The confined flame length in dimensionless form in terms of excess air number and air demand (mass basis) can be obtained from the computed results of the present study using regression analysis as follows:

$$\frac{L_f}{d_o} = 18.24\lambda^{-0.23}(1 + L)^{0.83} \tag{5.6}$$

Equation 5.6 was found for data in the following ranges: $2.46 \leq L \leq 17.3$; $1.1 \leq \lambda \leq 2.5$; and at $T_{air}= 20°C$; $T_o= 20°C$, and $d_{a,i}/D=1$. The prediction of this equation is presented in Fig. 5.40, the correlation can predict 100% of the numerical results within error $\pm 13\%$. From correlation 5.6 we can conclude that the flame length is direct proportional with air demand and reverse proportional with excess air number, and the confined flame length is higher than the free jet flame length. This is due to introduce of excess air number term in Eqn. 5.6 if it is compared with Eqn.4.2. In addition to the constant term in confined flame length correlation is higher than that of free jet flame length correlation.

Another flame length correlation in dimensionless form was correlated in terms of stoichiometric mean mixture fraction, fuel density, and stoichiometric density (density of combustion gas at stoichiometric mixture fraction) and excess air number. The predicted correlation was correlated from the computed results of the present study using regression analysis as follows:

$$\frac{L_f}{d_o} = \frac{5.5}{f_{st}} \left(\frac{\rho_o}{\rho_{st}} \right)^{1/2} \left(\frac{1}{\lambda^{0.23}} \right) \tag{5.7}$$

Equation 5.7 was found for data in the following ranges: $0.055 \leq f_{st} \leq 0.289$; $1.1 \leq \lambda \leq 2.5$; and at $T_{air}= 20°C$; $T_o= 20°C$, and $d_{a,i}/D=1$. The prediction of this equation is presented in Fig. 5.41, the correlation can predict 100% of the numerical results within $\pm 8\%$. On the same manner we can conclude that, the flame length is reverse proportional with both excess air number and stoichiometric mean mixture fraction. As well Eqn. 5.7 was obtained on the same shape of free jet flame length correlation (Eqn. 4.3) in addition to the excess air number term which introduced into the confined jet flame length correlation. On the same way of free jet simulation, we can use the same approximation term (see Eqn.4.4). The maximum deviation obtained between numerical correlation 5.7 and its approximation using Eqn. 4.4 is $\pm 8\%$.

On the other hand, flame length correlation in dimensionless form in terms of excess air number, air demand (mass basis) and air inlet diameter in dimensionless shape can be correlated from the computed results of the present study using regression analysis as follows:

$$\frac{L_f}{d_o} = 19.7\lambda^{-0.23}(1 + L)^{0.8} \left(\frac{d_{a,i}}{D} \right)^{0.06} \tag{5.8}$$

Equation 5.8 was correlated for data in the following ranges: $2.46 \leq L \leq 17.3$; $1.3 \leq \lambda \leq 2.5$; and $0.4 \leq d_{a,i}/D \leq 1$ at $T_{air}= 20°C$; $T_o= 20°C$. The prediction of this equation is presented in Fig. 5.42. This correlation can predict 83% of the numerical results within $\pm 11\%$. The previous correlation demonstrates that the flame length is direct proportional with both

air demand (mass basis) and air inlet diameter and reverse proportional with excess air number. Eqn. 5.8 is a modified shape for Eqn. 5.6 by introducing the effect of air inlet diameter size in dimensionless form. Finally, a modified correlation for Eqn. 5.7 and it was correlated by introducing the term of $d_{a,i}/D$ as an influencing parameter on the form of:

$$\frac{L_f}{d_o} = \frac{5.5}{f_{st}} \left(\frac{\rho_o}{\rho_{st}}\right)^{1/2} \left(\frac{1}{\lambda^{0.23}}\right) \left(\frac{d_{a,i}}{D}\right)^{0.06} \tag{5.9}$$

Equation 5.9 was correlated for data in the following ranges: $0.055 \leq f_{st} \leq 0.289$; $1.3 \leq \lambda \leq 2.5$; and $0.4 \leq d_{a,i}/D \leq 1$ at $T_{air} = 20°C$; $T_o = 20°C$. The prediction of this equation is presented in Fig. 5.43, the correlation can predict 98 % of the numerical results within ± 11 %.

5.1.9   Comparisons with literature

The comparisons between experimental measurements presented by Kim et al., 2007 [73] for confined jet flame and present CFD results were conducted and presented in Figs (5.44, 5.45 and 5.46) in order to validated the numerical models. Figure 5.44 displays a comparison between numerical simulation (with and without radiation) and experimental results, presented by Kim et al. (2007) [73], at $T_{air} = 300$ K; $T_o = 300$ K, $d_o = 2.7$ mm, and $\lambda = 6.17$ for axial temperature versus axial mean mixture fraction. As shown in the Figure the numerical results give good agreement with experimental measurements.

While, Fig. 5.45 presents the mass fraction of H_2 and CO against mean mixture fraction for both numerical and experimental results reported by Kim et al. [73] at same previous conditions. As shown in the Figure, the numerical results have the same trends with experimental results, but give higher values than experimental measurements. The difference between experimental and computed results owing to inherent simplifying assumptions in the turbulence and combustion models and due to experimental measurements error. Also a comparison between experimental and numerical flame lengths for both $d_o = 2.7$ mm and 4.4 mm at different fuel velocities was carried out and depicted in Fig. 5.46. As shown in the Figure the numerical simulation gives satisfactory agreement with experimental measurements. The discrepancy is due to the difference of definitions of the flame length, numerical assumptions and experimental uncertainty as we stated before. Also as we see in Fig. 5.46, the maximum deviation obtained between measured and computed flame length is ± 18 %.

Figure 5.47 shows the jet flame lengths in dimensionless form correlated with flame Froude numbers, only turbulent flame results are plotted in this Figure using Delichatsios's [24] flame Froude number and dimensionless flame length parameter, because most of industrial combustors operate in turbulent regime. The measured dimensionless flame lengths are well correlated by Delichatsios's [24] correlations expressed in Eqs. 2.5 and 2.6 correspond to measurements by Kalghatgi [64] for experimental data of Hydrogen, Propane, and Methane. As we see in Fig. 5.47 a comparison between computed results using Methane fuel for different nozzle diameters (2.7, 4.4 and 50 mm) and Kalghatgi measurements and Delichatsios's correlations was carried out and presented. The simulated results show that the flame Froude number has no effect on the dimensionless flame length and the dimensionless Methane flame length has approximately constant value $L^* \approx 13$. Also the computed Methane dimensionless flame lengths lay around the data of Kalghatgi and give satisfactory agreement with the measurements.
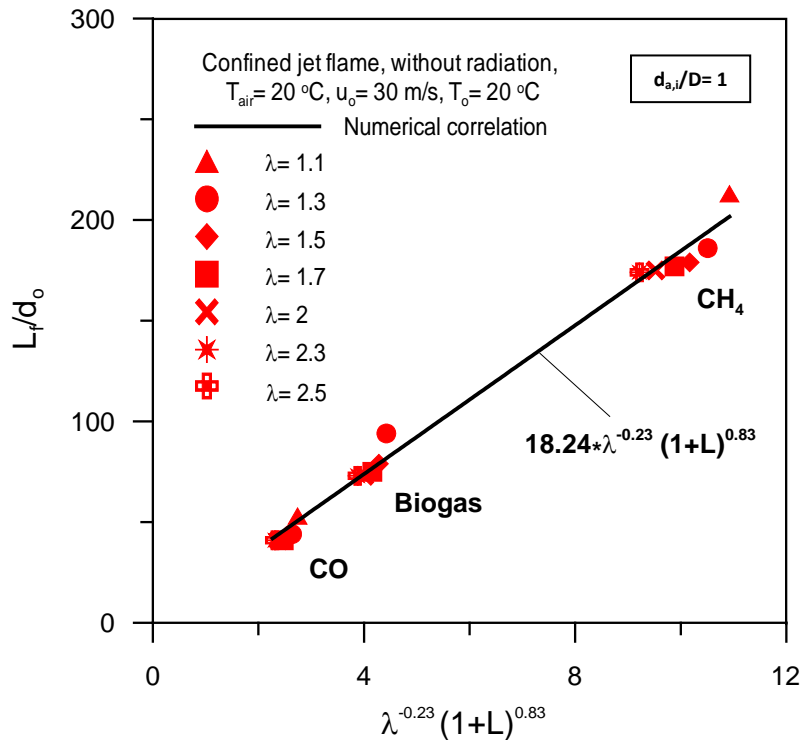
Figure 5.40: Prediction of dimensionless confined jet flame length correlation in terms of air demand (L) and excess air number (λ).
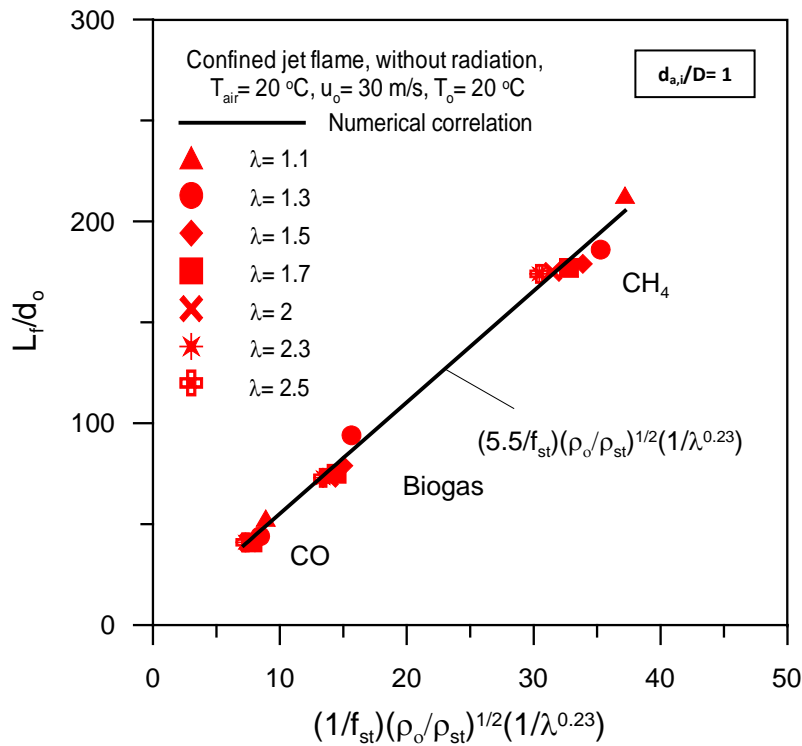

Figure 5.41: Prediction of dimensionless confined jet flame length correlation in terms of f_{st}, ρ_o, ρ_{st} and λ.
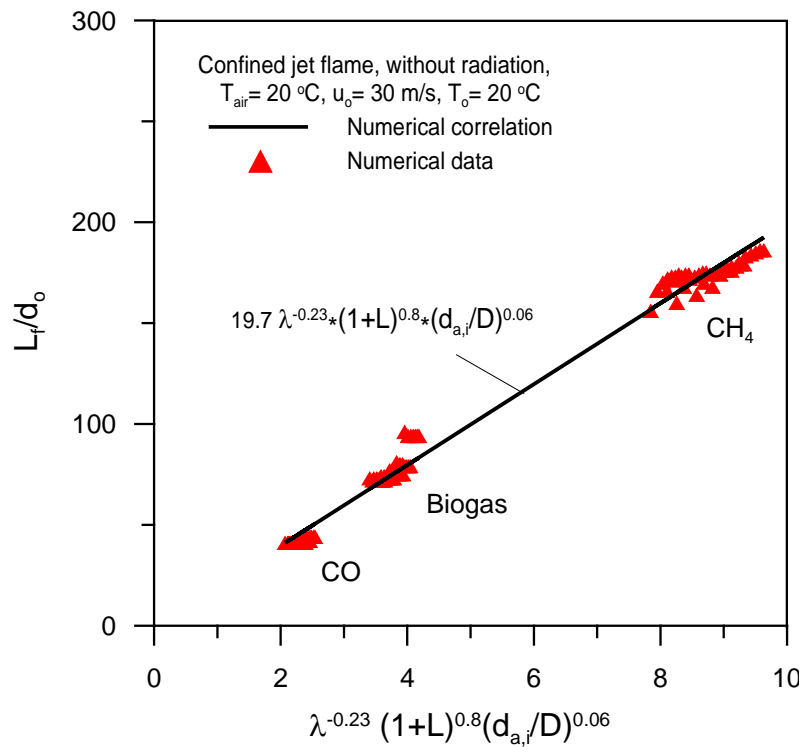
Figure 5.42: Prediction of dimensionless confined jet flame length correlation in terms of air demand (L) excess air number (λ) and dimensionless air inlet diameter ($d_{a,i}/D$).
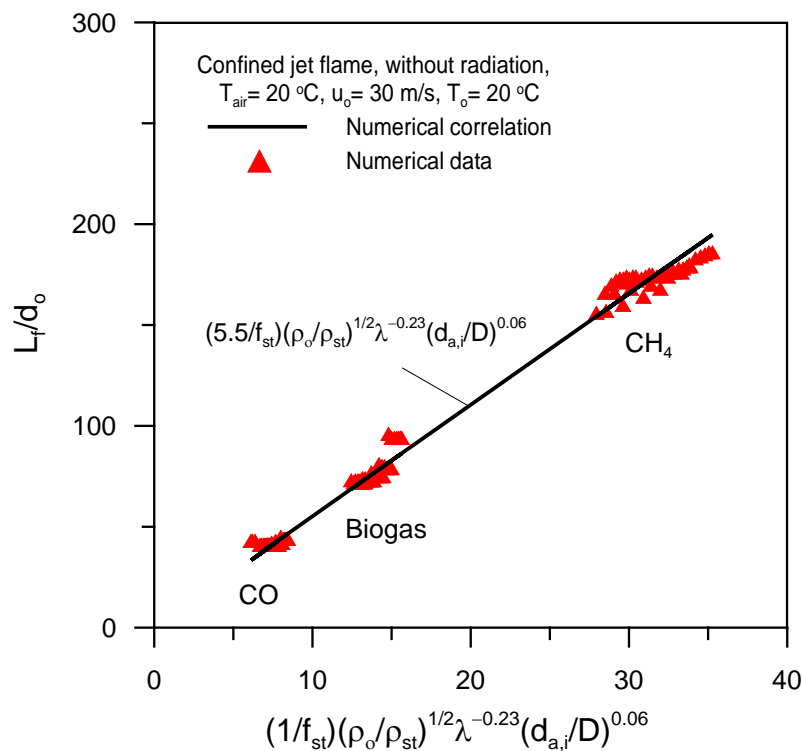

Figure 5.43: Prediction of dimensionless confined jet flame length correlation in terms of f_{st}, ρ_o, ρ_{st} and λ, and $d_{a,i}/D$.
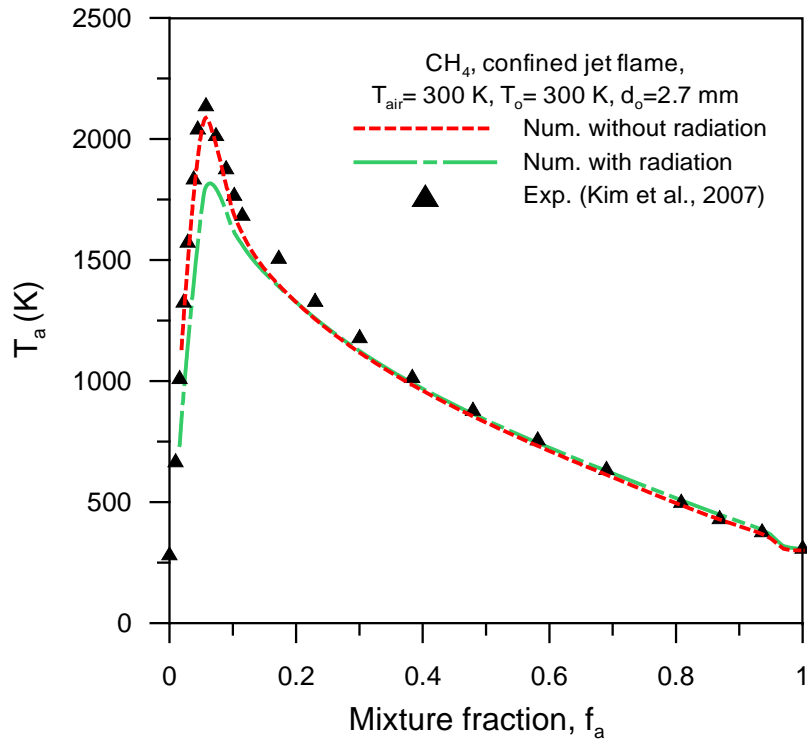
Figure 5.44: Comparison of numerical and experimental measurements of centerline axial temperature profiles versus mixture fraction.
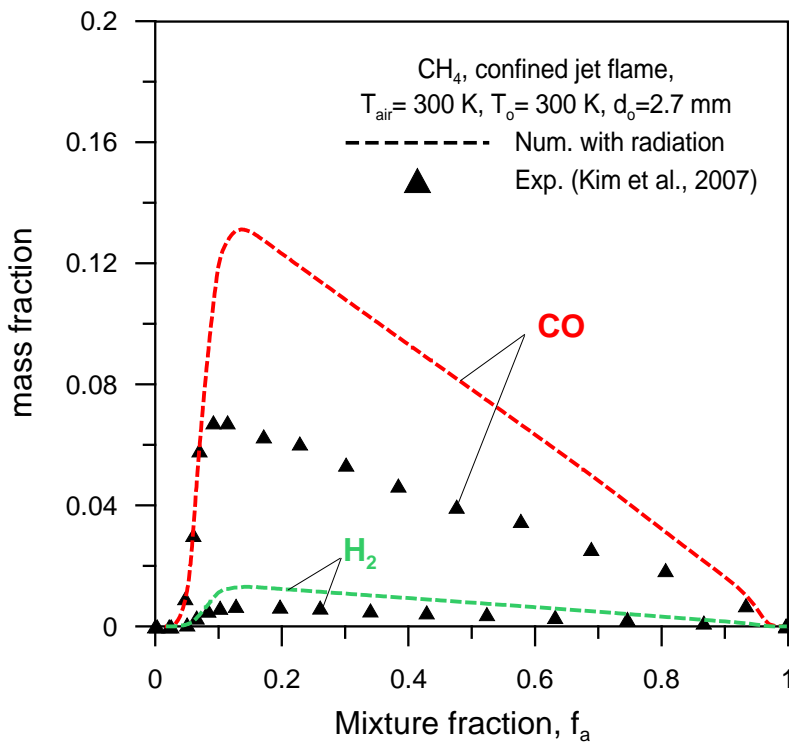

Figure 5.45: Comparison of numerical and experimental measurements for centerline axial mass fraction profiles of CO and H_2 versus mixture fraction.
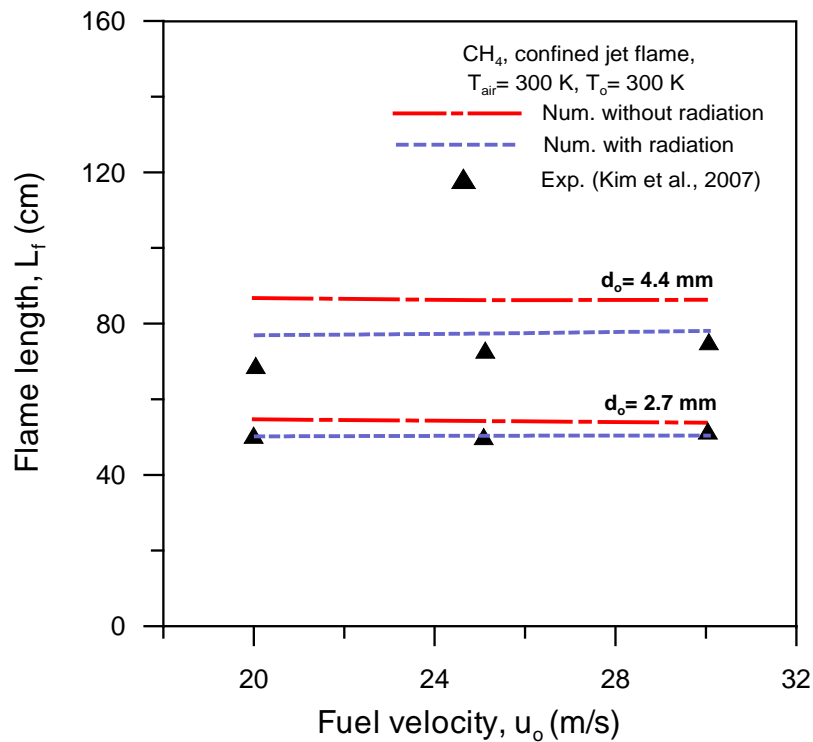
Figure 5.46: Comparison of numerical and experimental measurements of flame length versus fuel velocity at different fuel nozzle diameter using Methane fuel (CH_4).
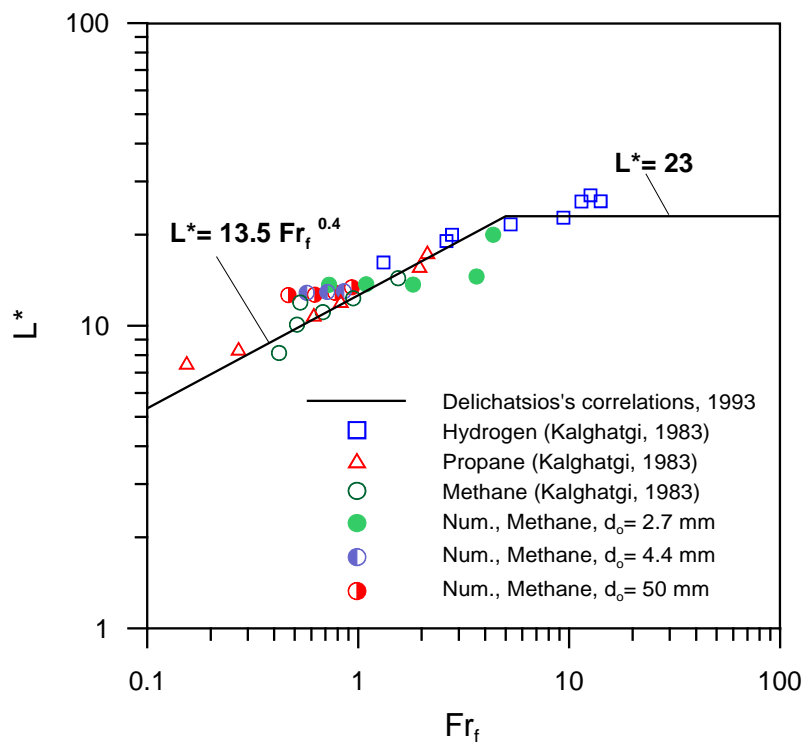

Figure 5.47: Comparison of numerical and experimental correlation and measurements of dimensionless flame length against flame Froude number for different fuels.

5.2   Annulus tube burner with fully opened cylinder for secondary air

As presented in Chapter 4 (free jet flame simulation), most of industrial burners are concentric type burners (i.e., annulus type). Now we want to show the effect of confinement on the flame behavior and flow visualization using annulus type burners. Therefore, the effects of primary air swirl, annulus diameter, secondary air temperature, secondary air velocity profiles and air swirl side on the flame characteristics were presented and discussed in the following subsections. In this section annulus tube burner with fully opened cylinder for secondary air was proposed to study (see Fig. 5.48). In the simulation the fuel nozzle diameter is 50 mm, the annulus diameter size in dimensionless form described as the ratio of primary air diameter to fuel nozzle diameter, d_p/d_o and has three simulated values of 2.3, 3.65 and 5.05, the primary air ratio (α) equals 0.1 and the excess air number (λ) equals 1.3. Methane was used as a fuel in this configuration at 30 m/s fuel velocity, 20°C fuel temperature and the radiation effect wasn't considered in this section.
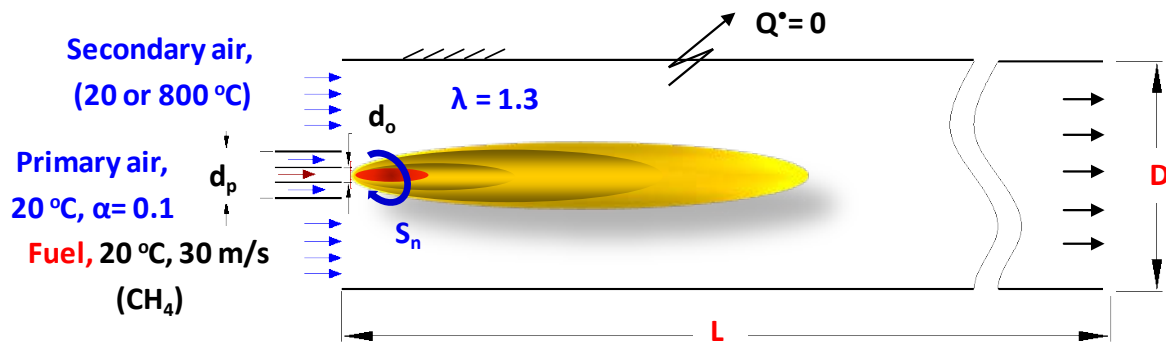

Figure 5.48: Schematic diagram of confined flame (annulus tube burner with fully opened cylinder for secondary air).

5.2.1   Effects of primary air swirl

The burner stability has a significant influence by air swirl as we explained in Chapter 4 (refer to Sec.4.3.3). By studying this influencing parameter, two cases were proposed for simulation at primary air swirl number (S_n) changes from 0 to 1. In the first case the primary air temperature (T_{pa}) is similar to the secondary air temperature (T_{sa}) and they presented as air temperature (T_{air}) and equals 20°C. Two annulus diameter sizes in dimensionless form were used d_p/d_o= 2.3 and 5 and the secondary air axial velocity profile was uniform distribution at the entrance of secondary air. While the second case has 20°C primary air temperature and 800°C secondary air temperature. The annulus diameter in dimensionless form which used is d_p/d_o= 2.3 and the secondary air axial velocity profile was linear distribution at the entrance of secondary air and obey to the following correlation:

$$u_a = 0.1977r - 0.0123 \tag{5.10}$$

Regarding to the former case, Figs.(5.49−5.53) show the effects of primary air swirl number (S_n) on the centerline axial temperature profiles, velocity vectors, inverted

dimensionless axial mean mixture fraction profiles and flame length for d_p/d_o= 2.3 and 5. Whereas, Figs. (5.55−5.54) display the effect of primary air swirl number on the centerline axial temperature profiles, axial wall temperature profiles, radial temperature profiles, and temperature contours for latter case.

Figure 5.49 explains the variation of centerline axial temperature profiles along the flame axis, with different annulus primary air swirl number as a parameter, and at different dimensionless annulus burner diameters (2.3 and 5) which compared with the reference case; without swirl (i.e., S_n= 0). As it was observed in the Figure, the peak flame temperature shifted to right by $\sim$20 % and $\sim$6 % with increasing the swirl number from 0 to 1 for d_p/d_o= 2.3 and 5, respectively and their values remain fixed. That means the effect of primary air swirl number on the location of peak flame temperature diminishes with increasing the annulus diameter size at certain excess air number. And vice versa with increasing the excess air number up to infinity value (i.e., free jet flame), at free jet case, the effect of primary air swirl is significant on the location of peak flame temperature (refer to Sec.4.3.3). The possible explanation is that the higher the primary air swirl the lower the recirculation zone size, and consequently less diffusion of air into the fuel (see Figs. 5.50 and 5.51). The less penetration of air into fuel causes an increase in the flame length and in consequence a shift in peak flame temperature can be obtained.

The influence of annulus air swirl on the inverted dimensionless axial mean mixture fraction profiles to estimate the effect of swirl on the flame length was explained in Fig. 5.52, for different annulus diameters (d_p/d_o= 2.3 and 5). As shown in the Figures, the swirl number has a considerable effect on the mixture fraction profiles and consequently on the flame length. Similarly as we explained above, the flame length increases with increasing the swirl number, this is because the less penetration of the air into fuel as a result of less diffusion of air into the fuel, hence the combustion process can't complete in short distance, therefor the flame must be expand to complete the oxidation reaction. The final result is an increasing in the flame length with increasing the air swirl number. This effect is considerable with low annulus air diameter and it diminishes with high annulus diameter at constant excess air number. Also as we see in the Figures the flame length increases by $\sim$20 % and $\sim$6 % with increasing the swirl number from 0 to 1 for d_p/d_o= 2.3 and 5, respectively. The computed results of the dimensionless flame lengths versus the primary air swirl number were presented in Fig. 5.73 for different annulus diameter sizes of 2.3 and 5. As shown in the Figure, the swirl number has a considerable effect on the flame length at d_p/d_o=2.3 and has a small effect on the flame length at d_p/d_o=5.

As it known that the preheated air temperature is common in the industrial furnaces for heat recovery in order to increase the furnace efficiency. Also the axial velocity profile of secondary air at the entrance assumed to be uniform distribution but actually it isn't uniform. Therefore the effects of primary air swirl number on the centerline axial temperature profiles, axial wall temperature profiles, radial temperature profiles, and temperature contours are depicted in Figs. (5.55, 5.56 and 5.54). Figure 5.55 (a) explains the influence of primary air swirl number, S_n (0, 0.3, 0.5, 0.7, and 1) on the axial temperature profiles along the flame for CH_4 fuel at d_p/d_o=2.3. As illustrated in the Figure, the centerline axial temperature profiles decreases with increasing the primary swirl number. This trend observed from $x/d_o \approx 40$ to $x/d_o \approx 140$, other than, the swirl number has no

effect on the temperature profiles. This can be attributed to the higher the primary air swirl with high secondary air temperature, the lower air diffusion into the fuel, hence the high temperature zone areas increase and concentrate away from the center (see Fig. 5.54).

The wall temperature is important parameter because its effect on the life time of the wall refractory. So, Fig. 5.55 (b) shows the influence of primary air swirl number on the axial wall temperature profiles. As shown in the Figure, the peak wall temperature shifted to lift with increasing air swirl number without changing its value. This is because the combined effect of primary air swirl and high secondary air temperature, the higher the air temperature, the lower the air density, so, the secondary air temperature reduces the air diffusion into the fuel, while the primary air swirl improves the mixing near the wall with help of the linear velocity profile, as a result in the high temperature zone area increases and the wall peak temperature moved towards the secondary air entrance with the increase of primary air swirl number (see Fig. 5.54).

The effect of primary air swirl on the radial temperature profiles at different distances from the burner tip (x=3 m and 5 m) is shown in Fig. 5.56. As shown in the Fig. 5.56 (a) at x=3 m, the radial temperature distribution increases with the increase of primary air swirl, this effect observed up $r/R = 0.5$. The reasons were explained above. Similarly, Fig. 5.56 (b) shows the same effect of primary air swirl at x=5 m, but this effect appears up $r/R = 0.2$. The final concluded remark is the radial temperature profile deviations decrease (i.e., tends to homogenous distribution) if the calculated plane far away from the burner tip.

5.2.2   Effects of annulus diameter

As explained in Chapter 4, concerning to the flame stability; the concentric type burners (i.e., annulus type) are used in most industrial burners which are commonly use with the confined flame. Therefore the effects of annulus diameter in dimensionless form on the centerline axial temperature profiles, inverted dimensionless axial mean mixture fraction profiles, velocity vectors, temperature contours and mean mixture fraction contours were presented in Figures 5.57 and 5.58 and discussed in the following paragraphs.

Fig. 5.57 (a) shows the centerline axial temperature profiles for different annulus diameter sizes in dimensionless form, d_p/d_o (2.3 and 5) and at T_{pa}=20°C, T_{sa}=20°C, and S_n=0.5. As displayed in the Figure, the temperature profile shifted to right with increasing the annulus diameter, and the value of peak flame temperature did't change. This can be attributed to the increase in the primary air velocity with decreasing the annulus diameter. Increasing the primary air velocity improves the mixing process between the air and fuel, hence the reaction between the oxidizer and fuel completed in short distance from the burner tip. As a result in the peak flame temperature shifted to left and consequently the flame length shortened with decreasing in annulus diameter size (see Fig. 5.57 (b)). As shown in Fig. 5.57 (a) and (b), the peak flame temperature shifted to right and the flame length increases by ∼19% and ∼19%, respectively with increasing d_p/d_o from 2.3 to 5.

The velocity vectors colored by temperature for different d_p/d_o (2.3 and 5) was depicted in Fig. 5.58 (a). As appeared in the figure the recirculation size decreases with

increasing the annulus diameter size. This recirculation effect shifted the peak flame temperature to right direction as shown in Fig. 5.58 (b) and it increased the flame length as presented in Fig. 5.58 (c).

5.2.3   Effects of secondary air temperature

Practically the preheated air temperature is common in the industrial furnaces for heat recovery to increase the furnace efficiency. Therefore the effects of secondary air temperature on the centerline axial temperature profiles, axial wall temperature profiles, temperature contours and velocity vectors are depicted in Figs. 5.59 and 5.60 and discussed as follows. Influence of the secondary air temperature (20, 200, 400, 600, 800, and 1000°C) on the centerline axial temperature profiles are shown in Fig. 5.59 (a) for CH_4 fuel at d_p/d_o=2.3, T_{pa}=20°C, T_{sa}=20°C and S_n=0. As shown in the Figure, the centerline axial temperature distribution increases with increasing the secondary air temperature from 20 to 200°C, other than, the temperature distribution decreases with increasing T_{sa}, up 600°C, the secondary air temperature has no effect on the centerline axial temperature profile. Fig. 5.59 (a) is similar to Fig. 5.23, but there is a small difference due to the parameter of primary air ratio by using concentric type burner instead of simple tube burner as in the latter Figure. On the same way, Fig. 5.59 (b) is similar to Fig. 5.24, where the peak wall temperature increases and shifted to left with increasing the secondary air temperature. This can be attributed to the higher air temperature the lower air density, and consequently the less diffusion of combustion air into the fuel. The final result is high temperature zone area closes to the air entrance with increasing the secondary air temperature (see Fig. 5.60 (a)). Also as shown in Fig. 5.60 (b), the recirculation size increases with increasing the secondary air temperature, this is because the secondary air momentum reduces with increasing secondary air temperature and it is lower enough to satisfy the requirements for entrainment, so the primary jet will entrain the secondary air causes recirculation, for more details refer to reference [41].

5.2.4   Effects of secondary air velocity profile

A comparison between uniform velocity profile and linear velocity profile for axial secondary air velocity at the entrance was conduced and presented in Figs. 5.61 and 5.62. The comparison study was performed on Methane fuel at d_p/d_o=2.3, T_{pa}=20°C, T_{sa}=800°C, and S_n=0.5. As shown in the Fig. 5.61 (a) the axial temperature profile of linear secondary air velocity profile is higher than the uniform velocity profile. And also as shown in Fig. 5.61 (b), the axial wall temperature profile and peak wall temperature are high in case of linear velocity profile. The possible explanation is that the higher velocity near the wall increases the heat transfer coefficient between the combustion gases and the wall and consequently increases the axial wall temperature distribution. while Fig. 5.61 (c) presents the radial temperature profile for both cases, also the linear velocity profile gives higher radial temperature distribution than uniform velocity. This is due to the linear velocity profile increases the secondary air momentum near the wall and consequently increases the mixing process in radial direction (see Fig.5.62 (a)), therefore, the radial temperature distribution increases in case of linear secondary air velocity profile. Also the linear secondary air velocity profile gives low recirculation size than the uniform velocity profile. This because the higher axial air velocity near the wall affect the recirculation length and size (see Fig.5.62 (b)).
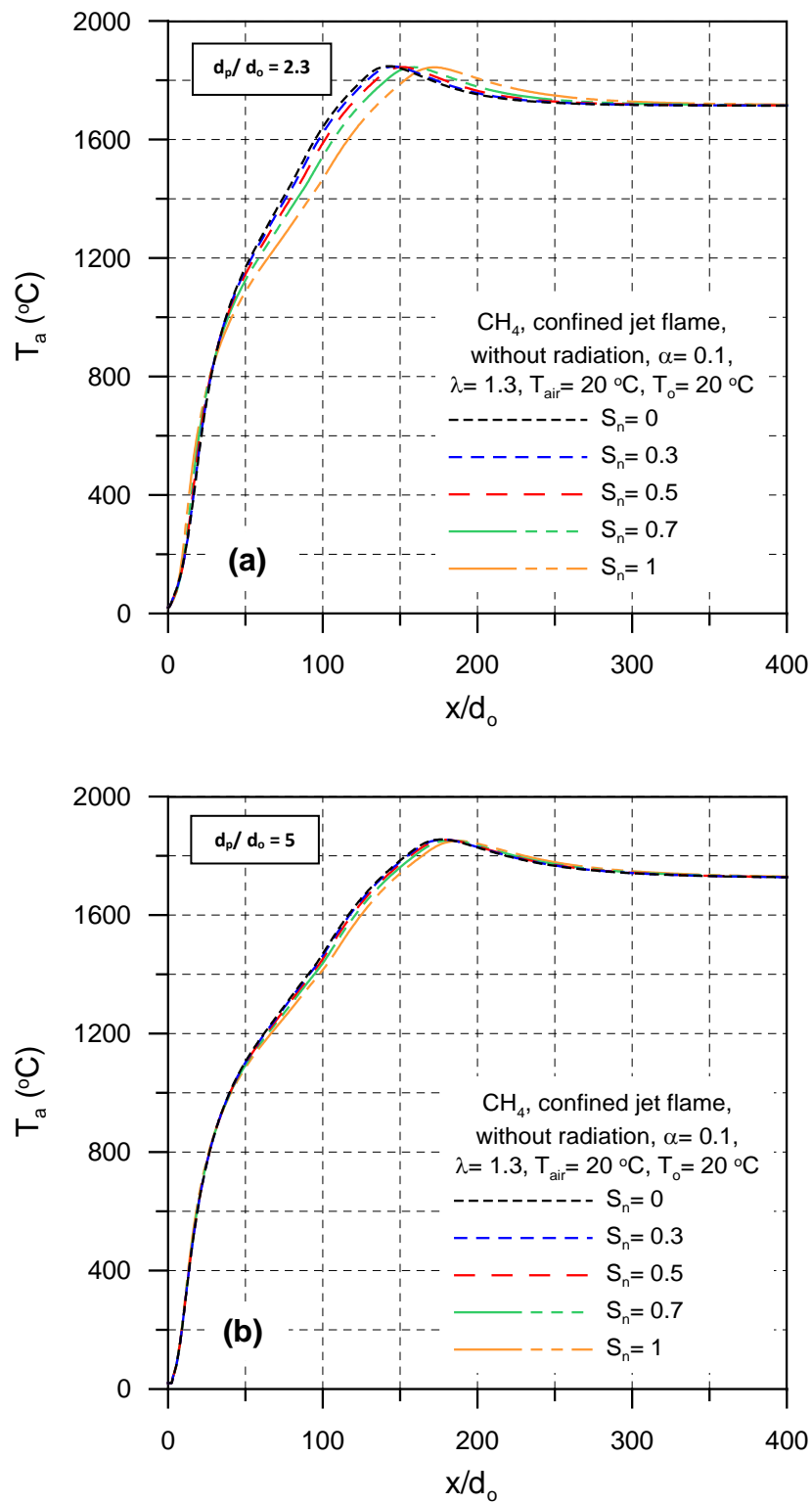
Figure 5.49: Influence of primary air swirl number on centerline axial temperature profiles using Methane fuel (CH_4): (a) $d_p/d_o= 2.3$ and (b) $d_p/d_o= 5$.
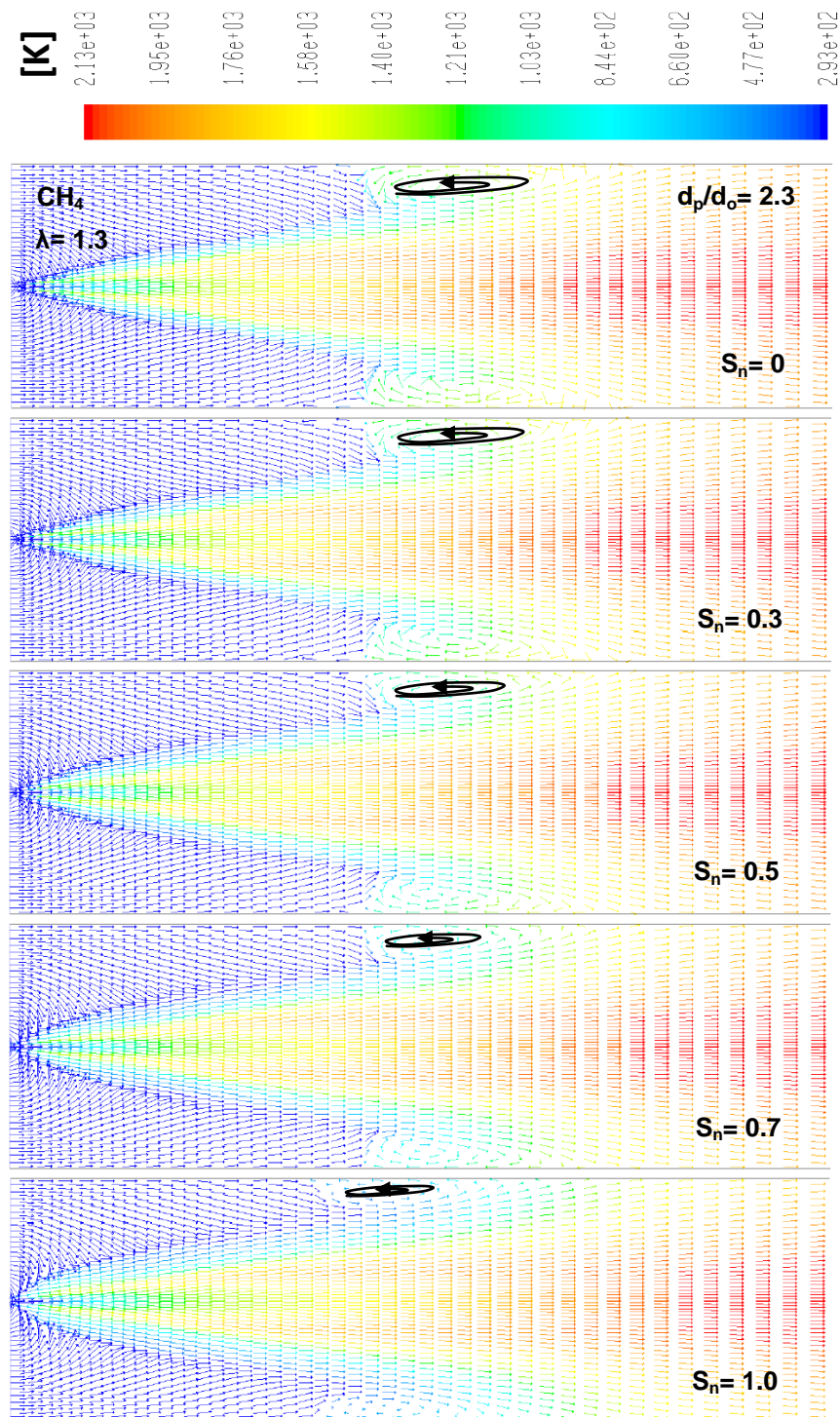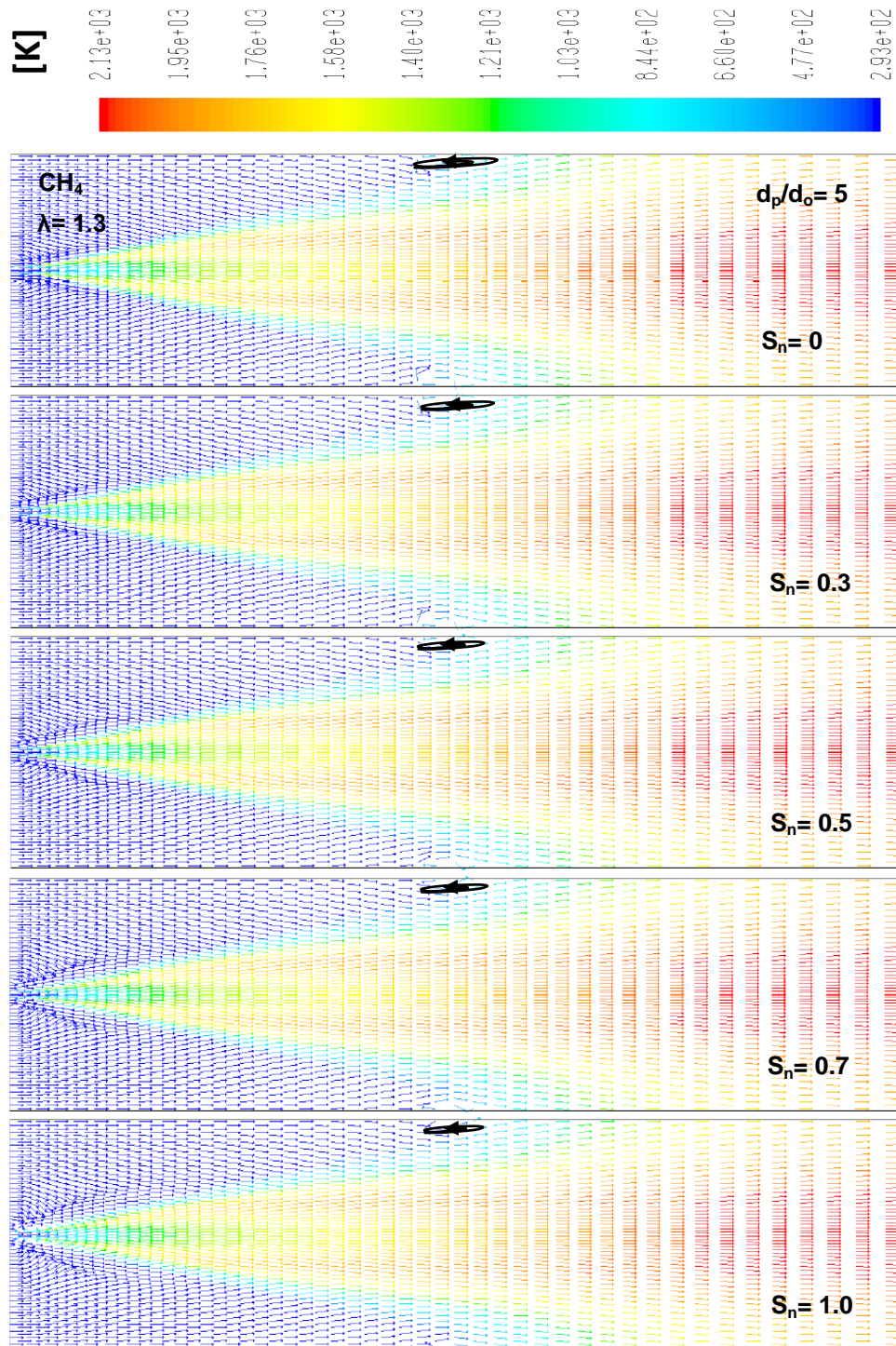
Figure 5.50: Influence of primary air swirl number on recirculation zones presented by velocity vectors colored by temperature along the flame using Methane fuel (CH_4) at $\alpha=$ 0.1, $\lambda=$ 1.3, $d_p/d_o=$ 2.3, $T_{air}=$ 20°C, $T_o=$ 20°C, and $u_o=$ 30 (m/s).
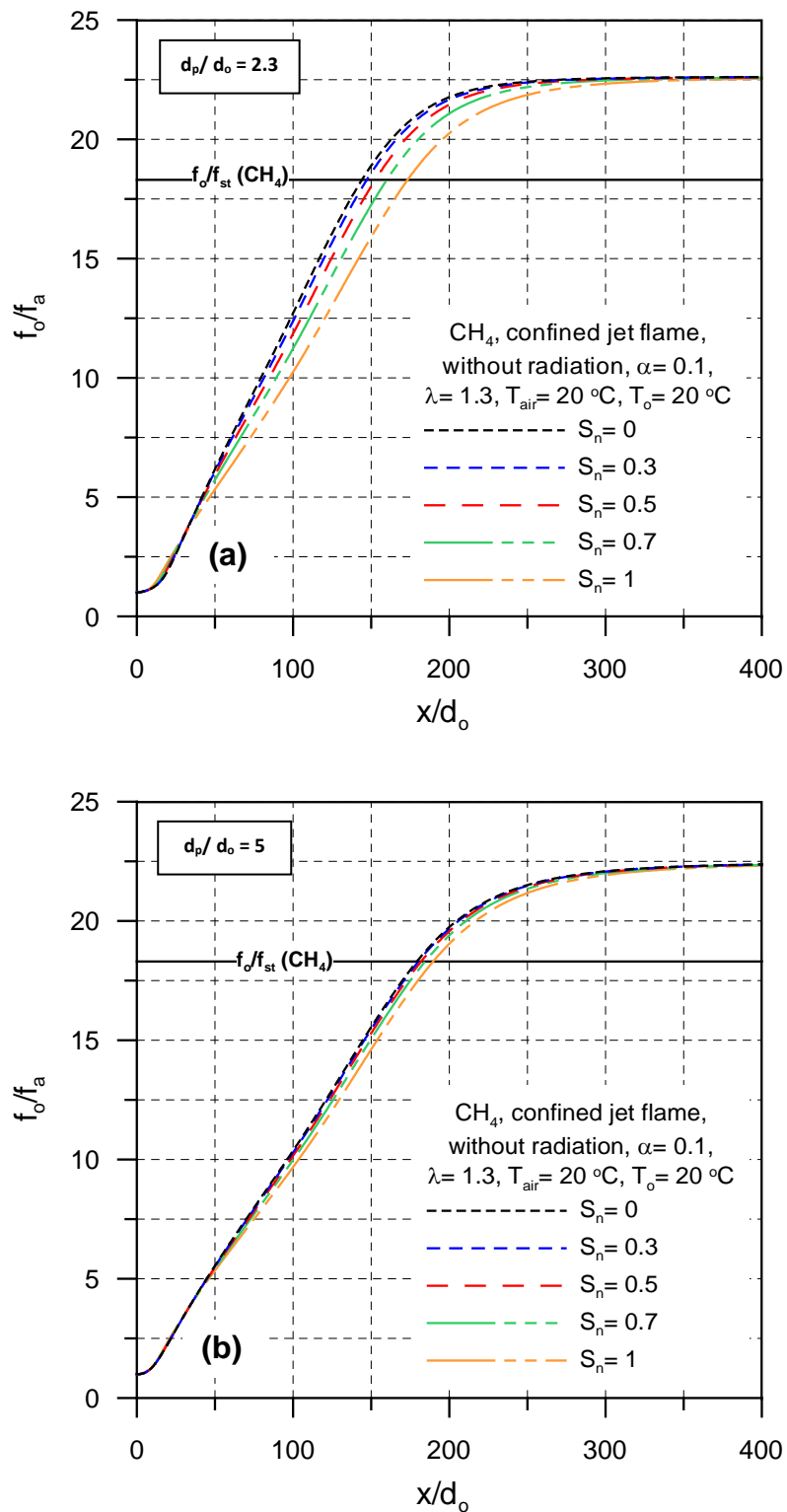
Figure 5.51: Influence of primary air swirl number on recirculation zones presented by velocity vectors colored by temperature along the flame using Methane fuel (CH_4) at $\alpha=$ 0.1, $\lambda=$ 1.3, $d_p/d_o=$ 5, $T_{air}=$ 20°C, $T_o=$ 20°C, and $u_o=$ 30 (m/s).

Figure 5.52: Influence of primary air swirl number on inverted dimensionless axial mean mixture fraction profiles along the flame using Methane fuel (CH_4): (a) d_p/d_o= 2.3 and (b) d_p/d_o= 5.
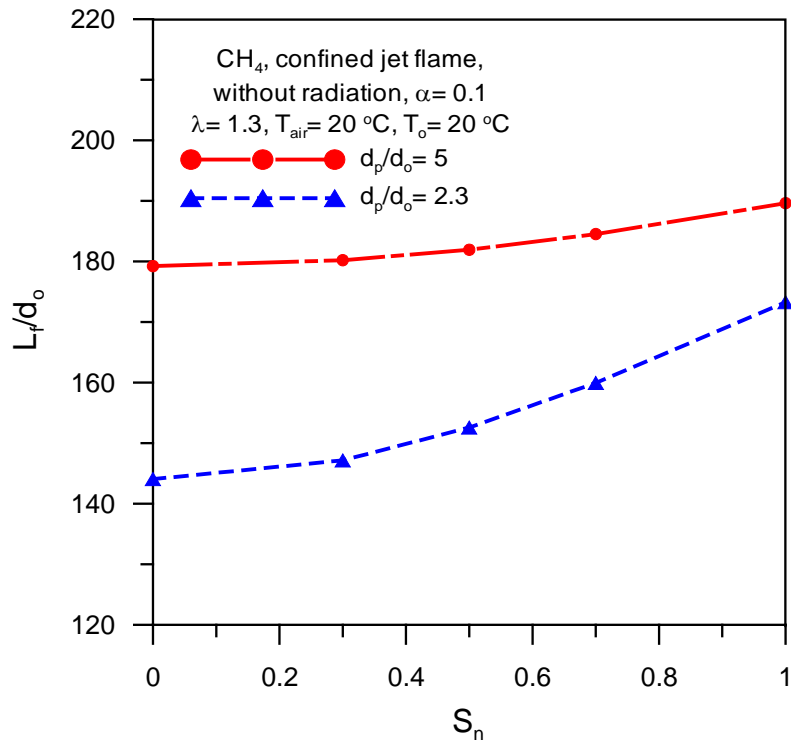
Figure 5.53: Influence of primary air swirl number on flame length using Methane fuel (CH_4) at different annulus diameters and u_o= 30 (m/s).
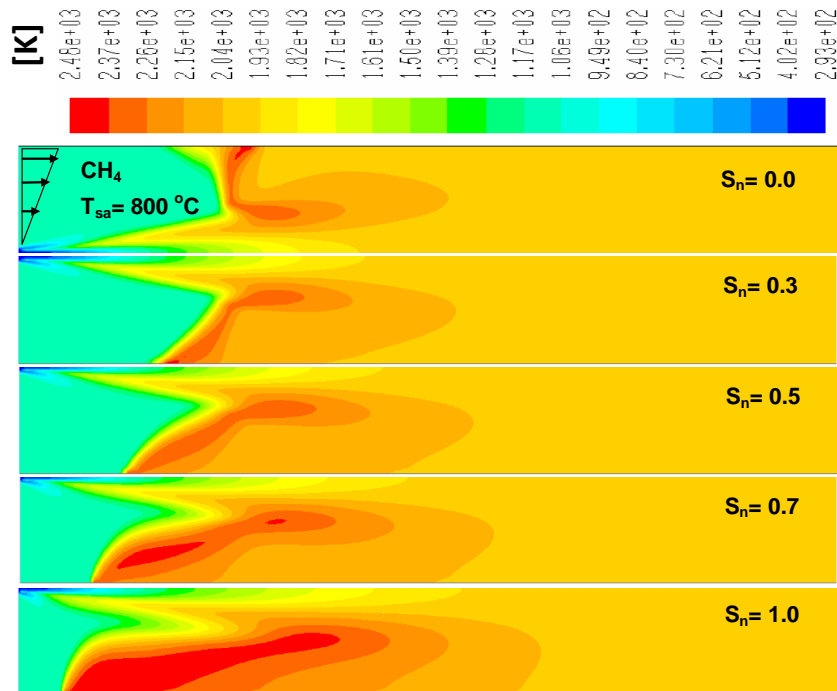

Figure 5.54: Influence of primary air swirl number on temperature contours using Methane fuel (CH_4) at α= 0.1, λ= 1.3, d_p/d_o= 2.3, T_{pa}= 20°C, T_o= 20°C, and u_o= 30 (m/s).
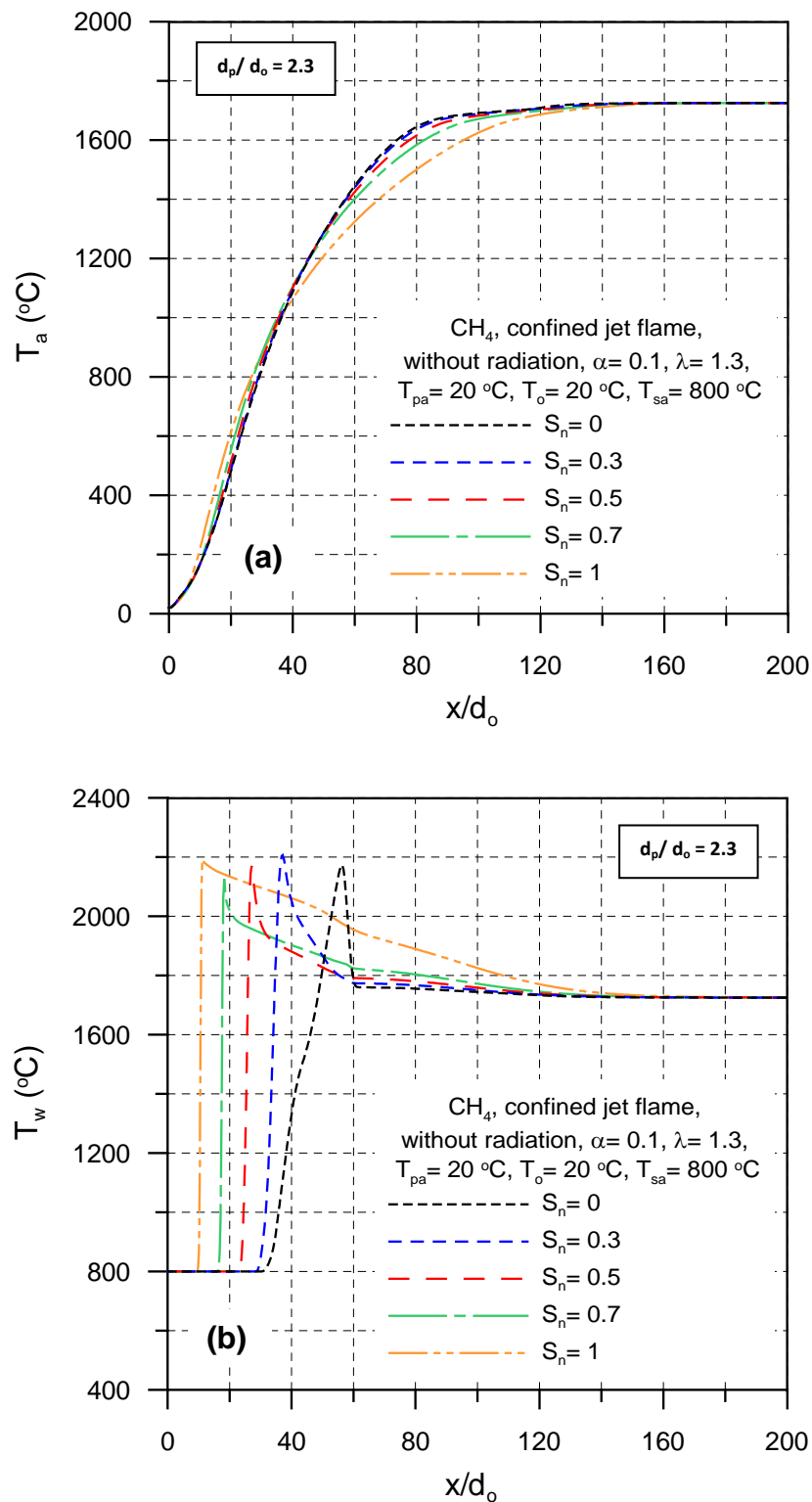
Figure 5.55: Influence of primary air swirl number on (a) centerline axial flame temperature profiles and (b) axial wall temperature profiles; using Methane fuel (CH_4) at $u_o=$ 30 (m/s).
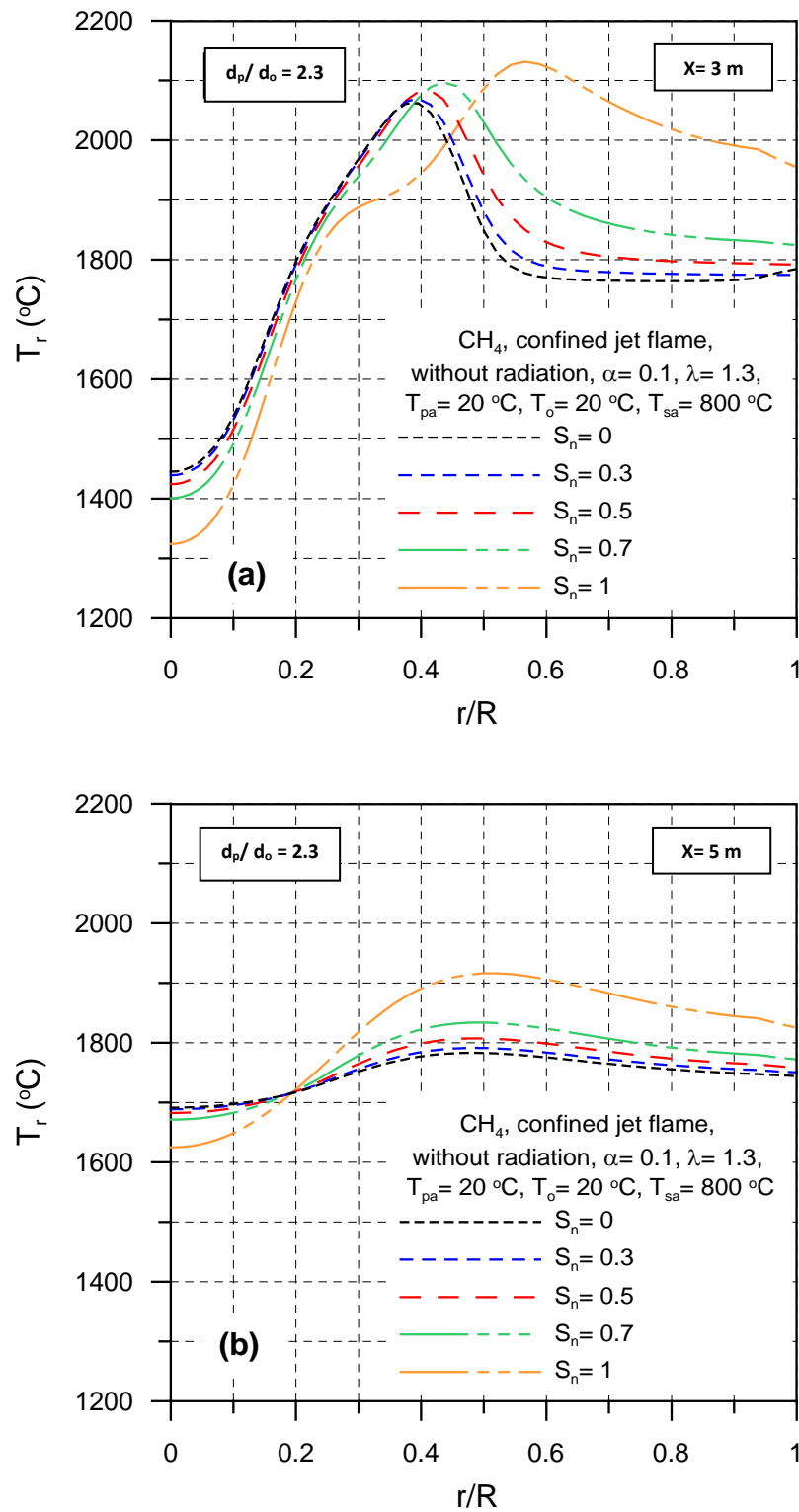
Figure 5.56: Influence of primary air swirl number on radial flame temperature profiles at different distances from burner tip: (a) x= 3m and (b) x= 5m using Methane fuel (CH_4) at u_o= 30 (m/s).
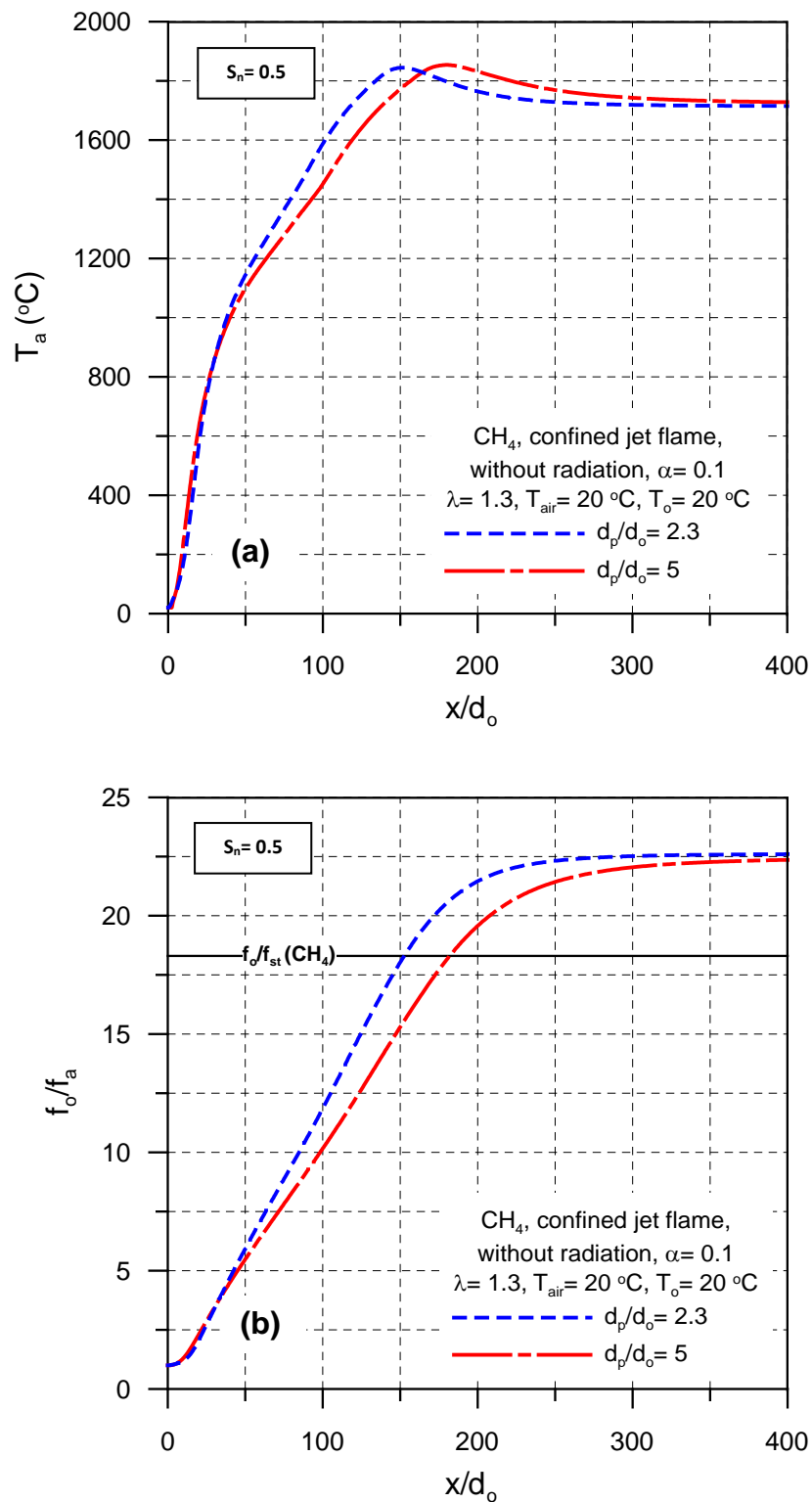
Figure 5.57: Influence of annulus diameter on (a) centerline axial temperature profiles, (b) inverted dimensionless axial mean mixture fraction profiles using Methane fuel (CH_4) at $u_o = 30$ (m/s).
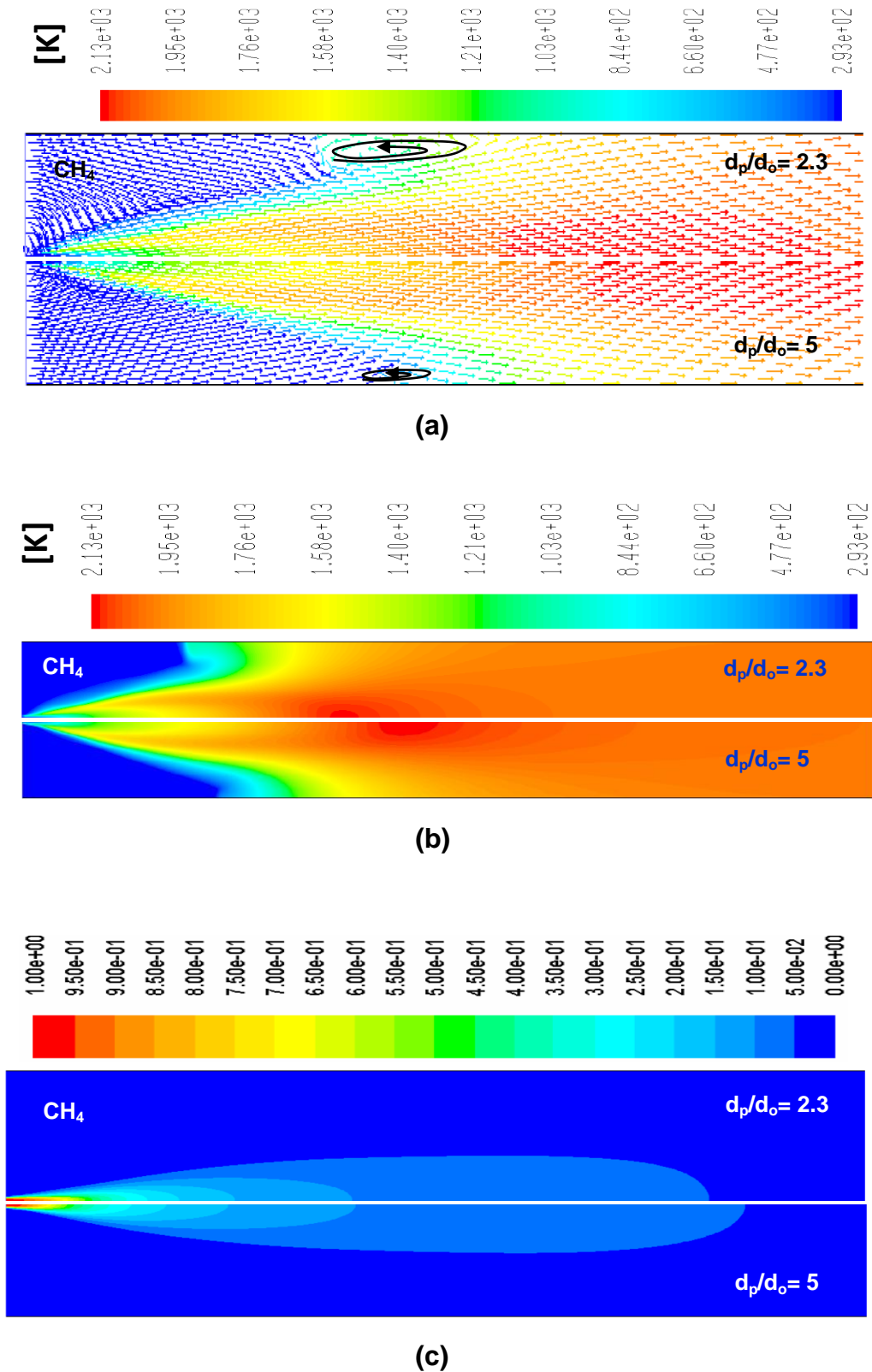
(a)

(b)

(c)

Figure 5.58: Influence of annulus diameter size on (a) recirculation zones presented by velocity vectors colored by temperature (b) temperature contours (c) mixture fraction contours, using Methane fuel (CH_4) at α= 0.1, λ= 1.3, S_n= 0.5, T_{air}= 20°C, T_o= 20°C, and u_o= 30 (m/s).
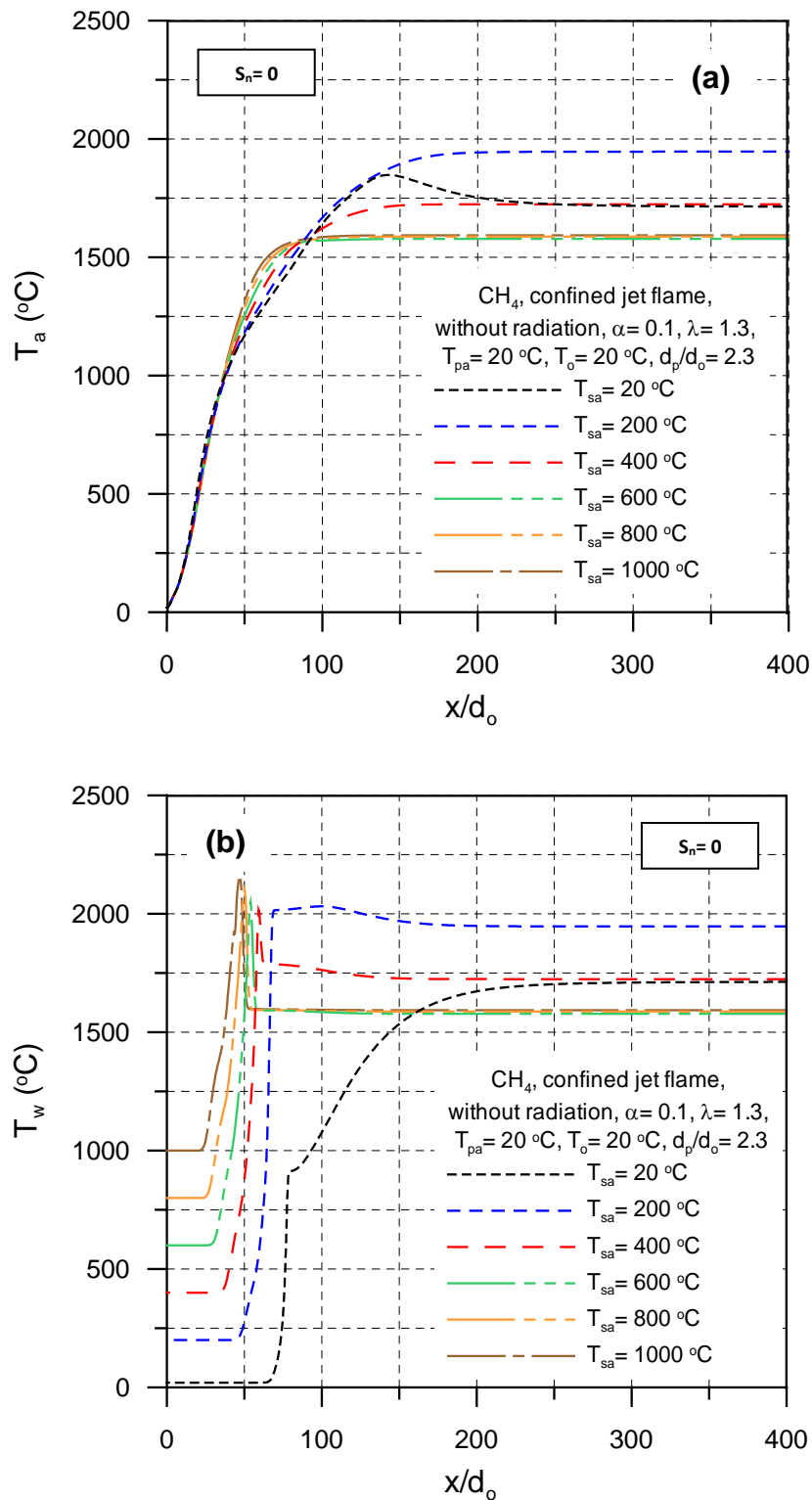
Figure 5.59: Influence of secondary air temperature on: (a) centerline axial temperature profiles, (b) axial wall temperature profiles using Methane fuel (CH_4) without radiation at different annulus diameter at u_o= 30 (m/s).

Figure 5.60: Influence of secondary air temperature on (a) temperature contours (b) velocity vectors colored by temperature using Methane fuel (CH_4) at $\alpha= 0.1$, $\lambda= 1.3$, $T_{sa}= 800°$C, $T_{pa}= 20°$C, $T_o= 20°$C, and $u_o= 30$ (m/s).

Figure 5.61: Influence of secondary air velocity profiles on (a) centerline axial flame temperature profiles (b) axial wall temperature profiles and (c) radial flame temperature profiles using Methane fuel (CH_4) at u_o= 30 (m/s).
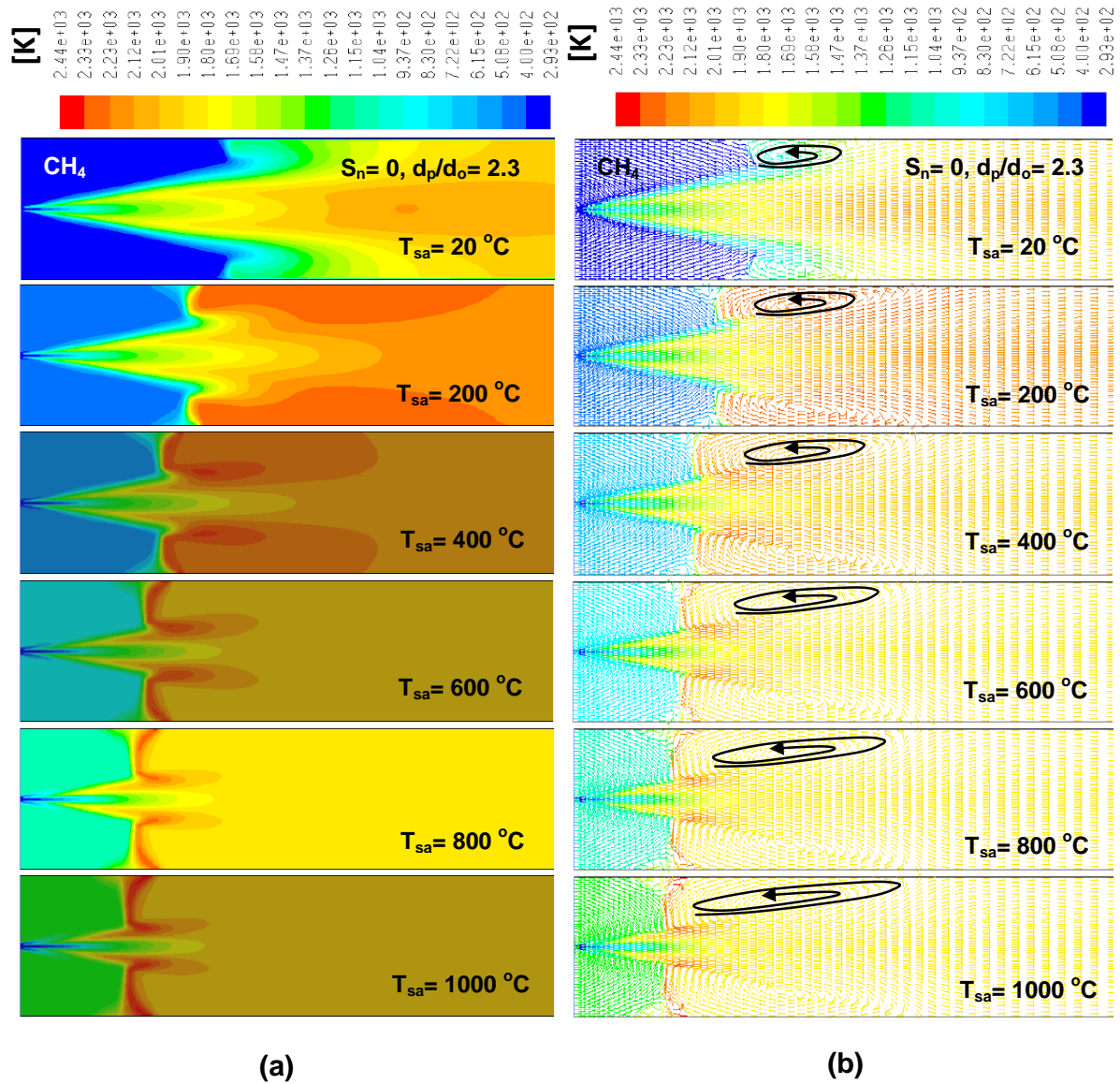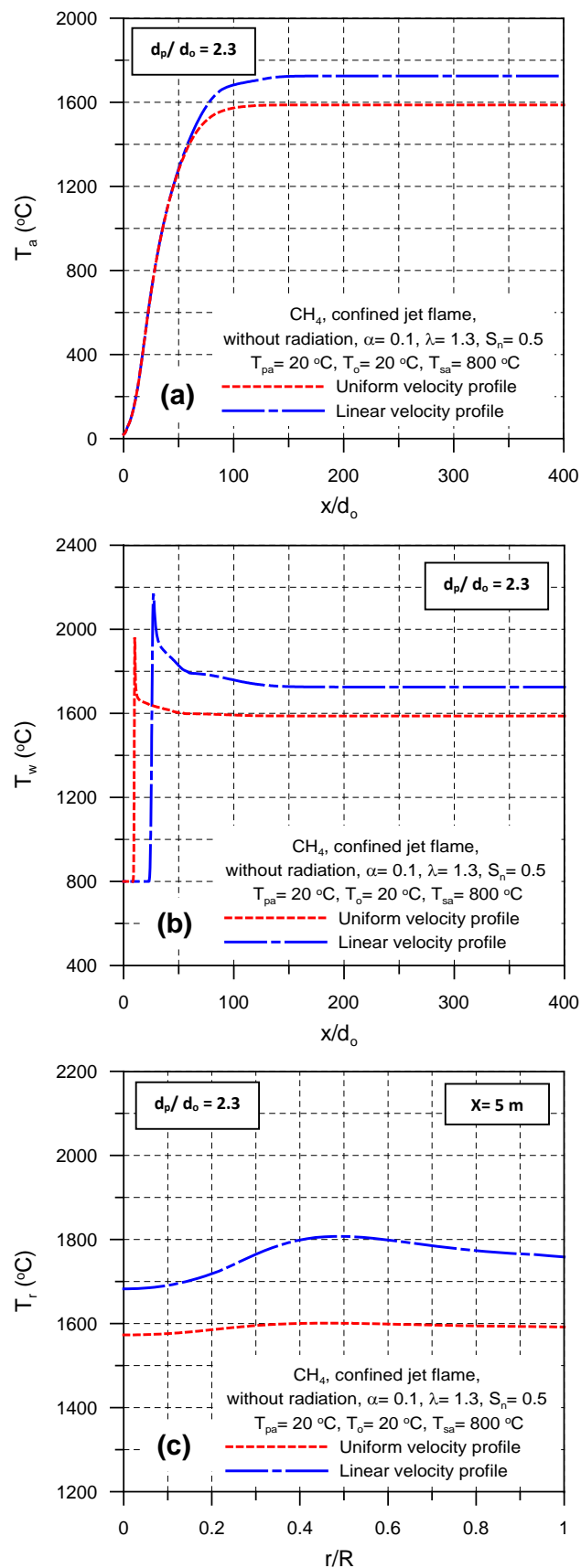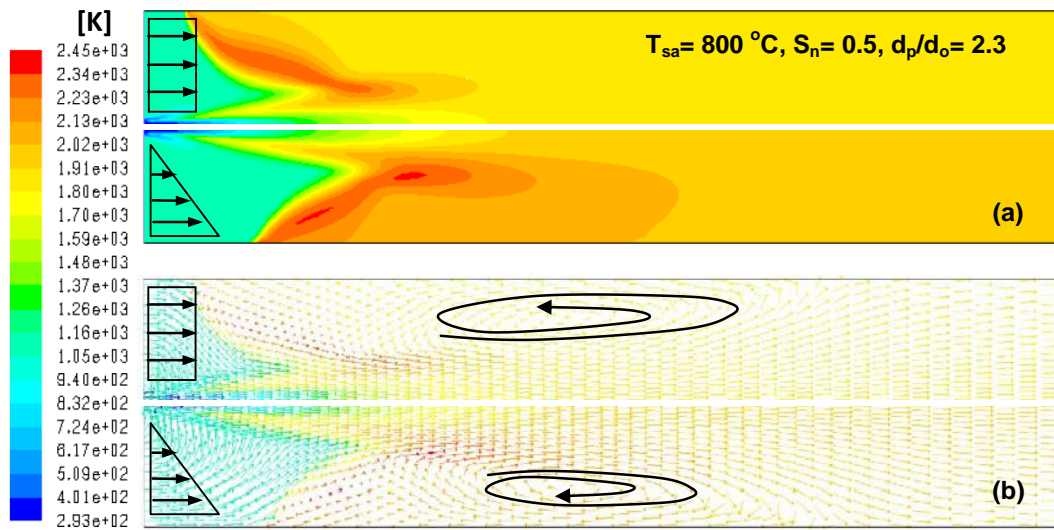
Figure 5.62: Influence of secondary air velocity profiles on (a) temperature contours, (b) velocity vectors colored by temperature using Methane fuel (CH_4) at u_o= 30 (m/s).

5.2.5   Effects of air swirl side

Correspondingly, a comparison between primary air swirl and secondary air swirl was carried out and presented in Figs. 5.63 and 5.64. The comparison study was fulfilled on Methane fuel at d_p/d_o=2.3, T_{pa}=20°C, T_{sa}=800°C, and S_n=1. The results of Fig. 5.63 (a) show that the centerline axial temperature distribution increases in case of secondary air swirl, this effect appears in the range of x/d_o from 40 to 120, other than, the swirl side has no effect on the axial temperature profiles. On the other hand the axial wall temperature profile and the peak wall temperature in case of primary air swirl is higher than that is in the case of secondary air swirl. As presented in Fig. 5.63 (b) the peak wall temperature increases by $\sim$5 % in case of primary air swirl than of use secondary air swirl. This can be attributed to the primary air swirl improves the mixing process between primary air and fuel, hence it increases the the combustion gas temperature, on the other hand the high secondary air temperature reduces the diffused air into the fuel, so the hot zones area located near the entrance. The final result is the primary air swirl improves the mixing process and consequently increases the axial wall temperature profile.

Figure 5.63 (c) presents the radial temperature profiles for both cases at distance of $x = 5m$, as shown in the Figure, up to $r/R = 0.2$ the secondary air swirl is dominant, but over $r/R = 0.2$ the primary air swirl increases the radial temperature distribution, this is due to improvement of the mixing process as it was explained and discussed above. The temperature contours and velocity vectors for both air sides swirl were depicted in Figs. 5.64 (a) and 5.64 (b), respectively. As shown in the Figures the primary air swirl has a bigger high temperature zone area and smaller recirculation size than the secondary air swirl.
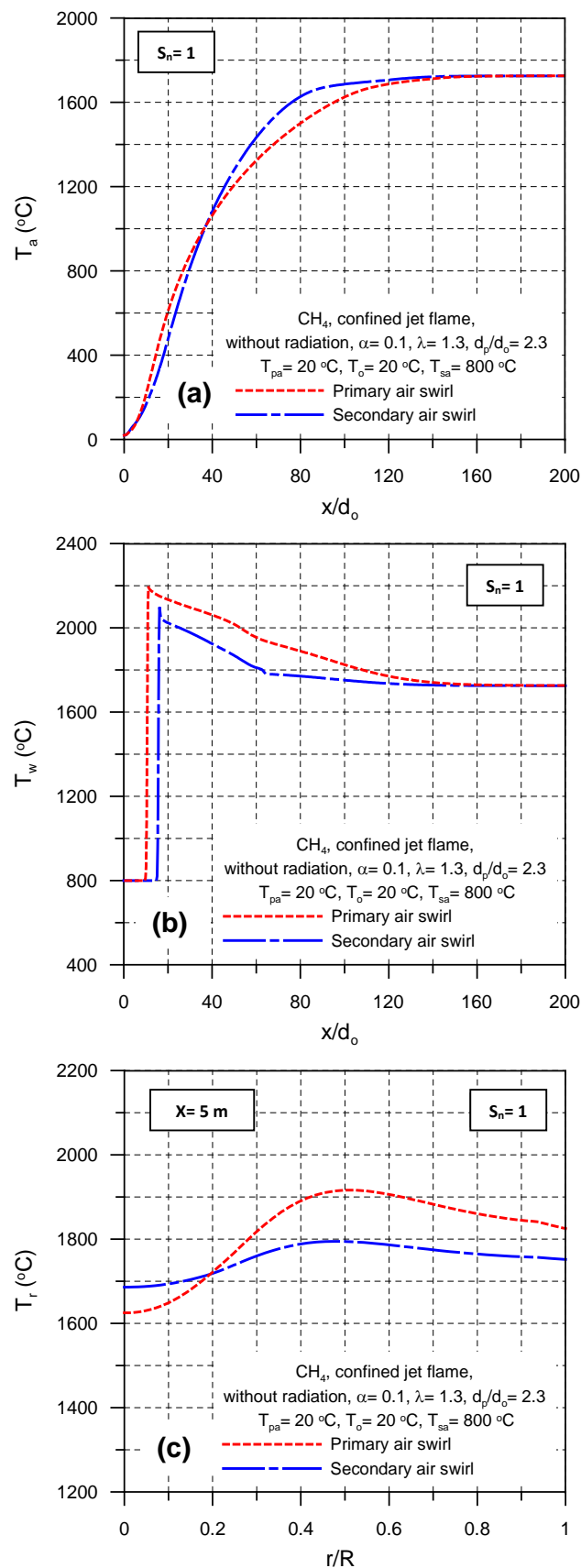
Figure 5.63: Influence of air swirl side on (a) centerline axial flame temperature profiles (b) axial wall temperature profiles and (c) radial flame temperature profiles using Methane fuel (CH_4) at u_o= 30 (m/s).
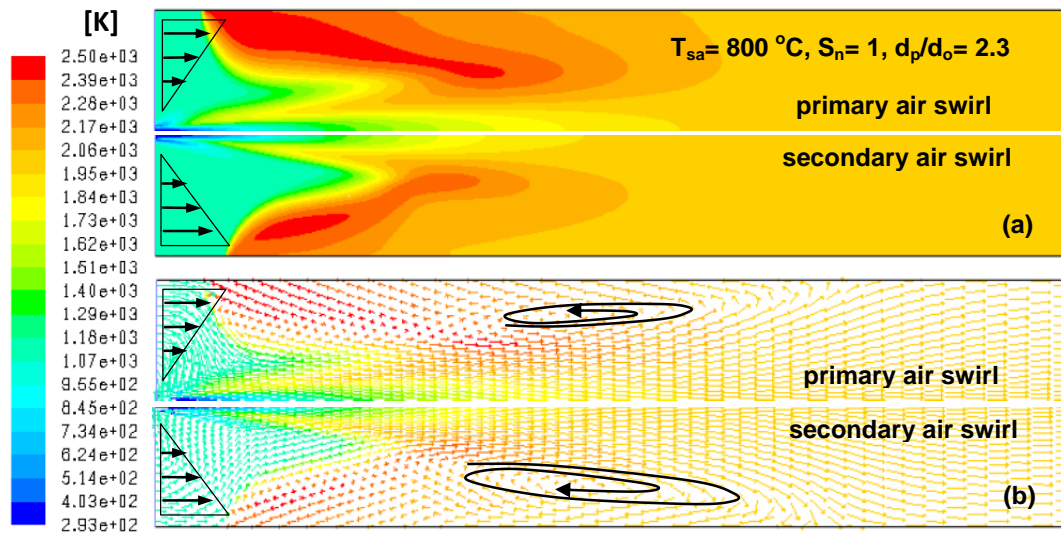
Figure 5.64: Influence of air swirl side on (a) temperature contours (b) velocity vectors colored by temperature using Methane fuel (CH_4) at $\alpha=0.1$, $\lambda=1.3$, $T_{pa}=20°C$, $T_o=20°C$ and $u_o=30$ (m/s).

5.2.6   Effects of primary air hydraulic diameter

New burner configuration was proposed for simulation to examine the effects of primary air hydraulic diameter on the flame length and flow field inside the cylinder (see Fig. 5.65). In addition to, primary air swirl number was studied and presented using this new burner configuration. As we explained before the concentric type burners (i.e., annulus type) are used in most industrial burners which are commonly use with the confined flame. Therefore, the effects of primary air hydraulic diameter on the centerline axial temperature profiles, inverted dimensionless axial mean mixture fraction profiles pathlines colored by temperature were presented in Figures (5.66, 5.67 and 5.68) and will discuss in the following paragraphs.

Figure 5.66 shows the centerline axial temperature profiles using Methane fuel (CH_4) for different primary air hydraulic diameters, dh_{pa} (20, 30, 40 and 50 m) and at $\alpha=0.1$, $\lambda=1.3$, $q_o=2.3$ MW, $T_{pa}=20°C$, $T_{sa}=20°C$, and $S_n=0$. As displayed in the Figure, the temperature profile shifted to right with increasing the primary air hydraulic diameter, and the value of peak flame temperature did't change. This can be attributed to the increase in the primary air velocity with decreasing the annulus diameter. Increasing the primary air velocity improves the mixing process between the air and fuel, hence the reaction between the oxidizer and fuel completed in short distance from the burner tip. As a result in the peak flame temperature shifted to right and consequently the flame length increased with increasing primary air hydraulic diameter (see Fig. 5.67). Also as shown in Figures, the peak flame temperature shifted to right and the flame length increases by $\sim17\%$ and $\sim17\%$, respectively with increasing dh_{pa} from 20 to 50 mm.

The pathlines colored by temperature for different dh_{pa} was depicted in Fig. 5.68. As appeared in the figure the recirculation size decreases with increasing the primary air hydraulic diameter. This due to, the higher the primary air hydraulic diameter, the lower primary air velocity and consequently the shorter recirculation length can be obtained.
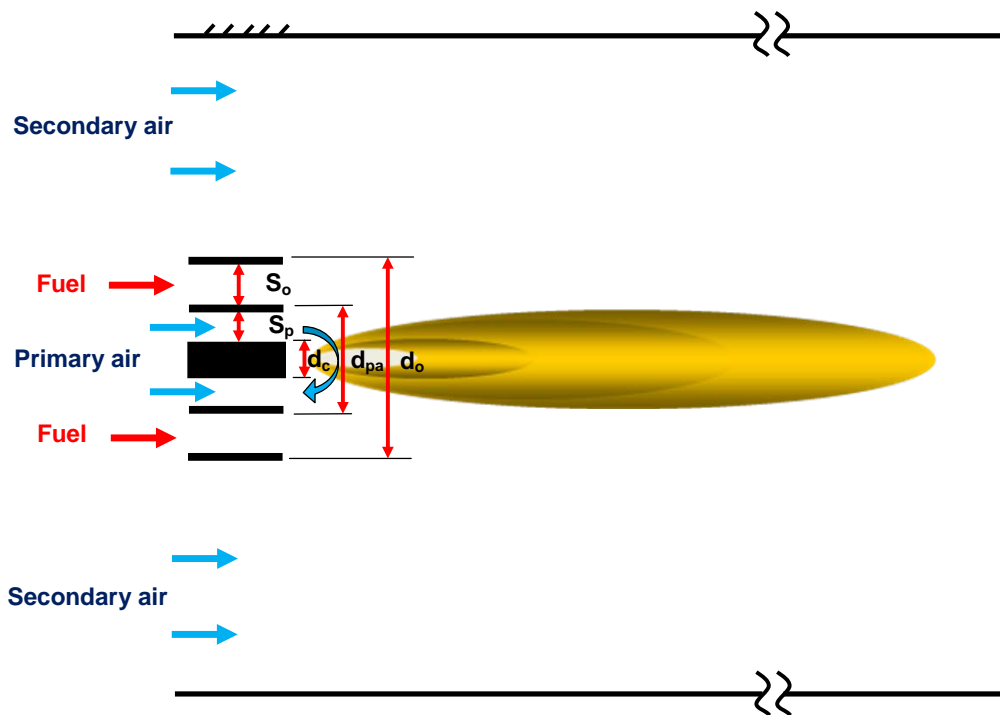
Figure 5.65: Schematic diagram of annulus new burner configuration with fully opened cylinder for secondary air).
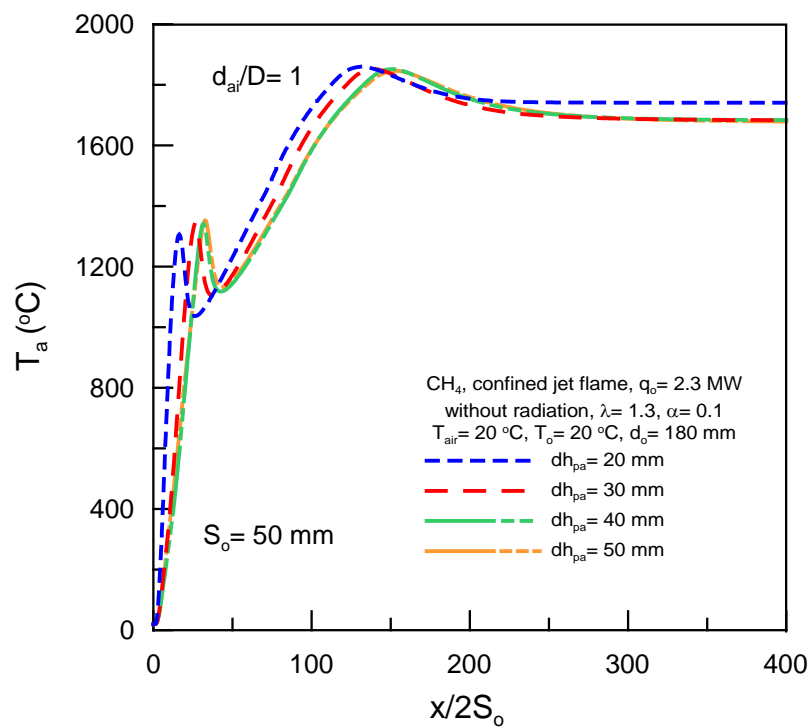
Figure 5.66: Influence of primary air hydraulic diameter on axial temperature profiles using Methane fuel (CH_4).
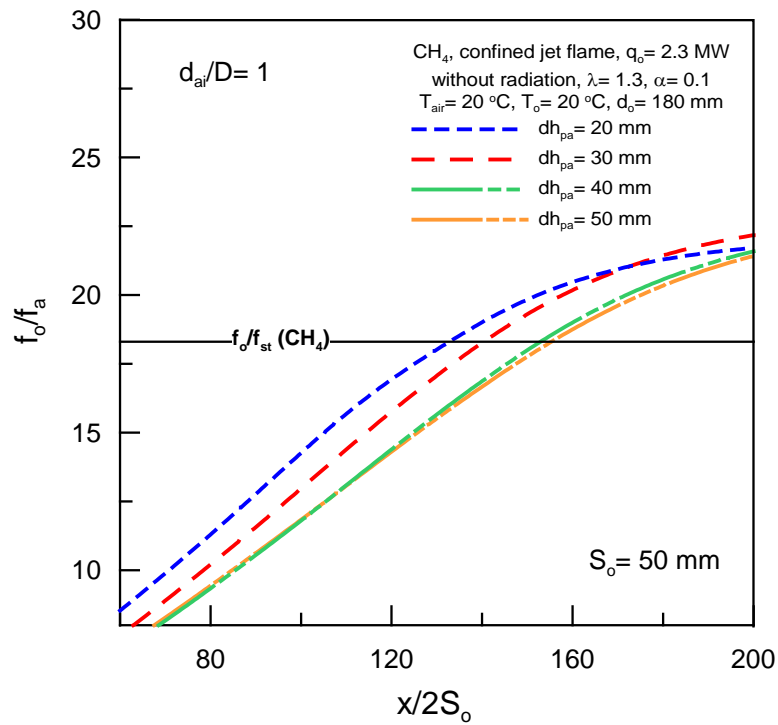
Figure 5.67: Influence of primary air hydraulic diameter on inverted dimensionless axial mean mixture fraction profiles using Methane fuel (CH_4).
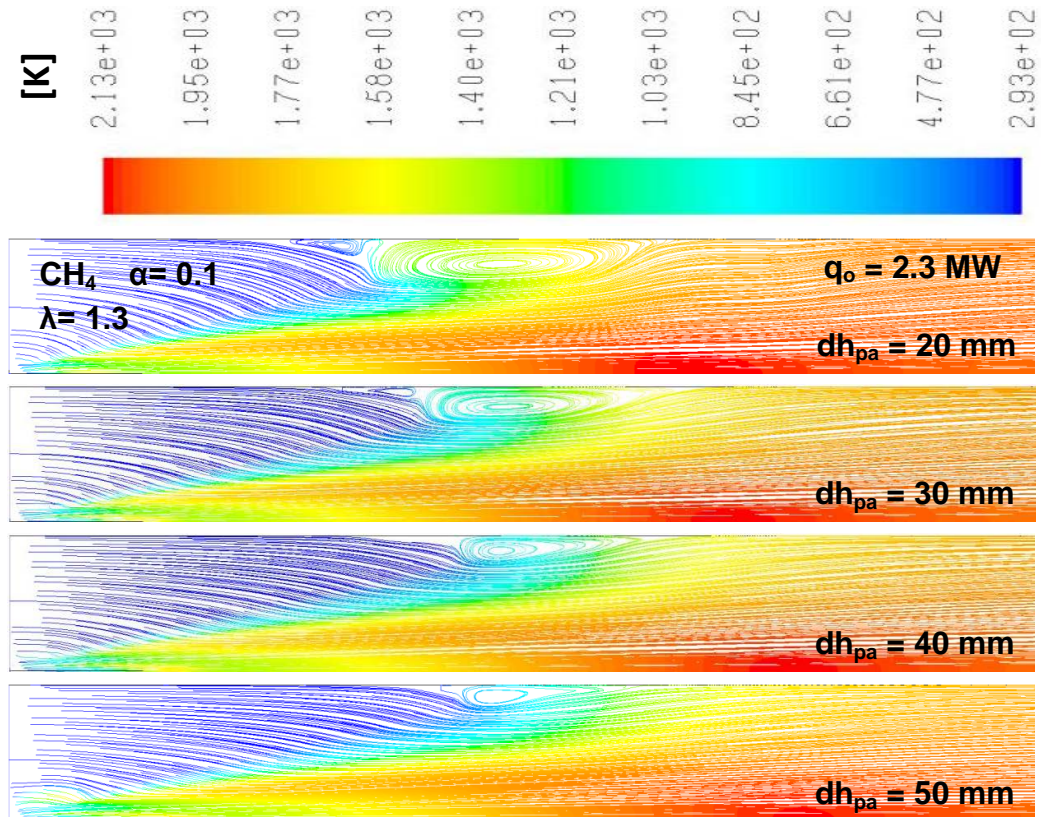
Figure 5.68: Influence of primary air hydraulic diameter on the pathlines colored by temperature using Methane fuel (CH_4).

5.3   Annulus tube burner with fully closed cylinder for secondary air

Concerning the flame stability, most of industrial burners are concentric type burners (i.e., annulus type) as we discussed in Chapter 4. Also some of industrial furnaces or combustors are fully closed for secondary air (i.e., the total combustion air entered the furnace as a primary air only around the fuel). Therefore, the influence of the annulus air swirl number on the flame behavior using fully closed cylinder for secondary air (see Fig. 5.69) was presented and discussed in this section. In the computational the fuel nozzle diameter is 50 mm, d_p/d_o changes (2.3, 3.65, and 5.05), α=1, and λ=1.3. Methane was used as a fuel in this configuration at 30 m/s fuel velocity, 20°C fuel temperature, and 20°C air temperature. The radiation model (P1) wasn't used (without radiation) in this configuration. Finally, the comparisons of numerical and experimental results like this configuration were conducted and presented.
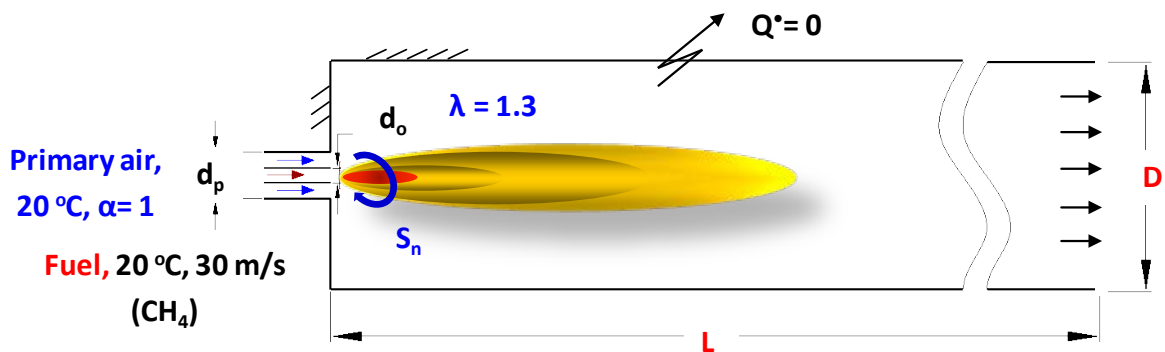

Figure 5.69: Schematic diagram of confined flame (annulus tube burner with fully closed cylinder for secondary air).

5.3.1   Effects of annulus air swirl

Figures (5.70−5.73) show the effects of annulus air swirl number (S_n) on the centerline axial temperature profiles, inverted dimensionless axial mean mixture fraction profiles, velocity vectors, men mixture fraction contours at d_p/d_o=5, and on the flame length at d_p/d_o= 2.3, 3.65 and 5.

Figure 5.70 (a) shows the axial temperature profiles along the flame at different annulus air swirl numbers (S_n=0, 0.3, 0.5, 0.7 and 1). As shown in the Figure the centerline axial temperature profiles and peak flame temperature shifted to left with increasing annulus air swirl number. Where, the peak flame temperature shifted to the left by ∼96 %, ∼95 %, and ∼86 % for d_p/d_o=2.3, 3.65 and 5, respectively, if the swirl number increased from 0 to 1. That means, the reduction in the location of peak flame temperature with increasing the swirl number decreases with increasing the annulus diameter. The possible explanation is that the recirculation size increases with the increase of air swirl number and the inner recirculation starts to appear at $S_n > 0.5$ (see Fig. 5.71). Increasing the recirculation size helps to obtain a short flame with a wide radial development (see Fig. 5.72). As a result in the peak flame temperature shifted to left, the same investigation had been done by ref. [104]. Also as shown in

Fig. 5.70 (a), the combustion gas temperature at the end of cylinder decreases with high swirl number (S_n=0.7 and 1). This can be attributed to the higher swirl number helps to draw air from the outside (ambient air) which reduces the combustion gas temperature.

The influence of annulus air swirl number on inverted dimensionless axial mean mixture fraction profiles was displayed in Fig. 5.70 (b). As shown in the Figure the annulus air swirl number has a significant effect on the flame length, where the flame length decreases by ∼96 %, ∼95 %, and ∼86 % f or d_p/d_o=2.3, 3.65 and 5, respectively, if the swirl number increased from to 0 to 1 (see Fig. 5.72). This is because, the swirl number increases the recirculation size and consequently improves the mixing process between the air and fuel. Improving the mixing process completes the combustion process in short distance, as a result in the flame length shortens. The same investigation had been done by ref. [104]. The computed results of the dimensionless flame lengths versus the annulus air swirl number were presented in Fig. 5.73 for different annulus diameters of 2.3, 3.65 and 5. As shown in the Figure, the swirl number has a considerable effect on the flame length up to S_n=0.7, other than the swirl number has approximately no effect on the flame length.

5.4 Comparisons with literature

A standard burner for confined flames with swirl using natural gas was developed by the German TECFLAM cooperation. The goals of the TECFLAM research programs are to establish of an extensive experimental database from selective flames and to validate and improve the mathematical combustion models. From this point the comparisons between experimental measurements of TECFLAM [105] and numerical results were presented in Figs. 5.74 and 5.75. The comparisons were fulfilled in order to validated the numerical models which used in my present confined swirling jet flame simulation. Therefore Figs. 5.74 (a), (b) and (c) show comparisons between numerical solutions and experimental measurements reported by TECFLAM [105] for radial distribution of axial velocity, radial velocity and tangential velocity components, respectively at two different distances from burner tip (x=30 mm and 60mm). Methane fuel was used in the simulation at T_{air}=300 K, T_o=300 K, λ=1.2, and S_n= 0.9. As well as Figs. 5.75 (a)....(f) present the comparisons of numerical and experimental measurements for radial distribution of mean mixture fraction at x=10 mm and x=90 mm, mean temperature at x=10 mm and x=20 mm, mass fraction of CO_2 at x=40 mm, and mass fraction of CH_4 at x=40 mm. As shown in the Figures the computed results give satisfactory agreement with the experimental measurements. The discrepancies between experimental and computed results due to simplifying assumptions in the turbulence and combustion models and also due to experimental uncertainty.
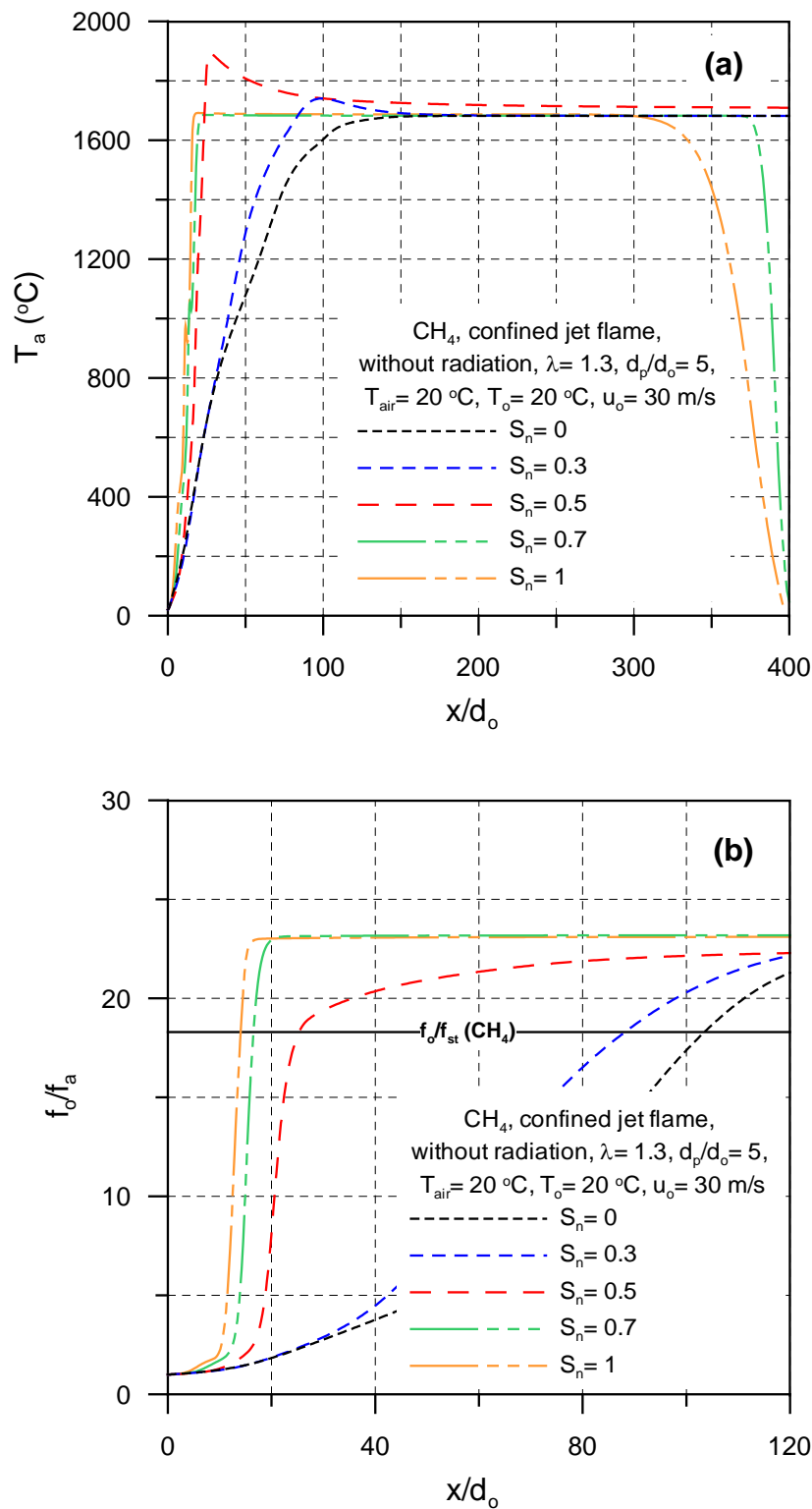
Figure 5.70: Influence of annulus air swirl on (a) centerline axial temperature profiles (b) inverted dimensionless axial mean mixture fraction profiles using Methane fuel (CH_4).
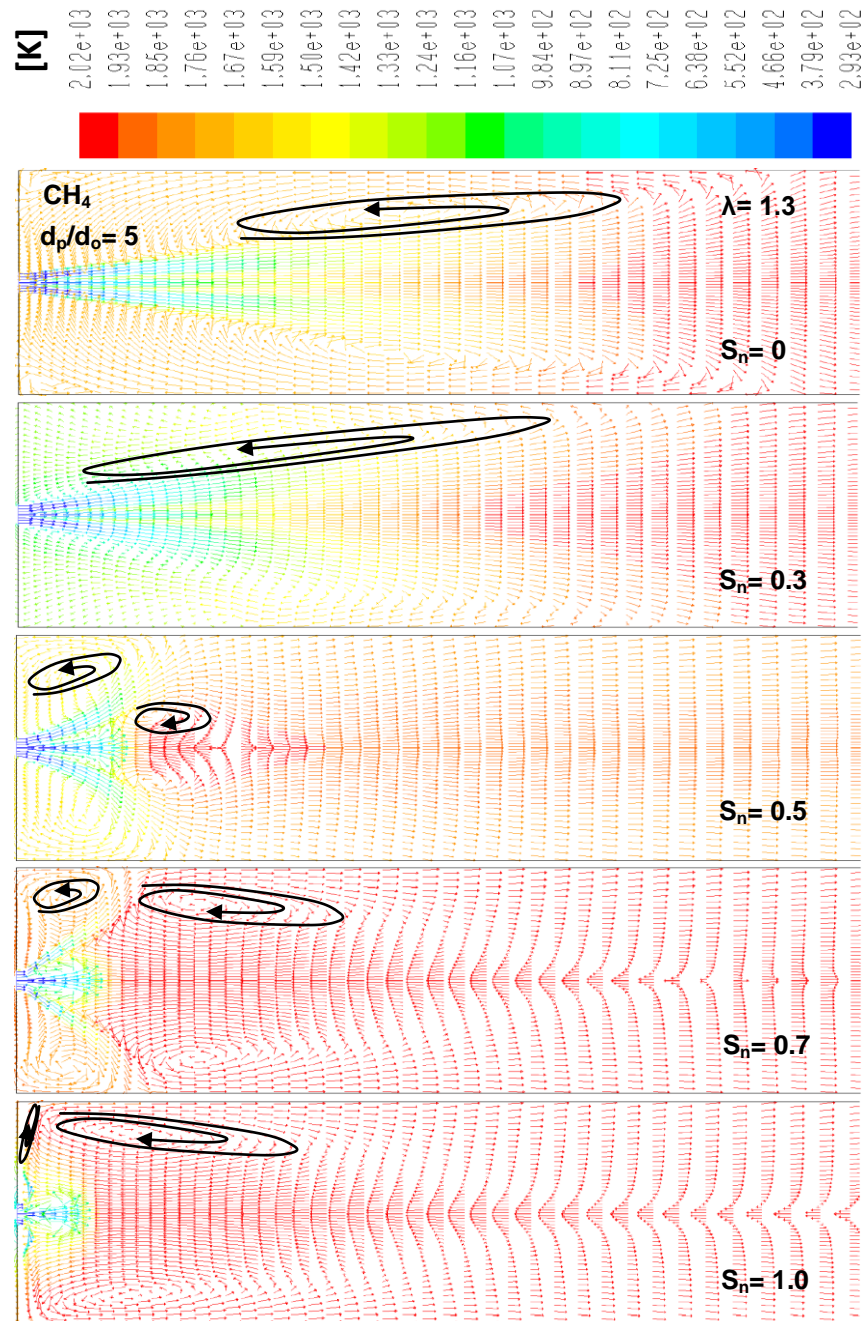
Figure 5.71: Influence of annulus air swirl on the velocity vectors colored by temperature using Methane fuel (CH_4) at T_{air}= 20°C, T_o= 20°C and u_o= 30 (m/s).
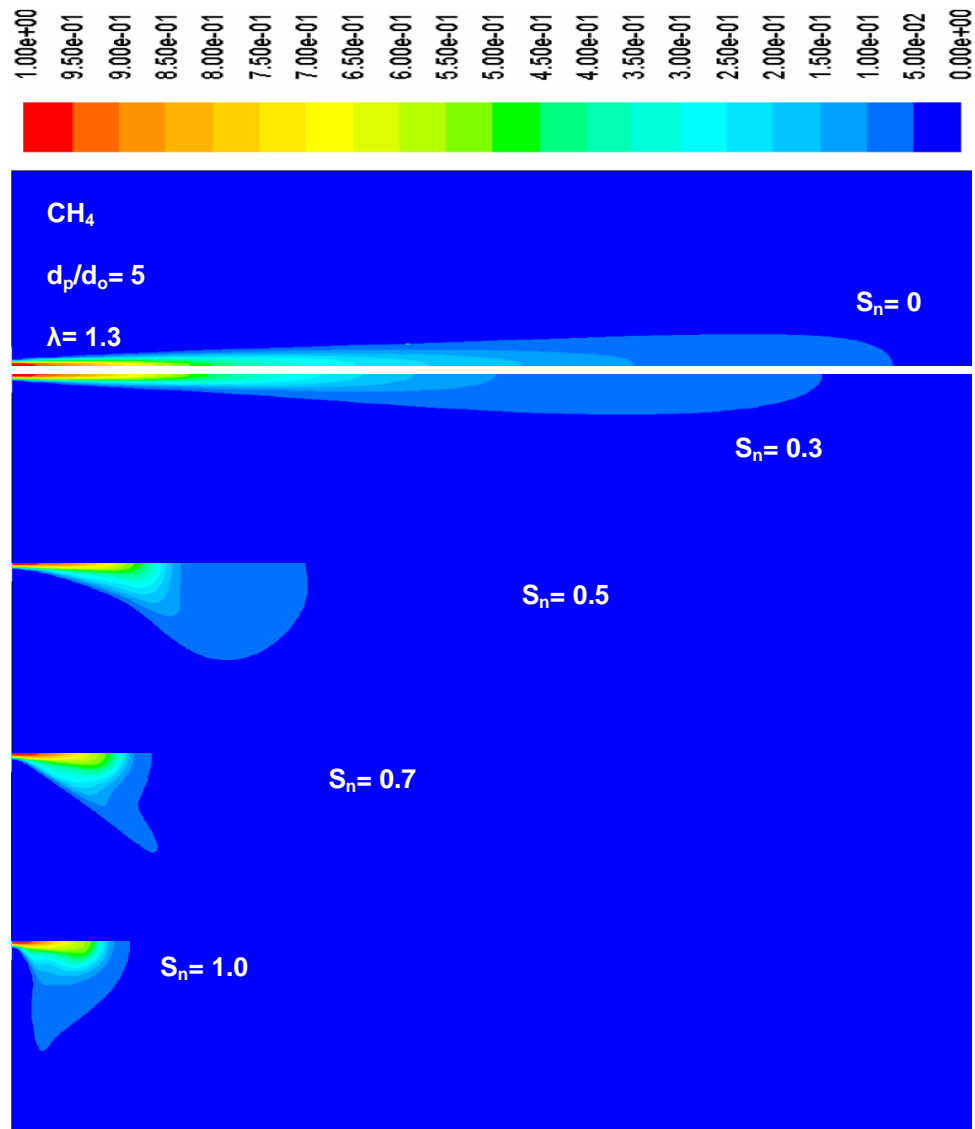
Figure 5.72: Influence of air swirl number on the mean mixture fraction contours using Methane fuel (CH_4) at $T_{air}=$ 20°C, $T_o=$ 20°C and $u_o=$ 30 (m/s).
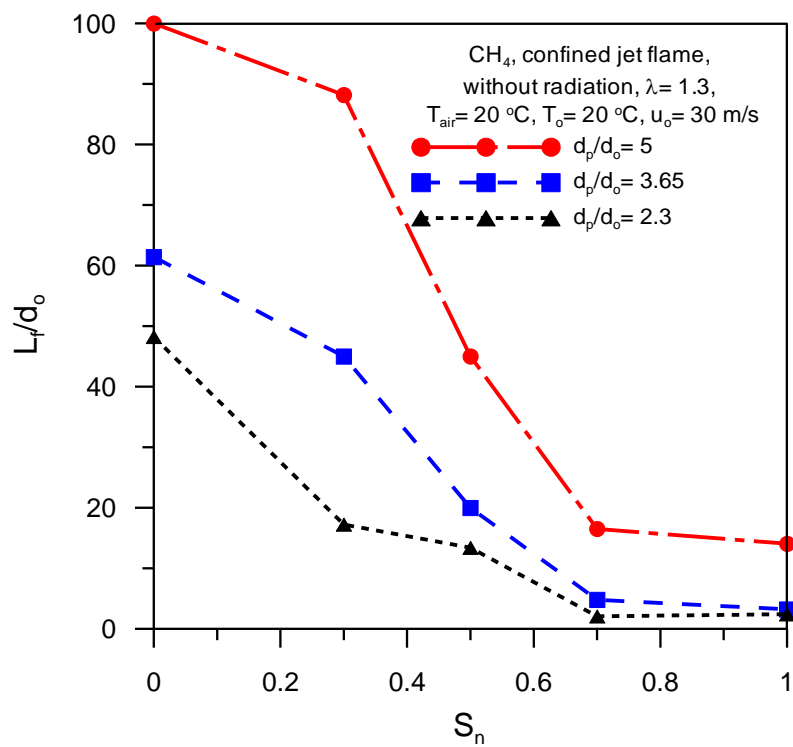
Figure 5.73: Influence of annulus air swirl number on the dimensionless flame length using Methane fuel (CH_4) at different annulus diameters.
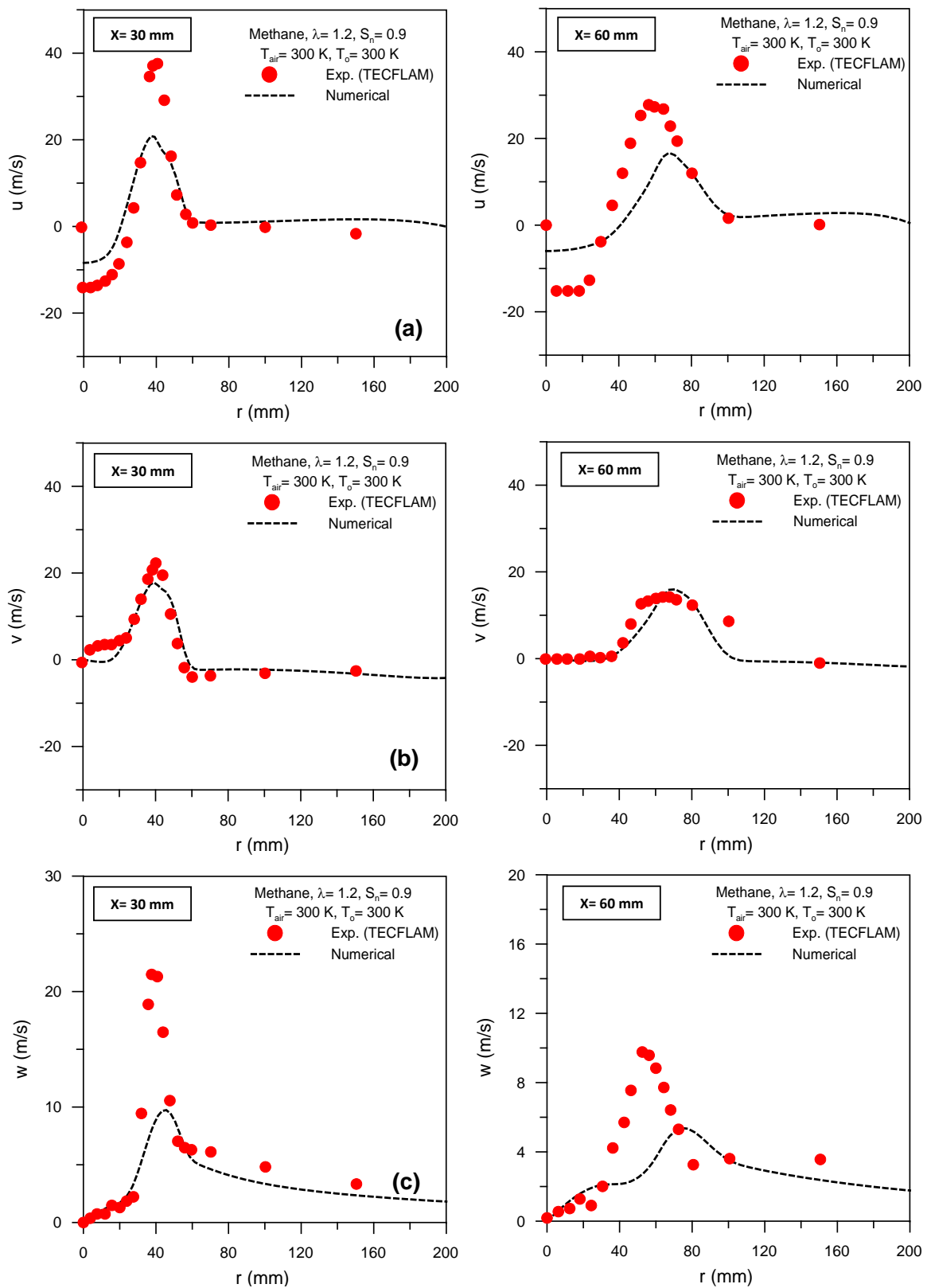
Figure 5.74: Comparisons of numerical and experimental measurements [105]: (a) radial distribution of mean axial velocity, u, (b) radial distribution of mean radial velocity, v, (c) radial distribution of mean tangential velocity, w.
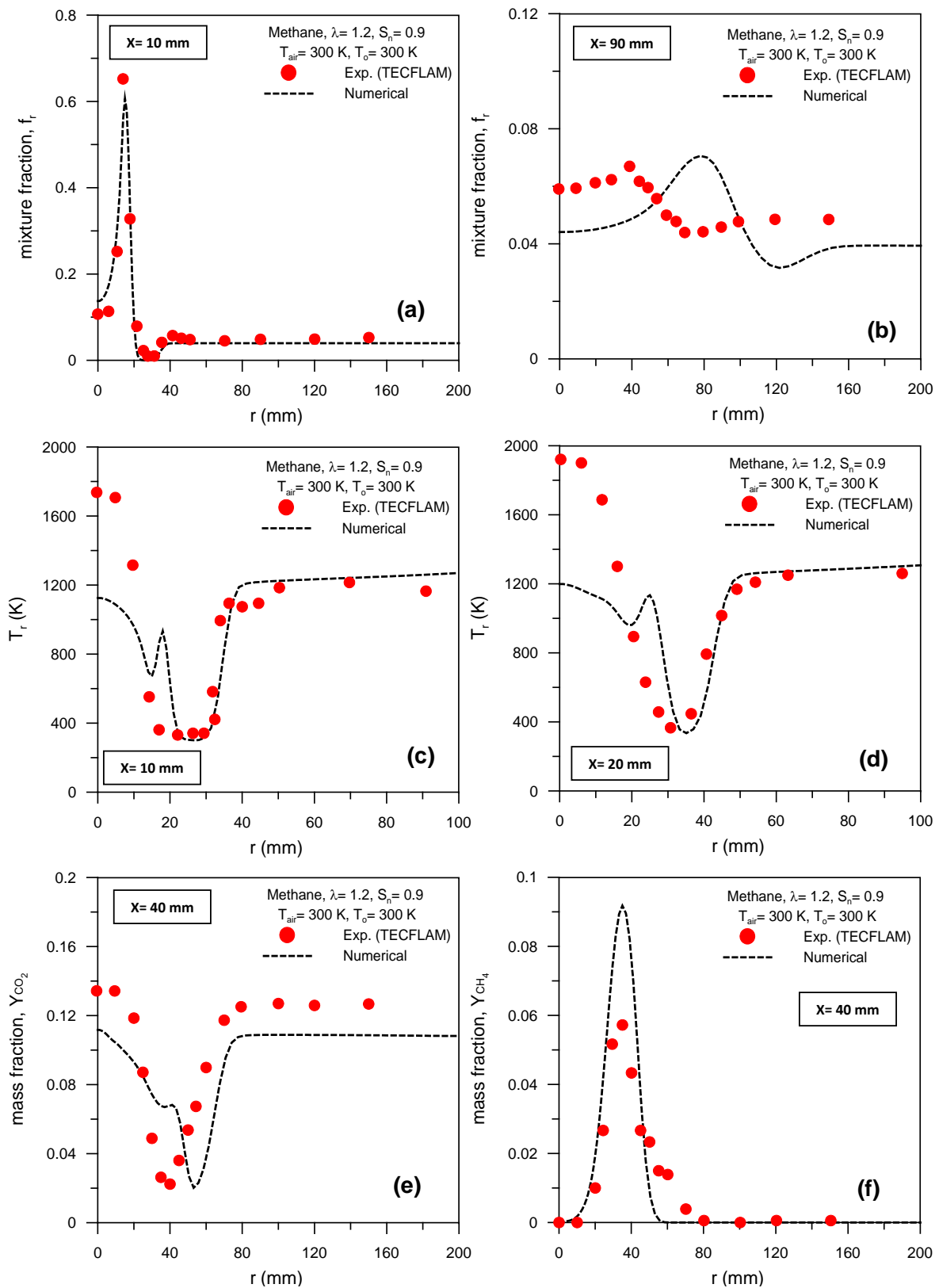
Figure 5.75: Comparisons of numerical and experimental measurements [105]; (a) radial distribution of mean mixture fraction, (b) radial distribution of mean mixture fraction, (c) radial distribution of mean temperature, (d) radial distribution of mean temperature, (e) radial distribution of mean mass fraction of CO_2, and (f) radial distribution of mean mass fraction of CH_4.

Chapter 6

3D-Full Scale Rotary Kiln Flame Simulation: Results and Discussions

In this Chapter, 3D-CFD simulation is applied on 4 meter kiln diameter and 40 meter length (see Fig. 3.11 (b)), firing Methane gas in order to understand the flame behavior under different operating and burner geometrical parameters. Challenges in the simulation of full-scale kilns are discussed. Design aspects of burner configuration, as they related to aerodynamics and heat transfer are investigated for two different burner configurations (see Fig. 3.11 (c)). Concerning the operating parameters; primary air ratio and burner power are presented and discussed in context of the burner configuration.

The results in this Chapter were divided into three main sections according to the influencing parameters; the first one is primary air ratio, the second one is related to burner configurations and the last one but not the least concerning to the burner power. So the influence of the previous operational and geometrical parameters on the center-line axial temperature profiles, inverted dimensionless axial mean mixture fraction profiles to estimate the flame lengths are simulated and presented. In addition to the flame radiation heat flux, wall received radiation heat flux, radiative heat transfer coefficient, temperature contours and pathlines colored by temperature to show the recirculation zones are conducted and discussed in the following sections.

6.1   Primary air ratio

Most of rotary kilns operate at primary air ratio (α) of about 12%, which is the fraction of primary air part. Owing to reducing the cost of combustion air, kiln designers and operators are interested in lowering this value to about 8% [31]. In this simulation a wide range of primary air ratios was studied ($0.1-1$). Also as discussed in Chapter 5, most of industrial kilns operate with concentric type burner (i.e., annulus burner) for the reason of flame stability. In industrial kilns, economics dictate that most of the combustion air is supplied as secondary air, where the induction fans and cooler fans drive the flow over the hot charge, it recycles heat back to the kiln, decreasing the overall energy consumption. Therefore, the secondary air not only supplies the oxygen needed for combustion, but also recuperates heat from the charge. In many kiln operations, utilizing the secondary air in the cooling of the hot solids is an essential part of the process, the secondary air flow is driven by the combined action of the primary jet and induction, induction and cooler fans. The flame stability and prober combustion are governed by the degree of

recirculation induced by the primary jet momentum. Also service life of the burner tip and the refractory wall influenced by primary air ratio. As well the primary air ratio affects the magnitude and location of peak flame temperature. In this study the effects of primary air ratio on the flame aerodynamics and heat transfer are fulfilled and discussed.

In general, the effects of primary air ratio varies from 0.1 to 1, firing CH_4 gas at 40 MW burner load, T_{pa}= 20°C, T_{sa}= 250°C and λ= 1.12 for burner (A) on the centerline axial temperature profiles, flame length, peak flame temperature, flame radiation heat flux, radiative heat transfer coefficient, recirculation zones and temperature contours are shown in Figs (6.1−6.8) for isothermal kiln walls (T_w= 250°C). The radiation is considered (i.e., the radiation model (P1) is used) and the kiln is fully opened for secondary air.

Figures (6.1 and 6.2) show the influence of primary air ratio (0.1, 0.3, 0.5, 0.7, 1) on the centerline axial temperature profiles and temperature contours, respectively, along the flame axis. As shown in the Fig. 6.1, the axial temperature distribution drops with increasing primary air ratio, this trend appears up to α= 0.7, other than the temperature distribution increases with primary air ratio. The possible explanation is that, up to α= 0.7 the mixing temperature between secondary air and primary air close to the temperature of primary air as a result of increasing the mass part of primary air. On the other side, up α= 0.7, there are two combined and opposite effects on the flame temperature, the first one is the mixing temperature which cool the flame and the second one is the primary air velocity which improves the mixing between the combustion air and fuel and consequently increases the flame temperature. The final result is the primary air velocity overcomes the mixing temperature between primary air and secondary air, hence the flame temperature increases with increasing primary air ratio up α= 0.7.

The effect of the primary air ratio on the inverted dimensionless axial mean mixture fraction profiles was illustrated in Fig. 6.3. As displayed in the Figure, the mixture fraction can reach to the stoichiometric value at high primary air ratio in consequence the flame length can be calculated. While, at low primary air ratio the mixture can't reach to the stoichiometric value. This can be attributed to the higher the primary air ratio at ambient temperature, the higher amount of diffused air into the fuel as a result in the combustion process can complete in short distance from the burner tip, hence the mixture fraction can reach to the stoichiometric value. On the other hand, at lower primary air ratio, the temperature of secondary air (i.e., preheated air) is dominant, hence less amount of diffused air into fuel due to less air density and consequently the flame spreads to complete the reaction process without reaching to the stoichiometric value. The final conclusion is that the flame length can be obtained at high primary air ratio, and vice versa.

Figure 6.4 explains the effect of primary air ratio on the peak flame temperature. As shown in the Figure, the peak flame temperature decreases with increasing the primary air ratio up to α= 0.7, after that the peak flame temperature increases with increasing the primary air ratio. As it was explained before, two combined and opposite factors affect the flame temperature; mixing temperature of primary and secondary air, and primary air velocity. Up to α= 0.7 the mixing temperature is dominant so the primary air drops the flame temperature, but up α= 0.7 the primary air velocity is

dominant and it increases the flame temperature due to improving the mixing process between combustion air and fuels.
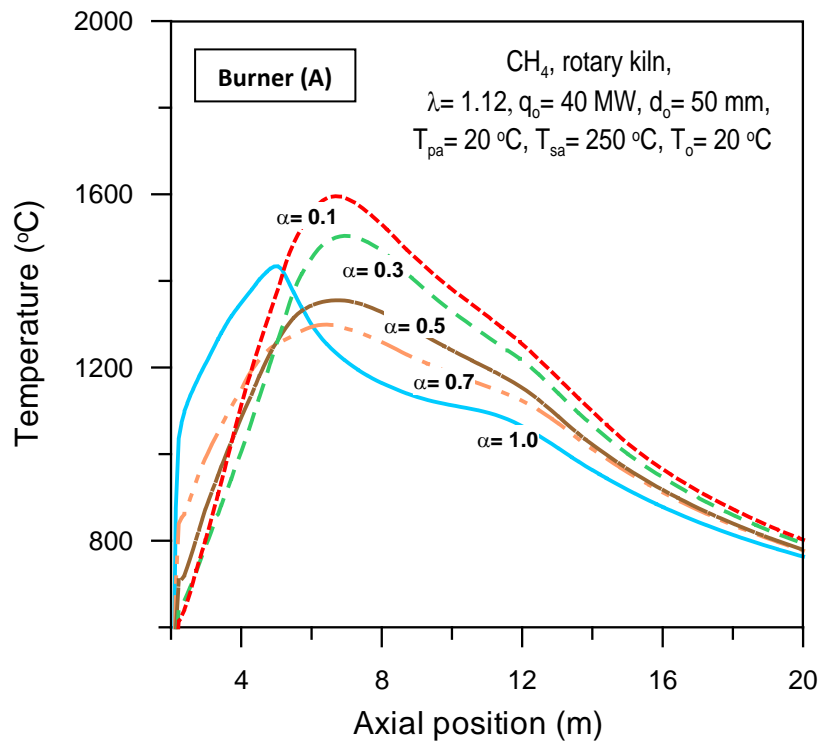
Figure 6.1: Influence of primary air ratio on the centerline axial temperature profiles, firing Methane gas at $T_w = 250°C$.
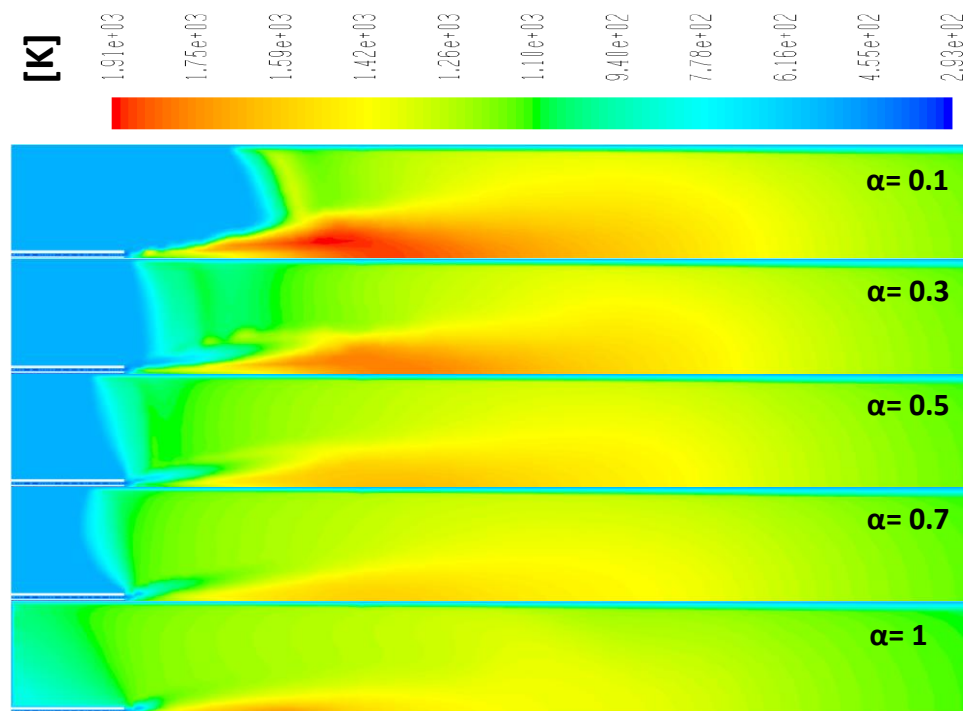
Figure 6.2: Influence of primary air ratio on temperature contours, firing Methane gas at burner load of 40 MW, $T_{pa} = 20°C$, $T_{sa} = 250°C$, $T_w = 250°C$ and $\lambda = 1.12$.

Figure 6.3: Influence of primary air ratio on the inverted dimensionless axial mean mixture fraction profiles, firing Methane gas at $T_w = 250°C$.
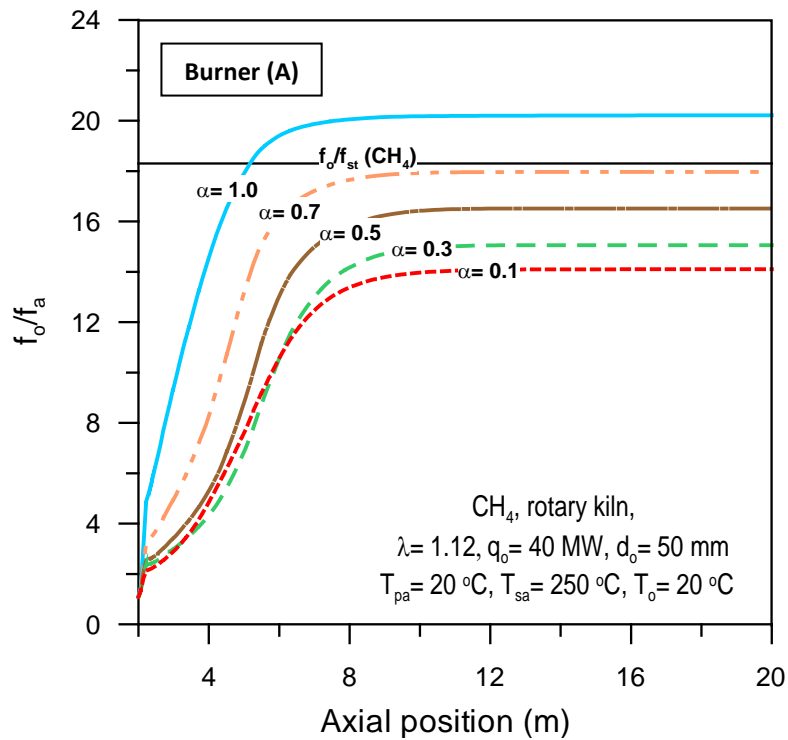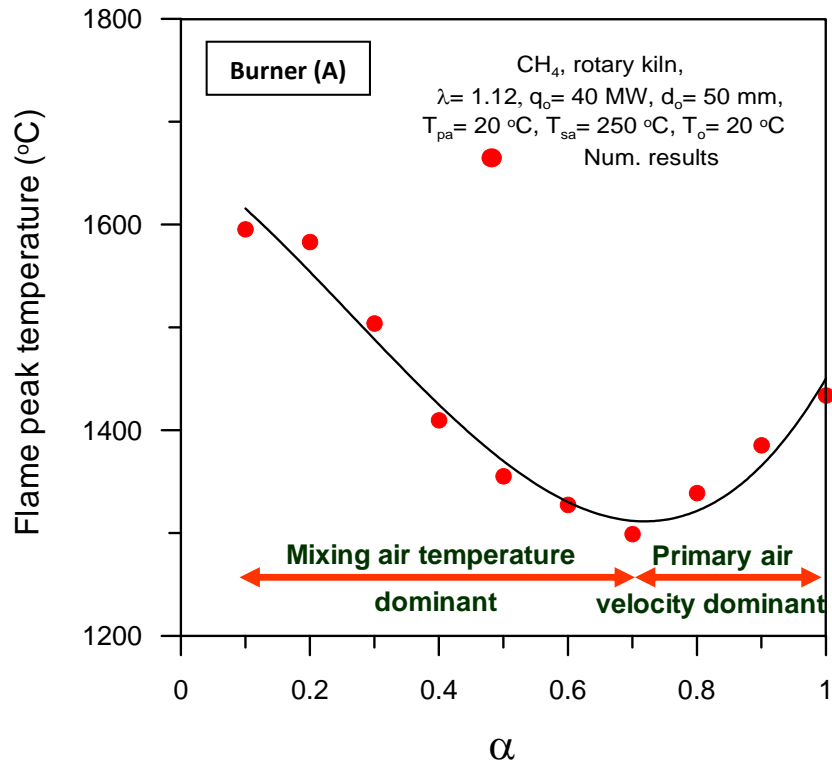

Figure 6.4: Influence of primary air ratio on the computed peak flame temperature, firing Methane gas at $T_w = 250°C$.

The amount of radiation coming from the flame which received by the load is presented by [106] and given by:

$$q_{f,rad} = \sigma A \varepsilon_f T_f^4 \tag{6.1}$$

where, σ is the Stefan-Boltzmann constant, A is the area radiating, T_f is the average absolute flame temperature and ε_f is the average flame emissivity. The flame emissivity varies with fuel type, for fuel gases with C:H weight ratio between 3.5 and 5, the flame emissivity can be calculated by either of two correlations [106]:

$$\varepsilon_f = 0.2\sqrt{\frac{LHV}{900}} \tag{6.2}$$

where, LHV is the lower heating value of the fuel in Btu/ft^3, or

$$\varepsilon_f = 0.048\sqrt{M_o} \tag{6.3}$$

where, M_o is the molecular weight of the fuel, then the flame emissivity for CH_4 gas is approximated as $\sim$0.2. Based on the Eqns. (6.2 and 6.3), Fig. 6.5 presents the effect of primary air ratio on the flame radiation heat flux. As shown in the Figure the axial flame radiation heat flux drops with increasing primary air ratio. This effect observed up to $\alpha= 0.7$, other than the flame radiation heat flux increases with primary air ratio. The possible explanation is that the flame radiation heat flux depends on the flame temperature according to Eqn. 6.2, therefore, Fig. 6.5 is similar shape to Fig. 6.1.

Similarly, the local radiative heat transfer coefficient between flame and walls can be calculated based on Eqn. 2.23 and Table 2.1. From this place, the effect of primary air ratio on the radiative heat transfer coefficient was presented in Fig. 6.6. As observed in the Figure the local radiative heat transfer coefficient drops with increasing primary air ratio. This effect appeared up to $\alpha= 0.7$, other than the local radiative heat transfer coefficient increases with primary air ratio. This is because of the local radiative heat transfer coefficient depends on the flame and wall temperatures according to Eqn. 2.23. So that Fig. 6.6 is similar shape to Figs. (6.5 and 6.1).

The wall received radiation was calculated using Eqn. 2.23 by assuming the material of the wall is fire clay (ε_{A_g}=0.75 [106]) therefore, Fig. 6.7 shows the flame radiation and wall received radiation heat fluxes for burner (A) at $\alpha= 0.1$. As we see in the Figure the wall received radiation heat flux is lower than the flame radiation heat flux. This can be attributed to part of heat released by flame radiation is stored in the combustion gas. It is well known that combustion occurs as a result of four steps in series: mixing, ignition, chemical reaction and dissipation of products. In the confined turbulent diffusion flame, the rate of combustion is controlled by mixing. The recirculation is responsible for intensify mixing and combustion, by recirculation of gases from downstream regions back to combustion zones. As we mentioned before the flame stability and proper combustion are governed by the degree of recirculation induced by the primary jet momentum. Fig. 6.8 presented the influence of primary air ratio on the recirculation size, also the reaction rates are higher in the presence of recirculation. As depicted in the Figure the recirculation size increases with increasing the primary air ratio, the same investigation

had been done by [31]. This is because of the primary jet momentum increases with increasing the primary air ratio due to an increase of the primary jet velocity.
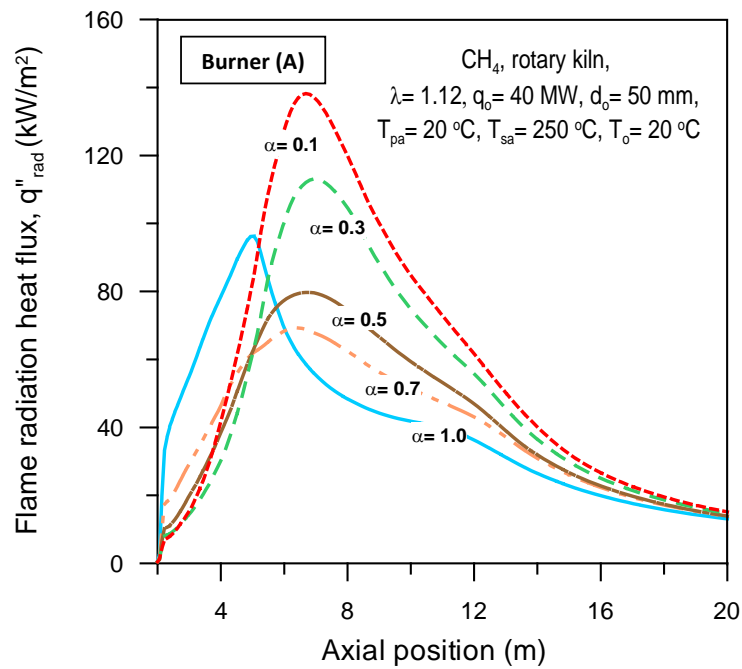
Figure 6.5: Influence of primary air ratio on the flame radiation heat flux, firing Methane gas at $T_w = 250°C$.

Figure 6.6: Influence of primary air ratio on the radiant heat transfer coefficient, firing Methane gas at $T_w = 250°C$.

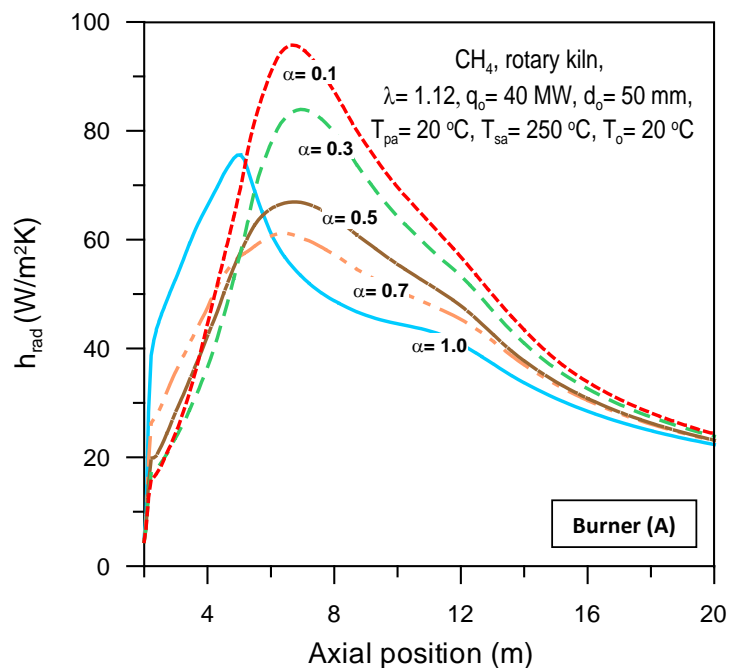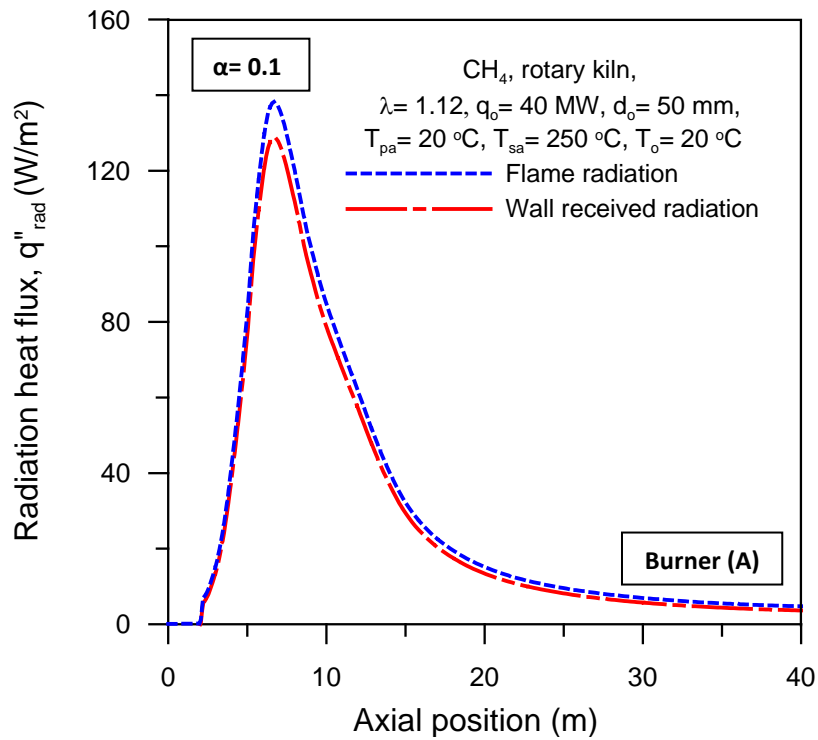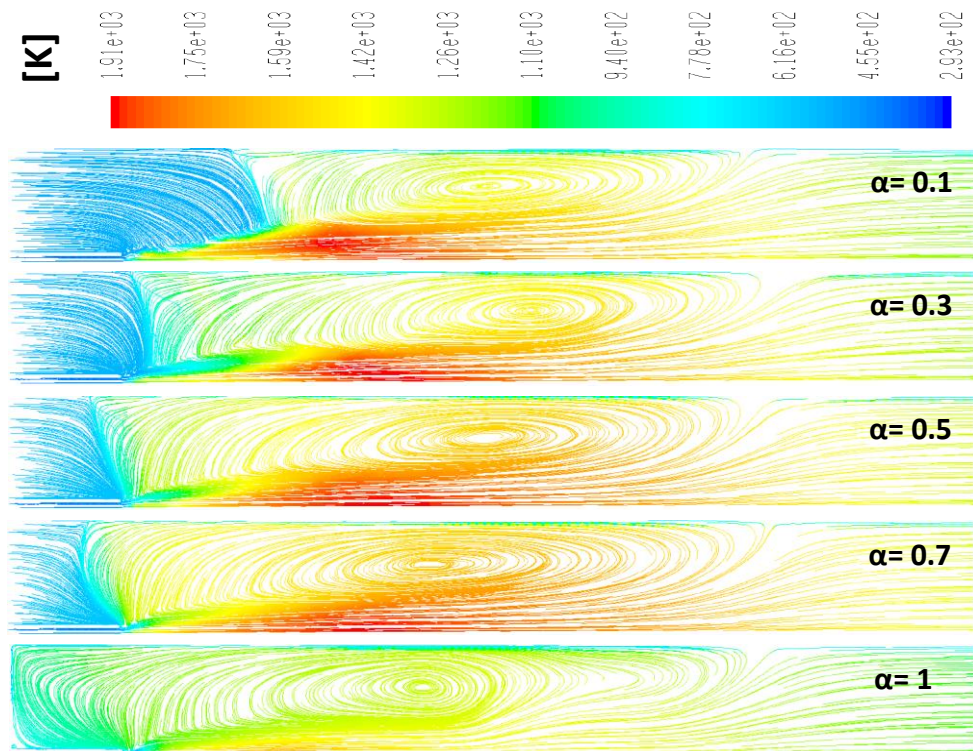Figure 6.7: Flame radiation and wall received radiation heat fluxes, firing Methane gas at $T_w = 250°C$.

Figure 6.8: Influence of primary air ratio on pathlines colored by temperature, firing Methane gas at $T_w = 250°C$.

6.2   Burner configuration

Two burner configurations are proposed to examine the influence of the burner config-uration on the flame flame aerodynamics and heat transfer in the rotary kiln; burner configuration A and burner configuration B. Burner configuration A has a 50 mm fuel nozzle diameter (fuel momentum flux, G_o ~249 kPa) surrounded by a primary air annulus of 100 mm ID and 200 mm OD. While, burner configuration B has 100 mm fuel nozzle diameter (fuel momentum flux, G_o ~16 kPa) and the primary jet annulus is 360 mm ID and 440 mm OD (see Fig. 3.11 (c)). To minimize the numerical effect of the inlet conditions, the inlet boundaries are set at 2 m upstream the burner outlet (see Fig. 3.11 (a)). From this situation, the effects of fuel-inlet diameter (50 and 100 mm) on the flame behavior are shown in Figs (6.9−6.17). In this section CH_4 gas was used at 40 MW burner load, T_{pa}= 20°C, T_{sa}= 20 and 250°C, T_w= 250°C, λ= 1.12 and α= 0.1 for both burner configurationss (A and B). The radiation is considered (i.e., the radiation model (P1) is used) and the kiln is fully opened for secondary air.

Figures 86.9 and 6.10) show the axial profiles of the center-line temperature for both configurations (burner A and burner B) at isothermal and adiabatic kiln walls, respectively. As shown in the Figures the peak flame temperature is higher 170°C and 145°C in the flames of burner A (higher jet momentum) than burner B (lower jet momentum) at isothermal and adiabatic kiln walls, respectively. Similarly, the peak flame temperature shifted to right by 3.5 and 7 m at isothermal and adiabatic kiln walls, respectively. This is experienced as a result of the increased primary jet momentum of burner A which improves the mixing process and consequently increase the flame temperature. Also as shown in the Figures, farther downstream, the center-line temperature profiles of burner B (lower jet momentum) is slightly and significantly higher for isothermal and adiabatic kiln walls, respectively. This is because of the elongation of reaction zone area as a result of lower primary jet momentum (see Fig. 6.17 (a)).

To the kiln operator, the wall temperature is more important than that of the gas temperature. As the solids pass through the flame zone, if the wall temperature is high enough, the material may reach to a semi-fused form, where it tends to stick to the wall. This causes rings formation, these rings act as a protective layers for refractory. If the wall temperature is much higher, these rings become thick and behaves as obstruction for solids flow. So the results of wall axial temperature profiles for both burner configurations at adiabatic kiln walls condition and at T_{sa}= 20°C and 250°C are shown in Figs. 6.11 and 6.12, respectively. As shown in the Fig. 6.11, the wall temperatures have a sudden increase, starting away 5 m and 9 m downstream of the burners and reach to a peak of 845°C and 1296.5°C at the wall hot spots which located at 13 m and 20 m downstream of burner A (higher jet momentum) and burner B (lower jet momentum), respectively. Also as shown in the Figure, the burner B (lower jet momentum) has a flatter wall temperature profile, and higher peak wall temperature by about 452°C with right shift by about 7 m. This can be attributed to the lower jet momentum the lower recirculation size and consequently flatter thermal distribution near the wall due to elongation of combustion zone (see Fig. 6.17).

Similarly, Fig. 6.12 presents the wall temperature profiles of burner A (higher jet momentum) and burner B (lower jet momentum). The results in the Figure show that,

the wall temperatures have a sudden increase, starting away 4.5 m and 7.5 m downstream of the burner and reach to a peak of 973°C and 1063.5°C at the wall hot spots, which located at 12 m and 15 m downstream of burner A (higher jet momentum) and burner B (lower jet momentum), respectively. Also as shown in the figure, the burner B (lower jet momentum) has a flatter wall temperature profile, and higher peak wall temperature with 90°C with right shift with 3 m.

Figure 6.13 explains the inverted dimensionless axial mean mixture fraction profiles a long the flame in order to calculate the flame length for both burner configurations; burner A (higher jet momentum) and burner B (lower jet momentum) at 40 MW burner load, T_{pa}= 20°C, T_{sa}= 20°C, λ= 1.12, α= 0.1 and adiabatic kiln walls. As shown in the Figure the flame of burner B (lower jet momentum) longer than the flame of burner A (higher jet momentum) with ~100 %. The possible explanation is that, burner A has a higher jet momentum as a result of higher jet velocity. Increasing the fuel jet velocity improves the mixing between the fuel and the oxidizer, improving the mixing process completes the combustion in short distance which reduces the flame length, the same investigation had been done by ref. [71]. Fig. 6.14 shows the effect of burner configurations on the mean mixture fraction contours to explain how the burner diameter has a significant effect on the flame length.

The flame radiation heat flux for both configurations (burner A and burner B) at 40 MW burner load, T_{pa}= 20°C, T_{sa}= 20°C, λ= 1.12, α= 0.1, and isothermal kiln walls (T_w=250°C) was depicted in Fig. 6.15. As shown in the Figure, the axial flame radiation heat flux (calculated based on Eqns 6.2 and 6.3) of burner A (higher jet momentum) is higher than that is released from burner B (lower jet momentum), this effect appears up to 10 m, farther downstream, however, the axial flame radiation heat flux of burner B (lower jet momentum) is slightly higher, this is because of the flame radiation heat flux depends on the flame temperature according to Eqn. .

Similarly, the local radiative heat transfer coefficient between flame and walls can be calculated based on Eqn.2.23 and Table 2.1. Therefore, the effect of burner configuration on the radiative heat transfer coefficient was presented in Fig. 6.16. As shown in the Figure, the local radiative heat transfer coefficient drops with increasing fuel-inlet diameter (burner B). This effect appeared up to 10 m, other than the local radiative heat transfer coefficient slightly increases with increasing fuel-inlet diameter (burner B). This is because of the local radiative heat transfer coefficient depends on the flame and wall temperatures according to Eqn. 2.23.

Comparisons between both burner configurations (burner A and burner B) to explain the influence of fuel-inlet diameter on the temperature contours, recirculation size presented by pathlines colored by temperature and species mass fraction for both CH_4 and CO_2 are shown in Fig.6.17. As illustrated in the Figure, the burner A (d_o= 50 mm) has a higher peak flame temperature, bigger recirculation zone size and lower mass fraction distributions for both CH_4 and CO_2. Vice versa with using burner B (d_o= 100 mm), this is due to the jet momentum which has strongly affect the flame aerodynamics and heat transfer inside the kiln, as it was discussed before.
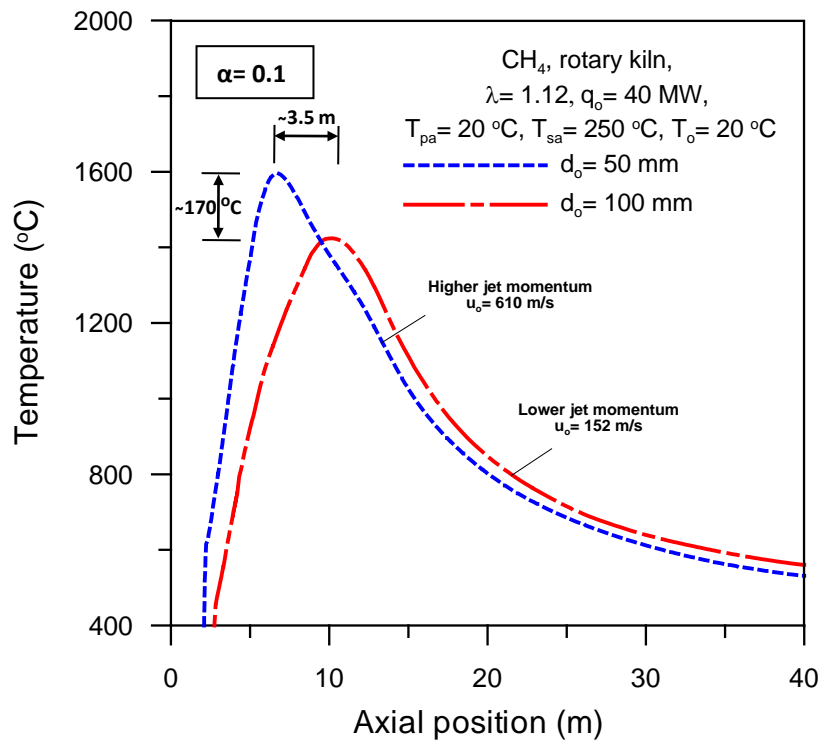
Figure 6.9: Influence of fuel-inlet diameter on the center-line axial temperature profiles, firing Methane gas for isothermal kiln walls ($T_w = 250°C$).
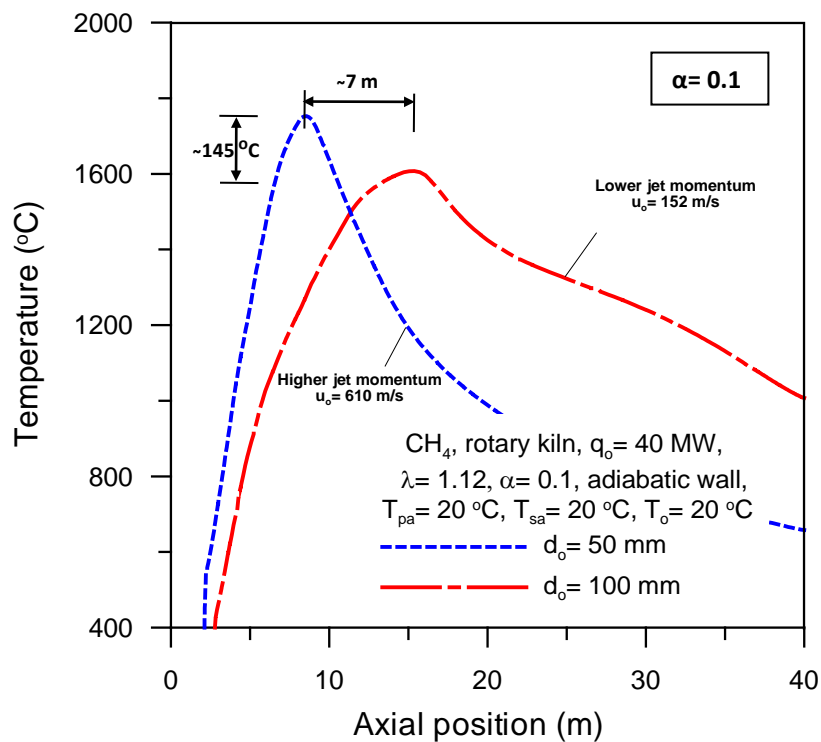
Figure 6.10: Influence of fuel-inlet diameter on the center-line axial temperature profiles, firing Methane gas for adiabatic kiln walls.
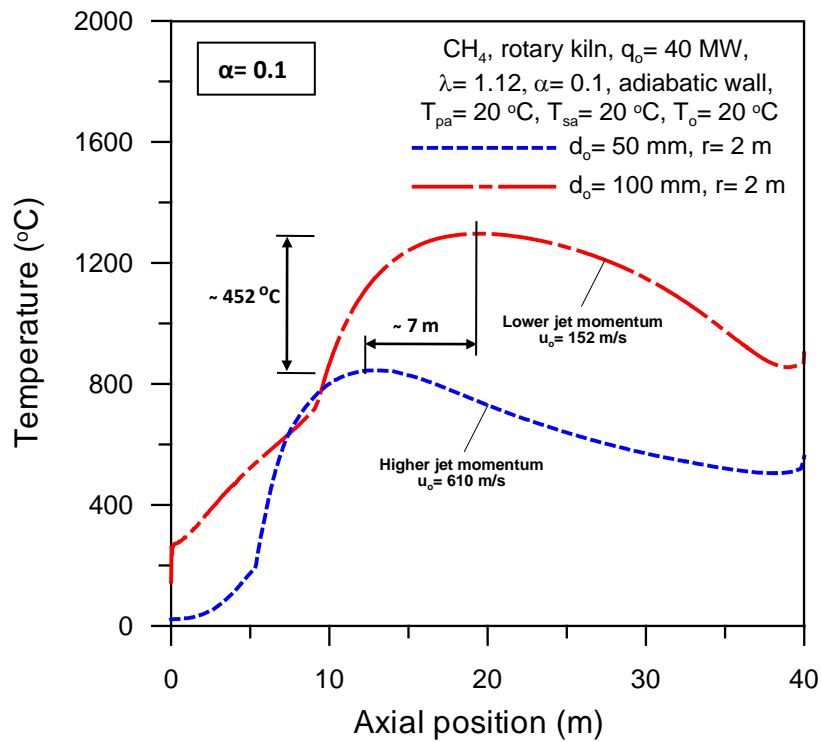
Figure 6.11: Influence of fuel-inlet diameter on the wall temperature profiles, firing Methane gas for adiabatic kiln walls and $T_{sa} = 20°C$.
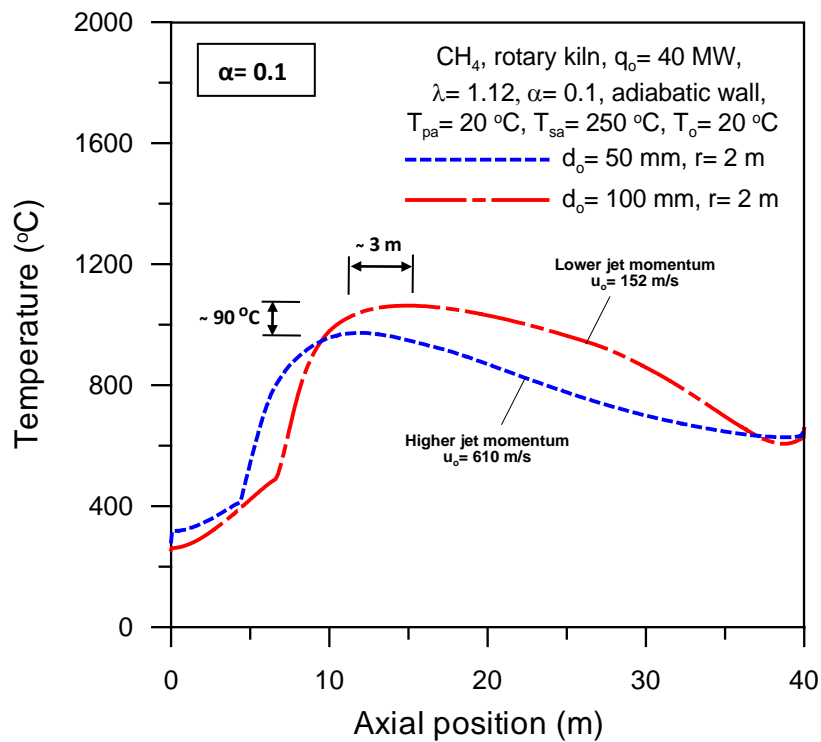
Figure 6.12: Influence of fuel-inlet diameter on the wall temperature profiles, firing Methane gas for adiabatic kiln walls and $T_{sa} = 250°C$.
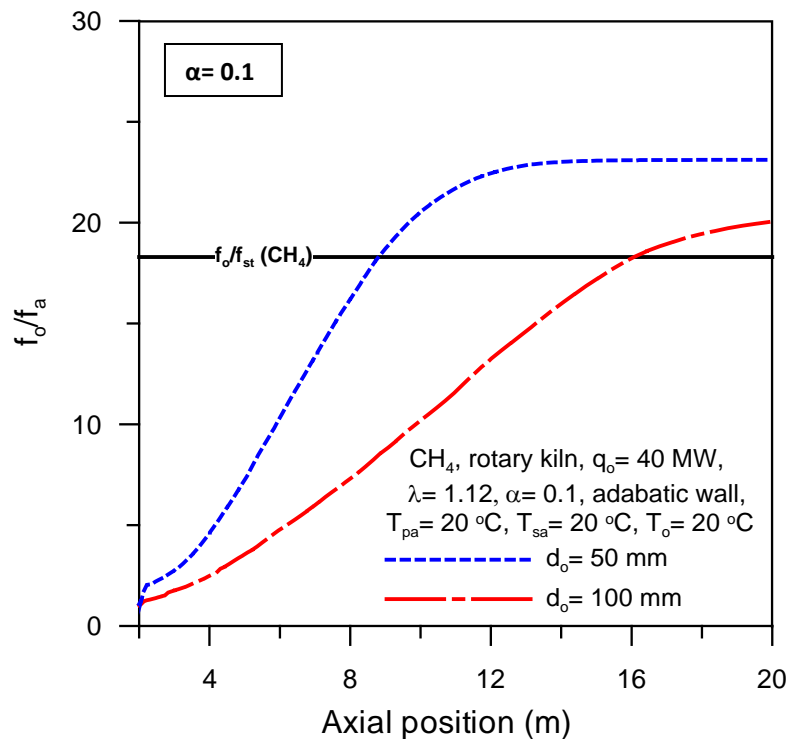
Figure 6.13: Influence of fuel-inlet diameter on the inverted dimensionless axial mean mixture fraction profiles, firing Methane gas.
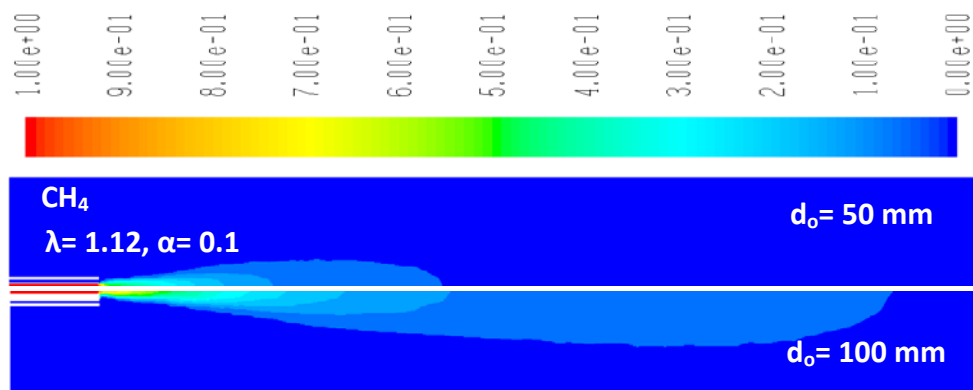
Figure 6.14: Influence of fuel-inlet diameter on the inverted dimensionless axial mean mixture fraction profiles, firing Methane gas for adiabatic kiln walls at burner load of 40 MW, $T_{pa} = 20°C$, $T_{sa} = 20°C$, $\lambda = 1.12$ and $\alpha = 0.1$.
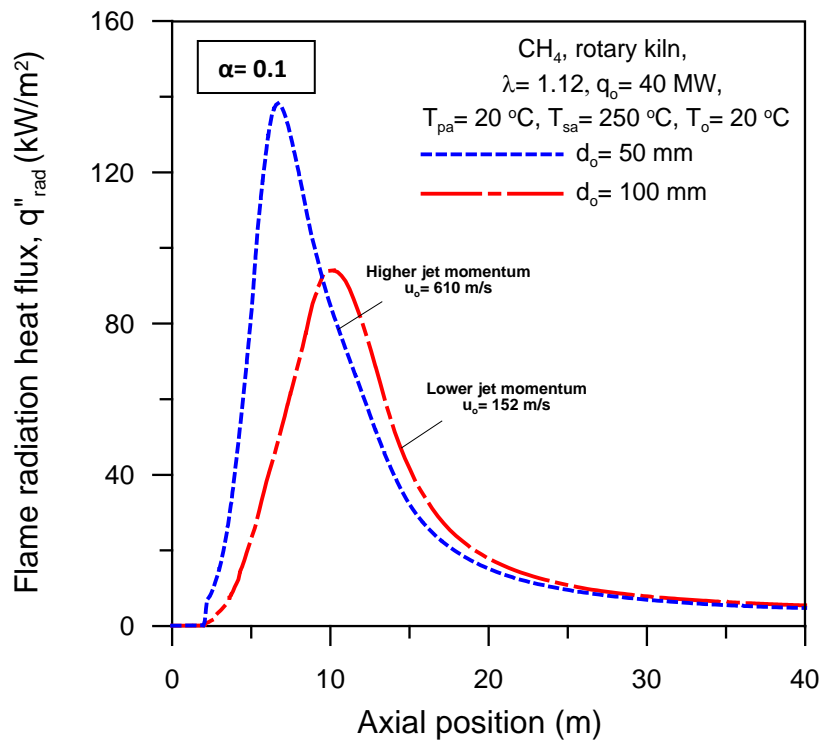
Figure 6.15: Influence of fuel-inlet diameter on the flame radiation heat flux, firing Methane gas at $T_w = 250°C$.
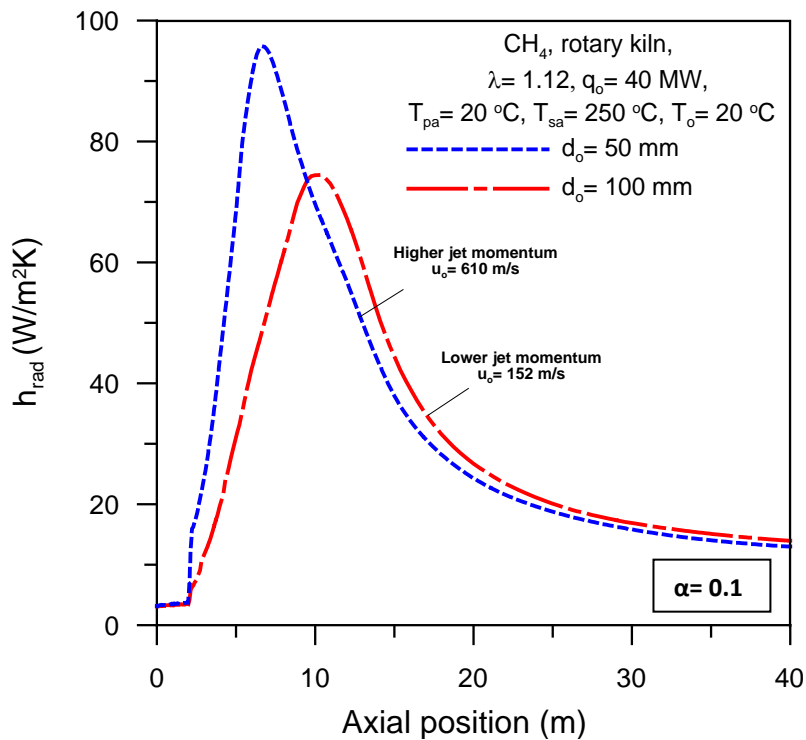
Figure 6.16: Influence of fuel-inlet diameter on radiant heat transfer coefficient, firing Methane gas at $T_w = 250°C$.
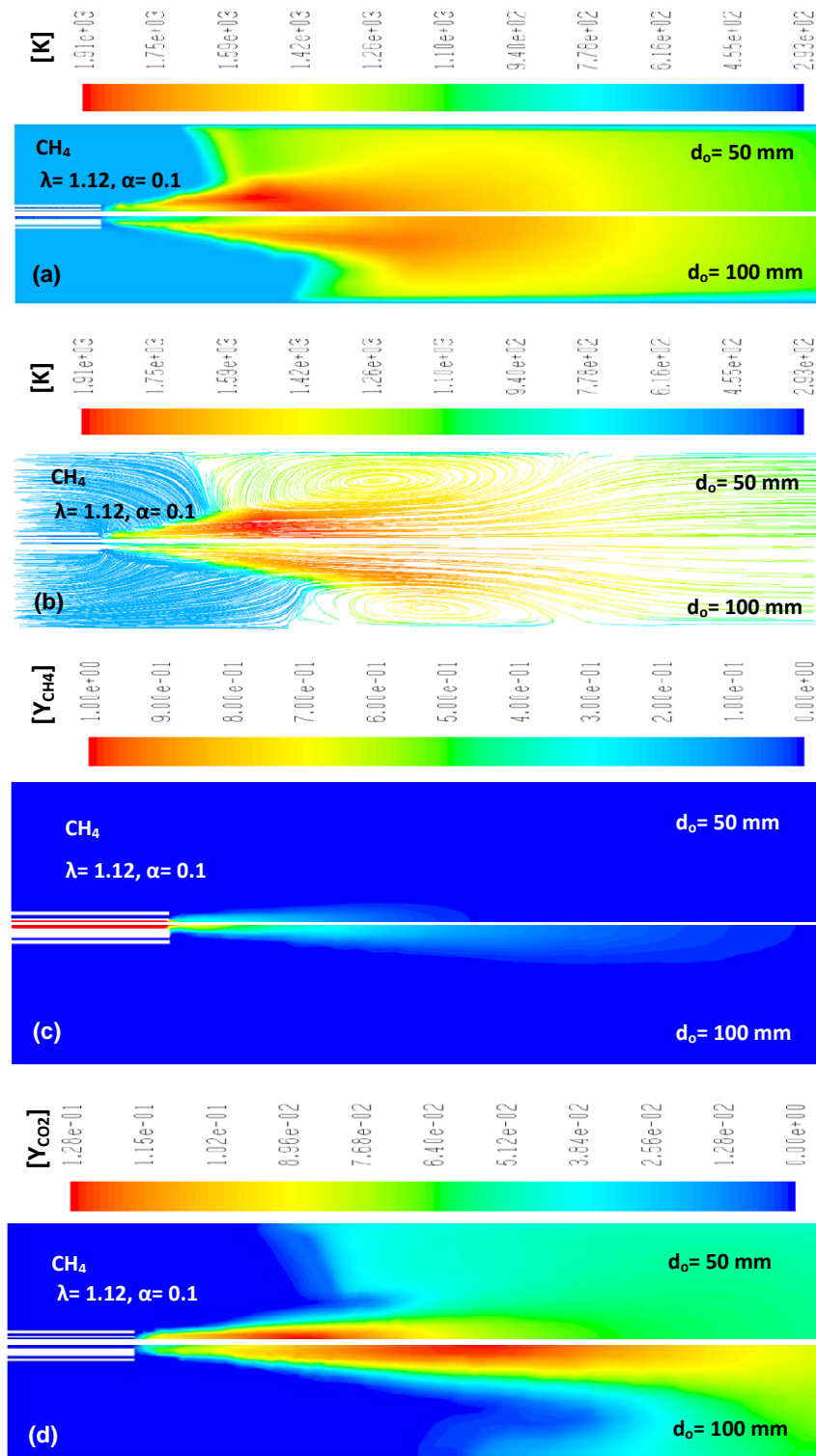
Figure 6.17: Influence of fuel-inlet diameter on the: (a) temperature contours, (b) path-lines colored by temperature, (c) CH_4 mass fraction contours, and (d) CO_2 mass fraction contours, firing Methane gas at burner load of 40 MW, $T_{pa}=20°C$, $T_{sa}=250°C$, $T_w=250°C$, $\lambda=1.12$, and $\alpha=0.1$.

6.3   Burner power

In this section, the influence of burner power on the flame aerodynamics and heat transfer inside the rotary kiln was carried out and discussed in the following paragraphs. Two burner powers (10 MW and 40 MW) were recommended to study. In the simulation, CH_4 gas was used at T_{pa}= 20°C, T_{sa}= 20°C, λ= 1.12, α= 0.1 for burner A and burner B with adiabatic kiln walls. The radiation is considered (i.e., the radiation model (P1) is used) and the kiln is fully opened for secondary air. Figure 6.18 shows the velocity vectors distribution colored by temperature for complete kiln using burner A at 10 MW burner power. However, the effects of burner powers (10 and 40 MW) on the flame behavior are shown in Figs (6.19−6.24).

The results in Figs. (6.19 (a) and (b)) show the influence of burner powers on the axial center-line and wall temperature profiles for burner A and burner B, respectively. As shown in the Figures the axial center-line and wall temperatures distribution increase with increasing the burner power. This trend is the same for both burner configurations, where, the peak flame temperature increases by ∼9 % and ∼26 % with the increasing of burner power from 10 to 40 MW for burner A and burner B, respectively. In addition to, the peak wall temperature (i.e., wall hot spot) increases by ∼17 % and ∼40 % with increasing of burner power from 10 to 40 MW for burner A and burner B, respectively. The possible explanation is that the amount of energy supplied by reactants (fuel and air) increases with increasing the burner power, hence the products outlet energy (combustion heat released) increases and consequently an increase in the flame temperature. The increasing effect of peak axial center-line and wall temperature is major in case of burner B, this is because of prolongation of reaction zone area due to lowering the jet momentum and recirculation size with increasing the burner power.

The influence of burner power on the inverted dimensionless axial mean mixture fraction profiles was presented in Figs. (6.20 (a) and (b)) for burner A and burner B, respectively, in order to examine the influence of burner power on the flame length. As shown in Figs. (6.20 (a) and 6.24 (c)) for burner A (higher jet momentum, d_o= 50 mm), the burner power has approximately no effect on the flame length, this investigation is matched with [71] and [73]. On the other hand for burner B (lower jet momentum, d_o= 100 mm), the burner power has a considerable effect on the flame length, where, the flame length increases by ∼6.5 % with increasing of burner power from 10 to 40 MW. This can be attributed to the prolongation of reaction zone area due to lowering the jet momentum and recirculation size with increasing the burner power, as we discussed before.

It is well known that the flame radiation heat flux related with the flame temperature, as we mentioned in the previous sections. Therefore, the influence of burner powers (10 MW and 40 MW) on the flame radiation heat flux for both cases (burner A and burner B) at T_{pa}= 20°C, T_{sa}= 20°C, λ= 1.12, and α= 0.1 with adiabatic kiln walls was presented in Fig. 6.21. As displayed in the Figure and as explained in Sec.6.2, the axial flame radiation heat flux (calculated based on Eqns ?? and 6.3) of burner A (higher jet momentum) is higher than that is released from burner B (lower jet momentum). As well, the axial flame radiation heat flux increases with increasing the burner power, this is because of the amount of energy releases from combustion increases with increasing the input energy to reactants, in consequence the flame released heat flux increases.

Where, the peak flame radiation heat flux increased by $\sim$48 (kW/m^2) and $\sim$76 (kW/m^2) with increasing the burner bower from 10 MW to 40 MW for burner A (higher jet momentum) and burner B (lower jet momentum), respectively. The final result is that, the burner power has a considerable effect on the flame radiation heat flux and this effect is gradually increases with increasing the fuel-inlet diameter as in the configuration of burner B.

Similarly, Fig. 6.22 shows the flame radiation and wall received radiation heat fluxes for burner A with different burner powers (10 MW and 40 MW) as a parameter at $T_{pa}=$ 20°C, $T_{sa}=$ 20°C, $\lambda=$ 1.12, and $\alpha=$ 0.1 with adiabatic kiln walls. As shown in the Figure, the wall received radiation heat flux is lower than the flame radiation heat flux. This can be attributed to, part of heat is released by radiation from flame is stored in combustion gas. The influence of burner power on the local radiative heat transfer coefficient for burner A was presented in Fig. 6.23 at the same previous operating conditions. As shown in the Figure, the local radiative heat transfer coefficient increases with increasing burner power. As well, the maximum radiative heat transfer coefficient located at 12 m and increased by $\sim$27 % with increasing the burner power from 10 MW to 40 MW. The possible explanation is that the local radiative heat transfer coefficient depends on the flame and wall temperatures according to Eqn. 2.23, where, the flame temperature increases with increasing the burner power (see Fig.6.19), therefore, the local radiative heat transfer coefficient increasing with burner power.

The influence of burner power (10 MW and 40 MW) for burner configuration A at $T_{pa}=$ 20°C, $T_{sa}=$ 20°C, $\lambda=$ 1.12, and $\alpha=$ 0.1 with adiabatic kiln walls on the temperature contours, recirculation size presented by pathlines colored by temperature, and mean mixture fraction contours to examine the flame length is shown in Fig.6.24. As displayed in the Fig.6.24 (a), the higher flame temperature (i.e., larger high temperature zone area) and bigger flame volume are related with burner power of 40 MW, this due to the bigger reaction zone area as a result of increasing the contact area between the oxidizer and fuel. While, Fig.6.24 (b) shows that, the burner power has approximately no effect on the recirculation size as well as the flame length, as presented in Fig.6.24 (c). These conclusions are related with burner A ($d_o=$ 50 mm) only, and not completely for burner B ($d_o=$ 100 mm).
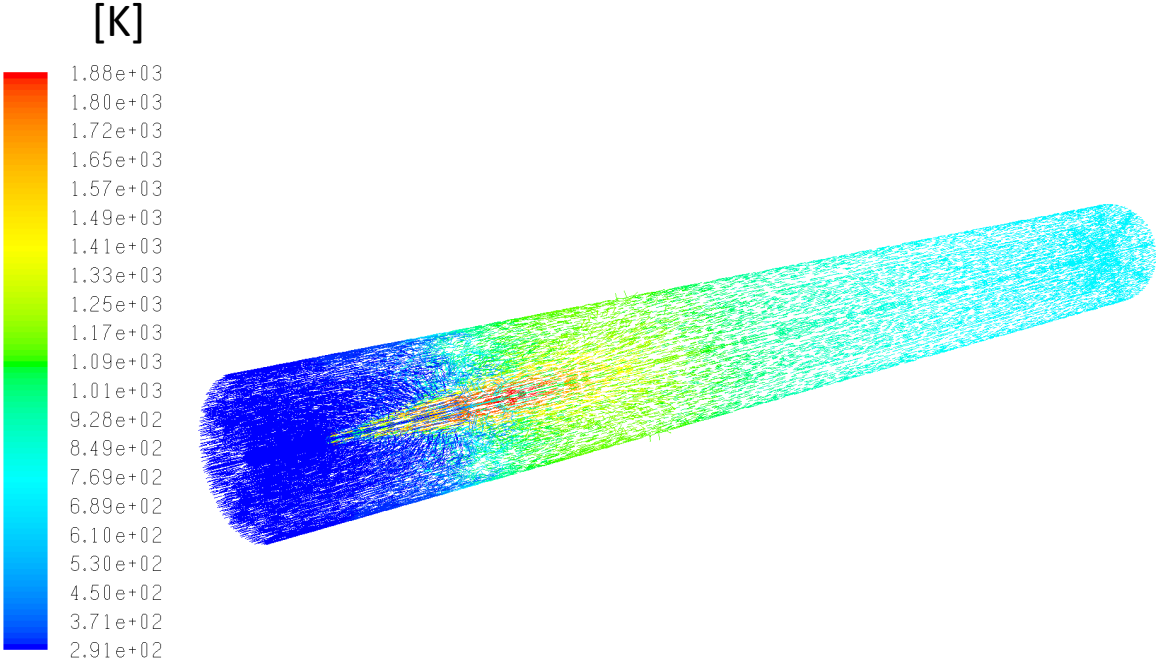
Figure 6.18: Velocity vectors distribution colored by temperature whole the kiln for burner A at T_{pa}= 20°C, T_{sa}= 20°C, λ= 1.12, and α= 0.1 and 10 MW burner power.
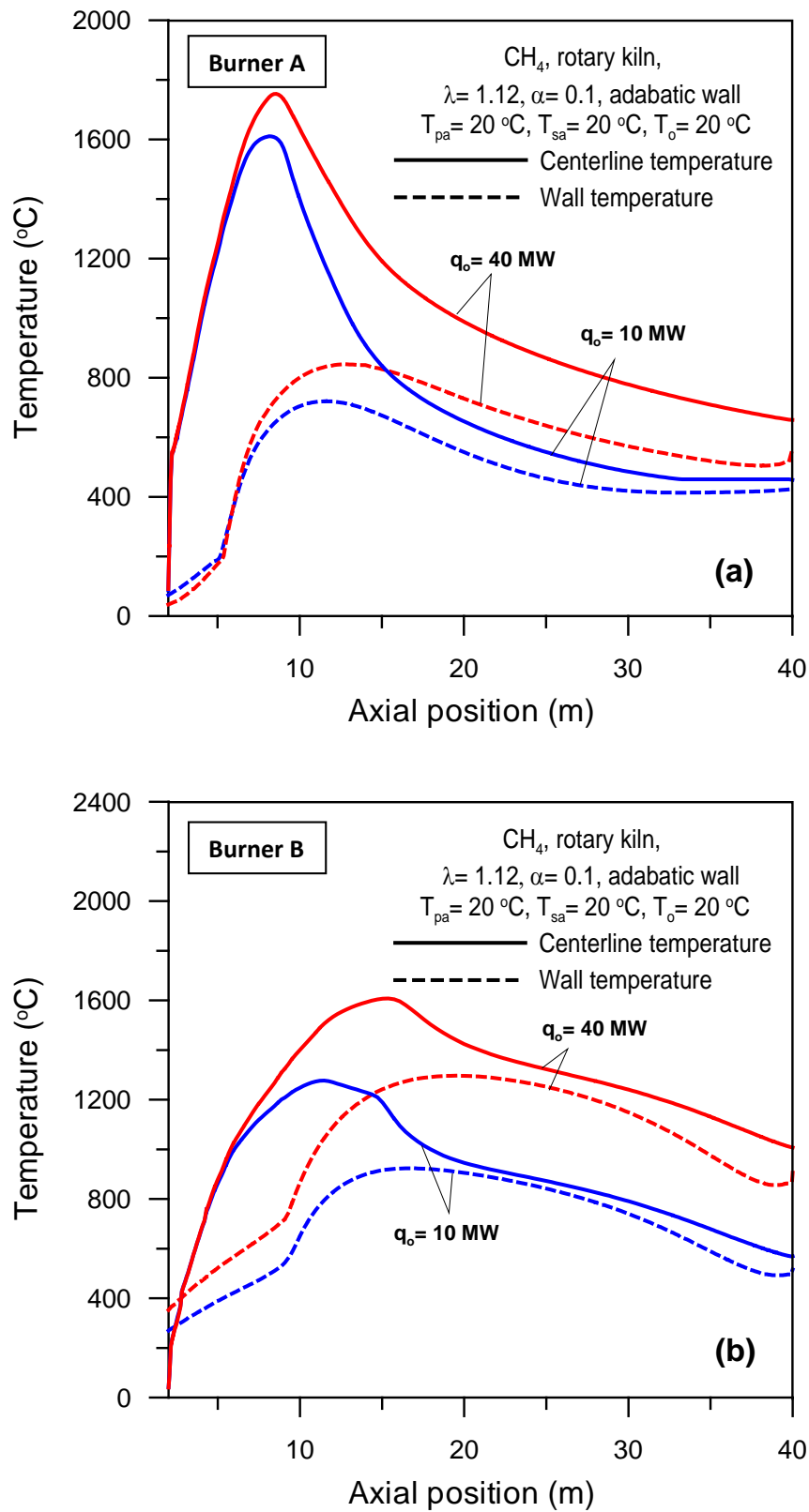
Figure 6.19: Influence of burner power on the centerline and wall temperature profiles, firing Methane gas: (a) burner A, (b) burner B.
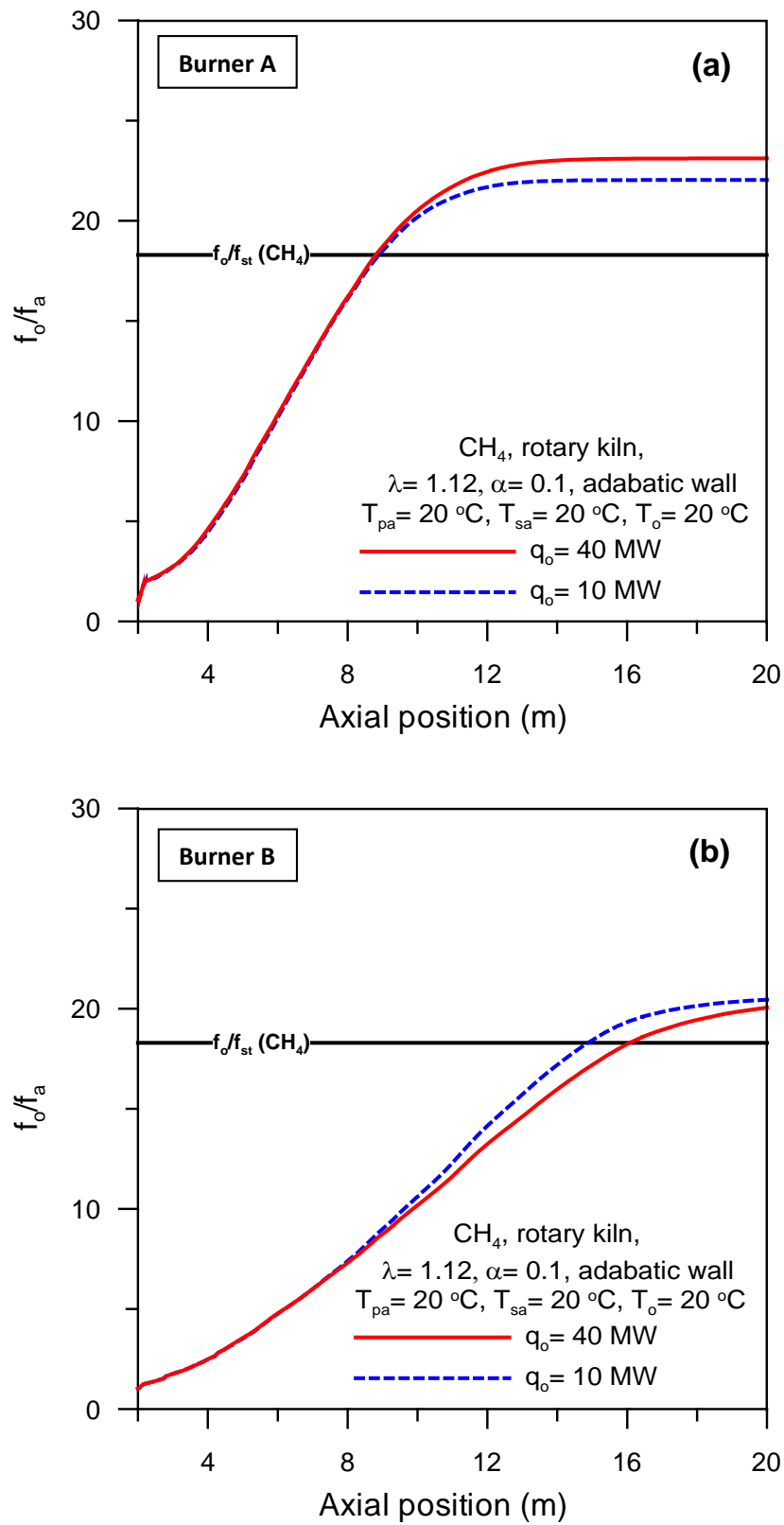
Figure 6.20: Influence of burner power on the inverted dimensionless axial mean mixture fraction profiles, firing Methane gas: (a) burner A, (b) burner B.
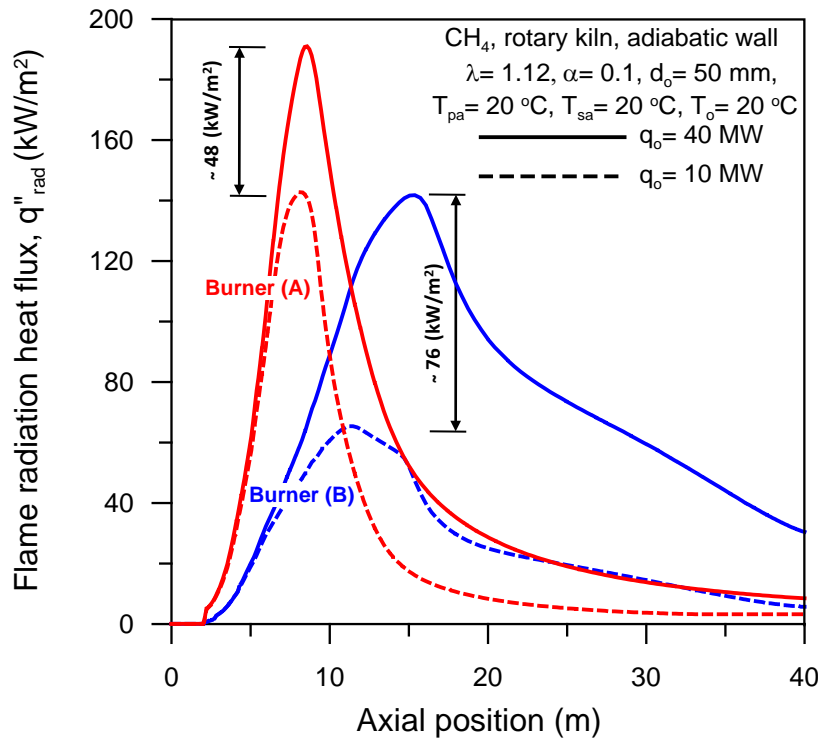
Figure 6.21: Influence of burner power on the flame radiation heat flux, firing Methane gas for burner A, and burner B.
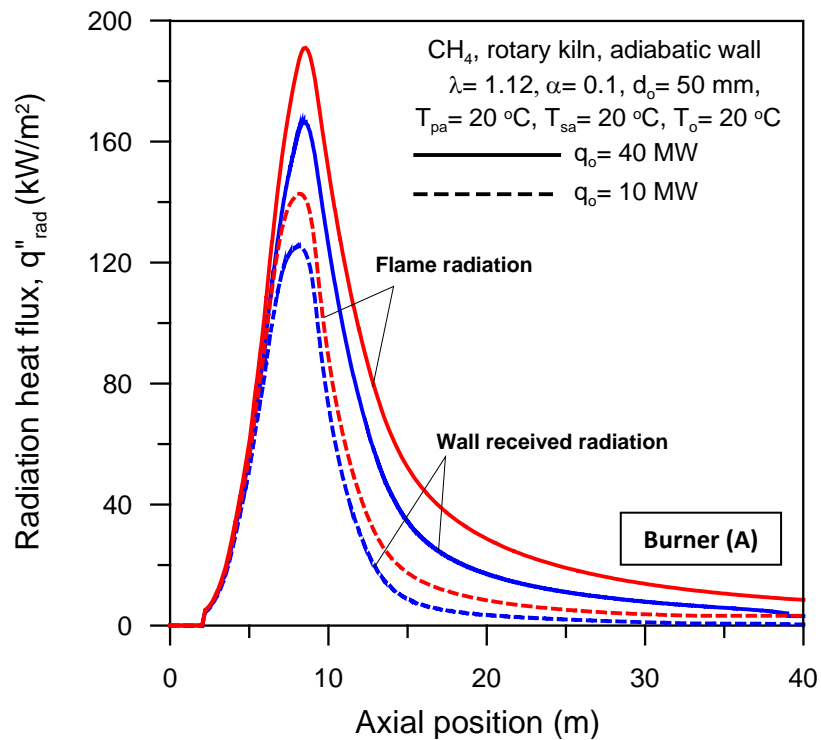
Figure 6.22: Influence of burner power on the flame and wall received radiation heat flux, firing Methane gas for burner A.
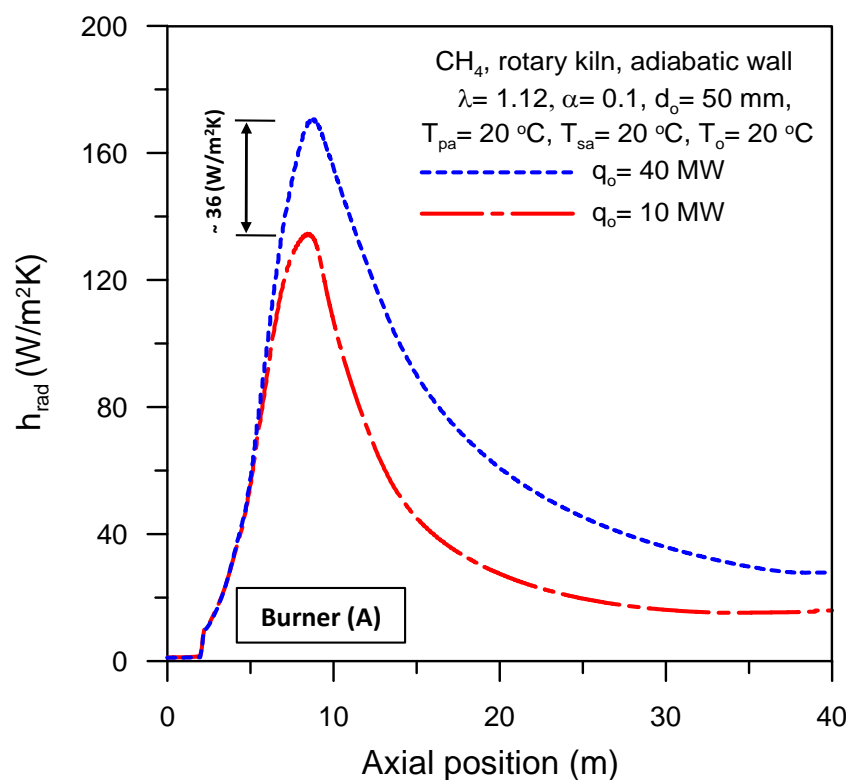
Figure 6.23: Influence of burner power on the radiant heat transfer coefficient, firing Methane gas for burner A.
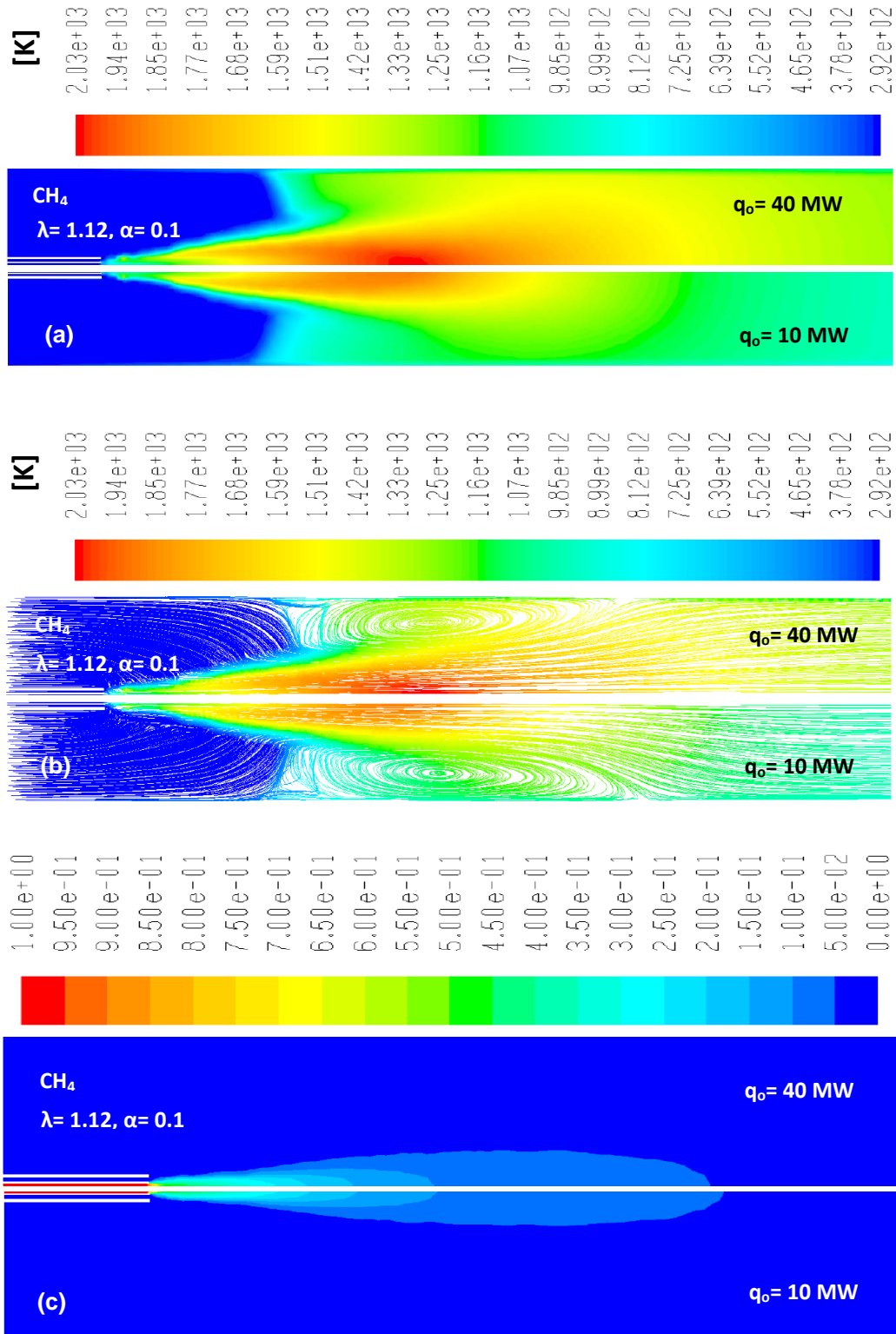
Figure 6.24: Influence of burner power on the: (a) temperature contours, (b) pathlines colored by temperature, and (c) mean mixture fraction contours, firing Methane gas at T_{pa}= 20°C, T_{sa}= 20°C, λ= 1.12, α= 0.1, and adiabatic kiln walls for burner A.

Chapter 7

Summary and Conclusions

7.1 Summary

2D and 3D-CFD simulations using commercial CFD code (FLUENT 6.3) for free jet, confined jet, and rotary kiln flames, utilizing axi-symmetric modeling were conducted and presented in order to understand the main operating and geometrical parameters affect the flame behavior (aerodynamics and heat transfer). In free jet flame simulation, 2D modeling is applied on three burner configurations (see Fig. 3.7) using different gases (CH_4, $Biogas$, and CO) as fuels. Free jet flame length and velocity correlations were developed and presented in terms of operating and burner design parameters. These correlations were compared with analytical and experimental correlations from literatures and they have given good agreement. As well, 2D free jet flame simulation is used as a basic and preliminary step for confined jet flame simulation, in addition to select and validate the turbulence model which used in the simulation. Whereas, 2D simulation of confined jet flame was performed also on three recommended flame confinements and burner geometries (see Fig. 3.9) using three gases (CH_4, $Biogas$, and CO) as fuels to simulate the industrial kilns. In this stage, confined flame length correlations were predicted as a function of operational and geometrical parameters. Comparisons between experimental measurements of TECFLAM [105] and numerical results were performed and they have given satisfactory agreement. Finally, in order to avoid undesirable thermal distributions inside the kiln and to improve the kiln efficiency, 3D-CFD full scale rotary kiln flame simulation has presented and discussed. The influence of kiln operating conditions and burner geometrical parameters have been examined on the flame behavior (aerodynamics and heat transfer), using two burner configurations, firing CH_4 gas as a fuel. The results of my research (free jet flame, confined jet flame, and rotary kiln flame simulations) were summarized and presented as follows:

7.1.1 2D-Free Jet Flame Simulation

As demonstrated by the results, the flame length is independent of the inlet fuel velocity (i.e., burner power) and wall-supported burner. On the other hand the air temperature, burner annulus diameter and annulus air swirl number have a considerable effect on the flame length and the peak flame temperature. Whereas, both of the flame length and the peak flame temperature increase with increasing the air temperature, burner annulus diameter and annulus air swirl number. Also as concluded from results, the radiation has a reasonable effect on the flame length and peak flame temperature,

where, the flame temperature drops and the flame length shortens with radiation consideration in flame simulation. On the same way, the flame temperature drops and the flame length shortens if we use N_2 as a recycled gas for NO_x emission controlling. A comparison between three gases (CH_4, $Biogas$, and CO) was performed and discussed. The results show that CO has the highest peak flame temperature and shortest flame length (i.e., smallest flame volume), while CH_4 has the longest flame length (i.e., biggest flame volume) and intermediate peak flame temperature between CO and $Biogas$.

General correlation for (u_o/u_a) was developed in terms of axial distance from burner tip, fuel nozzle diameter, fuel density and average flame density. This correlation can predict 85 % of computed results within error ± 15 %. Also general flame length correlation in dimensionless form (L_f/d_o) in terms of stoichiometric air demand (mass basis) was developed from computed results with maximum error ± 0.73 %. Another flame length correlation in dimensionless form (L_f/d_o) was obtained and presented as a function of stoichiometric mixture fraction, fuel density, and density of stoichiometric mixture. The latter correlation can describe 100 % of numerical results within error ± 9.5 %. Approximated term was introduced into the latter correlation to give new flame length correlation in terms of stoichiometric mixture fraction, fuel to N_2 molecular weight ratio and stoichiometric to fuel absolute temperature ratio, this approximated correlation can give ± 8 % maximum deviation with original predicted correlation. A comparison between predicted flame length correlation from numerical results and experimental correlation from literature was performed and it was found that the maximum deviation obtained was ± 9.4 %.

7.1.2 2D-Confined Jet Flame Simulation

As explained by the results, the flame length increases with increasing of air inlet diameter, primary air swirl number (fully opened cylinder), and burner annulus air diameter. While, the flame length decreases with increasing of excess air number, annulus air swirl number (fully closed cylinder) and with radiation consideration. On the other hand the peak flame temperature increases with increasing the air inlet diameter, and decreases with increasing both of excess air number and radiation consideration. While, the annulus air swirl number and dimensionless annulus diameter (fully opened cylinder) have no effect on the value of peak flame temperature. On the same manner, the peak wall temperature increases with increasing air inlet or secondary air temperatures, and it was higher enough in case of use secondary air linear velocity profile than uniform velocity profile. As well, the primary air swirl side gives higher peak wall temperature than the secondary air swirl side.

Four general dimensionless confined flame length correlations in dimensionless form (L_f/d_o) were obtained and presented in terms of geometrical and operating parameters. The first correlation in terms of stoichiometric air demand (mass basis) and excess air number, this correlation associated with ± 13 % maximum error. The second correlation was a function in stoichiometric mean mixture fraction, fuel density, density of stoichiometric mixture and excess air number and this correlation associated with ± 8 % maximum error. The third correlation in terms of stoichiometric air demand (mass basis), excess air number and dimensionless air inlet diameter. This correlation can describe 83 % of computed results within error ± 11 %. The last correlation was a function in

stoichiometric mean mixture fraction, fuel density, density of stoichiometric mixture, excess air number and dimensionless air inlet diameter. The correlation can describe 98 % of numerical results within error ±11 %. An approximated term was introduced into the second and last correlations by replacing the density ratio term with fuel to N_2 molecular weight ratio multiplied by stoichiometric to fuel absolute temperature ratio term. The approximated correlation using approximation term can give ±8 % maximum deviation with original predicted correlation. Finally, comparisons between experimental measurements of TECFLAM [105] and numerical results were performed, and the computed results give satisfactory agreement with the experiments.

7.1.3   3D-Full Scale Rotary Kiln Flame Simulation

Primary air ratio, burner configuration and burner power were found to have a significant effect of the flame aerodynamics and heat transfer inside the kiln. The higher peak flame temperature, flame radiation heat flux, wall received radiation heat flux and radiative heat transfer coefficient can be obtained by operating the kiln with higher jet momentum, lower primary air ratio and higher burner power. On the other hand, the magnitude and location of the peak wall temperature (wall hot spot) can be relocated by changing the flame aerodynamics, whereas the peak wall temperature can be obtained by operating the kiln at higher burner power and lower jet momentum (larger fuel-inlet diameter). The stable flames and higher recirculation size can be obtained by operating the kiln with higher primary air ratio and higher jet momentum (narrower fuel-inlet diameter). The recirculation was found to have a significant influence on the flame length, whereas the shorter flame length can be obtained by operating the kiln under higher primary air ratio, higher jet momentum and lower burner power with lower jet momentum (larger fuel-inlet diameter). In addition to, the burner power with higher jet momentum (narrower fuel-inlet diameter) has approximately no effect on the flame length. In general, there are no exact comprehensive conditions to be suggested for operating rotary kilns. Depending on the special kiln, the CFD simulation can be applied particularly to optimize a certain aspect of operating practice or design.

7.2   Conclusions

The major conclusions drawn from this study are as follows:

- Realizable k-ϵ turbulence model is the best turbulence model fit with analytical and experimental results for non-premixed flames simulation.

- The operating conditions and burner geometrical parameters such as air temperature, burner annulus diameter, radiation consideration and annulus air swirl number have a significant effect on the free jet flame length and peak flame temperature.

- The confined jet flame length, peak flame temperature and peak wall temperature have strongly influenced by excess air number, air inlet diameter, annulus air swirl number, radiation consideration and burner-annulus air diameter.

- The primary air ratio, burner configuration and burner power were found to have a significant effect of the flame aerodynamics and heat transfer inside the kiln.

- The magnitude and location of peak kiln wall temperature (wall hot spots, whs) can be relocated by adjusting the flame aerodynamics (i.e., adjusting the flame operating conditions).

- Recirculation degree induced by primary jet momentum was found to have a significant effect on the kiln flame length and the wall heat transfer.

- General free jet velocity correlation in dimensionless form (u_o/u_a) was developed in terms of axial distance from burner tip (x), fuel nozzle diameter (d_o), fuel density (ρ_o) and average flame density (ρ).

- General free jet flame length correlation in dimensionless form (L_f/d_o) in terms of stoichiometric air demand$-$mass basis (L) was obtained from computed results with maximum error $\pm 0.73\,\%$.

- General free jet flame length correlation in dimensionless form (L_f/d_o) as a function of stoichiometric mixture fraction (f_{st}), fuel density (ρ_o) and density of stoichiometric mixture (ρ_{st}) was obtained and presented within error $\pm 9.5\,\%$. This correlation gave good agreement in comparison with experimental correlation within error $\pm 9.4\,\%$.

- General dimensionless confined jet flame length correlation (L_f/d_o) was obtained and presented in terms of stoichiometric air demand$-$mass basis (L) and excess air number (λ), this correlation associated with $\pm 13\,\%$ maximum error.

- General dimensionless confined jet flame length correlation (L_f/d_o) was predicted as a function in stoichiometric mean mixture fraction (f_{st}), fuel density (ρ_o), density of stoichiometric mixture (ρ_{st}) and excess air number (λ), and this correlation associated with $\pm 8\,\%$ maximum error.

- General dimensionless confined jet flame length correlation (L_f/d_o) was obtained and presented in terms of stoichiometric air demand$-$mass basis (L), excess air number (λ) and dimensionless air inlet diameter ($d_{a,i}/D$), and this correlation can describe $83\,\%$ of computed results within error $\pm 11\,\%$.

- General dimensionless confined jet flame length correlation (L_f/d_o) was obtained and presented as a function in stoichiometric mean mixture fraction (f_{st}), fuel density (ρ_o), density of stoichiometric mixture (ρ_{st}), excess air number (λ) and dimensionless air inlet diameter ($d_{a,i}/D$). The correlation can describe $98\,\%$ of numerical results within error $\pm 11\,\%$.

Chapter 8

Recommendations for Future Work

During the course of this study, the lack of information on the number of topics became evident. Therefore, the following subjects are recommended for further investigations:

- An experimental investigation with combustion (at a laboratory scale level) should be conducted. In a laboratory scale setup, the operation is better controlled and measurements of flame length, temperature and velocity profiles can be conducted to test the validity of the results reported here. This will be almost impossible in realistic rotary kilns, because of lack of access to the kiln. There are different facilities around the world where a comprehensive scale up study can be conducted.

- CFD and experimental investigations on the combustion aerodynamics and heat transfer inside rotary kilns, in the presence of a reacting bed to provide knowledge on effects such as surface roughness and bed reaction kinetics on the heat transfer. In addition to address detailed design and operating issues such as feed rate and product quality control.

- 3D-CFD simulation of non symmetrical flow in rotary kilns including bed behavior.

- CFD flame simulation in rotary kilns using liquid, solid (coal or waste), alternative (Non-Condensable Gases, NCG, Refuse Derived Fuel, RDF), or combined fuels. In order to understand the kiln performance under different kinds of fuels.

- CFD flame stability in rotary kilns, in order to examine the parameters which affect the flame stability such as recirculation, buoyancy, ...etc.

- CFD optimization for rotary kiln-burner design parameters, such as size and location of primary air ratio, which is strongly affect the thermal distribution inside the kiln.

Bibliography

[1] http://en.wikipedia.org/wiki/Rotary_kiln.

[2] R. Jauhari, M. R. Gray, and J. H. Masliyah, "Gas-solid mass transfer in a rotating drum," *Canadian Journal of Chemical Engineering*, vol. 76, no. 2, pp. 224–232, 1998.

[3] W. J. Peray, K.E., *The Rotary Cement Kiln.* Chemical Publishing Co., New York, 1972.

[4] E. K. W. Manitius, A.and Kursyusz, "Mathematical model of the aluminium oxide rotary kiln," *Chem. Process Des. Develop.*, vol. 13, no. 2, pp. 132–142, 1974.

[5] R. T. Bui, G. Simard, A. Charette, Y. Kocaefe, and J. Perron, "Mathematical modeling of the rotary coke calcining kiln," *Canadian Journal of Chemical Engineering*, vol. 73, no. 4, pp. 534–545, 1995.

[6] M. Georgallis, "Mathematical modeling of lime kilns," Ph.D. dissertation, The University of Britisch Columbia, Vancouver, BC, 2004.

[7] http://www.flsmidth.com.

[8] M. Rovaglio, D. Manca, and G. Biardi, "Dynamic modeling of waste incineration plants with rotary kilns: Comparisons between experimental and simulation data," *Chemical Engineering Science*, vol. 53, no. 15, pp. 2727–2742, 1998.

[9] I. Abe, T. Fukuhara, S. Iwasaki, K. Yasuda, K. Nakagawa, Y. Iwata, H. Kominami, and Y. Kera, "Development of a high density carbonaceous adsorbent from compressed wood," *Carbon*, vol. 39, no. 10, pp. 1485–1490, 2001.

[10] G. San Miguel, G. D. Fowler, M. Dall'Orso, and C. J. Sollars, "Porosity and surface characteristics of activated carbons produced from waste tyre rubber," *Journal of Chemical Technology and Biotechnology*, vol. 77, no. 1, pp. 1–8, 2002.

[11] O. A. Ortiz, G. I. Sua'rez, and A. Nelson, "Dynamic simulation of a pilot rotary kiln for charcoal activation," *Computers and Chemical Engineering*, vol. 29, no. 8, pp. 1837–1848, 2005.

[12] C. A. Cook and V. A. Cundy, "Study of parameters influencing wall-to-bed heat transfer in low-temperature rotary desorbers," *Journal of Energy Resources Technology, Transactions of the ASME*, vol. 117, no. 1, pp. 50–57, 1995.

[13] T. Rensch, "Beitrag zum prozeß der thermischen bodendekontamination im drehrohrofen," Ph.D. dissertation, Uni Magdeburg, Germany, 2001.

[14] C&C ENGINEERING, Inc., http://www.cceng.com.tw/RKI.htm.

[15] P. Barr, "Heat transfer processes in rotary kilns," Ph.D. dissertation, The University of Britisch Columbia, Vancouver, BC, 1986.

[16] A. Aloqaily, "A study of aerodynamics in rotary kilns with two burners," Ph.D. dissertation, University of Toronto, Canada, 2008.

[17] D. W. Dahlstrom, "Innovations in energy conservation for rotary calciners." *Chemical Engineering Progress*, vol. 81, no. 11, pp. 43–47, 1985.

[18] R. Stanev, "Perfection of mixing between gaseous fuel and air in industrial burners-technical and terminological problems," *Journal of the Unevirsity of Chemical Technology and Metallurgy*, vol. 44, no. 4, pp. 395–402, 2009.

[19] http://en.wikipedia.org/wiki/Diffusion_flame.

[20] H. C. Hottel, "Burning in laminar and turbulent fuel jets," *Symposium (International) on Combustion*, vol. 4, no. 1, pp. 97–113, 1953.

[21] W. R. Hawthorne, D. S. Weddell, and H. C. Hottel, "Mixing and combustion in turbulent gas jets," *Symposium on Combustion and Flame, and Explosion Phenomena*, vol. 3, no. 1, pp. 266–288, 1949.

[22] K. Wohl, C. Gazley, and N. Kapp, "Diffusion flames," *Symposium on Combustion and Flame, and Explosion Phenomena*, vol. 3, no. 1, pp. 288–300, 1949.

[23] H. A. Becker and D. Liang, "Visible length of vertical free turbulent diffusion flames," *Combustion and Flame*, vol. 32, no. C, pp. 115–137, 1978.

[24] M. A. Delichatsios, "Transition from momentum to buoyancy-controlled turbulent jet diffusion flames and flame height relationships," *Combustion and Flame*, vol. 92, no. 4, pp. 349–364, 1993.

[25] T. R. Blake and M. McDonald, "An examination of flame length data from vertical turbulent diffusion flames," *Combustion and Flame*, vol. 94, no. 4, pp. 426–432, 1993.

[26] S. R. Turns and R. Bandaru, "Oxides of nitrogen emissions from turbulent hydrocarbon/air jet diffusion flames," in *Final Report- Phase II, GRI 92/0470, Gas Research Institute*, September 1992.

[27] S. R. Turns and F. H. Myhr, "Oxides of nitrogen emissions from turbulent jet flames: Part i - fuel effects and flame radiation," *Combustion and Flame*, vol. 87, no. 3-4, pp. 319–335, 1991.

[28] U. Hegde, Z.-g. Yuan, D. Stocker, and M. Y. Bahadori, "Characteristics of non-premixed turbulent flames in microgravity," N. C. P. (10194), Ed., 1997, pp. 185–190.

[29] N. Peters, *Turbulent Combustion.* Cambridge University, Cambridge, United Kingdom, 2000.

[30] P. B. L. F. D. Moles, D. Watson, "The aerodynamics of the rotary cement kiln," *Journal of the Institute of Fuel*, pp. 353–362, 1973.

[31] A. H. Alyaser, "Fluid flow and combustion in rotary kilns," Ph.D. dissertation, The University of Britisch Columbia, Vancouver, Canada, 1998.

[32] http://www.metso.com.

[33] http://www.coen.com.

[34] http://www.northstarcombustion.com.

[35] http://www.unitherm.co.at.

[36] http://www.khd.com.

[37] http://www.fctinternational.com.

[38] http://www.pillard.de.

[39] http://www.grecoenfil.com.

[40] http://www.polysius.com.

[41] R. Curtet, "Confined jets and recirculation phenomena with cold air," *Combustion and Flame*, vol. 2, no. 4, pp. 383–411, 1958.

[42] W. Ruhland, "Investigation in the cement rotary kiln," *Journal of the Institute of Fuel*, vol. 40, pp. 69–75, 1967.

[43] F. P. Ricou and D. B. Spalding, "Measurements of entrainment by axisymmetrical turbulent jets," *J. Fluid Mech.*, vol. 11, pp. 21–32, 1961.

[44] M. W. Thring and M. P. Newby, "Combustion length of enclosed turbulent jet flames," *4th Int. Symposium on Combustion*, pp. 789–796, 1953.

[45] J. O. Hinze, *Turbulence.* McGraw-Hill, Inc., second edition, 1975.

[46] A. Craya and R. Curtet, "On the spreading of a confined jet," *C. R., Acad. Sci, Paris*, vol. 241, pp. 621–622, 1955.

[47] A. A. Boateng, *Rotary Kilns Transport Phenomena and Transport Processes.* Elsevier Inc., Oxford, UK, 2008.

[48] H. C. Hottel and A. Sarofim, *Radiative Transfer.* McGraw-Hill, Inc., New York, N. Y., 1967.

[49] J. P. Gorog, J. K. Brimacombe, and T. N. Adams, "Radiative heat transfer in rotary kilns," *Metallurgical Transactions B*, vol. 12, no. 1, pp. 55–70, 1981.

[50] H. C. Hottel and E. S. Cohen, "Radiant heat exchange in a gas-filled enclosure: Allowance for nonuniformity of gas temperature," *Transactions of the Institution of Chemical Engineers*, vol. 4, no. 1, pp. 3–14, 1958.

[51] B. G. Jenkins and F. D. Moles, "Modelling of heat transfer from a large enclosed flame in a rotary kiln." *Transactions of the Institution of Chemical Engineers*, vol. 59, no. 1, pp. 17–25, 1981.

[52] J. P. Gorog, "Radiative heat transfer in rotary kilns," Ph.D. dissertation, The University of British Columbia, Vancouver, BC, 1981.

[53] F. Kreith, *Principles of Heat Transfer*. Harper and Row, New York, N. Y., 1973.

[54] V. Venkateswaran and J. K. Brimacombe, "Mathematical model of the sl/rn direct reduction process," *Metallurgical Transactions B*, vol. 8, no. 2, pp. 387–398, 1977.

[55] A. Sass, "Simulation of the heat-transfer phenomena in a rotary kiln," *I and EC Process Design and Development*, vol. 6, no. 4, pp. 532–535, 1967.

[56] J. Riffaud, B. Koehret, and B. Coupal, "Modelling and simulation of an alumina kiln," *Brit. Chem. Eng.& Proc. Tech.*, vol. 17, no. 5, pp. 413–419, 1972.

[57] K. Pearce, "A heat transfer model for rotary kilns," *Journal of the Institute of Fuel*, pp. 363–371, 1973.

[58] M. Imber and V. Paschkis, "A new theory for a rotary-kiln heat exchanger," *International Journal of Heat and Mass Transfer*, vol. 5, no. 7, pp. 623–638, 1962.

[59] A. P. Watkinson and J. K. Brimacombe, "Heat transfer in a direct-fired rotary kiln - 2. heat flow results and their interpretation." *Metall Trans B*, vol. 9 B, no. 2, pp. 209–219, 1978.

[60] V. I. Golovichev and V. A. Yasakov, "Analysis of a reacting submerged hydrogen jet," *Combustion, Explosion, and Shock Waves*, vol. 8, no. 1, pp. 41–56, 1974.

[61] V. K. Baev, P. P. Kuznetsov, I. A. Mogil'nyi, P. K. Tret'yakov, and V. A. Yasakov, "Length of diffusion flames," *Combustion, Explosion, and Shock Waves*, vol. 10, no. 4, pp. 420–426, 1974.

[62] G. G. Shevyakov and V. F. Komov, "Effect of non-combustible admixtures on length of an axisymmetric on-port turbulent diffusion flame," *Combustion, explosion and shock waves*, vol. 13, pp. 563–566, 1977.

[63] R. Günther, *Gaswärme*, vol. 15, p. 376, 1966.

[64] G. T. Kalghatgi, "Lift-off heights and visible lengths of vertical turbulent jet diffusion flames in still air," *Combustion Science and Technology*, vol. 41, pp. 17–29, 1984.

[65] R. W. Wade and J. P. Gore, "Visible and chemical flame lengths of acetylene/air jet diffusion," N. I. of Standards and M. Technology. Annual Conference on Fire Research: Book of Abstracts, Gaithersburg, Eds., October 28-31, 1996, pp. 41–42.

[66] V. H. Morcos and Y. M. Abdel-Rahim, "Parametric study of flame length characteristics in straight and swirl light-fuel oil burners," *Fuel*, vol. 78, no. 8, pp. 979–985, 1999.

[67] B. Choi and H. Kim, "Comparison of theoretically and experimentally determined simulated coal syngas turbulent jet flame lengths," *Journal of Industrial and Engineering Chemistry*, vol. 8, no. 6, pp. 578–585, 2002.

[68] H. N. Mogi, T. and S. Horiguchi, "Flame characteristics of high-pressure hydrogen gas jet," in *Proceedings of the 1st ICHS, Pisa.*, Septemper 2005.

[69] V. Molkov, "Hydrogen non-reacting and reacting jets in stagnant air: Overview and state-of-the-art," in *10th International Conference on Fluid Control, Measurements, and Visualization, Moscow, Russia*, August 17-21, 2009.

[70] A. Pinto and S. R. Gollahalli, *Proc. Okla. Acad. Sci.*, vol. 59, pp. 64–69, 1979.

[71] W. Yang and W. Blasiak, "Chemical flame length and volume in liquified propane gas combustion using high-temperature and low-oxygen-concentration oxidizer," *Energy and Fuels*, vol. 18, no. 5, pp. 1329–1335, 2004.

[72] A. Sinha, R. Ganguly, and I. K. Puri, "Control of confined nonpremixed flames using a microjet," *International Journal of Heat and Fluid Flow*, vol. 26, no. 3, pp. 431–439, 2005.

[73] H. K. Kim, Y. Kim, S. M. Lee, and K. Y. Ahn, "Studies on combustion characteristics and flame length of turbulent oxy-fuel flames," *Energy and Fuels*, vol. 21, no. 3, pp. 1459–1467, 2007.

[74] A. Aloqaily, D. C. S. Kuhn, P. Sullivan, and H. Tran, "Flame length in lime kilns with a separate noncondensible gas burner," *Tappi Journal*, vol. 6, no. 12, pp. 21–26, 2007.

[75] B. F. Magnussen, "Prediction of characteristics of enclosed turbulentjet flames," *Symposium (International) on Combustion*, vol. 14, no. 1, pp. 553–565, 1973.

[76] B. R. Pai, W. Richter, and T. M. Lowes, "Flow and mixing in confined axial flows." *J Inst Fuel*, vol. 48, no. 397, pp. 185–196, 1975.

[77] J. Perron, T. H. Nguyen, L. Castonguay, and R. T. Bui, "Optimization of coke calcining kiln operation using mathematical modelling," T. M. M. . M. S. T. Light Metals 1990, Ed. by C. M. Bickert, Ed., 1990, pp. 559–563.

[78] C. B. Leger, V. A. Cundy, and A. M. Sterling, "A three-dimensional detailed numerical model of a field-scale rotary kiln incinerator," *Environmental Science and Technology*, vol. 27, no. 4, pp. 677–690, 1993.

[79] Y. Y. Chen and D. J. Lee, "A steady state model of a rotary kiln incinerator," *Hazardous Waste and Hazardous Materials*, vol. 11, no. 4, pp. 541–559, 1994.

[80] A. A. Boateng and P. V. Barr, "A thermal model for the rotary kiln including heat transfer within the bed," *International Journal of Heat and Mass Transfer*, vol. 39, no. 10, pp. 2131–2147, 1996.

[81] E. Mastorakos, A. Massias, C. D. Tsakiroglou, D. A. Goussis, V. N. Burganos, and A. C. Payatakes, "Cfd predictions for cement kilns including flame modelling, heat transfer and clinker chemistry," *Applied Mathematical Modelling*, vol. 23, no. 1, pp. 55–76, 1999.

[82] M. A. Martins, L. S. Oliveira, and A. S. Franca, "Modeling and simulation of petroleum coke calcination in rotary kilns," *Fuel*, vol. 80, no. 11, pp. 1611–1622, 2001.

[83] F. Marias, "A model of a rotary kiln incinerator including processes occurring within the solid and the gaseous phases," *Computers and Chemical Engineering*, vol. 27, no. 6, pp. 813–825, 2003.

[84] A. Ma, J. Zhou, J. Ou, and W. Li, "Cfd prediction of physical field for multi-air channel pulverized coal burner in rotary kiln," *Journal of Central South University of Technology (English Edition)*, vol. 13, no. 1, pp. 75–79, 2006.

[85] V. G. Torgunakov, "3d simulation in ir thermographic inspection of rotary kilns," *Russian Journal of Nondestructive Testing*, vol. 42, no. 1, pp. 1–11, 2006.

[86] S. Wang, J. Lu, W. Li, J. Li, and Z. Hu, "Modeling of pulverized coal combustion in cement rotary kiln," *Energy and Fuels*, vol. 20, no. 6, pp. 2350–2356, 2006.

[87] K. S. Mujumdar and V. V. Ranade, "Simulation of rotary cement kilns using a one-dimensional model," *Chemical Engineering Research and Design*, vol. 84, no. 3 A, pp. 165–177, 2006.

[88] K. S. Mujumdar, K. V. Ganesh, S. B. Kulkarni, and V. V. Ranade, "Rotary cement kiln simulator (rocks): Integrated modeling of pre-heater, calciner, kiln and clinker cooler," *Chemical Engineering Science*, vol. 62, no. 9, pp. 2590–2607, 2007.

[89] U. Kssel, D. Abel, M. Schumacher, and M. Weng, "Modeling of rotary kilns and application to limestone calcination," I. Proceedings 7th Modelica Conference, Como, Ed., Sep. 20-22, 2009, pp. 814–822.

[90] T. P. Bhad, S. Sarkar, A. Kaushik, and S. Herwadkar, "Cfd modeling of a cement kiln with multi channel burner for optimization of flame profile," in *Seventh International Conference on CFD in the Minerals and Process Industries, CSIRO, Melbourne, Australia*, 9-11 December 2009.

[91] J. E. Macphee and J. M. T. E. Sellier, M., "Cfd modelling of pulverized coal combustion in a rotary lime kiln," in *Seventh International Conference on CFD in the Minerals and Process Industries, CSIRO, Melbourne, Australia*, 9-11 December 2009.

[92] P. R. Davies, M. J. S. Norton, D. I. Wilson, J. F. Davidson, and D. M. Scott, "Gas flow in rotary kilns," *Particuology*, vol. 8, no. 6, pp. 613–616, 2010.

[93] K. S. Stadler, J. Poland, and E. Gallestey, "Model predictive control of a rotary cement kiln," *Control Engineering Practice*, vol. 19, no. 1, pp. 1–9, 2011.

[94] R. V. Vichnevetsky, *Computer Methods for Partial Differential Equations.* Prentice Hall, Englewood Cliffs, NJ, 1981.

[95] F. Inc., *FLUENT 6.3 User's Guide, Tutorial Guide, FLUENT User Services Center.* Fluent Inc., Lebanon, NH, 2006.

[96] T. H. Shih, W. W. Liou, A. Shabbir, Z. Yang, and J. Zhu, "A new k-ϵ eddy viscosity model for high reynolds number turbulent flows," *Computers and Fluids*, vol. 24, no. 3, pp. 227–238, 1995.

[97] R. Jeschar and R. Alt, *Ähnlichkeitstheoretische Herleitung der Gesetze für den unverdrallten, isothermen Freistrahl.* Institut für Energieverfahrenstechnik und Brennstofftechnik, TU Clausthal, 1997.

[98] W. Meier, R. S. Barlow, Y. . Chen, and J. . Chen, "Raman/rayleigh/lif measurements in a turbulent ch4/h2/n2 jet diffusion flame: Experimental techniques and turbulence-chemistry interaction," *Combustion and Flame*, vol. 123, no. 3, pp. 326–343, 2000.

[99] E. Specht, *Lecture Note of Combustion Technology.* University of Magdeburg, Germany, 2008.

[100] A. Giese, "Nummerische untersuchungen zur bestimmung der flammenlängen in drehrohröfen," Ph.D. dissertation, Otto-von-Guericke-Universität Magdeburg, Magdeburg, Deutschland, 2003.

[101] E. Specht, *Lecture Note of air pollution control.* University of Magdeburg, Germany, 2009.

[102] J. Charles E. Baukal, *Industrial burners handbook.* CRC Press LLC, United States of America, 2004.

[103] P. D. Sunavala, C. Hulse, and M. W. Thring, "Mixing and combustion in free and enclosed turbulent jet diffusion flames," *Combustion and Flame*, vol. 1, no. 2, pp. 179–193, 1957.

[104] A. Frassoldati, S. Frigerio, E. Colombo, F. Inzoli, and T. Faravelli, "Determination of nox emissions from strong swirling confined flames with an integrated cfd-based procedure," *Chemical Engineering Science*, vol. 60, no. 11, pp. 2851–2869, 2005.

[105] TECFLAM cooperation, www.tu-darmstadt.de/fb/mb/ekt/tecflam.

[106] J. Charles E. Baukal, *Heat Transfer in Industrial Combustion.* CRC Press LLC, United States of America, 2000.

Curriculum Vitae

Personal Information

Name:	Hassan Elattar
Birth date:	24.09.1976 in Cairo, Egypt
Nationality:	Egyptian
E-mail:	hassanelattar@yahoo.com
Social status:	Married, 2 children

Education

Oct. 2008 - Sep. 2011	Ph.D. in Engineering (Dr.-Ing.), Faculty of Process and System Engineering, Otto-von-Guericke-Magdeburg University, Magdeburg, Germany.
March 2001 - July 2006	M.Sc. in Mechanical Engineering Technology, Benha High Institute of Technology, Benha University, Benha, Egypt.
Sep. 1994 - Aug. 1999	B.Sc. in Mechanical Engineering Technology, Benha High Institute of Technology, Benha University, Benha, Egypt.
Sep. 1991 - Aug. 1994	Secondary school, Cairo, Egypt.
Sep. 1989 - Aug. 1991	Primary school, Cairo, Egypt.
Sep. 1983 - Aug. 1989	Elementary school, Cairo, Egypt.

Professional Occupation

March 2000 - July 2006	Demonstrator at Benha High Institute of Technology, Benha university, Benha, Egypt.
July 2006 - Sep. 2008	Assistant lecturer at Benha High Institute of Technology, Benha university, Benha, Egypt.
Oct. 2008 - Sep. 2011	Scientific assistant (Ph.D student) at Otto-von-Guericke-Magdeburg University, Magdeburg, Germany.

Field of Interest

- CFD flame simulation in industrial furnaces
- Refrigeration and air conditioning systems